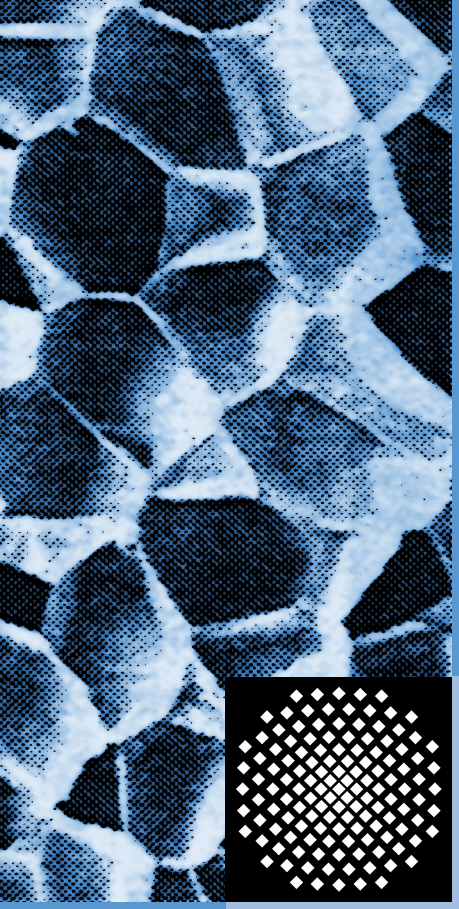

Universität Stuttgart
Germany

Institut für Mechanik (Bauwesen)
Lehrstuhl für Kontinuumsmechanik
Prof. Dr.-Ing. Dr. h. c. W. Ehlers

Partially Saturated Porous Solids under Dynamic Hydraulic Fracturing

Alixa Sonntag

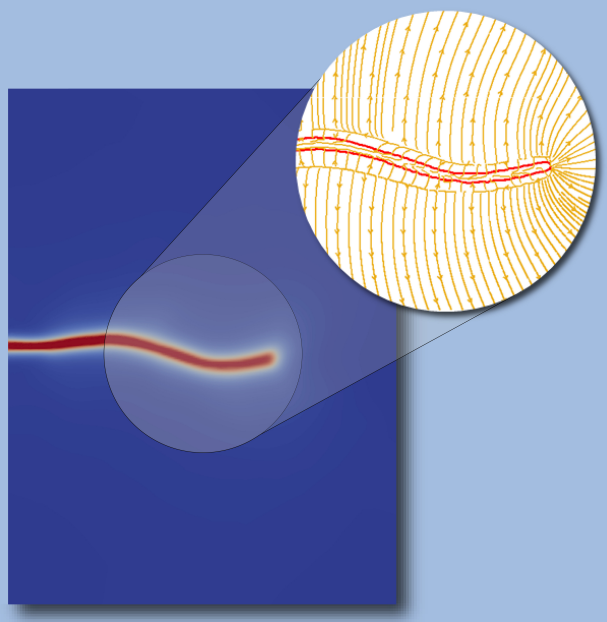

Report No.: II-40 (2023)

Partially Saturated Porous Solids under Dynamic Hydraulic Fracturing

Von der Fakultät Bau- und Umweltingenieurwissenschaften
sowie dem Stuttgarter Zentrum für Simulationswissenschaft
der Universität Stuttgart zur Erlangung der Würde
einer Doktor-Ingenieurin (Dr.-Ing.)
genehmigte Abhandlung

vorgelegt von

Alixa Sonntag

aus
München

Hauptberichter:	Prof. Dr.-Ing. Dr. h. c. Wolfgang Ehlers
Mitberichterin:	Prof. Dr. Laura De Lorenzis
Mitberichter:	Priv.-Doz. Dr.-Ing. Arndt Wagner

Tag der mündlichen Prüfung: 24. November 2023

Institut für Mechanik (Bauwesen) der Universität Stuttgart
Lehrstuhl für Kontinuumsmechanik
Prof. Dr.-Ing. H. Steeb

2023

Report No. II-40
Institut für Mechanik (Bauwesen)
Lehrstuhl für Kontinuumsmechanik
Universität Stuttgart, Germany, 2023

Editor:
Prof. Dr.-Ing. Dr. h. c. W. Ehlers

Institut für Mechanik (Bauwesen)
Lehrstuhl für Kontinuumsmechanik
Universität Stuttgart
Pfaffenwaldring 7
70569 Stuttgart, Germany

ISBN 978 – 3 – 937399 – 40 – 9
(D 93 – Dissertation, Universität Stuttgart)

Acknowledgements

I completed this thesis during my time as a research assistant at the Institute of Applied Mechanics (Civil Engineering), Chair of Continuum Mechanics, at the University of Stuttgart. I express my deepest gratitude to all of those who supported me and contributed in many ways to the realisation of this work.

First and foremost, I sincerely thank my supervisor Professor Wolfgang Ehlers for his outstanding lead throughout my entire doctoral work. His structured way of working and rigorous regard to scientific questions has significantly guided my work. I am also very thankful for his appreciative approach, and the cordial atmosphere that he created for my research.

I also thank Professor Laura De Lorenzis for her interest in my work. Her inspiring publications have had a significant influence on my work, and I was honoured that she evaluated my thesis.

Furthermore, I express my deep appreciation to Priv.-Doz. Dr.-Ing. Arndt Wagner for his constant assistance, enthusiasm, and valuable advice. He always had an open ear for all my concerns. I am very grateful to him for that.

I thank Professor Holger Steeb and all my former and current colleagues at the Institute of Applied Mechanics for providing such a helpful and congenial working atmosphere. I fully enjoyed my time at the institute. I thank all my colleagues for their willingness to share experiences and knowledge of many formal, scientific, and programming issues. As well, I'm deeply grateful for all the private chats that made even the challenging times cheerful.

Moreover, I thank the members of the SFB 1313 for the friendly atmosphere during the conferences and seminars. Special thanks belong to Professor Rainer Helmig for many lively and fruitful discussions, which helped me improve this thesis.

I thank my wonderful family for their limitless support, and their belief and trust in me. Their understanding and empathy in every respect encouraged me to keep going until I reached my goal.

Also, I thank all my friends for the many encouragements they have given me and the balance they created outside work.

Finally, my deepest thanks to my husband Florian for his unconditional support. His great understanding and his comforting patience over the years have brought me calm in every situation.

Stuttgart, November 2023 Alixa Sonntag

Contents

Deutschsprachige Zusammenfassung

Hydraulic-Fracturing (deutsch auch hydraulische Risserzeugung genannt) ist eine Verfahrenstechnik, um die Durchlässigkeit des Gesteins zu erhöhen. Dabei wird das sogenannte Fracking-Fluid – eine Suspension aus Wasser, Stützmitteln und Additiven – unter hohem Druck über eine Zugangsbohrung in den Boden gepresst, um bestehende Risse im Gestein zu erweitern bzw. neue Risse zu erzeugen. Die hydraulische Risserzeugung wird für eine Vielzahl von Anwendungen in gesättigten und ungesättigten porösen Materialien eingesetzt, wie zum Beispiel bei der Förderung fossiler Energieträger, bei der Tiefen-Geothermie, bei der Erschließung tiefer Grundwasservorkommen und bei der Abfallentsorgung. Obwohl diese Technik in der Praxis weit verbreitet ist, wird das Verfahren kontrovers diskutiert. Gegenüber wirtschaftlichen Vorteilen stehen Umwelt- und Gesundheitsrisiken wie die Verunreinigung von Grundwasser, die Freisetzung von Treibhausgasen oder die Gefahr von Mikroerdbeben. Die Anwendungen beruhen in erster Linie auf empirischen Methoden, da die Wechselwirkungen bei der hydraulischen Risserzeugung wissenschaftlich noch nicht vollständig erfasst sind. Die erwähnten Risiken des Verfahrens verdeutlichen die Relevanz, den Rissprozess zu verstehen, um das Gefährdungspotential weitestgehend ausschließen zu können. Eine Herausforderung ist die komplexe, mehrphasige Gesteinszusammensetzung im Untergrund, welche aufgrund der schwierigen Zugänglichkeit nicht direkt beobachtet werden kann. Es ist deshalb wichtig, ein effizientes Modell und Simulationsverfahren für fluidgetriebene Risse zu entwickeln, um ein besseres Verständnis der Wirkzusammenhänge zu erlangen und somit Verfahrensrisiken präventiv vorbeugen zu können.

Hydraulisch induzierte Risse in vollständig gesättigten porösen Materialien wurden bereits umfangreich untersucht. Diese Dissertation erweitert das Verständnis gekoppelter Rissprozesse in teilgesättigen porösen Medien basierend auf der Entwicklung eines theoretischen Modells. In diesem Fall ist der Porenraum des Festkörperskeletts nun sowohl mit einer inkompressiblen Flüssigkeit, wie Wasser oder Öl, als auch mit einem kompressiblen Porengas, wie Luft oder Erdgas, gefüllt. Hierzu müssen zwei Phänomene gleichzeitig betrachtet und gekoppelt werden: Einerseits die mehrphasigen Wechselwirkungen zwischen Festkörper und Fluiden im porösen Medium und anderseits die Rissentstehung und -ausbreitung im Festkörperskelett.

Die Theorie Poröser Medien (TPM) ermöglicht eine konsistente Formulierung des gekoppelten Verhaltens der drei oben genannten Phasen. Der Aufbau des kontinuumsmechanischen Modells basiert auf den Grundsätzen der Thermodynamik. Über eine virtuelle statistische Homogenisierung der Elementarvolumina wird ein makroskopisches Modell mit sich überlagernden Konstituierenden geschaffen. Durch die Einführung von Volumenanteilen wird die lokale Zusammensetzung weiterhin berücksichtigt. Für jeden Bestandteil des porösen Mediums werden in der TPM eine individuelle Bewegungsfunktion und ein spezifischer Satz an Bilanzgleichungen betrachtet. Letztere sind über sogenannte Produktionsterme miteinander gekoppelt. In Hinblick auf hydraulische Risserzeugung ermöglicht dieses Vorgehen die Kopplung der Festkörperverformung mit dem Druckfeld

des injizierten Fluids. Somit kann der Einfluss der Injektion (besser gesagt der Druck des injizierten Fluids) auf das Verzerrungsfeld des Festkörpers beschrieben werden, welches wiederum die Rissausbreitung hervorruft.

Um den Bruchprozess im porösen Medium einzubeziehen, wird die Phasenfeldmethode in das zuvor erarbeitete TPM-Modell eingebettet. Dabei wird mithilfe einer skalaren Variable – das Phasenfeld – zwischen intaktem und gerissenem Zustand des Festkörperskeletts unterschieden. Durch einen Längenskalenparameter wird das Phasenfeld geglättet, was eine kontinuierliche Übergangszone zwischen intaktem und vollständig gerissenem Material ermöglicht. Dieser Ansatz vermeidet Sprünge im Bruchprozess und erleichtert somit die numerische Umsetzung. Das Phasenfeld wird als Prozessvariable eingeführt und in die Formulierung des Helmholtz-Potentials integriert. Letzteres basiert auf einer spektralen Zerlegung der Festkörperverzerrung, so dass das Phasenfeld die elastische Energie allein unter Zug und nicht unter Druck verringert. Darüber hinaus wird für die Phasenfeldvariable eine Evolutionsgleichung vom Typ Ginzburg-Landau in den Satz der Bilanzgleichungen aufgenommen. Um die Irreversibilität des Bruchprozesses zu gewährleisten, wird ein lokales Geschichtsfeld eingeführt, welches den Maximalwert der spannungsinduzierten Festkörperenergie aufzeichnet.

Weiterhin wird das Modell um den sogenannten Crack-Opening-Indicator innerhalb der konstitutiven Beziehungen der Fluide erweitert. Dieses Verfahren ermöglicht die Unterscheidung zwischen offenen und geschlossenen Rissen, begleitet von einem bidirektionalen Wechsel zwischen einer Darcy-Strömung im intakten porösen Bereich und einer Navier-Stokes-Strömung in vollständig gebrochenen Gebieten. Neben dem veränderlichen Flussverhalten spielt auch der Fluiddruck im teilgesättigten Medium eine wichtige Rolle und wird in dieser Dissertationsschrift ausführlich untersucht. In teilweise gesättigten porösen Materialien interagieren die flüssigen und gasförmigen Phasen im Gleichgewichtszustand unter Kapillarkräften. Dieses Verhalten wird z. B. durch die bekannten Modelle von Brooks und Corey oder van Genuchten beschrieben. Da es sich bei der Injektion und den hydraulischen Rissvorgängen allerdings um einen hochdynamischen Prozess handelt, sind die üblichen hydromechanischen Beziehungen nicht anwendbar. In dieser Arbeit wird daher eine modifizierte Differenzdruck-Sättigungs-Beziehung ausgearbeitet, die sowohl statische als auch dynamische Prozesse abbildet.

Darüber hinaus basiert die numerische Studie auf der Finite-Elemente-Methode. Die gekoppelten partiellen Differentialgleichungen werden monolithisch mithilfe des numerischen Codes PANDAS gelöst. Es werden verschiedene numerische Beispiele gerechnet. Um die Konsistenz des mehrphasigen Modells zu überprüfen, wird ein Entwässerungsvorgang berechnet und mit experimentellen Daten verglichen. Zur Verifizierung des Bruchmodells werden ferner die Ergebnisse einer Rissausbreitung unter Druck mit den analytischen Ergebnissen der linear-elastischen Bruchmechanik verglichen. Ziel dieser Arbeit ist es, die Relevanz der dreiphasigen Modellierung für Brüche auch unter dynamischen Bedingungen zu verstehen. Hierfür wird – ausgehend von einem einzelnen Riss – das gekoppelte Verformungs- und Bruchverhalten des Festkörperskeletts durch die verschiedenen Energieanteile untersucht. Anschließend wird die Wechselwirkung der Fluide während des Risses umfassend betrachtet. Unter anderem werden eine Gaskompression und ein anschließender Gasrückfluss in den Riss beobachtet. Ein Vergleich der Ergebnisse von

vollständig und teilweise gesättigten Medien verdeutlicht zudem, dass das Einbeziehen gasförmiger Fluide den Rissbildungsprozess verlangsamt. Diese Verlangsamung resultiert aus einem verzögertem Aufbau des Porendrucks, der durch die Kompressibilität des Gases verursacht wird.

Um einen weiteren Schritt in Richtung realistischer Szenarien zu gehen, werden schließlich zwei Arten von Heterogenitäten untersucht.

Erstens werden (globale) Heterogenitäten, die durch äußere Lasten verursacht werden, berücksichtigt. Dieser Fall ist relevant, da Böden und Gesteine in der Natur häufig externen Belastungen ausgesetzt sind, z. B. aufgrund tektonischer und thermischer Spannungen oder durch die Belastung des darüber liegenden Gesteins. Es werden numerische Beispiele mit zwei unterschiedlich orientierten Rissen unter verschiedenen Belastungsbedingungen berechnet und verglichen. Diese Beispiele zeigen die Fähigkeit des Modells, offene und geschlossene Risse zu beschreiben. Das Fließverhalten der flüssigen und gasförmigen Phasen wird für beide Fälle diskutiert.

Zweitens werden (lokale) Heterogenitäten in der porösen Struktur durch die Definition statistisch verteilter, ortsabhängiger Materialparameter betrachtet. Hierbei wird der fluidgetriebene Rissbildungsprozess im homogenen Fall gegenüber einem Modell mit vordefinierten Bereichen höherer Steifigkeit verglichen. Infolgedessen wird im Zweifeld-Modell eine Rissverzweigung beobachtet. Durch eine statistisch verteilte Implementierung der geomechanischen Eigenschaften wird das Modell zusätzlich erweitert. Um den Einfluss dieser Felder zu untersuchen, werden numerische Beispiele mit unterschiedlichen statistischen Korrelationslängen verglichen. Durch die statistisch verteilten Festkörpereigenschaften variieren die lokalen Spannungen räumlich, und der Risspfad weicht charakteristisch ab.

Zusammenfassend wird in dieser Arbeit die Phasenfeldmethode im Rahmen der Theorie Poröser Medien für dynamische Rissvorgänge in teilgesättigten poröser Medien angewendet. Es wird gezeigt, dass die Gasphase die Rissausbreitung verlangsamt. Des Weiteren wird untersucht, inwieweit lokale und globale Heterogenitäten das Riss- und Strömungsverhalten beeinflussen. Das vorgestellte methodische Modell kann für viele Anwendungen, z. B. im Bereich der Geoenergie, genutzt werden.

Abstract

Hydraulic fracturing is a technique, where fracking fluids are pressed into the ground to initiate and open fractures, increasing the rock's permeability. This stimulation technique is used for a wide variety of geophysical applications in saturated and unsaturated porous materials, such as for the exploitation of oil and natural gas, for geothermal purposes, for the stimulation of deep ground-water resources and for waste disposals, to give some examples. Although this technique is widely used in practice, the fracturing process is controversially discussed. The economic benefits conflict with environmental and health hazards, like water contamination, air pollution, the triggering of earthquakes, and resulting risks to public health. In addition, interactions during hydraulic fracturing are scientifically still not well established, and applications are primarily based on empirical methods. The main difficulty is based on the fact that the underground is a complicated matter of rock or soil filled with fluids, such as water and air, and that direct subsurface observation is challenging. The risks of hydraulic fracturing mentioned above highlight the necessity of understanding the fracturing process and the importance of developing an appropriate and efficient model and simulation technique for fluid-driven fractures.

Many contributions consider hydraulically induced fractures in fully saturated porous materials, where a single pore fluid saturates the solid – only a few treat partially saturated media. Based on methodical developments, this doctoral thesis enlarges the understanding of the coupled processes occurring during fluid-driven fracturing in partially saturated porous media, where the pore space of the solid skeleton contains both an incompressible liquid, such as water or oil, and a compressible pore gas, such as air or natural gas. Two main issues are treated simultaneously: the multiphasic nature of solid-fluid interactions in porous media and the crack initiation and propagation in the solid skeleton.

The Theory of Porous Media (TPM) allows a rigorous and consistent formulation of the coupled behaviour of the abovementioned three phases. The setup of the continuum-mechanical model is based on first principles of continuum thermodynamics. Moreover, following a virtual statistical homogenisation over a representative elementary volume, the microscopic structure is smeared out, leading to a macroscopic model of superimposed and interacting continua. The volume-fractions concept considers the local composition. Furthermore, the TPM provides for each constituent of the porous medium an individual motion function and a set of balance equations coupled to each other by introducing so-called production terms. In the context of hydraulic fracturing, this approach enables to couple the deformation of the solid skeleton with the pressure field of the injected fluid under the thermodynamic restrictions of the entropy inequality. Thus, the injection (pressure) triggers the solid strain field, which induces crack propagation.

In addition, considering the fracturing process in porous media, the phase-field approach to fracture is embedded in the previously elaborated TPM model. Thereby, the unbroken and broken states of the solid skeleton are differentiated with a scalar phase-field variable. This variable is smoothened according to a length-scale parameter, leading to a diffuse transition zone between the two extreme states of intact and fully broken material. This

method avoids the occurrence of a discontinuous jump in the fracturing process and facilitates numerical implementation. The phase field is added to the process variables and integrated into the free-energy formulation. The latter is based on a spectral decomposition of the solid strain, such that the phase-field variable reduces the elastic energy only under tension and not under compression. In addition to that, a Ginzburg-Landau-type evolution equation for the phase-field variable is added to the set of balance equations. Therein, a history variable recording the maximum value of the tension-induced solid strain energy is introduced to ensure the irreversibility of the fracturing process.

The model is further enhanced by introducing a crack-opening indicator into the fluid constitutive relations. This procedure enables the distinction between open and closed cracks accompanied by a switch between Darcy-type and Navier-Stokes-type flow situations in the intact porous domain and fully broken areas, respectively. Moreover, special attention is given to the fluid pressure. The liquid and gas phases interact in partially saturated porous material under equilibrium through capillary forces. This behaviour is covered, for example, by the well-known Brooks-Corey or van Genuchten models. However, considering injection is a highly dynamic process, the standard hydromechanical relations do not apply here. Therefore, a modified pressure-difference-saturation relation, mapping both equilibrium and dynamic fluid interactions, is proposed and discussed in this thesis.

The numerical study builds on the Finite-Element Method. The coupled partial differential equations are solved monolithically with the numerical code PANDAS. Different numerical examples are computed. Specifically, to verify the consistency of the multiphasic model, a drainage problem is computed and compared to experimental data. For verifying the fracture model, the results of pressurised crack propagation are compared to analytical ones of linear-elastic fracture mechanics. This thesis aims to understand the relevance of triphasic modelling for fracture under dynamic conditions. Therefore, proceeding from a single crack, the solid skeleton's coupled deformation and fracturing behaviour is examined by considering the different energy proportions. Then, the mutual interaction of the fluids during fracturing is considered in detail. Among others, a gas pressure compression and subsequent gas reflux into the crack are observed. A comparison of fully saturated and partially saturated simulations reveals that the existence of pore gas mainly slows down the fracturing process. This deceleration results from a slower pore pressure build-up induced by the gas compressibility.

Finally, two kinds of heterogeneities are assessed, going one step further towards realistic scenarios.

First, (global) heterogeneities caused by external loads are evaluated. This case is relevant as soils and rocks are frequently under external stresses in nature, i. e. due to the loading of overlying rocks or tectonic and thermal stresses. Numerical examples with two differently oriented cracks are computed under distinct loading conditions, and the results are compared. These examples show the model's capability to describe open and closed cracks and lead to a discussion of the flow behaviour of the liquid and gas phases in both cases.

Second, (local) heterogeneities in the porous structure are considered by defining location-

dependent material parameters. In this sense, a fluid-driven fracturing process with predefined imperfection areas of higher stiffness is juxtaposed to the homogenous case. As a result, crack branching is observed in the two-field case. Additionally, the model is improved by implementing statistical fields of geomechanical properties. In order to study the influence of this latter, numerical examples with different statistical correlation lengths are compared. Due to the statistical fields of the solid properties, the local stresses spatially vary, and the crack path deviates characteristically.

In conclusion, this thesis applies the phase-field approach to fracture within the Theory of Porous Media for fully dynamical problems of partially saturated porous media. It is shown that the gas phase slows down the crack propagation and to what extent local and global heterogeneities influence the crack and flow behaviour. The presented methodical and basis-oriented model can be used for various applications.

Nomenclature

The notation in this thesis follows the conventions of modern tensor calculus, such as in Ehlers [79] and de Boer [37]. Furthermore, the particular symbols used in the context of porous-media theories are chosen according to the established nomenclature given by, e. g., de Boer [39] and Ehlers [84, 86].

Conventions

General conventions

$(\bullet)$			placeholder for arbitrary quantities
$a, b, \ldots$	or	$\phi, \psi, \ldots$	scalars (zero-order tensors)
$\mathbf{a}, \mathbf{b}, \ldots$	or	$\boldsymbol{\phi}, \boldsymbol{\psi}, \ldots$	vectors (first-order tensors)
$\mathbf{A}, \mathbf{B}, \ldots$	or	$\boldsymbol{\Phi}, \boldsymbol{\Psi}, \ldots$	tensors of second order

Index and suffix conventions

$i, j, k, n, \ldots$	indices (control variables) as super- or subscripts
$(\bullet)_\alpha$	subscripts indicate kinematic quantities of a constituent within porous-media or mixture theories
$(\bullet)^\alpha$	superscripts indicate non-kinematic quantities of a constituent within porous-media or mixture theories
$(\bullet)_0$	initial values at time t_0
$\dot{(\bullet)} = \mathrm{d}(\bullet)/\mathrm{d}t$	total time derivatives with respect to the overall aggregate φ
$(\bullet)'_\alpha = \mathrm{d}_\alpha(\bullet)/\mathrm{d}t$	material time derivatives following the motion of φ^α
$\mathrm{d}(\bullet)$	differential operator
$\partial(\bullet)$	partial derivative operator
$\delta(\bullet)$	test functions of primary unknowns
$\hat{(\bullet)}$	production terms of mechanical quantities
$\bar{(\bullet)}$	prescribed quantities (boundary conditions)
$(\bullet)^\alpha_{EF}$	extra (effective) quantities of a constituent φ^α
$(\bullet)^\alpha_{EQ}$, $(\bullet)^\alpha_{NEQ}$	equilibrium and non-equilibrium parts of quantities
$(\bullet)^h$	spatially discretised quantities within numerical investigations
$(\bullet)_n$, $(\bullet)_{n+1}$	discretised quantities in time within numerical investigations
$(\bullet)^T, (\bullet)^{-1}$	transposed and inverse form of a tensor

Symbols

Greek letters

Symbol	Unit	Description
α		constituent identifier for L, G, S and F in super- and subscript
β		identifier for the pore fluids L and G in super- and subscript
$\gamma^{\beta R}$	$[\,\mathrm{N/m^3}\,]$	effective weight of a fluid constituent φ^β
γ_s	$[\,\mathrm{N/m}\,]$	surface tension
Γ^S	$[\,1/\mathrm{m}\,]$	fracture energy of the solid per critical energy release rate
δ_i^j		Kronecker symbol or Kronecker delta
ϵ	$[\,\mathrm{m}\,]$	phase-field length-scale parameter
ε, ε^α	$[\,\mathrm{J/kg}\,]$	mass-specific internal energy of φ and φ^α
$\hat{\varepsilon}^\alpha$	$[\,\mathrm{J/m^3\,s}\,]$	volume-specific direct energy production of φ^α
$\varepsilon_i, \varepsilon_{Si}$	[-]	eigenvalues of the (solid) deformation tensor
$\varepsilon_{\text{tol.}}$		pre-defined tolerance used in the Newton solver
$\hat{\zeta}^\alpha$	$[\,\mathrm{J/K\,m^3\,s}\,]$	volume-specific direct entropy production of φ^α
η, η^α	$[\,\mathrm{J/K\,kg}\,]$	mass-specific entropy of φ and φ^α
η_r , η_r^S	[-]	residual (solid) stiffness coefficient
$\hat{\eta}$, $\hat{\eta}^\alpha$	$[\,\mathrm{J/K\,m^3\,s}\,]$	volume-specific total entropy production of φ and φ^α
θ, θ^α	$[\,\mathrm{K}\,]$	absolute Kelvin's temperature of φ and φ^α
κ	[-]	exponent governing the deformation dependency of K^S
κ_r^β	[-]	relative permeability factor of φ^β
λ	[-]	pore size distribution parameter for Brooks-Corey law
λ^S	$[\,\mathrm{N/m^2}\,]$	first Lamé constant of φ^S
μ	$[\,\cdot\,]$	mean value
μ^β, $\mu^{\beta R}$	$[\,\mathrm{N\,s/m^2}\,]$	partial and effective dynamic viscosity of φ^β
μ^{K_G}		weighted scalar voxel information at the Gauss point K_G
μ^S	$[\,\mathrm{N/m^2}\,]$	second Lamé constant of φ^S
π	[-]	circle constant
ρ	$[\,\mathrm{kg/m^3}\,]$	density of the overall aggregate φ
ρ^α, $\rho^{\alpha R}$	$[\,\mathrm{kg/m^3}\,]$	partial and effective (realistic) density of φ^α
$\hat{\rho}^\alpha$	$[\,\mathrm{kg/m^3\,s}\,]$	volume-specific mass production term of φ^α
σ, σ^α		scalar-valued supply terms of mechanical quantities in Chapter 2
σ	$[\,\cdot\,]$	standard deviation in Chapter 5
σ_c	$[\,\mathrm{N/m^2}\,]$	critical tensile stress for crack propagation
σ_η, σ_η^α		volume-specific external entropy supply of φ and φ^α in Chapter 2

τ	$[\,\mathrm{kg/m\,s}\,]$	damping coefficient
Υ		arbitrary field function (steady and steady differentiable)
φ, φ^α		entire aggregate model and particular constituent
ϕ, ϕ^S	$[\,\text{-}\,]$	phase-field variable and solid phase-field variable
ψ, ψ^α	$[\,\mathrm{J/kg}\,]$	mass-specific Helmholtz free energy of φ and φ^α
$\psi_0^\pm$	$[\,\mathrm{J/kg}\,]$	mass-specific tensile/compression energy
Ψ, Ψ^α	$[\,\cdot/\mathrm{m}^3\,]$	volume-specific densities of scalar mechanical quantities
$\hat{\Psi}$, $\hat{\Psi}^\alpha$	$[\,\cdot/\mathrm{m}^3\,]$	volume-specific productions of scalar mechanical quantities
Ω, $\partial\Omega$		spatial domain and boundary of the aggregate body $\mathcal{B}$
$\partial\Omega_{\boldsymbol{u}}$		domain boundary of a primary variable
$\partial\Omega_D^{\boldsymbol{u}}$		Dirichlet boundary with essential boundary conditions for $\boldsymbol{u}$
$\partial\Omega_N^{(\cdot)}$		Neumann boundary with natural boundary conditions
Ω_e, Ω^h		a finite element and the discretised finite element domain
$\boldsymbol{\sigma}$, $\boldsymbol{\sigma}^\alpha$		vector-valued supply terms of mechanical quantities
$\boldsymbol{\Upsilon}$		arbitrary field function (steady and steady differentiable)
$\boldsymbol{\phi}$, $\boldsymbol{\phi}^\alpha$		vector-valued efflux terms of mechanical quantities
$\boldsymbol{\phi}_\eta$, $\boldsymbol{\phi}_\eta^\alpha$	$[\,\mathrm{J/K\,m^2\,s}\,]$	entropy efflux vector of φ and φ^α
$\boldsymbol{\chi}_\alpha$, $\boldsymbol{\chi}_\alpha^{-1}$		motion and inverse motion functions of the constituents φ^α
$\boldsymbol{\Psi}$, $\boldsymbol{\Psi}^\alpha$	$[\,\cdot/\mathrm{m}^3\,]$	volume-specific densities of vectorial mechanical quantities
$\boldsymbol{\varepsilon}_S$	$[\,\text{-}\,]$	linearised contravariant Green-Lagrangean solid strain tensor
$\boldsymbol{\varepsilon}_S^\pm$	$[\,\text{-}\,]$	linearised solid strain tensor containing only the positive/negative eigenvalues
$\boldsymbol{\mu}$	$[\,\cdot\,]$	mean value field
$\boldsymbol{\sigma}_{EF}^S$	$[\,\mathrm{N/m^2}\,]$	linear effective solid stress
$\boldsymbol{\Sigma}$		covariance matrix with coefficients Σ_{ij}
$\hat{\boldsymbol{\Psi}}$, $\hat{\boldsymbol{\Psi}}^\alpha$	$[\,\cdot/\mathrm{m}^3\,]$	volume-specific productions of vectorial mechanical quantities
$\boldsymbol{\tau}^\alpha$	$[\,\mathrm{N/m^2}\,]$	Kirchhoff stress tensors of φ^α
$\boldsymbol{\Phi}$, $\boldsymbol{\Phi}^\alpha$		general tensor-valued mechanical quantities

Latin letters

Symbol	Unit	Description
a	$[\,\mathrm{m}\,]$	half crack length in Section 5.1.2
a, b, c, d		fitting parameter for pressure-difference-saturation relation
c	$[\,\mathrm{m}\,]$	phase-field regularisation parameter in Section 2.5
$d^{\mathrm{data,n}}$	$[\,\mathrm{m}\,]$	spatial distance of material parameter data to the considered integration point
$\mathrm{d}m^\alpha$	$[\,\mathrm{kg}\,]$	local mass element of φ^α

$\mathrm{d}t$	$[\,\mathrm{s}\,]$	time increment
$\mathrm{d}v$, $\mathrm{d}v^\alpha$	$[\,\mathrm{m}^3\,]$	current volume element of φ and φ^α
$\mathrm{d}V_\alpha$	$[\,\mathrm{m}^3\,]$	reference volume element of φ^α
$\hat{e}^\alpha$	$[\,\mathrm{J/m^3\,s}\,]$	volume-specific total energy production of φ^α
E	$[\,\text{-}\,]$, $[\,\mathrm{N/m^2}\,]$	number of non-overlapping finite elements Ω_e in Chapter 4, Young's modulus elsewhere
E_l	$[\,\mathrm{N/m^2}\,]$	Young's modulus in plain strain cases
F		identifier for the pore fluid constituent with $\varphi^F = \varphi^L$ for fully saturated case, $\varphi^F = \bigcup_\beta \varphi^\beta$ for partially saturated case
g	$[\,\text{-}\,]$	degradation function
G		identifier for the pore gas φ^G
I_{S1}, I_{S2}, I_{S3}	$[\,\text{-}\,]$	principal invariants of the deformation tensors
J_α	$[\,\text{-}\,]$	Jacobian determinant of φ^α
K_{Ic}	$[\,\mathrm{N\,m^{-3/2}}\,]$	fracture toughness under mode I
K_G		integration points for the Gaussian quadrature scheme
K^β	$[\,\mathrm{m/s}\,]$	specific permeability of the fluid constituents φ^β
K_r^β	$[\,\mathrm{m/s}\,]$	relative fluid conductivities
K^S	$[\,\mathrm{m^2}\,]$	isotropic (deformation-dependent) permeability of φ^S
ℓ	$[\,\mathrm{m}\,]$	statistical correlation length
L		identifier for the pore liquid φ^L
n^α, n^β	$[\,\text{-}\,]$	volume fractions of φ^α and φ^β
n^F	$[\,\text{-}\,]$	porosity, total fluid volume fraction
n^S	$[\,\text{-}\,]$	solidity, volume fraction of φ^S
N	$[\,\text{-}\,]$	number of nodal points
N_v	$[\,\text{-}\,]$	number of discretisation points
p_c	$[\,\mathrm{N/m^2}\,]$	critical pore pressure for fracture
p^c, p^C	$[\,\mathrm{N/m^2}\,]$	microscopic and macroscopic capillary pressure
$p^C_{\text{dyn.}}$	$[\,\mathrm{N/m^2}\,]$	dynamic macroscopic capillary pressure
p^D	$[\,\mathrm{N/m^2}\,]$	pressure difference between the pore gas and pore liquid
p^{GR}_{excess}	$[\,\mathrm{N/m^2}\,]$	excess gas pressure
p^{FR}, $p^{\beta R}$	$[\,\mathrm{N/m^2}\,]$	overall pore pressure and fluid pore pressures
p^{nw}, p^w	$[\,\mathrm{N/m^2}\,]$	microscopic pressure of the non-wetting and wetting fluid
P^j		nodal point in a finite element Ω_e
Q^j_{dof}		scalar global basis function of a degree of freedom
r, r^α	$[\,\mathrm{J/kg\,s}\,]$	mass-specific external heat supply (radiation) of φ and φ^α in Chapter 2
r	$[\,\mathrm{m}\,]$	tube's radius of an idealised pore at the microscale in Chapter 3

R	$[\,\mathrm{J/mol\,K}\,]$	universal gas constant
R_{K_G}	$[\,\mathrm{m}\,]$	influence radius for the weighting of voxel information
s^β	$[\,\text{-}\,]$	saturation function of the pore fluids φ^β
s_r^β	$[\,\text{-}\,]$	residual saturation of the pore fluids φ^β
$s_\mathrm{eff.}^L$	$[\,\text{-}\,]$	effective liquid saturation
S		identifier for the solid skeleton constituent φ^S
t, t_0, t_n, t_{n+1}	$[\,\mathrm{s}\,]$	current/initial time and temporally discretised time steps
$\bar{v}^\beta$	$[\,\mathrm{m^3/m^2\,s}\,]$	area-specific volume efflux of φ^β over the boundary
V, V_α	$[\,\mathrm{m^3}\,]$	overall volume of $\mathcal{B}$ and partial volume of $\mathcal{B}^\alpha$
$w^{\mathrm{data,n}}$	$[\,\text{-}\,]$	weight for the voxel information at the considered K_G
W^S	$[\,\mathrm{J/m^3}\,]$	volume-specific solid strain energy function
$W^{S\pm}$	$[\,\mathrm{J/m^3}\,]$	tensile/compression part of the volume-specific solid strain energy W^S
W_e^{S+}	$[\,\mathrm{J/m^3}\,]$	effective tensile elastic energy
$\mathbf{b}$, $\mathbf{b}^\alpha$	$[\,\mathrm{m/s^2}\,]$	mass-specific body force vector
$\mathbf{d}_\alpha$	$[\,\mathrm{m/s}\,]$	diffusion velocity vector of φ^α
$\mathrm{d}\mathbf{a}$	$[\,\mathrm{m^2}\,]$	oriented current area element
$\mathrm{d}\mathbf{A}_\alpha$	$[\,\mathrm{m^2}\,]$	oriented reference area element of φ^α
$\mathrm{d}\mathbf{x}$	$[\,\mathrm{m}\,]$	current line element
$\mathrm{d}\mathbf{X}_\alpha$	$[\,\mathrm{m}\,]$	reference line element of the constituent φ^α
$\mathbf{e}_i$	$[\,\text{-}\,]$	(Cartesian) basis of orthonormal vectors
$\mathbf{f}$, $\mathbf{f}^\alpha$	$[\,\mathrm{N}\,]$	volume force vector acting on $\mathcal{B}$ and $\mathcal{B}^\alpha$ from a distance
$\mathbf{g}$	$[\,\mathrm{m/s^2}\,]$	constant gravitation vector with $\lvert\mathbf{g}\rvert = g = 9.81\,\mathrm{m/s^2}$
$\mathbf{h}$	$[\,\mathrm{kg/m\,s}\,]$	local moment of momentum of the overall aggregate φ
$\hat{\mathbf{h}}^\alpha$	$[\,\mathrm{N/m^2}\,]$	volume-specific total angular momentum production of φ^α
$\mathbf{k}^\alpha$, $\mathbf{k}_c^\alpha$, $\mathbf{k}_v^\alpha$	$[\,\mathrm{N}\,]$	total, contact and volume force element of φ^α
$\hat{\mathbf{m}}^\alpha$	$[\,\mathrm{N/m^2}\,]$	volume-specific direct angular momentum production of φ^α
$\mathbf{n}$	$[\,\text{-}\,]$	outward-oriented unit surface normal vector
$\hat{\mathbf{p}}^\alpha$	$[\,\mathrm{N/m^3}\,]$	volume-specific direct momentum production of φ^α
$\hat{\mathbf{p}}_{EQ}^\alpha$, $\hat{\mathbf{p}}_{NEQ}^\alpha$	$[\,\mathrm{N/m^3}\,]$	volume-specific equilibrium/non-equilibrium direct momentum production of φ^α
$\mathbf{q}$, $\mathbf{q}^\alpha$	$[\,\mathrm{J/m^2\,s}\,]$	heat influx (convection) vector of φ and φ^α
$\hat{\mathbf{s}}^\alpha$	$[\,\mathrm{N/m^3}\,]$	volume-specific total momentum production of φ^α
$\mathbf{t}, \mathbf{t}^\alpha$	$[\,\mathrm{N/m^2}\,]$	surface traction vector of the overall aggregate and φ^α
$\bar{\mathbf{t}}, \bar{\mathbf{t}}^\beta$	$[\,\mathrm{N/m^2}\,]$	surface traction vector of the overall aggregate and φ^β (boundary condition)
$\mathbf{u}_S$	$[\,\mathrm{m}\,]$	solid displacement vector
$\mathbf{w}_\beta$	$[\,\mathrm{m/s}\,]$	seepage velocity vector of φ^β

$\mathbf{x}$	$[\,\mathrm{m}\,]$	current position vector of φ
$\mathbf{X}_\alpha$	$[\,\mathrm{m}\,]$	reference position vector of $\mathcal{P}^\alpha$
$\dot{\mathbf{x}}$, $\ddot{\mathbf{x}}$	$[\,\mathrm{m/s}\,]$, $[\,\mathrm{m/s^2}\,]$	barycentric velocity and acceleration of the aggregate φ
$\overset{\prime}{\mathbf{x}}_\alpha = \mathbf{v}_\alpha$, $\overset{\prime\prime}{\mathbf{x}}_\alpha$	$[\,\mathrm{m/s}\,]$, $[\,\mathrm{m/s^2}\,]$	velocity and acceleration of the constituent φ^α
$\mathbf{A}_\alpha$	$[\,\text{-}\,]$	contravariant Almansian strain tensor of φ^α (AC)
$\mathbf{B}_\alpha$	$[\,\text{-}\,]$	covariant left Cauchy-Green deformation tensor of φ^α (AC)
$\mathbf{C}_\alpha$	$[\,\text{-}\,]$	contravariant right Cauchy-Green deformation tensor (RC)
$\mathbf{D}_\alpha$	$[\,\cdot/\mathrm{s}\,]$	symmetric deformation velocity tensor of φ^α
$\overset{3}{\mathbf{E}}$	$[\,\text{-}\,]$	Ricci permutation tensor (third-order fundamental tensor)
$\mathbf{E}_\alpha$	$[\,\text{-}\,]$	contravariant Green-Lagrangean strain tensor (RC)
$\mathbf{F}_\alpha$	$[\,\text{-}\,]$	material deformation gradient of φ^α
$\mathbf{I}$	$[\,\text{-}\,]$	identity tensor (second-order fundamental tensor)
$\mathbf{K}^S$	$[\,\mathrm{m^2}\,]$	(anisotropic) intrinsic permeability of φ^S
$\mathbf{L}_\alpha$	$[\,\cdot/\mathrm{s}\,]$	spatial velocity gradient of φ^α
$\mathbf{P}^\alpha$	$[\,\mathrm{N/m^2}\,]$	first Piola-Kirchhoff or nominal stress tensors of φ^α
$\mathbf{Q}^j_{\mathrm{dof}}$		vectorial global basis function of a DOF
$\mathbf{S}^\alpha$	$[\,\mathrm{N/m^2}\,]$	second Piola-Kirchhoff stress tensors of φ^α
$\mathbf{T}$, $\mathbf{T}^\alpha$	$[\,\mathrm{N/m^2}\,]$	overall and partial Cauchy (true) stress tensor of φ and φ^α
$\mathbf{T}^S_{EF}$	$[\,\mathrm{N/m^2}\,]$	partial Cauchy effective stress tensor of φ^S
$\mathbf{T}^\alpha_{EQ}$, $\mathbf{T}^\alpha_{NEQ}$	$[\,\mathrm{N/m^2}\,]$	equilibrium/non-equilibrium part of the partial Cauchy stress tensor of the constituent φ^α
$\mathbf{W}_\alpha$	$[\,\cdot/\mathrm{s}\,]$	skew-symmetric spin tensor

Calligraphic letters

Symbol	Unit	Description
$\mathcal{A}^{\boldsymbol{u}}$		ansatz (trial) functions of the primary variables
$\mathcal{B}$, $\mathcal{B}^\alpha$		aggregate body and body of the constituent φ^α
$\mathcal{D}$	$[\,\mathrm{J/m^3\,s}\,]$	dissipative part in the entropy inequality
$\mathcal{G}_{\boldsymbol{u}}$		weak formulation of a governing equation related to a DOF
$\mathcal{H}$	$[\,\mathrm{J/kg}\,]$	history variable
$\mathcal{H}^1(\Omega)$		Sobolev space
$\mathcal{O}$		origin of a coordinate system
$\mathcal{P}$, $\mathcal{P}^\alpha$		material points of φ and φ^α
$\mathcal{P}$	$[\,\mathrm{N/m^2}\,]$	Lagrangean multiplier
$\mathcal{R}$		set of response functions

$\mathcal{S}$, $\mathcal{S}^\alpha$	surface of the overall and the constituent body
$\mathcal{T}^{\boldsymbol{u}}$	test functions of the primary variables
$\mathcal{V}, \mathcal{V}^1$	set and reduced subset of independent process variables
$\boldsymbol{f}$	generalised force vector
$\boldsymbol{\mathcal{F}}$	vector containing the global and local system of equations
$\boldsymbol{\mathcal{G}}_{\boldsymbol{u}}$	abstract function vectors containing the weak forms
$\boldsymbol{u}$, $\boldsymbol{u}_1$, $\boldsymbol{u}_2$	abstract vectors containing the set of the primary variables
$\boldsymbol{y}$	abstract vector containing all nodal DOF
$\Delta \boldsymbol{y}_n^k$	vector of stage increments at current Newton step k
$\boldsymbol{\mathcal{D}}$	generalised damping matrix
$\boldsymbol{J}_n^k$	residual tangent (Jacobian matrix) at current Newton step k
$\boldsymbol{\mathcal{K}}$	generalised stiffness matrix
$\boldsymbol{R}_n^k$	non-linear functional of residual at current Newton step k

Selected acronyms

Symbol	Description
2-d, 3-d	two-dimensional, three-dimensional
AC	actual (current) configuration
BC	boundary condition
COI	crack-opening-indicator
DOF	degrees of freedom
FEM	finite-element method
FS	fully saturated
GMRES	generalised minimal residual method
IBVP	initial-boundary-value problem
LBB	Ladyshenskaya-Babuška-Brezzi
LEFM	linear elastic fracture mechanics
PANDAS	Porous media Adaptive Nonlinear finite element solver based on Differential Algebraic Systems
PFM	phase-field method
PS	partially saturated
RAM	random access memory
RC	referential configuration
REV	representative elementary volume
TM	Theory of Mixtures
TPM	Theory of Porous Media

Chapter 1:
Introduction and Overview

1.1 Motivation

Hydraulically induced fractures are frequently used in saturated and unsaturated porous media for several exploitation techniques in the energy sector, even though the control of this technique is still widely based on empirical methods. The main idea is to create, widen and stabilise fractures in the deep subsurface to enhance the rock's permeability. In particular, for electricity generation in enhanced geothermal energy plants, naturally occurring cracks of the rock are widened by the injection of highly pressurised cold water to augment the rock's permeability and, thus, increase the flow rate of heated water at the output, see, e. g., Olasolo *et al.* [204]. Furthermore, in hydrocarbon exploitation, artificial fissures and cracks are created by fluid injections to enhance the availability of oil and gas in subterranean natural reservoirs. Therein, additives like propping agents and chemicals are mixed with high-pressurised water to maintain the fracture open. The development of this technology, also called "fracking", is outlined, e. g., in the book of Smith & Montgomery [224]. Besides these, hydraulically induced fractures are also applied to stimulate deep aquifers for water extraction and for the measurements of *in-situ* stresses, see, Banks *et al.* [17]. Moreover, fluid-driven fractures increase the rock's permeability for waste disposal. Mainly, hydraulically induced fractures enhance the effectiveness of remediating volatile waste contaminants deep into rock. This process is particularly advantageous in the case of soil vapour extraction. The interested reader is referred, e. g., to the work of Frank & Barkley [110]. The permeability's increase due to hydraulic fracturing is also used for carbon reservoir injection and storage processes, compare Fu *et al.* [112] and Huerta *et al.* [145]. Thus, there is a broad application of hydraulically driven cracks in soil and rock.

Nevertheless, the potential environmental effects are disputed issues. Especially in the context of hydrocarbon exploitation, the risk of water contamination is highly discussed, compare, among others, Myers [201], Jackson *et al.* [150], Vidic *et al.* [242], Engelder *et al.* [103] and Birdsell *et al.* [34]. Moreover, the stresses released during the fracturing processes cause micro-seisms, see Howarth *et al.* [144], Kerr [157], Ellsworth [101] and Olasolo *et al.* [204], to name a few. In addition, hydraulic fracturing activity implies health risks, compare, for example, Finkel & Hays [107], Wright & Muma [252] and Bamber *et al.* [16].

A systematic theoretical understanding of fluid-driven fractures in porous media is crucial to enlarge the knowledge of the occurring processes and to prevent severe geological consequences. Though, a fundamental difficulty is that the direct observation of propagating fractures enveloped in the underground is complex, and only a few data are accessible, namely monitoring the pressure variation at the injection pump and recording the acoustic emissions at the soil surface, cf. Secchi & Schrefler [222]. Besides this, scattered subsurface

samples can be analysed; however, these are small and inconclusive regarding the large scale of geological applications.

For this reason, modelling and simulation techniques provide a good option for gaining insight into the fracturing process and preventing severe consequences. In this context, many contributions already consider hydraulically induced fractures in fully saturated porous materials, where a single pore fluid percolates the pore space. Nonetheless, some hydraulic fracturing techniques are also used in a partially saturated porous material, see, for example, the work of Bruner & Smosna [59] and Engelder [102] for the shale-gas extraction and the work of Frank & Barkley [110] for the waste remediation in the vadose zone. This thesis aims to model and discuss fracturing porous solids with arbitrary pore content to understand better the importance of triphasic modelling under dynamic conditions, where a liquid and gaseous fluid fill the pore space of the deformable solid skeleton.

1.2 Scope, Aims and State of the Art

Hydraulic fracturing describes a process of fracture initiation and propagation driven by pressing fracking fluids into the pore space of porous media, such as soil or rock. In the past decades, several numerical models on the continuum and the meso- and micro-scales have been developed to describe fluid-driven fracture propagation scenarios. An overview and discussion of the different approaches can be found, for example, in Lecampion *et al.* [168]. Modelling a hydraulic fracturing process, even in its simplest form, is challenging. The main difficulty relies on the fact that two complex issues have to be treated simultaneously. On the one hand, the strongly coupled behaviour of the deformable porous material with arbitrary pore content has to be characterised adequately. On the other hand, the fracturing process of the solid skeleton and its impact on the fluid flow have to be modelled. Following this, the development of numerical techniques for hydraulic fracturing scenarios is driven by advances in both issues, porous-media modelling and fracture mechanics. This thesis restricts to continuum mechanics, refer, e. g., to the work of Gurtin [123], Haupt [131, 132], Malvern [181] and Chadwick [63]. In contrast, fracture models based on multiscale models, cf., e. g., Belytschko *et al.* [24], Nguyen *et al.* [203], molecular dynamics, cf., e. g., Holian & Ravelo [141], Rountree *et al.* [212], and lattice models, cf., e. g., Pan *et al.* [207], Schlangen & Van Mier [218], to name a few, are left out. The interested reader of these approaches is referred to the citations above and references therein.

Porous media modelling

First, it is necessary to model the mechanical behaviour, particularly the deformation, of the underlying porous material and the interaction between the multiple components of the medium. Thereby, it is worth mentioning that the porous medium consists of a solid skeleton containing an interconnected pore space filled with arbitrary fluids in which they can flow. The inner pore structure is usually unknown when dealing with geomaterials such as soil or rock. Thus, resolving the inner geometry and describing these materials

with the standard singlephasic continuum mechanics is not possible. It is, therefore, convenient in most applications to proceed with a homogenisation technique and model the material as a multiphasic aggregate on the macroscale. There are two main approaches to describe this multi-component and multiphasic nature of solid-fluid interactions in porous media on the macroscale. On the one hand, based on the consolidation study of Biot [31–33], a poroelasticity theory has been established, compare, for example, Coussy [67], Detournay & Cheng [72] and Steeb & Renner [231]. On the other hand, the continuum Theory of Mixtures (TM) was established on the work of Truesdell [237, 238, 239], Truesdell & Toupin [241] and Bowen [51]. The first advances in the TM are outlined in Bedford & Drumheller [22], while an extensive overview of the TM can be found, e. g., in the work of Hassanizadeh & Gray [127, 128] and Helmig [138]. Moreover, Katsube & Carroll [155] and Coussy *et al.* [68] provide a comparison between Biot's theory and the TM. Furthermore, for the description of miscible components, i. e. dissolved ions, the Hybrid Theory of Mixture, cf., e. g., Bennethum & Cushman [25, 26], arising from the TM, is advantageous. Besides this, Bowen enhanced the TM with the concept of volume fractions (stating back to Woltman [251] and Delesse [71]) to capture the microscopic information of the inner composition of the system for immiscible and incompressible constituents in [52] and extended his considerations for more general compressible cases in [53]. On this basis, the Theory of Porous Media (TPM) was developed, compare, particularly, the work of de Boer [38, 39], de Boer & Ehlers [40, 42, 43] and Ehlers [84, 85, 86]. The interested reader is referred to de Boer [38], de Boer & Ehlers [41] and Ehlers [87] for a historical review of this theory. The TPM is a robust and rigorous framework for the macroscopic modelling of flow and transport processes within multi-component and multiphasic material in various fields, i. e. in geomechanics, cf., e. g., Ehlers [85], Graf [119], Häberle [124], engineering applications, cf., e. g., Leichsenring *et al.* [169], Specht *et al.* [229], and biomechanics, cf., e. g., Karajan [153], Wagner [243], Ehlers *et al.* [97], to name a few. Moreover, the classical hydromechanical relations (like Darcy [70], Forchheimer [108] and Brinkman [56] relations) are recovered in the consistent continuum mechanical and thermodynamical framework of the TPM, see Ehlers [88], even though these relations were mainly discovered on field and laboratory experiments. Finally, for this monograph, the TPM is regarded as suitable for successfully modelling the coupled nature of the hydraulic fracturing problem. It will not only fulfil the first continuum-mechanical principles but also satisfy thermodynamical restrictions by meeting the requirements of the second law of thermodynamics.

Fracture mechanics

The field of brittle fracture mechanics inevitably leads to the pioneering work of Griffith [120, 121]. Based on a global energy approach, Griffith stated that the crack propagates when the energy required for crack propagation equals the available stored elastic energy. An alternative method examines the stress state around the crack tip with Inglis [147] analytical solution of the stress concentration at the crack tip. Irwin [148, 149] extended the concept toward the stress intensity factors. These latter depend not only on the applied load but also on the problem's geometry. Moreover, Irwin [148] classified macroscopic fracture scenarios into three modes. Besides this, Dugdale [78] and Barenblatt [18]

introduced a cohesive zone model, where cohesive traction stresses oppose the separation of the material bonds. The abovementioned three fracture theories are equivalent and can be linked. However, none of them is sufficient on its own to address the complete fracture behaviour, including initiation, propagation and crack direction. A comparison of additional fracture criteria can be found, for example, in the work of Bouchard *et al.* [48]. Moreover, all three theories treat the fracture as a local geometric (sharp) discontinuity. Considering mesh-based numerical methods, like the Finite-Element Method (FEM), such discrete approaches can lead to numerical problems, requiring explicit (cf., e. g., Bouchard *et al.* [48], Ortiz & Pandolfi [206], Xu & Needleman [256]) or implicit (cf. eXtended Finite-Element Method, e. g., in Belytschko & Black [23], Moës *et al.* [197]) re-meshing of the discontinuity. These issues motivate the development of continuous fracture approaches, where the displacement field remains continuous in the whole system while the stiffness and stresses degrade gradually.

Phase-field method to fracture for brittle solids

One important method that has gained more and more attention in recent years in this context is the phase-field method (PFM) to fracture which will be considered in this monograph. Francfort & Marigo [109] proposed a variational formulation for brittle fracture based on Griffith energy criterium (cf. Griffith [120]). To make it applicable to numerical treatment, Bourdin *et al.* [50] regularised the variational formulation following the regularisation idea of Ambrosio & Tortorelli [10] in image segmentation, cf. Mumford & Shah [199]. Almost at the same time, a conceptually similar approach based on the Ginzburg-Landau theory is introduced by Karma *et al.* [154] and Hakim & Karma [125]. All the same, a scalar order parameter or phase-field variable is introduced to distinguish between the intact and broken state of the material and regularises the sharp crack discontinuity by a diffuse transition zone. Similar considerations can be found in damage models, also compare de Borst & Verhoosel [47]. Since the phase-field approach to fracture provides a continuous crack representation, it avoids the complexities associated with meshing and re-meshing, which is a major advantage compared to discontinuous models. It can simulate complex crack patterns including branching in two and three dimensions. Furthermore, the phase-field approach is self-contained and naturally captures the initiation and propagation of cracks within the energetic formulation through a degradation function without additional *ad-hoc* criteria. Specifically, the crack evolution results implicitly from the coupled system of equations. In this context, different approaches were developed for the degradation function. Starting from a quadratic polynomial, cf. Bourdin *et al.* [50], more complex polynomial functions were proposed in the literature, compare, for example, the work of Kuhn *et al.* [166]. Moreover, the first energy density formulations were isotropic[1], inducing fracture in tension and compression, compare, among others, Bourdin *et al.* [50] and Kuhn & Müller [164]. To overcome this unrealistic material behaviour, anisotropic models of the stored energy function are introduced to prevent from cracking

[1]Note that in the literature of the PFM to fracture, the terms *isotropic* and *anisotropic* fracture behaviour refer to an energy split and are unrelated to directional mechanical properties from continuum mechanics. As far as the author is aware, this terminology was first introduced by Miehe *et al.* [193] and further used in the community, refer, e. g., to the work of Ambati *et al.* [8] and Wu *et al.* [253].

in compression. To name a few, Amor *et al.* [12] proposed decomposing the free energy into volumetric and deviatoric contributions. A similar model but for shear fractures was suggested by Lancioni & Royer-Carfagni [167]. Miehe *et al.* [190, 193] split the elastic energy based on the spectral decomposition of the strain tensor. Moreover, Miehe *et al.* introduced a history field of the maximum tension-induced strain energy to ensure the irreversibility of the crack evolution. Besides these, Steinke & Kaliske [232] presented a directional split of the energy density based on the decomposition of the stress tensor with respect to the crack orientation. Ambati *et al.* [8] proposed a hybrid formulation within a staggered approach, combining the advantage of computational costs of an isotropic model with the realistic crack evolution comparable to an anisotropic model. In this case, different energy functions are considered for the phase-field evolution and the solid stress field. Another approach to converge faster and reduce computational cost is a higher-order model formulation, as proposed, for example, by Borden *et al.* [45]. Therein, the surface energy comprises higher-order derivatives of the phase-field variable. Note that the abovementioned models deal with brittle solids. The interested reader for PFM to ductile fracture is referred, e. g., to the work of Borden *et al.* [44], Miehe *et al.* [189], Ambati & De Lorenzis [6], Ambati *et al.* [7, 9] and Alessi *et al.* [3], and citations therein. In subsequent studies, the latter research group extended their investigation into additional aspects of phase-field modelling to fracture. They addressed topics such as predicting fracture initiation in shell structures through isogeometric analysis in Kiendl *et al.* [158] and simulating fatigue behaviour in Alessi *et al.* [4] and Carrara *et al.* [62]. Finally, an extended discussion together with an overview of various applications of the phase-field method to fracture can be found in the contribution of Ambati *et al.* [8] for brittle fracture and Wu *et al.* [253] for a more global approach. In addition, a recent review article comparing the phase-field model to fracture with peridynamics has been published by Diehl *et al.* [76], while a short review of variational fracture has been presented by Bourdin & Francfort [49].

PFM to fracture for fully saturated porous media

In the framework of porous-media mechanics, Mikelić *et al.* [194] were among the first researchers to apply the phase-field approach to fracture to solve fracking problems in fluid-saturated porous media. In their article, use is made of a quasi-static Biot-type *u-p* (displacement-pressure) formulation accompanied by a sequential coupling algorithm, where the phase-field problem is firstly solved individually, followed by a computation of the porous-media problem with the result of the phase-field variable computed before. In an additional article, Mikelić *et al.* [195] investigated the coupling of the solid displacement, the phase field and the pore pressure, thus providing a rigorous mathematical justification in the sense of an existence proof of such models and extensions from there. They furthermore proceeded from the exploitation of free energies. Besides, Miehe *et al.* [192] and Miehe & Mauthe [191] applied their phase-field model (cf. [190, 193]) based on minimisation principles to porous media with a Darcy-Biot-type fluid transport for finite strain. In Mauthe & Miehe [188] they extended their development to a geometrically linear framework. Wu & De Lorenzis [254] also combined Biot-theory with the phase-field approach in porous media, focusing on diffusion. They coupled the PFM to diffusion

and studied the diffusivity changes due to crack patterns. Apart from that, Wilson & Landis [249] proceeded from a variational approach describing a linear poroelastic Biot-type model combined with the phase-field approach to fracture and a Stokes-type flow in the fracture regime. Further studies are made by Chukwudozie *et al.* [64], who used a variational phase-field fracture model and combined this with a modified fixed-stress splitting scheme for decoupling and iteratively solving the flow and mechanical models. Santillán *et al.* [215] combined a poroelastic fracturing solid with the fluid-flow problem in fractures based on the Reynolds lubrication equation, while Bilgen & Weinberg [30] used the phase-field approach for the description of pneumatic fracture with anisotropic crack resistance in plaque-covered arteries.

Based on the Theory of Porous Media (TPM), fully saturated problems under the assumption of quasi-static situations have been studied by Markert & Heider [186] and Heider & Markert [135], where the standard *u-p* formulation has been extended towards the inclusion of the phase-field variable ϕ^S yielding a *u-p-*ϕ^S formulation. As in Mikelić *et al.* [194], the porous-media problem has been computed monolithically, while a staggered procedure has added the phase-field problem. In addition, Heider & Markert [135] considered local physical changes of the porous material dependent on the phase field, such as the porosity and permeability. Concerning the modelling approach, the abovementioned contributions used materially incompressible solid and liquid constituents. Furthermore, Heider *et al.* [136] added gas bubbles to the pore liquid such that the overall pore fluid becomes compressible. In their contribution, they also compared qualitatively and quantitatively the phase-field porous media model with experimental data. Also, Pise *et al.* [209] proposed a quasi-static TPM model with embedded phase-field fracture for an elastoplastic porous material, where the elastic and the plastic energy is coupled to the phase field. Regarding a dynamic setting, Ehlers & Luo [93, 94] presented a fully dynamic model of hydraulic fracturing homogeneous, fully saturated porous media within the TPM. Therein, a monolithic scheme that derives all solutions simultaneously was applied. Moreover, Pillai *et al.* [208] introduced a dynamic phase-field fracture model for heterogeneous saturated material based on a macroscopic statistical distribution of material properties.

A challenge in modelling hydraulic fracturing in porous media concerns the fluid flow within the fracture. Even if the fracturing process only occurs in the solid skeleton, it significantly influences the flow behaviour of the fluids in the pore space. While the fluids follow Darcy's law in the intact bulk volume, the fluid velocity is higher in the broken domains. An overview of modelling and discretisation methods for flow in fractured porous media can be found, e. g., in the work of Berre *et al.* [28]. One approach to model this particular behaviour is following the Poiseuille law for laminar flow within the crack and interpolating to Darcy's flow in the surrounding porous medium. Witherspoon *et al.* [250] showed experimentally the validity of the cubic law for open and closed fractures. In this context, Schrefler *et al.* [221] proposed a permeability dependent on the crack's aperture for the broken domains, yielding a Poiseuille-type flow within the crack based on a cohesive model. This approach has also been applied to a phase-field fracture, see, e. g., Miehe *et al.* [192], Wilson & Landis [249] and Heider & Markert [135]. A different approach treats the damaged and intact areas separately as two subdomains with distinct flow behaviour and couples these through adequate interface conditions,

compare, for example, Mikelić *et al.* [196], Santillán *et al.* [214] and Yoshioka *et al.* [258]. Therein, special attention has to be paid to the formulation of the crack width. Besides these, Ehlers & Luo [93] showed in a recent article on dynamic hydraulic fracturing in saturated porous media that considering dynamical momentum balances of solid and pore fluid not only provides the possibility to tackle dynamical fracturing problems but also opens the chance to switch between a Darcy-flow regime in the porous medium and a Navier-Stokes regime in fully broken zones. In a follow-up publication, Ehlers & Luo [94] introduced the crack-opening indicator (COI). By means of the COI, one can distinguish between open and closed fractures, such that not only freshly broken areas where fracking fluid is pressed in can be described. Instead, pre-existing fractures of the soil or rock body can also be tackled, whether or not they are open or closed or if they are opening through the actual fracking. In this context, simplifications of the problem towards the assumption that the velocities of solid and fluids are approximately the same, as sometimes assumed in wave-propagation scenarios, do not meet the requirements of fully dynamical systems. Quasi-static systems proceeding from the assumption that acceleration terms can be neglected, such that the fluid velocities can be substituted by seepage velocities that pressure gradients can furthermore express, do not only contradict the requirements of fully dynamical problems but yield further implications by dropping out the liquid and gas velocities as primary variables. Dropping out these terms hinders computing the fluid deformation velocities, such that a description of the transition between Darcy and Navier-Stokes flow of the pore liquid in porous and broken domains would not be possible.

PFM to fracture for partially saturated porous media

Apart from fully saturated media, the PFM has also been applied to quasi-static, variably saturated and unsaturated porous media, compare, for example, Cajuhi *et al.* [61], Heider & Sun [137] and Luo *et al.* [179]. These articles proceed from a staggered solution of the porous media and the phase-field problem and consider also drying-induced fracturing. In the category of partially saturated problems, the pore content can be split into liquid and gaseous portions, or both, liquid and pore gas, can be treated together as a liquid-gas mixture, including diffusion processes. In this context, Cajuhi *et al.* and Luo *et al.* used the standard Biot formulation with a so-called passive air-phase assumption, where the pressure of the pore gas is assumed to continuously stick to the atmospheric pressure. As a result, the computation of the porous-media problem can be restricted to the overall momentum balance and the fluid mass balance compared to the standard u-p formulation. In contrast, Heider & Sun considered barotropic fluids and used the TPM of partially saturated porous media for hydraulic fracturing. They restricted their computation to a staggered procedure, where the porous-media problem and the (drying or hydraulic) fracturing description are solved separately and then united by the staggered procedure.

In this regard, this thesis applies the PFM for dynamic hydraulic fracturing to partially saturated porous media, where the interconnected pore space can be filled at the same time with both a liquid, such as water or oil, and a gas, such as air or natural gas, and this without the assumption of a passive or a static gas phase or a liquid-gas mixture. This approach increases the complexity of the model made from a porous solid, a pore liquid

and a pore gas. As a result, one obtains a ternary model with three different constituents exhibiting simultaneously three different phases, namely a brittle elastic solid, a viscous liquid and an ideal gas. The solid and the liquid are treated as intrinsically incompressible constituents while the gas phase is assumed to be compressible.

An essential difficulty of modelling fracking scenarios in partially saturated media lies in the circumstance that the interaction of the fluids in the pore space needs to be constitutively described. In equilibrium state, where the fluids in the pore space react to the capillary effect, a capillary-pressure law of either Brooks-Corey [57] or van Genuchten type [115] can be used. However, hydraulic fracturing is a highly dynamic process, and the abovementioned standard hydromechanical relations are no longer valid near the crack. On this account, a modified pressure-difference-saturation relation, relating the pressure difference to the liquid saturation, is developed in Sonntag *et al.* [226] and took up in this thesis to encompass both equilibrium and dynamic fluid interactions.

Heterogeneities

Moreover, natural porous materials are generally heterogeneous, with material imperfections on the microscale. Therefore, modelling homogeneous porous material may oversimplify the behaviour of the fracturing process. Considering purely brittle solids, Nguyen *et al.* [202] studied the PFM crack initiation and propagation in heterogeneous cementitious materials. They defined the heterogeneities based on direct imaging of their microstructure. Späth *et al.* [227] presented a heterogeneous multi-phase-field model, composed of brittle solid and ductile porous material, also under purely mechanical loading conditions. Furthermore, Gerasimov *et al.* [117] applied stochastic phase-field modelling, resulting in all possible fracture solutions and the probabilities of their occurrence. Regarding porous materials, Pillai *et al.* [208] addressed the PFM to fully saturated heterogeneous material within the TPM. They considered a variation of Young's modulus based on a Weibull distribution. This thesis considers heterogeneities in the partially saturated porous media TPM model. The material imperfections and inhomogeneities in the porous structure are included by defining location-dependent material parameters, following a deterministic ansatz. Thereby, predefined imperfection areas and statistical fields of geomechanical properties are assessed.

Numerical procedure

Regarding the numerical treatment, partial differential equations can be solved using monolithic or staggered schemes. A comparison of the pros and cons of monolithic and staggered computations of saturated porous media can be found in Markert *et al.* [187]. Gerasimov & De Lorenzis [116], on the other hand, focused on non-porous phase-field fracture problems and employed a line-search approach to evaluate their findings in comparison to staggered computations. For more details regarding monolithic solutions, the articles authored by Wick [248] and Kopaničáková *et al.* [162] provide additional informa-

tion. Here, the finite-element solver PANDAS[2] solves the coupled problem monolithically. This research code has been started at the TU Darmstadt and is actively developed and maintained at the Institute of Applied Mechanics (CE), Chair of Continuum Mechanics, at the University of Stuttgart, see also Ehlers & Ellsiepen [90], Ellsiepen [100] and Ammann [11].

To conclude, this thesis aims to develop a partially saturated porous model within the Theory of Porous Media with an embedded phase-field approach to fracture for dynamic hydraulic fracturing. The model focuses on the fluid interaction within the intact and fractured porous medium. Moreover, the model is extended towards more realistic scenarios considering local and global heterogeneities. The methodical and basis-oriented model can be employed in diverse applications and enlarged for further studies.

1.3 Outline of the Thesis

This monograph is divided into six main chapters. The current **Chapter 1** introduces the dissertation's topic and motivates the model.

Chapter 2 provides the necessary theoretical fundamentals for understanding the developed model in the following chapters. First, it reviews the basic continuum-mechanical principles of the Theory of Porous Media. Thereby, the modelling approach of the TPM, as well as the relevant kinematics and general balance equations, are presented. Later, the multiphasic model will be enhanced with a phase field to describe fracturing processes. Therefore, Chapter 2 concludes with an overview of the phase-field approach to fracture.

After introducing in Chapter 2 both the TPM and the phase field method in general, the specific triphasic model composed of an incompressible solid and liquid, a compressible gas phase and an embedded phase field to fracture is discussed in **Chapter 3**. The specific balance equations and the entropy inequality are adapted and evaluated for the model under study. This thermodynamically consistent formulation provides the framework for the subsequent developed constitutive relations for the solid and fluids, whereby the focus lies on the latter one, particularly on the interaction of the liquid and gas in the pore space. The chapter finalises the theoretical aspect of the dissertation by providing the closure problem of the specific triphasic model and a reduction to a biphasic model to also consider fully saturated porous media with an embedded phase field for the later numerical study.

Chapter 4 deals with the numerical treatment of the presented triphasic TPM model with embedded phase field within the framework of the finite-element method. In this context, Chapter 4 presents the weak forms of the balance equations and points out the space and time discretisation of the model. Problem-specific requirements for the phase field, particularly the fracture's irreversibility condition and the definition of initial cracks, are specified at the end of the chapter.

Chapter 5 applies the theoretical and numerical developments to several numerical ex-

[2]Porous media Adaptive Nonlinear finite element solver based on Differential Algebraic Systems, http://www.get-pandas.com

amples. Firstly, the model consistency concerning capillarity and fracture behaviour is reflected. Then, proceeding from a single crack in a quasi-two-dimensional and three-dimensional setting, the solid skeleton's fracturing behaviour and the fluids' mutual interaction during the fracturing process are considered in detail. As the fracture evolution reacts to pressures and forces exerted on the solid by the interacting pore fluids, a comparison of fully saturated and partially saturated simulations reveals that the existence of pore gas mainly slows down the fracking process resulting from a slower buildup of the pore pressure. In a second group of examples, two initial cracks, horizontal and vertical, are applied to the specimen, accompanied by different ratios of horizontal to vertical displacements to study open and closed cracks. Finally, a numerical model with material heterogeneities is treated to enhance the model's applicability. A deterministic approach is proposed to account for predefined imperfection areas and statistical fields of geomechanical properties.

A final summary of the thesis and an outlook on possible improvements of the presented model are given in **Chapter 6**.

To conclude, an appendix provides additional information for better comprehensibility of the thesis. Namely, **Appendix A** compiles the required mathematical aspects of the tensor calculus, **Appendix B** some mechanical supplements and **Appendix C** numerical complements.

1.4 List of publications

This thesis was achieved within the Collaborative Research Center 1313 on "Interface-Driven Multi-Field Processes in Porous Media – Flow, Transport and Deformation". Parts of the research presented in this monograph have previously been published in the following articles.

Wang, J.; Sonntag, A.; Lee, D.; Xotta, G.; Salomoni, V. A.; Steeb, H.; Ehlers, W. & Wagner, A.: Modelling and simulation of natural hydraulic fracturing applied to experiments on natural sandstone cores (2023), submitted.

Sonntag, A.; Wagner, A. & Ehlers, W.: Dynamic hydraulic fracturing in partially saturated porous media. *Computer Methods in Applied Mechanics and Engineering* **414** (2023), 116121, 34 pages.

Wagner, A.; Sonntag, A.; Reuschen, S.; Nowak, W. & Ehlers, W.: Hydraulically induced fracturing in heterogeneous porous media using a TPM-phase-field model and geostatistics. *Proceedings in Applied Mathematics and Mechanics* **23** (2023), e202200118, 6 pages.

Ehlers, W.; Sonntag, A. & Wagner, A.: On hydraulic fracturing in fully and partially saturated brittle porous material. In Aldakheel, F.; Hudobivnik, B.; Soleimani, M.; Wessels, H.; Weißenfels, C. & Marino, M. (eds.): *Current Trends and Open Problems in Computational Mechanics*. Springer International Publishing, Cham 2022, pp. 111–119.

Ehlers, W.; Sonntag, A.; Wagner, A.: Hydraulic fracturing under fully and partially saturated conditions. Published in accordance with the decision of the Academic Council of the State Higher Educational Institution "Donetsk National Technical University" (DonNTU), Minutes № 1 (17), 2021, 5 pages.

Sonntag, A.; Wagner, A. & Ehlers, W.: Modelling fluid-driven fractures for partially saturated porous materials. *Proceedings in Applied Mathematics and Mechanics* **20** (2021), e202000033, 2 pages.

Chapter 2:
Theoretical Fundamentals

This chapter encompasses the theoretical fundamentals necessary for the presented continuum-mechanical problem with application to hydraulic fracturing of partially saturated porous media. Thereby, special attention is given to the macroscopic consideration of the porous material within the Theory of Porous Media (TPM), including its kinematics and stress description. Then, the master balances are outlined as a key element of the TPM. Finally, the phase-field approach for brittle solid fracture is introduced to describe the fracturing process.

2.1 Macroscopic modelling approach

Porous materials show a complex, multiphasic character. They usually consist of a porous solid skeleton saturated by one or more pore fluids, whereby the solid's internal pore structure is often unknown in geoscience and engineering applications. However, this information is required if the material is described with the standard singlephasic continuum mechanics of solids and fluids on the microscale. It is, therefore, convenient to proceed with a homogenisation technique and model the material as a multiphasic aggregate on the macroscale. A continuum-mechanical framework which enables such a consideration is the Theory of Porous Media. A comparison of the macroscopic view of the porous medium by the TPM with the classical continuum mechanics approaches of single-phase materials can be found in Ehlers [84, 86]. This monograph concentrates on a TPM model for fracturing porous media as they occur in geomaterials, such as soil or rock. Please refer to Wagner [244] and citations therein for applications considering biomaterials, plant tissues or chemical components.

Proceeding from a virtual statistical homogenisation over a representative elementary volume (REV), the microscopical structure of the porous material is smeared out, leading to a macroscopic model of superimposed and interacting continua. Thereby, the TPM provides that all constituents simultaneously occupy the complete domain, which ensures a continuous description of the material, compare Figure 2.1. Note that for proper homogenisation, the REV has to be sufficiently large to allow a statistical average, on the one hand, and, on the other hand, small enough to allow a resolution of the local information of the system.

The porous material is regarded as an immiscible mixture φ of interacting constituents φ^α, where the index α stands for the individual constituent. In this monograph, either a single liquid fluid $\varphi^F = \varphi^L$ saturates the solid skeleton φ^S, or a liquid and a gaseous fluid, $\varphi^F = \varphi^L \cup \varphi^G$, percolate the interconnected pore space for the additional consideration

of partially saturated porous material, i. e.:

$$\varphi = \bigcup_{\alpha} \varphi^{\alpha} = \varphi^{S} \cup \varphi^{F} \quad \text{with} \quad \begin{cases} \text{fully saturated:} & \varphi^{F} = \varphi^{L}, \\ \text{partially saturated:} & \varphi^{F} = \bigcup_{\beta} \varphi^{\beta},\ \beta = \{L,\, G\}\,. \end{cases} \tag{2.1}$$

Note that the index F stands for the pore fluid and can take the following values in this monograph: L when considering a fully saturated porous media and $\{L \cup G\}$ when a partially saturated porous media is regarded. In other applications, the fluid might also be composed of a fluid mixture or an immiscible combination of a fluid mixture and a gas, compare, e. g., Bowen [52, 53], Wagner [243] and Heider *et al.* [136].

Figure 2.1 sketches the macroscopic, multiphasic modelling approach in this monograph.

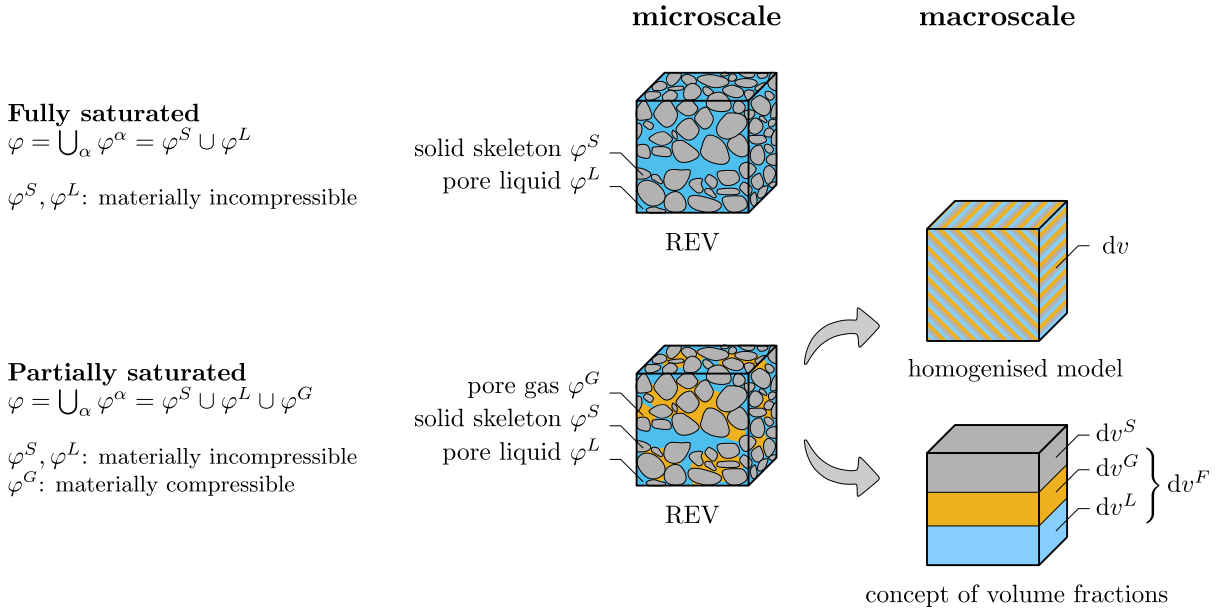

Figure 2.1: *Macroscopic modelling approach over an idealised representative elementary volume (REV).*

As mentioned in the introduction, the TPM enhances the Theory of Mixtures with the concept of volume fractions, taking the local composition of the aggregate into account with a statistically averaged scalar variable n^{α}. Thereby, the ratio of the partial volume element $\mathrm{d}v^{\alpha}$ to the total volume element $\mathrm{d}v$ defines the volume fraction of the respective component φ^{α}:

$$n^{\alpha} := \frac{\mathrm{d}v^{\alpha}}{\mathrm{d}v}. \tag{2.2}$$

It is assumed that the overall aggregate contains no vacant space. Consequently, the saturation condition

$$\sum_{\alpha} n^{\alpha} = n^{S} + n^{F} = n^{S} + n^{L} + n^{G} = 1 \tag{2.3}$$

has to be fulfilled at any point in the system. In order to avoid confusion, it should be mentioned that in this monograph, the expression “partially saturated” does not refer to

vacant space but rather to the fact that the solid skeleton is percolated by at least two fluid phases, namely a liquid and a gaseous phase. Since these fluid phases are immiscible and, therefore, occupy different pore volumes, it is convenient to introduce a saturation variable

$$s^\beta := \frac{\mathrm{d}v^\beta}{\mathrm{d}v^F} \quad \text{with} \quad \beta = \{L, G\}, \tag{2.4}$$

which accounts for the portion of occupied volume of the fluid phase φ^β, viz. $\mathrm{d}v^\beta$, with respect to the total pore volume $\mathrm{d}v^F$, compare Figure 2.1. Obviously, the liquid saturation equals one in the case of a fully saturated porous material. In analogy to (2.3), also the saturations add up to one, i. e.

$$\sum_\beta s^\beta = 1. \tag{2.5}$$

Note that the saturation condition (2.5) concerns the pore space, while the relation (2.3) refers to the overall volume. As a result of (2.2) and (2.4), the specific pore-fluid volume fraction of the constituent φ^β can be rewritten to

$$n^\beta = s^\beta n^F. \tag{2.6}$$

Proceeding from the concept of volume fractions, two densities are associated with each constituent, namely

$$\rho^{\alpha R} := \frac{\mathrm{d}m^\alpha}{\mathrm{d}v^\alpha} \quad \text{and} \quad \rho^\alpha := \frac{\mathrm{d}m^\alpha}{\mathrm{d}v}. \tag{2.7}$$

With this, the material (realistic or effective) density $\rho^{\alpha R}$ relates the local mass element $\mathrm{d}m^\alpha$ to the volume element of the respective constituent $\mathrm{d}v^\alpha$. In contrast, the partial density ρ^α relates the local mass element $\mathrm{d}m^\alpha$ to the bulk volume element $\mathrm{d}v$. Both densities are linked to each other by the volume fraction, i. e.

$$\rho^\alpha = n^\alpha \, \rho^{\alpha R}. \tag{2.8}$$

Thus, material incompressibility, i. e. $\rho^{\alpha R} \equiv$ const., does not lead to macroscopic incompressibility of the constituent defined by $\rho^\alpha \equiv$ const., since this latter one may still change with a variation of the volume fraction n^α. Here, for the fully saturated model, the solid and fluid are assumed to be materially incompressible, with $\rho^{\alpha R} =$ const. Apart from that, for the partially saturated model, the solid and liquid phases are considered materially incompressible with $\rho^{SR} =$ const. and $\rho^{LR} =$ const., while the gas phase is compressible in the sense of an ideal gas. Finally, the density of the overall aggregate results in

$$\rho = \sum_\alpha \rho^\alpha. \tag{2.9}$$

2.2 Kinematics

The kinematic relations of multiphasic material are based on the continuum mechanics of singlephasic material. An overview of these latter is given, among others, in Altenbach [5], Ehlers [82], Haupt [132] and Holzapfel [142]. In this section, the focus will be on

the motion functions of the constituents in the considered aggregate and the essential deformation and strain measures necessary for the following model approach. A detailed description of the kinematic relations in multiphasic material can be found, e. g., in Ehlers [84, 86].

2.2.1 Motion functions

The spatial manifold of material points $\mathcal{P}$ defines the overall aggregate body $\mathcal{B}$. The set of material points on the boundary demarcates the body's surface $\mathcal{S}$, on which the boundary conditions will be applied in the later numerical investigation. The idea of superimposed continua in the framework of the TPM implies that each spatial point is simultaneously and only occupied by one single material point $\mathcal{P}^\alpha$ of each constituent φ^α at time $t > t_0$, see Figure 2.2, right.

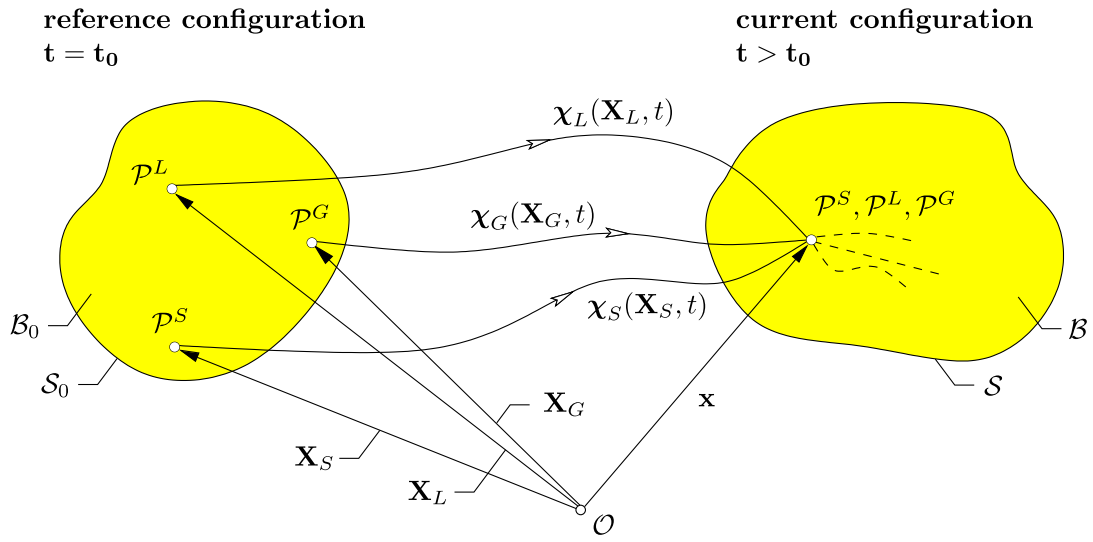

Figure 2.2: *Kinematics of a triphasic material with a solid constituent φ^S, a gaseous pore fluid φ^G and a liquid pore fluid φ^L.*

Nevertheless, each constituent may come from an individual reference position $\mathbf{X}_\alpha$. In that sense, the TPM provides each constituent with an individual Lagrangean motion function $\boldsymbol{\chi}_\alpha(\mathbf{X}_\alpha, t)$, which relates the material point in its initial configuration at time $t = t_0$ to a spatial point in the current configuration ($t > t_0$), viz.:

$$\mathbf{x} = \boldsymbol{\chi}_\alpha(\mathbf{X}_\alpha, t). \tag{2.10}$$

Each constituent's corresponding velocity and acceleration fields are given as

$$\overset{\prime}{\mathbf{x}}_\alpha = \frac{\partial \boldsymbol{\chi}_\alpha(\mathbf{X}_\alpha, t)}{\partial t} = \overset{\prime}{\mathbf{x}}_\alpha(\mathbf{X}_\alpha, t) \quad \text{and} \quad \overset{\prime\prime}{\mathbf{x}}_\alpha = \frac{\partial^2 \boldsymbol{\chi}_\alpha(\mathbf{X}_\alpha, t)}{\partial t^2} = \overset{\prime\prime}{\mathbf{x}}_\alpha(\mathbf{X}_\alpha, t) \tag{2.11}$$

in a Lagrangean (material) representation. Considering an Eulerian (spatial) representation, where the quantities are expressed with regard to the current configuration, the

requirement of a unique motion function becomes relevant through

$$\mathbf{X}_\alpha = \boldsymbol{\chi}_\alpha^{-1}(\mathbf{x},t) \quad \text{with} \quad J_\alpha := \det\frac{\partial \boldsymbol{\chi}_\alpha}{\partial \mathbf{X}_\alpha} \neq 0, \tag{2.12}$$

which yields the condition of a non-singular Jacobian determinant J_α. Following this, the velocity and acceleration fields are given in an Eulerian (spatial) representation with

$$\begin{aligned} \overset{\prime}{\mathbf{x}}_\alpha &= \overset{\prime}{\mathbf{x}}_\alpha(\boldsymbol{\chi}_\alpha^{-1}(\mathbf{x},t),t) = \overset{\prime}{\mathbf{x}}_\alpha(\mathbf{x},t) = \mathbf{v}_\alpha(\mathbf{x},t)\,, \\ \overset{\prime\prime}{\mathbf{x}}_\alpha &= \overset{\prime\prime}{\mathbf{x}}_\alpha(\boldsymbol{\chi}_\alpha^{-1}(\mathbf{x},t),t) = \overset{\prime\prime}{\mathbf{x}}_\alpha(\mathbf{x},t). \end{aligned} \tag{2.13}$$

Note that the spatial argument $\mathbf{x}$ depends implicitly on the time t in an Eulerian setting, cf. (2.10). Thus, when considering the total time derivative in (2.13), one has to take into account the local temporal changes at a fixed position and, additionally, the non-local (convective) temporal change resulting from the inner derivation of $\mathbf{x}(t)$. In that context, the total time derivative with respect to the constituent φ^α results for an arbitrary but continuous and sufficiently often continuous differentiable field function (scalar-valued $\Upsilon(\mathbf{x},t)$ or vector-valued $\boldsymbol{\Upsilon}(\mathbf{x},t)$) in

$$\begin{aligned} (\Upsilon)'_\alpha &= \frac{\mathrm{d}_\alpha}{\mathrm{d}t}\,\Upsilon(\mathbf{x}(t),t) = \frac{\partial \Upsilon}{\partial t} + \frac{\partial \Upsilon}{\partial \mathbf{x}} \cdot \Big(\frac{\partial \mathbf{x}}{\partial t}\Big)_\alpha = \frac{\partial \Upsilon}{\partial t} + \operatorname{grad}\Upsilon \cdot \overset{\prime}{\mathbf{x}}_\alpha\,, \\ (\boldsymbol{\Upsilon})'_\alpha &= \frac{\mathrm{d}_\alpha}{\mathrm{d}t}\,\boldsymbol{\Upsilon}(\mathbf{x}(t),t) = \frac{\partial \boldsymbol{\Upsilon}}{\partial t} + \frac{\partial \boldsymbol{\Upsilon}}{\partial \mathbf{x}}\Big(\frac{\partial \mathbf{x}}{\partial t}\Big)_\alpha = \frac{\partial \boldsymbol{\Upsilon}}{\partial t} + (\operatorname{grad}\boldsymbol{\Upsilon})\,\overset{\prime}{\mathbf{x}}_\alpha\,. \end{aligned} \tag{2.14}$$

Hereby, $\operatorname{grad}(\cdot)$ denotes the spatial gradient operator in the current configuration with $\operatorname{grad}(\cdot) := \partial(\cdot)/\partial\mathbf{x}$.

Remark: Since the position vector $\mathbf{x}$ describes the location of material points of all constituents in the current configuration at time t, it is not necessary to specify the relative constituent when dealing with the spatial gradient $\operatorname{grad}(\cdot)$. However, this is different when considering the material gradient $\operatorname{Grad}_\alpha(\cdot) := \partial(\cdot)/\partial\mathbf{X}_\alpha$. This latter is related to the reference configuration through $\mathbf{X}_\alpha$, making it essential to specify the referred constituent through the subscript α. This clarification is particularly relevant regarding the deformation and strain measures, cf. Subsection 2.2.2. □

In addition, the local velocity $\dot{\mathbf{x}}$ of the centre of gravity of all constituents, also known as barycentric velocity, is given by

$$\dot{\mathbf{x}} := \frac{1}{\rho}\sum_\alpha \rho^\alpha\, \overset{\prime}{\mathbf{x}}_\alpha\,. \tag{2.15}$$

In this regard, the total time derivative with respect to the overall aggregate yields for the scalar-valued field function $\Upsilon(\mathbf{x},t)$ and the vector-valued field function $\boldsymbol{\Upsilon}(\mathbf{x},t)$:

$$\dot{\Upsilon} = \frac{\mathrm{d}\Upsilon}{\mathrm{d}t} = \frac{\partial \Upsilon}{\partial t} + \operatorname{grad}\Upsilon \cdot \dot{\mathbf{x}} \quad \text{and} \quad \dot{\boldsymbol{\Upsilon}} = \frac{\mathrm{d}\boldsymbol{\Upsilon}}{\mathrm{d}t} = \frac{\partial \boldsymbol{\Upsilon}}{\partial t} + (\operatorname{grad}\boldsymbol{\Upsilon})\,\dot{\mathbf{x}}\,. \tag{2.16}$$

For the later numerical study, it is furthermore convenient to use the displacement function $\mathbf{u}_S$ and the spatial velocity $\mathbf{v}_S$ to describe the motion of the solid skeleton via

$$\mathbf{u}_S = \mathbf{x} - \mathbf{X}_S \quad \text{and} \quad \mathbf{v}_S = (\mathbf{u}_S)'_S = \overset{\prime}{\mathbf{x}}_S\,. \tag{2.17}$$

Moreover, it is suitable to consider the temporal changes of all constituents with respect to the skeleton motion. Therefore, following (2.14), the total material time derivative with respect to the fluid phases φ^β, with $\beta = \{L, G\}$, of a scalar-valued or vector-valued field function, $\Upsilon(\mathbf{x}, t)$ and $\boldsymbol{\Upsilon}(\mathbf{x}, t)$, respectively, can be reformulated with respect to the skeleton motion to

$$\begin{array}{rcl} (\Upsilon)'_\beta & = & (\Upsilon)'_S + \operatorname{grad}\Upsilon \cdot \mathbf{w}_\beta \,, \\ (\boldsymbol{\Upsilon})'_\beta & = & (\boldsymbol{\Upsilon})'_S + (\operatorname{grad}\boldsymbol{\Upsilon})\,\mathbf{w}_\beta \,. \end{array} \tag{2.18}$$

Therein, the seepage velocities of the fluid phases are defined trough

$$\mathbf{w}_\beta(\mathbf{x}, t) = \overset{\prime}{\mathbf{x}}_\beta(\mathbf{x}, t) - \overset{\prime}{\mathbf{x}}_S(\mathbf{x}, t) = \mathbf{v}_\beta(\mathbf{x}, t) - \mathbf{v}_S(\mathbf{x}, t) \,. \tag{2.19}$$

Finally, the diffusion velocity of mixture theories of a constituent φ^α is given by its relative velocity to the barycentric velocity of the aggregate

$$\mathbf{d}_\alpha := \overset{\prime}{\mathbf{x}}_\alpha - \dot{\mathbf{x}} \,. \tag{2.20}$$

Considering the definition of the barycentric velocity (2.15), it can be concluded that the sum of the local diffusion mass flows vanishes

$$\sum_\alpha \rho^\alpha \mathbf{d}_\alpha = \underbrace{\sum_\alpha \rho^\alpha \overset{\prime}{\mathbf{x}}_\alpha}_{\rho\,\dot{\mathbf{x}}} - \dot{\mathbf{x}} \underbrace{\sum_\alpha \rho^\alpha}_{\rho} = \mathbf{0} \,. \tag{2.21}$$

2.2.2 Deformation and strain measures

Deformation measures and transport theorems

The basis for deformation measures in continuum mechanics is the material deformation gradient. From (2.10) and (2.12), the material deformation gradient $\mathbf{F}_\alpha$ of the constituent φ^α and its corresponding inverse $\mathbf{F}_\alpha^{-1}$ are defined as

$$\begin{array}{rcl} \mathbf{F}_\alpha & := & \dfrac{\partial \boldsymbol{\chi}_\alpha(\mathbf{X}_\alpha, t)}{\partial \mathbf{X}_\alpha} = \dfrac{\partial \mathbf{x}}{\partial \mathbf{X}_\alpha} = \operatorname{Grad}_\alpha \mathbf{x} \,, \\ \mathbf{F}_\alpha^{-1} & = & \dfrac{\partial \boldsymbol{\chi}_\alpha^{-1}(\mathbf{x}, t)}{\partial \mathbf{x}} = \dfrac{\partial \mathbf{X}_\alpha}{\partial \mathbf{x}} = \operatorname{grad} \mathbf{X}_\alpha \,. \end{array} \tag{2.22}$$

Remark: Note that per definition, in the undeformed state at time $t = t_0$, the deformation tensor results in the second-order identity tensor, viz. $\mathbf{F}_\alpha(t_0) = \operatorname{Grad}_\alpha \mathbf{X}_\alpha = \mathbf{I}$, whereby its determinant equals one, viz. $\det \mathbf{F}_\alpha(t_0) = \det \mathbf{I} = 1$. From these considerations and the condition of a non-singularity from $(2.12)_2$, the domain of the Jacobian determinant is finally restricted to

$$J_\alpha = \det \mathbf{F}_\alpha > 0. \tag{2.23}$$

□

With the definition (2.22) of the deformation gradient and its inverse, one can directly map differential line elements $\mathrm{d}\mathbf{X}_\alpha$ from the referential configuration to the corresponding elements $\mathrm{d}\mathbf{x}$ in the current configuration and *vice versa*:

$$\mathrm{d}\mathbf{x} = \mathbf{F}_\alpha \, \mathrm{d}\mathbf{X}_\alpha \quad \leftrightarrow \quad \mathrm{d}\mathbf{X}_\alpha = \mathbf{F}_\alpha^{-1} \, \mathrm{d}\mathbf{x}. \tag{2.24}$$

This representation makes the two-field characteristic of the material deformation tensor in a natural basis system apparent. The transport mechanism in $(2.24)_1$ is termed push-forward transformation (from reference to current configuration), while its counterpart in $(2.24)_2$ is called pull-back transformation (from current to reference configuration). Further push-forward transport mechanisms can be derived for the local area and volume elements in the reference configuration, $\mathrm{d}\mathbf{A}_\alpha$ and $\mathrm{d}V_\alpha$, respectively:

$$\begin{aligned} \mathrm{d}\mathbf{a} &= (\det\mathbf{F}_\alpha) \, \mathbf{F}_\alpha^{T-1} \, \mathrm{d}\mathbf{A}_\alpha \,, \\ \mathrm{d}v &= (\det\mathbf{F}_\alpha) \, \mathrm{d}V_\alpha \,, \end{aligned} \tag{2.25}$$

where $\mathrm{d}\mathbf{a}$ and $\mathrm{d}v$ are the corresponding area and volume elements in the current configuration. Based on this, since there are no changes in the local partial mass element $\mathrm{d}m^\alpha$, the initial partial density ρ_0^α of the constituent φ^α at time $t = t_0$ can now be derived from $(2.7)_2$ and $(2.25)_2$:

$$\rho_0^\alpha = (\det\mathbf{F}_\alpha) \, \rho^\alpha \,. \tag{2.26}$$

This latter relation will be of particular use for the constitutive modelling of the solid skeleton, compare Chapter 3. Regarding the squares of the line elements introduced in (2.24), one derives the right and left Cauchy-Green deformation tensors, $\mathbf{C}_\alpha$ and $\mathbf{B}_\alpha$, respectively:

$$\begin{aligned} \mathrm{d}\mathbf{x} \cdot \mathrm{d}\mathbf{x} &= \mathbf{F}_\alpha \, \mathrm{d}\mathbf{X}_\alpha \cdot \mathbf{F}_\alpha \, \mathrm{d}\mathbf{X}_\alpha = \mathrm{d}\mathbf{X}_\alpha \cdot (\mathbf{F}_\alpha^T \, \mathbf{F}_\alpha) \, \mathrm{d}\mathbf{X}_\alpha =: \mathrm{d}\mathbf{X}_\alpha \cdot \mathbf{C}_\alpha \, \mathrm{d}\mathbf{X}_\alpha \,, \\ \mathrm{d}\mathbf{X}_\alpha \cdot \mathrm{d}\mathbf{X}_\alpha &= \mathbf{F}_\alpha^{-1} \, \mathrm{d}\mathbf{x} \cdot \mathbf{F}_\alpha^{-1} \, \mathrm{d}\mathbf{x} = \mathrm{d}\mathbf{x} \cdot (\mathbf{F}_\alpha^{T-1} \, \mathbf{F}_\alpha^{-1}) \, \mathrm{d}\mathbf{x} =: \mathrm{d}\mathbf{x} \cdot \mathbf{B}_\alpha^{-1} \, \mathrm{d}\mathbf{x} \,. \end{aligned} \tag{2.27}$$

Strain measures

Besides these deformation measures, it is convenient to introduce some strain measures, which allow a comparison of the deformed state of the body with the undeformed one. Proceeding from the difference of the squares of the local line elements introduced in (2.27),

$$\begin{aligned} \mathrm{d}\mathbf{x} \cdot \mathrm{d}\mathbf{x} - \mathrm{d}\mathbf{X}_\alpha \cdot \mathrm{d}\mathbf{X}_\alpha &= \mathrm{d}\mathbf{X}_\alpha \cdot (\mathbf{C}_\alpha - \mathbf{I}) \, \mathrm{d}\mathbf{X}_\alpha =: \mathrm{d}\mathbf{X}_\alpha \cdot 2\mathbf{E}_\alpha \, \mathrm{d}\mathbf{X}_\alpha \,, \\ \mathrm{d}\mathbf{x} \cdot \mathrm{d}\mathbf{x} - \mathrm{d}\mathbf{X}_\alpha \cdot \mathrm{d}\mathbf{X}_\alpha &= \mathrm{d}\mathbf{x} \cdot (\mathbf{I} - \mathbf{B}_\alpha^{-1}) \, \mathrm{d}\mathbf{x} =: \mathrm{d}\mathbf{x} \cdot 2\mathbf{A}_\alpha \, \mathrm{d}\mathbf{x} \,. \end{aligned} \tag{2.28}$$

one identifies the Green-Lagrangean and Almansi strain tensors, $\mathbf{E}_\alpha$ and $\mathbf{A}_\alpha$, respectively:

$$\begin{aligned} \mathbf{E}_\alpha &= \tfrac{1}{2}(\mathbf{C}_\alpha - \mathbf{I}) \quad \rightarrow \quad \mathbf{E}_\alpha = \tfrac{1}{2}(\mathbf{F}_\alpha^T \, \mathbf{F}_\alpha - \mathbf{I}) \,, \\ \mathbf{A}_\alpha &= \tfrac{1}{2}(\mathbf{I} - \mathbf{B}_\alpha^{-1}) \quad \rightarrow \quad \mathbf{A}_\alpha = \tfrac{1}{2}(\mathbf{I} - \mathbf{F}_\alpha^{T-1} \, \mathbf{F}_\alpha^{-1}) \,. \end{aligned} \tag{2.29}$$

Further strain tensors can be found, e. g., in Ehlers [86], but will not be subject of this monograph.

Deformation and strain rate

For the later constitutive approach, it is convenient to introduce some quantities concerning the temporal changes in deformation. In this context, the rate of the deformation gradient $\mathbf{F}_\alpha$ can be either introduced in a Lagrangean description via

$$(\mathbf{F}_\alpha)'_\alpha = \frac{\mathrm{d}_\alpha}{\mathrm{d}t}\left(\frac{\partial \mathbf{x}}{\partial \mathbf{X}_\alpha}\right) = \frac{\partial \overset{\prime}{\mathbf{x}}_\alpha(\mathbf{X}_\alpha, t)}{\partial \mathbf{X}_\alpha} = \mathrm{Grad}_\alpha \overset{\prime}{\mathbf{x}}_\alpha\,, \tag{2.30}$$

yielding the material velocity gradient, or in an Eulerian setting, considering

$$(\mathbf{F}_\alpha)'_\alpha = \frac{\mathrm{d}_\alpha}{\mathrm{d}t}\left(\frac{\partial \mathbf{x}}{\partial \mathbf{X}_\alpha}\right) = \frac{\partial \overset{\prime}{\mathbf{x}}_\alpha(\mathbf{x}, t)}{\partial \mathbf{X}_\alpha} = \frac{\partial \overset{\prime}{\mathbf{x}}_\alpha}{\partial \mathbf{x}}\frac{\partial \mathbf{x}}{\partial \mathbf{X}_\alpha} =: \mathbf{L}_\alpha\,\mathbf{F}_\alpha \quad \text{with} \quad \mathbf{L}_\alpha := \mathrm{grad}\,\overset{\prime}{\mathbf{x}}_\alpha. \tag{2.31}$$

Therein, $\mathbf{L}_\alpha$ is denoted the spatial velocity gradient for the constituent φ^α. For convenience, this latter can be split into a symmetric ($\mathbf{D}_\alpha = \mathbf{D}_\alpha^T$) and skew-symmetric ($\mathbf{W}_\alpha = -\mathbf{W}_\alpha^T$) part, namely

$$\mathbf{L}_\alpha = \mathbf{D}_\alpha + \mathbf{W}_\alpha \quad \text{with} \quad \mathbf{D}_\alpha = \tfrac{1}{2}(\mathbf{L}_\alpha + \mathbf{L}_\alpha^T) \quad \text{and} \quad \mathbf{W}_\alpha = \tfrac{1}{2}(\mathbf{L}_\alpha - \mathbf{L}_\alpha^T)\,. \tag{2.32}$$

Moreover, from (2.31), the trace of the spatial velocity gradient can be reformulated as the divergence of the velocity, viz.

$$\mathbf{L}_\alpha \cdot \mathbf{I} = \mathrm{grad}\,\overset{\prime}{\mathbf{x}}_\alpha \cdot \mathbf{I} = \mathrm{div}\,\overset{\prime}{\mathbf{x}}_\alpha. \tag{2.33}$$

Finally, applying the differentiation rule and considering $(2.27)_1$ and (2.31), the right Cauchy-Green deformation rate results in

$$\begin{aligned}(\mathbf{C}_\alpha)'_\alpha &= (\mathbf{F}_\alpha^T\,\mathbf{F}_\alpha)'_\alpha = (\mathbf{F}_\alpha^T)'_\alpha\,\mathbf{F}_\alpha + \mathbf{F}_\alpha^T\,(\mathbf{F}_\alpha)'_\alpha \\ &= \mathbf{F}_\alpha^T\,\mathbf{L}_\alpha^T\,\mathbf{F}_\alpha + \mathbf{F}_\alpha^T\,\mathbf{L}_\alpha\,\mathbf{F}_\alpha = 2\,\mathbf{F}_\alpha^T\,\mathbf{D}_\alpha\,\mathbf{F}_\alpha\,,\end{aligned} \tag{2.34}$$

leading to the rate of the Green-Lagrange strain tensor (2.29)

$$(\mathbf{E}_\alpha)'_\alpha = \tfrac{1}{2}(\mathbf{C}_\alpha)'_\alpha = \mathbf{F}_\alpha^T\,\mathbf{D}_\alpha\,\mathbf{F}_\alpha\,. \tag{2.35}$$

2.3 Forces and state of stress

An external load on a body does not only lead to deformation but also to an (inner) stress state. In the context of the TPM, each constituent can be affected by individual volume forces $\mathbf{k}_v^\alpha$ acting from a distance on every material point of the body $\mathcal{B}$ and contact forces $\mathbf{k}_c^\alpha$ acting from the near vicinity on the material points at the surface $\mathcal{S}$:

$$\mathbf{k}^\alpha = \underbrace{\int_{\mathcal{B}} \mathbf{f}^\alpha \mathrm{d}v}_{\mathbf{k}_v^\alpha} + \underbrace{\int_{\mathcal{S}} \mathbf{t}^\alpha \mathrm{d}a}_{\mathbf{k}_c^\alpha}\,. \tag{2.36}$$

Here, the external body force $\mathbf{f}^\alpha$ is postulated proportional to the partial density ρ^α and body force $\mathbf{b}^\alpha$ per mass element, viz. $\mathbf{f}^\alpha = \rho^\alpha \mathbf{b}^\alpha$. Moreover, $\mathbf{b}^\alpha$ is interpreted as the gravitation force $\mathbf{g}$ acting on all constituents. Other possible external volume forces are, e. g., magnetic forces. Finally, the external body force acting on the constituent φ^α results in

$$\mathbf{k}_v^\alpha = \int_{\mathcal{B}} \rho^\alpha \mathbf{g} \, \mathrm{d}v \,. \tag{2.37}$$

Furthermore, the contact force $\mathbf{t}^\alpha = \mathbf{t}^\alpha(\mathbf{x},\, t,\, \mathbf{n})$ per surface area in (2.36) is a function of the current position $\mathbf{x}$, the time t and the outward-oriented surface normal vector $\mathbf{n}$. In order to avoid the dependency of the stress measure from the surface orientation, Cauchy's theorem is applied, yielding

$$\mathbf{t}^\alpha(\mathbf{x},\, t,\, \mathbf{n}) = [\mathbf{T}^\alpha(\mathbf{x},\, t)]\, \mathbf{n} \,, \tag{2.38}$$

where the partial Cauchy stress $\mathbf{T}^\alpha$ of the constituent φ^α is independent of the surface orientation. Thus, the contact force $\mathbf{k}_c^\alpha$ results in

$$\mathbf{k}_c^\alpha = \int_{\mathcal{S}} \mathbf{T}^\alpha \, \mathrm{d}\mathbf{a} \tag{2.39}$$

with $\mathrm{d}\mathbf{a} = \mathbf{n} \, \mathrm{d}a$ as the oriented current area element.

Remark: The partial Cauchy stress $\mathbf{T}^\alpha$ is also called true stress tensor since the contact force $\mathbf{t}^\alpha$ and the oriented area element $\mathrm{d}\mathbf{a}$ are both in the current configuration. Alternative stress measurements can be introduced by pull-back transports of either the area element or both the contact force and area element into the reference configuration, i. e.

$$\begin{aligned} \mathbf{P}^\alpha &= (\det\mathbf{F}_\alpha)\mathbf{T}^\alpha \, \mathbf{F}_\alpha^{T-1} && : \text{first Piola-Kirchhoff stress tensor,} \\ \mathbf{S}^\alpha &= (\det\mathbf{F}_\alpha)\mathbf{F}_\alpha^{-1} \, \mathbf{T}^\alpha \, \mathbf{F}_\alpha^{T-1} && : \text{second Piola-Kirchhoff stress tensor.} \end{aligned} \tag{2.40}$$

Moreover, relating the contact force to a weighted area element of the current configuration leads to the Kirchhoff stress $\boldsymbol{\tau}^\alpha$, viz.

$$\mathbf{k}_c^\alpha = \int_{\mathcal{S}} \boldsymbol{\tau}^\alpha \, \mathrm{d}\bar{\mathbf{a}}_\alpha \quad \text{with} \quad \begin{cases} \boldsymbol{\tau}^\alpha &= (\det\mathbf{F}_\alpha)\, \mathbf{T}^\alpha \\ \mathrm{d}\bar{\mathbf{a}}_\alpha &= (\det\mathbf{F}_\alpha)^{-1} \, \mathrm{d}\mathbf{a} \,. \end{cases} \tag{2.41}$$

□

For completeness, the forces $\mathbf{k}$ acting on the overall aggregate arise from the forces acting on the individual constituents:

$$\mathbf{k} = \underbrace{\int_{\mathcal{B}} \mathbf{f} \, \mathrm{d}v}_{\mathbf{k}_v} + \underbrace{\int_{\mathcal{S}} \mathbf{t} \, \mathrm{d}a}_{\mathbf{k}_c} \quad \text{with} \quad \mathbf{f} = \sum_\alpha \mathbf{f}^\alpha = \rho\, \mathbf{g} \quad \text{and} \quad \mathbf{t} = \sum_\alpha \mathbf{t}^\alpha \,. \tag{2.42}$$

Thereby, the contact force $\mathbf{t}$ also follows Cauchy's theorem with the Cauchy stress tensor $\mathbf{T}$ of the overall aggregate, viz. $\mathbf{t}(\mathbf{x}, t, \mathbf{n}) = \mathbf{T}(\mathbf{x}, t)\, \mathbf{n}$.

2.4 Balance relations

After the introduction of the kinematic and stress quantities, it is now possible to look at the balance relations as the fundament of continuum mechanics, stating the conservation of mechanical and thermodynamical quantities. In this section, the master balance relations will be introduced both for the overall aggregate and for the individual constituents. A detailed description and derivation of these relations can be found in Ehlers [84] and citations therein.

2.4.1 Master balances

Balance relations presume an equilibrium between the temporal changes of a mechanical (mass, momentum, moment of momentum) or thermodynamical (energy, entropy) quantity with the external loads and the internal production of the physical quantity. It is possible to embed all balance relations into an overall formula, the master balance, from which the individual relations are axiomatically derived by inserting the corresponding quantities.

Balances for the overall aggregate

The master balances for the overall aggregate are introduced according to the continuum mechanics of singlephasic material. A detailed overview of these latter can be found, e. g., in Ehlers [83], Haupt [131, 132] and Holzapfel [142] and will not be deepened here. For a scalar-valued and vector-valued physical quantity, Ψ and $\boldsymbol{\Psi}$, respectively, the master balances for the overall aggregate read

$$\begin{aligned} \frac{\mathrm{d}}{\mathrm{d}t}\int_{\mathcal{B}} \Psi \,\mathrm{d}v &= \int_{\mathcal{S}} (\boldsymbol{\phi}\cdot\mathbf{n})\,\mathrm{d}a + \int_{\mathcal{B}} \sigma \,\mathrm{d}v + \int_{\mathcal{B}} \hat{\Psi}\,\mathrm{d}v\,, \\ \frac{\mathrm{d}}{\mathrm{d}t}\int_{\mathcal{B}} \boldsymbol{\Psi} \,\mathrm{d}v &= \int_{\mathcal{S}} (\boldsymbol{\Phi}\,\mathbf{n})\,\mathrm{d}a + \int_{\mathcal{B}} \boldsymbol{\sigma} \,\mathrm{d}v + \int_{\mathcal{B}} \hat{\boldsymbol{\Psi}}\,\mathrm{d}v\,. \end{aligned} \tag{2.43}$$

Therein, $\boldsymbol{\phi}\cdot\mathbf{n}$ and $\boldsymbol{\Phi}\,\mathbf{n}$ are the effluxes through the body's surface $\mathcal{S}$ (actions at the vicinity), σ and $\boldsymbol{\sigma}$ are the supplies from an external source (actions from the body's distance), and $\hat{\Psi}$ and $\hat{\boldsymbol{\Psi}}$ stand for the total production of the physical quantity within the body $\mathcal{B}$. The production terms describe the interaction of the aggregate with the surrounding of the system. In this monograph, the overall aggregate is considered to be a closed system, where there is no interaction of the balanced quantities of the aggregate with the surrounding except for the entropy production according to the second law of thermodynamics. Moreover, assuming steady and steadily differentiable integrands, the local form of the master balance can be found with differentiation of the left-hand side of (2.43) and transformation of the surface integral on the right-hand side in a volume integral with the Gaussian theorem, yielding

$$\begin{aligned} \dot{\Psi} + \Psi \operatorname{div}\dot{\mathbf{x}} &= \operatorname{div}\boldsymbol{\phi} + \sigma + \hat{\Psi}\,, \\ \dot{\boldsymbol{\Psi}} + \boldsymbol{\Psi} \operatorname{div}\dot{\mathbf{x}} &= \operatorname{div}\boldsymbol{\Phi} + \boldsymbol{\sigma} + \hat{\boldsymbol{\Psi}}\,. \end{aligned} \tag{2.44}$$

Truesdell's metaphysical principles

In the context of multiphasic material, each constituent is provided with an individual set of balance relations within the Theory of Mixture, cf. the work of Truesdell [239], Truesdell & Toupin [241], Kelly [156] and Bowen [51]. Particularly, the formulation of the constituents' balances is based on Truesdell's three "metaphysical principles" of mixture theories [239], formulated as follows:

1. *All properties of the mixture must be mathematical consequences of properties of the constituents.*

2. *So as to describe the motion of a constituent, we may in imagination isolate it from the rest of the mixture, provided we allow properly for the actions of the other constituents upon it.*

3. *The motion of the mixture is governed by the same equations as is a single body.*

These principles presume that the balance equations of multiphasic material can be derived from the regular balance relations of continuum mechanics of singlephasic material, provided the interaction between the different constituents is taken into account by additional production terms. Furthermore, these principles state that the balance equations of the overall aggregate equate to those of singlephasic material.

Balances for the individual constituents

According to Truesdell's second metaphysical principle, the individual balance relations for each constituent φ^α are postulated in analogy to the master balances of the overall aggregate (2.43) and (2.44). Consequently, the scalar and vectorial master balance equations for the individual constituents are given by

$$\begin{aligned} \frac{\mathrm{d}_\alpha}{\mathrm{d}t} \int\limits_{\mathcal{B}} \Psi^\alpha \, \mathrm{d}v &= \int\limits_{\mathcal{S}} (\boldsymbol{\phi}^\alpha \cdot \mathbf{n}) \, \mathrm{d}a + \int\limits_{\mathcal{B}} \sigma^\alpha \, \mathrm{d}v + \int\limits_{\mathcal{B}} \hat{\Psi}^\alpha \, \mathrm{d}v \,, \\ \frac{\mathrm{d}_\alpha}{\mathrm{d}t} \int\limits_{\mathcal{B}} \boldsymbol{\Psi}^\alpha \, \mathrm{d}v &= \int\limits_{\mathcal{S}} (\boldsymbol{\Phi}^\alpha \, \mathbf{n}) \, \mathrm{d}a + \int\limits_{\mathcal{B}} \boldsymbol{\sigma}^\alpha \, \mathrm{d}v + \int\limits_{\mathcal{B}} \hat{\boldsymbol{\Psi}}^\alpha \, \mathrm{d}v \end{aligned} \tag{2.45}$$

with $(\cdot)^\alpha$ the quantities of the constituent φ^α, and the corresponding local formulations read

$$\begin{aligned} (\Psi^\alpha)'_\alpha + \Psi^\alpha \operatorname{div} \overset{\prime}{\mathbf{x}}_\alpha &= \operatorname{div} \boldsymbol{\phi}^\alpha + \sigma^\alpha + \hat{\Psi}^\alpha \,, \\ (\boldsymbol{\Psi}^\alpha)'_\alpha + \boldsymbol{\Psi}^\alpha \operatorname{div} \overset{\prime}{\mathbf{x}}_\alpha &= \operatorname{div} \boldsymbol{\Phi}^\alpha + \boldsymbol{\sigma}^\alpha + \hat{\boldsymbol{\Psi}}^\alpha \,. \end{aligned} \tag{2.46}$$

Remark: Even if the overall aggregate was assumed to be a closed system, each constituent is considered an open system in the mixture. Thus the production terms of the individual constituents are generally unequal zero. □

Coupling terms

Truesdell's first metaphysical principle states that the summation of the constituents' balances (2.46) and the overall aggregate's balances (2.44) have to yield identical mechanical results. From this postulation, the following restrictions for the coupling terms arise:

$$\begin{aligned} \Psi &= \textstyle\sum_\alpha \Psi^\alpha\,, \quad \boldsymbol{\phi}\cdot\mathbf{n} = \sum_\alpha[\boldsymbol{\phi}^\alpha - \Psi^\alpha(\overset{\prime}{\mathbf{x}}_\alpha - \dot{\mathbf{x}})]\cdot\mathbf{n}\,, \quad \sigma = \textstyle\sum_\alpha \sigma^\alpha\,, \quad \hat{\Psi} = \sum_\alpha \hat{\Psi}^\alpha\,, \\ \boldsymbol{\Psi} &= \textstyle\sum_\alpha \boldsymbol{\Psi}^\alpha\,, \quad \boldsymbol{\Phi}\,\mathbf{n} = \sum_\alpha[\boldsymbol{\Phi}^\alpha - \boldsymbol{\Psi}^\alpha\otimes(\overset{\prime}{\mathbf{x}}_\alpha - \dot{\mathbf{x}})]\,\mathbf{n}\,, \quad \boldsymbol{\sigma} = \textstyle\sum_\alpha \boldsymbol{\sigma}^\alpha\,, \quad \hat{\boldsymbol{\Psi}} = \sum_\alpha \hat{\boldsymbol{\Psi}}^\alpha\,. \end{aligned} \tag{2.47}$$

2.4.2 Specific balance equations

In the above relations, the physical quantities Ψ and $\boldsymbol{\Psi}$, as well as Ψ^α and $\boldsymbol{\Psi}^\alpha$, are placeholders for the balanced quantities. In the following, the specific balance equations for mass, momentum, angular momentum, energy and entropy will be summarised in their local form for the overall aggregate φ and the constituents φ^α. For a complete derivation of these equations, the interested reader is referred to Ehlers [84].

Conservation of mass

For the balance of mass, the mechanical quantity is the partial density, while the efflux and supply terms are zero. Since the overall body is considered as closed system, mass production is excluded for the aggregate. In the case of the constituents, the balance states that the mass of the constituent is constant with respect to the production term $\hat{\rho}^\alpha$. This latter accounts for mass exchanges between the constituents within the aggregate, for example, chemical reactions or phase transitions. For the latter one, the interested reader is referred to Graf [119], Häberle [124] and Eurich [104]. The summary of the quantities is given by

$$\begin{aligned} &\text{mechanical quantity:} && \Psi \to \rho\,, && \Psi^\alpha \to \rho^\alpha\,, \\ &\text{efflux:} && \boldsymbol{\phi} \to \mathbf{0}\,, && \boldsymbol{\phi}^\alpha \to \mathbf{0}\,, \\ &\text{supply:} && \sigma \to 0\,, && \sigma^\alpha \to 0\,, \\ &\text{production:} && \hat{\Psi} \to 0\,, && \hat{\Psi}^\alpha \to \hat{\rho}^\alpha\,. \end{aligned} \tag{2.48}$$

With $(2.44)_1$ and $(2.46)_1$, this yields the following local mass balances

$$\begin{aligned} \dot{\rho} &+ \rho\,\mathrm{div}\,\dot{\mathbf{x}} &&= 0\,, \\ (\rho^\alpha)'_\alpha &+ \rho^\alpha \mathrm{div}\,\overset{\prime}{\mathbf{x}}_\alpha &&= \hat{\rho}^\alpha\,. \end{aligned} \tag{2.49}$$

of the overall aggregate and individual constituents. Moreover, the correlations $(2.47)_1$ request

$$\rho = \sum_\alpha \rho^\alpha \quad \text{and} \quad \sum_\alpha \hat{\rho}^\alpha = 0\,. \tag{2.50}$$

Note that the first condition is already given per definition in (2.9).

Balance of linear momentum

The balance of linear momentum equates the temporal change of the local momentum, $\rho\,\dot{\mathbf{x}}$ or $\rho^\alpha\,\overset{\prime}{\mathbf{x}}_\alpha$, to the forces from the vicinity (efflux term), namely $\operatorname{div}\mathbf{T}$ or $\operatorname{div}\mathbf{T}^\alpha$, the forces from a distance (supply term), $\mathbf{b}$ and $\mathbf{b}^\alpha$, e. g. gravitational forces $\mathbf{g}$ per unit volume, and possible productions, viz.

$$\begin{aligned}
&\text{mechanical quantity:} && \boldsymbol{\Psi} \to \rho\,\dot{\mathbf{x}}\,, && \boldsymbol{\Psi}^\alpha \to \rho^\alpha\,\overset{\prime}{\mathbf{x}}_\alpha\,,\\
&\text{efflux:} && \boldsymbol{\Phi} \to \mathbf{T}\,, && \boldsymbol{\Phi}^\alpha \to \mathbf{T}^\alpha\,,\\
&\text{supply:} && \boldsymbol{\sigma} \to \rho\,\mathbf{b}\,, && \boldsymbol{\sigma}^\alpha \to \rho^\alpha\,\mathbf{b}^\alpha\,,\\
&\text{production:} && \hat{\boldsymbol{\Psi}} \to \mathbf{0}\,, && \hat{\boldsymbol{\Psi}}^\alpha \to \hat{\mathbf{s}}^\alpha\,.
\end{aligned} \tag{2.51}$$

In the constituent's case, the production term is the total momentum production $\hat{\mathbf{s}}^\alpha$. This latter comprises a direct part $\hat{\mathbf{p}}^\alpha$, standing for the interaction forces between the constituents, and an additional part arising from the density production $\hat{\rho}^\alpha\overset{\prime}{\mathbf{x}}_\alpha$, viz.

$$\hat{\mathbf{s}}^\alpha = \hat{\mathbf{p}}^\alpha + \hat{\rho}^\alpha\,\overset{\prime}{\mathbf{x}}_\alpha\,. \tag{2.52}$$

Inserting (2.51) in the local master balances $(2.44)_2$ and $(2.46)_2$ yields the local momentum balances for the overall aggregate and the constituent

$$\begin{aligned}
\rho\,\ddot{\mathbf{x}} &= \operatorname{div}\mathbf{T} + \rho\,\mathbf{b}\,,\\
\rho^\alpha\,\overset{\prime\prime}{\mathbf{x}}_\alpha &= \operatorname{div}\mathbf{T}^\alpha + \rho^\alpha\mathbf{b}^\alpha + \hat{\mathbf{p}}^\alpha\,,
\end{aligned} \tag{2.53}$$

respectively. The coupling terms $(2.47)_2$ provide the following constraints:

$$\begin{aligned}
\rho\,\dot{\mathbf{x}} &= \sum_\alpha \rho^\alpha\,\overset{\prime}{\mathbf{x}}_\alpha\,, \qquad \mathbf{T} = \sum_\alpha \left(\mathbf{T}^\alpha - \rho^\alpha\,\mathbf{d}_\alpha \otimes \mathbf{d}_\alpha\right),\\
\rho\,\mathbf{b} &= \sum_\alpha \rho^\alpha\,\mathbf{b}^\alpha\,, \qquad \mathbf{0} = \sum_\alpha \hat{\mathbf{s}}^\alpha = \sum_\alpha (\hat{\mathbf{p}}^\alpha + \hat{\rho}^\alpha\,\overset{\prime}{\mathbf{x}}_\alpha)\,.
\end{aligned} \tag{2.54}$$

Thereby, $(2.54)_1$ verifies the definition of the barycentric velocity, cf. (2.15), while $(2.54)_3$ recovers the definition of the total density (2.9) in the case of uniform body forces, e. g. gravitational forces $\mathbf{b} = \mathbf{b}^\alpha = \mathbf{g}$. The restriction $(2.54)_2$ is valid in mixture theories and not treated further in the TPM.

Balance of angular momentum

The balance of angular momentum or rather moment of momentum (m.o.m.) states that the temporal change of angular momentum of a body $\mathcal{B}$ corresponds to the sum of moments of all forces acting on $\mathcal{B}$ related to the same origin point. The quantities of the

master balances can be summarised to

$$\begin{aligned}
&\text{mechanical quantity:} && \boldsymbol{\Psi} \to \mathbf{x} \times (\rho\, \dot{\mathbf{x}})\,, && \boldsymbol{\Psi}^\alpha \to \mathbf{x} \times (\rho^\alpha\, \overset{\prime}{\mathbf{x}}_\alpha)\,,\\
&\text{efflux:} && \boldsymbol{\Phi} \to \mathbf{x} \times \mathbf{T}\,, && \boldsymbol{\Phi}^\alpha \to \mathbf{x} \times \mathbf{T}^\alpha\,,\\
&\text{supply:} && \boldsymbol{\sigma} \to \mathbf{x} \times (\rho\, \mathbf{b})\,, && \boldsymbol{\sigma}^\alpha \to \mathbf{x} \times (\rho^\alpha\, \mathbf{b}^\alpha)\,,\\
&\text{production:} && \hat{\boldsymbol{\Psi}} \to \mathbf{0}\,, && \hat{\boldsymbol{\Psi}}^\alpha \to \hat{\mathbf{h}}^\alpha\,.
\end{aligned} \tag{2.55}$$

Therein, $\hat{\mathbf{h}}^\alpha$ denotes the spin production of the constituent. After some reformulations of the master balance $(2.44)_2$ and with the help of the mass and linear momentum balances, $(2.49)_1$ and $(2.53)_1$, respectively, combined with the property of the axial vector, the local m. o. m. balance of the overall aggregate results in the symmetry constraint of the Cauchy stress tensor $\mathbf{T}$, viz.

$$\mathbf{0} = \mathbf{I} \times \mathbf{T} \quad \to \quad \mathbf{T} = \mathbf{T}^T\,. \tag{2.56}$$

In analogy, the local m. o. m. balance for the constituent φ^α reads

$$\mathbf{0} = \mathbf{I} \times \mathbf{T}^\alpha + \hat{\mathbf{m}}^\alpha \quad \to \quad (\mathbf{T}^\alpha)^T = \mathbf{T}^\alpha + \hat{\mathbf{M}}^\alpha\,, \tag{2.57}$$

where $\hat{\mathbf{m}}^\alpha$ is the direct part of the spin production $\hat{\mathbf{h}}^\alpha = \hat{\mathbf{m}}^\alpha + \mathbf{x} \times \hat{\mathbf{s}}^\alpha$, and $\hat{\mathbf{M}}^\alpha$ is called the "angular momentum coupling tensor" and stands for the skew-symmetric part of $\mathbf{T}^\alpha$. The constraint from $(2.47)_2$ states with $(2.55)_4$ that $\sum_\alpha \hat{\mathbf{h}}^\alpha = \mathbf{0}$, yielding $\sum_\alpha \hat{\mathbf{m}}^\alpha = \mathbf{0}$ and $\sum_\alpha \hat{\mathbf{M}}^\alpha = \mathbf{0}$. Consequently, the sum of the partial stress tensors must be symmetric, viz.

$$\sum_\alpha \mathbf{T}^\alpha = \sum_\alpha (\mathbf{T}^\alpha)^T\,. \tag{2.58}$$

In the case of non-polar materials (Cauchy-Boltzmann continua), Hassanizadeh & Gray [127] and Ehlers [84] showed by homogenisation that symmetric stresses on the microscale lead to symmetric stresses on the macroscale, as homogenisations do not yield new informations. Therefore, for non-polar materials,

$$\mathbf{T}^\alpha = (\mathbf{T}^\alpha)^T \quad \text{and} \quad \hat{\mathbf{m}}^\alpha \equiv \mathbf{0} \tag{2.59}$$

applies. However, in this other case of micropolar materials, the particles might rotate and lead to asymmetric partial stress tensors. Micropolar materials (Cosserat continua) in the framework of the TPM are presented, e. g., in Diebels & Ehlers [74], Diebels [73], Ehlers [84], Scholz [219] and Bidier [29].

Energy conservation law

The energy conservation law, also known as the first law of thermodynamics, equals the temporal change of the internal and kinetic energy of the body $\mathcal{B}$ with the mechanical power at a vicinity and from a distance, and non-mechanical power from heat flux and

heat supply. The summary of the master quantities for the overall aggregate and the constituent is

$$\begin{aligned}
&\text{mechanical quantity:} && \Psi \to \rho\,(\varepsilon + \tfrac{1}{2}\,\dot{\mathbf{x}}\cdot\dot{\mathbf{x}})\,, && \Psi^\alpha \to \rho^\alpha\,(\varepsilon^\alpha + \tfrac{1}{2}\,\overset{\prime}{\mathbf{x}}_\alpha\cdot\overset{\prime}{\mathbf{x}}_\alpha)\,,\\
&\text{efflux:} && \boldsymbol{\phi} \to \mathbf{T}^T\,\dot{\mathbf{x}} - \mathbf{q}\,, && \boldsymbol{\phi}^\alpha \to (\mathbf{T}^\alpha)^T\,\overset{\prime}{\mathbf{x}}_\alpha - \mathbf{q}^\alpha\,,\\
&\text{supply:} && \sigma \to \rho\,(\mathbf{b}\cdot\dot{\mathbf{x}} + r)\,, && \sigma^\alpha \to \rho^\alpha\,(\mathbf{b}^\alpha\cdot\overset{\prime}{\mathbf{x}}_\alpha + r^\alpha)\,,\\
&\text{production:} && \hat{\Psi} \to 0\,, && \hat{\Psi}^\alpha \to \hat{e}^\alpha\,.
\end{aligned} \tag{2.60}$$

Therein, ε and ε^α stand for the specific internal energies, $\mathbf{q}$ and $\mathbf{q}^\alpha$ denote the heat influxes via the surface, and r and r^α indicate the heat supplies from a distance for the overall aggregate and the constituent, respectively. In addition, $\hat{e}^\alpha$ is the total constituent's energy production, which can be split into a direct part $\hat{\varepsilon}^\alpha$ and parts from the momentum and mass exchanges. With the local master balance $(2.44)_1$, the local energy balance for the mixture yields

$$\rho\,\dot{\varepsilon} = \mathbf{T}\cdot\mathbf{L} - \operatorname{div}\mathbf{q} + \rho\,r\,. \tag{2.61}$$

In analogy, the constituent's local energy balance reads with $(2.46)_1$, $(2.49)_1$ and $(2.53)_1$

$$\begin{aligned}
&\rho^\alpha\,(\varepsilon^\alpha)'_\alpha = \mathbf{T}^\alpha\cdot\mathbf{L}_\alpha - \operatorname{div}\mathbf{q}^\alpha + \rho^\alpha\,r^\alpha + \hat{\varepsilon}^\alpha\,,\\
&\text{where}\quad \hat{e}^\alpha = \hat{\varepsilon}^\alpha + \hat{\mathbf{p}}^\alpha\cdot\overset{\prime}{\mathbf{x}}_\alpha + \hat{\rho}^\alpha\,(\varepsilon^\alpha + \tfrac{1}{2}\,\overset{\prime}{\mathbf{x}}_\alpha\cdot\overset{\prime}{\mathbf{x}}_\alpha)\,.
\end{aligned} \tag{2.62}$$

From the coupling constraints (2.47), the following dependencies can be derived

$$\begin{aligned}
\varepsilon &= \frac{1}{\rho}\sum_\alpha \rho^\alpha\,(\varepsilon^\alpha + \tfrac{1}{2}\,\mathbf{d}_\alpha\cdot\mathbf{d}_\alpha)\,,\\
\mathbf{q} &= \sum_\alpha [\mathbf{q}^\alpha - (\mathbf{T}^\alpha)^T\mathbf{d}_\alpha + \rho^\alpha\,\varepsilon^\alpha\,\mathbf{d}_\alpha + \tfrac{1}{2}\,\rho^\alpha\,(\mathbf{d}_\alpha\cdot\mathbf{d}_\alpha)\,\mathbf{d}_\alpha]\,,\\
r &= \frac{1}{\rho}\sum_\alpha \rho^\alpha\,(r^\alpha + \mathbf{b}^\alpha\cdot\mathbf{d}_\alpha)\,,\\
0 &= \sum_\alpha \hat{e}^\alpha\,.
\end{aligned} \tag{2.63}$$

In thermal processes, the energy balance determines the temperature of the overall aggregate and constituent, compare, e. g., Häberle [124] and Eurich [104]. In the case of isothermal processes, the energy balance is only exploited for the formulation of the entropy inequality.

Entropy principle

The entropy balance states that the temporal change of the entropy equals the sum of external entropy changes (effluxes and supplies) and internal entropy production. Here, the entropy effluxes and supplies are given by *a priori* constitutive assumptions in analogy

to singlephasic materials, compare Ehlers [83–86]:

$$\begin{aligned}
&\text{mechanical quantity:} && \Psi \to \rho\,\eta\,, && \Psi^\alpha \to \rho^\alpha\,\eta^\alpha\,,\\
&\text{efflux:} && \boldsymbol{\phi} \to -\frac{\mathbf{q}}{\theta}\,, && \boldsymbol{\phi}^\alpha \to -\frac{\mathbf{q}^\alpha}{\theta^\alpha}\,,\\
&\text{supply:} && \sigma \to \frac{\rho\,r}{\theta}\,, && \sigma^\alpha \to \frac{\rho^\alpha\,r^\alpha}{\theta^\alpha}\,,\\
&\text{production:} && \hat{\Psi} \to \hat{\eta} \geq 0\,, && \hat{\Psi}^\alpha \to \hat{\eta}^\alpha\,.
\end{aligned} \tag{2.64}$$

Therein, η and η^α are the mass-specific entropies, θ and θ^α the absolute temperatures in Kelvin, and $\hat{\eta}$ and $\hat{\eta}^\alpha$ the entropy productions of the overall aggregate φ and the constituents φ^α, respectively. The interpretation (2.64) leads with the local master balances $(2.44)_1$ and $(2.46)_1$, and the mass balances (2.49) to the local form of the entropy balance for the aggregate and the specific constituent:

$$\begin{aligned}
\rho\,\dot{\eta} \quad &+ \quad \operatorname{div}\frac{\mathbf{q}}{\theta} \quad - \quad \frac{\rho\,r}{\theta} \quad = \quad \hat{\eta}\,,\\
\rho^\alpha(\eta^\alpha)'_\alpha \quad &+ \quad \operatorname{div}\frac{\mathbf{q}^\alpha}{\theta^\alpha} \quad - \quad \frac{\rho^\alpha\,r^\alpha}{\theta^\alpha} \quad = \quad \hat{\zeta}^\alpha
\end{aligned} \tag{2.65}$$

with $\hat{\zeta}^\alpha$ the direct part of the entropy production, viz. $\hat{\eta}^\alpha = \hat{\zeta}^\alpha + \hat{\rho}^\alpha\,\eta^\alpha$. The dependencies arising from (2.47) request

$$\begin{aligned}
\eta &= \frac{1}{\rho}\sum_\alpha \rho^\alpha\,\eta^\alpha\,,\\
\frac{\mathbf{q}}{\theta} &= \textstyle\sum_\alpha \left(\dfrac{\mathbf{q}^\alpha}{\theta^\alpha} + \rho^\alpha\eta^\alpha\mathbf{d}_\alpha\right),\\
\frac{\rho\,r}{\theta} &= \textstyle\sum_\alpha \dfrac{\rho^\alpha\,r^\alpha}{\theta^\alpha}\,,\\
\hat{\eta} &= \textstyle\sum_\alpha \hat{\eta}^\alpha \geq 0\,.
\end{aligned} \tag{2.66}$$

Remark: The postulate of a common entropy inequality of all constituents is a necessary and sufficient condition for the existence of dissipation mechanisms within the mixture. Therefore, only $\hat{\eta} \geq 0$ is prescribed to fulfil the second law of thermodynamics in multiphasic materials. A detailed discussion of this topic can be found in Truesdell [238] and Ehlers [86]. □

The restriction $(2.66)_4$ can be rewritten with $(2.65)_2$ and the split of the direct entropy production, i. e. $\hat{\zeta}^\alpha = \hat{\eta}^\alpha - \hat{\rho}^\alpha\,\eta^\alpha$, to

$$\hat{\eta} = \sum_\alpha \hat{\eta}^\alpha = \sum_\alpha [\,\rho^\alpha(\eta^\alpha)'_\alpha + \hat{\rho}^\alpha\eta^\alpha + \operatorname{div}\frac{\mathbf{q}^\alpha}{\theta^\alpha} - \frac{\rho^\alpha\,r^\alpha}{\theta^\alpha}] \geq 0\,. \tag{2.67}$$

Here, it is convenient to introduce the mass-specific Helmholtz free energy ψ^α of the constituent φ^α through

$$\psi^\alpha := \varepsilon^\alpha - \theta^\alpha \eta^\alpha \,. \tag{2.68}$$

Finally, by substituting the entropy η^α with (2.68) in (2.67) and with the energy balance (2.62), the second law of thermodynamics is recovered for multiphasic materials in the so-called Clausius-Duhem inequality:

$$\begin{aligned} \sum_\alpha \frac{1}{\theta^\alpha} \Big[\mathbf{T}^\alpha \cdot \mathbf{L}_\alpha - \rho^\alpha [(\psi^\alpha)'_\alpha + (\theta^\alpha)'_\alpha \eta^\alpha] - \hat{\mathbf{p}}^\alpha \cdot \overset{\prime}{\mathbf{x}}_\alpha - \\ - \hat{\rho}^\alpha (\psi^\alpha + \tfrac{1}{2} \overset{\prime}{\mathbf{x}}_\alpha \cdot \overset{\prime}{\mathbf{x}}_\alpha) - \frac{\mathbf{q}^\alpha}{\theta^\alpha} \cdot \operatorname{grad} \theta^\alpha + \hat{e}^\alpha \Big] \geq 0. \end{aligned} \tag{2.69}$$

No physical quantity will be directly derived from the entropy inequality (2.69), though, it is the basis for the constitutive modelling in Chapter 3.

2.5 Phase-field method to solid fracture mechanics

The phase-field method (PFM) to fracture has gained significant attention in recent years due to its ability to model crack initiation, propagation, and branching in a computationally efficient and physically realistic manner. Unlike discrete approaches like the linear elastic fracture mechanics (Griffith [120] and Irwin [149]) or cohesive zone models (Dugdale [78] and Barenblatt [18]), the phase-field approach represents cracks as continuous and diffuse interfaces within a material, allowing a continuous displacement field across the fracture surfaces on a fixed mesh. An extensive review of the historical development of the phase-field method of fracture can be found, for example, in the work of Ambati *et al.* [8], Wu *et al.* [253], Spatschek *et al.* [228] or in the article of Heider [134] with a focus on hydraulic fracturing. In the following, the PFM to brittle solid fracture is briefly introduced.

The phase-field variable

The physics and mechanics communities have developed the phase-field method for fracture processes independently. Even though the overall approach and the derivation of the constitutive equations are different, both communities propose a continuous field variable, the phase-field variable or order parameter ϕ, to differentiate the cracked and unbroken states of the solid skeleton, i. e.

$$\phi(\mathbf{x}, t) \in [0, 1] \quad \text{with} \quad \begin{cases} \phi = 0 & : \text{intact solid phase,} \\ 0 < \phi < 1 & : \text{diffuse interface,} \\ \phi = 1 & : \text{fully broken solid phase.} \end{cases} \tag{2.70}$$

Remark: Most of the contributions in the field of phase-field method to fracture introduce the phase-field variable as in (2.70). However, some groups define the phase field

alternatively as $\phi = 0$ for the broken and $\phi = 1$ for the intact state, compare, among others, the group of Aranson *et al.* [15], Bourdin *et al.* [50], Kuhn & Müller [164], Mikelić *et al.* [196], Heider & Markert [135] and related groups. □

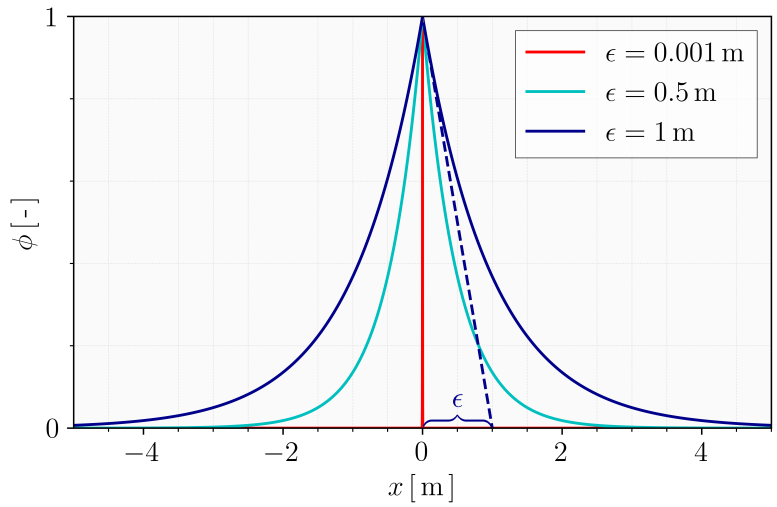

Figure 2.3: *Depiction of a smoothed phase field ϕ with respect to different length-scale parameters ϵ, where the axial position $x = 0$ defines the crack center. The abscissa of the tangent at $x = 0$ corresponds to the length-scale parameter (depicted here for $\epsilon = 1$ m, dashed line).*

In the damaged zone $0 < \phi < 1$, the phase-field variable is smoothed out according to a length-scale parameter ϵ with $\phi = \exp^{-|x|/\epsilon}$, cf. Lancioni & Royer-Carfagni [167] and Miehe *et al.* [193], see Figure 2.3. This approach leads to a diffuse transition zone between the unbroken and broken domain without a discontinuous jump, which is a major advantage of the phase-field method compared to a discrete approach. The length-scale parameter has the dimension of a length and regulates the transition zone's width. For the case that ϵ becomes infinitesimally small, a discrete crack pattern is recovered. However, due to the arbitrary choice of the length-scale parameter, the phase-field method is limited when determining the aperture of a fracture. Moreover, the element's size within a finite element formulation has to be small enough with respect to the length-scale parameter to resolve the diffuse interface, leading to computational costs.

Energy functional

In the physics community, the energetic formulation of the phase-field method to fracture initially stems from the Ginzburg-Landau theory, which was developed for the phase transition of supra-conductive materials, cf. Ginzburg & Landau [118]. From this, different energetic formulations have been developed. Among the most popular are the models according to Aranson *et al.* [15], Karma *et al.* [154], Henry & Levine [139] and Spatschek *et al.* [228].

In contrast, the approaches of the mechanical community originate from the variational formulation by Francfort & Marigo [109]. Based on the classical Griffith criterion, cf.

Griffith [120], this mathematical model treats the quasi-static growth of brittle fracture in elastic solids. Unlike Griffith's theory, the model can capture crack initiation and predict the crack path by minimisation of an energy functional. Thereupon, Bourdin *et al.* [50] suggested a regularised version of the variational formulation introducing a secondary field variable ϕ – the crack parameter – to enable efficient numerical implementation. The proposed total energy functional to minimise reads

$$\begin{aligned} E(\boldsymbol{\varepsilon},\phi) &= \int_{\Omega} g(\phi)\psi_0(\boldsymbol{\varepsilon})\,\mathrm{d}v + G_c \int_{\Omega} \left(\frac{\phi^2}{4c} + c\,|\mathrm{grad}\phi|^2 \right) \mathrm{d}v \\ \text{with} \quad & g(\phi) = (1-\phi)^2 + \eta_r\,, \end{aligned} \tag{2.71}$$

where ψ_0 stands for the elastic energy density function, c is a regularisation parameter, G_c represents the material fracture toughness, and $g(\phi)$ denotes the degradation function with a dimensionless parameter η_r assuring an artificial residual stiffness in the fully broken case. Note that Bourdin *et al.* [50] defined the field variable alternatively to (2.70) with $\phi = 0$ for the broken and $\phi = 1$ for the intact state in the original article and that the notation has been adapted in (2.71) for unification purpose. Moreover, the regularisation parameter c corresponds to the double length-scale parameter used in this monograph, viz. $c = 2\epsilon$ in (2.71). When the parameter c tends to zero, the regularised formulation (2.71) converges to the energy functional of Francfort & Marigo [109], which complies with Griffith's fracture theory, compare Bourdin *et al.* [50]. Besides the applied degradation function $g(\phi) = (1-\phi)^2 + \eta_r$ according to Bourdin *et al.*, other groups developed different models to link the mechanical behaviour and the phase field. A review of some energetic degradation models can be found, e. g., in Sargado *et al.* [216] and Wu *et al.* [253].

Remark: In [190, 193], Miehe *et al.* introduced an energy functional in a geometric context with regard to the definition of a dissipation potential. Even if the approach differs from the derivation of the energy functional according to Bourdin *et al.* [50] based on the definition of a regularised surface energy, both models lead to similar results. □

Evolution equation

In addition to (2.71), Hakim & Karma [125], Kuhn & Müller [164, 165] and Miehe *et al.* [190, 193], among others, define a Ginzburg-Landau type evolution equation, cf. [118], for the phase-field variable:

$$\dot{\phi} = \frac{1}{M}\left[2(1-\phi)\,\psi_0(\boldsymbol{\varepsilon}) - G_c\Big(\frac{\phi}{\epsilon} - \epsilon\,\mathrm{div}\,\mathrm{grad}\phi \Big) \right]. \tag{2.72}$$

The notation of ϕ has been adapted according to (2.70) for unification purposes. Moreover, in their original paper, Hakim & Karma and Kuhn & Müller define the mobility parameter M, which controls the energy dissipation rate within the fracturing process, reciprocally to (2.72).

"Anisotropic" stored energy

So far, the elastic energy density function ψ_0 corresponds to the Helmholtz free energy of isotropic[1] material behaviour for an elastic material. However, this isotropic material behaviour can lead to unrealistic fracturing processes, predicting, for example, fracturing under compression. To cope with this shortcoming, several groups proposed an anisotropic fracture model through a split of ψ_0 into a positive part ψ_0^+, contributing to damage, and a negative part ψ_0^-, resisting damage. Some anisotropic fracture models consider, for example, a volumetric and deviatoric split of the elastic energy, such as Lancioni & Royer-Carfagni [167] and Amor *et al.* [12]. Besides these, Miehe *et al.* [193] define an energy function for anisotropic fracture behaviour based on a spectral decomposition of the linearised strain

$$\boldsymbol{\varepsilon} = \sum_{i=1}^{3} \varepsilon_i \, \mathbf{n}_i \otimes \mathbf{n}_i \tag{2.73}$$

with ε_i the principal strains and $\mathbf{n}_i$ the principal strain directions. A summary of the spectral decomposition of the strain tensor can be found in Appendix B.1. With this, the positive (tension) and negative (compression) parts of the elastic energy yield

$$\psi_0^{\pm}(\boldsymbol{\varepsilon}) := \lambda^S \, \frac{\langle \varepsilon_1 + \varepsilon_2 + \varepsilon_3 \rangle_{\pm}^2}{2} + \mu^S \Big[\langle \varepsilon_1 \rangle_{\pm}^2 + \langle \varepsilon_2 \rangle_{\pm}^2 + \langle \varepsilon_3 \rangle_{\pm}^2 \Big] \, . \tag{2.74}$$

Therein, λ^S and μ^S are the Lamé constants and the Macauley brackets are defined through $\langle \cdot \rangle_{\pm} = (|\cdot| \pm \cdot)/2$. The degradation function only affects the tension part of the elastic energy, leading to the stored elastic energy

$$\psi(\boldsymbol{\varepsilon}, \phi) = \big[(1-\phi)^2 + \eta_r \big] \psi_0^+(\boldsymbol{\varepsilon}) + \psi_0^-(\boldsymbol{\varepsilon}) \, . \tag{2.75}$$

This anisotropic material model completely prevents cracking in compression.

In the following chapter, the phase-field method is embedded in the prior framework of the TPM to evaluate hydraulic fracturing processes in a triphasic porous material.

[1] Note that as mentioned in the introduction, Section 1.2, the terms *isotropic* and *anisotropic* fracture behaviour refer to an energy split in the literature of the PFM to fracture and are unrelated to directional mechanical properties from continuum mechanics.

Chapter 3:
Model adaptation and constitutive modelling

This chapter applies the previously introduced theoretical fundamentals to hydraulic fracturing porous media. First, the model assumptions for the problem under study are outlined, and the specific balance equations are reformulated. Since there are more unknown variables as balance equations, further relations must be determined to close the problem. As mentioned in Subsection 2.4.2, the entropy inequality will give the restrictive frame for these relations. Therefore, the entropy inequality is adapted to the particular problem. The constitutive modelling will be developed exemplarily for a partially saturated porous material. Finally, the closure problem for the coupled system is recapitulated at the end of the chapter.

3.1 Preliminary model assumptions

For this monograph, two multiphasic models are considered. Either a single liquid pore fluid saturates the solid, leading to a biphasic model $\varphi = \varphi^S \cup \varphi^L$, or a liquid and a gaseous pore fluid inhibit the solid skeleton for the additional consideration of partially saturated porous material, leading to a triphasic model $\varphi = \varphi^S \cup \varphi^L \cup \varphi^G$. In both cases, a common (spatially and temporally) constant temperature is assumed for the mixture and all constituents, viz. $\theta = \theta^\alpha \equiv$ constant. Note that the energy balance is not considered further from this assumption of isothermal processes. Apart from that, an inert, brittle-elastic solid skeleton φ^S is regarded in both models. For the consideration of elastoplastic or viscoelastic solid skeletons within the TPM, the interested reader is referred, e. g., to the work of Ehlers [80–82, 86] and Ehlers & Markert [95, 96], respectively. Also, incompressibility is assumed for the solid skeleton φ^S and the pore liquid φ^L in both the partially and the fully saturated model:

$$\{\rho^{SR},\, \rho^{LR}\} \equiv \text{constant}. \tag{3.1}$$

In the case of the triphasic model, the gas phase is considered compressible in the sense of an ideal gas, yielding $\rho^{GR} = \rho^{GR}(p^{GR})$.

Moreover, in this thesis, no mass exchanges, such as phase transitions or chemical reactions, are regarded. Thus, the mass production vanishes for all constituents, viz.

$$\hat{\rho}^\alpha \equiv 0\,. \tag{3.2}$$

In addition, all constituents are subject to gravity as the only and constant body force, i. e. $\mathbf{b} = \mathbf{b}^\alpha = \mathbf{g}$.

Furthermore, the material is considered non-polar. Therefore, the angular momentum balance results in the symmetry statement of the stress tensors, namely

$$\mathbf{T} = \mathbf{T}^T \quad \text{and} \quad \mathbf{T}^\alpha = (\mathbf{T}^\alpha)^T \,. \tag{3.3}$$

3.2 Adaptation of balance relations

The adaptation of balance relations and the following constitutive approach will be presented for the triphasic model. However, the biphasic model can be recovered by leaving out the gas phase. Besides, a detailed derivation of the biphasic fracturing model can be found in Luo [178]. In Section 3.5, the closure problem will be summarised for both models.

3.2.1 Mass and volume balances

The local mass balance $(2.49)_2$ for the constituent φ^α simplifies with the exclusion of mass exchanges (3.2) to

$$(\rho^\alpha)'_\alpha + \rho^\alpha \operatorname{div} \overset{\prime}{\mathbf{x}}_\alpha = 0 \,. \tag{3.4}$$

For easier readability, the spatial velocity $\overset{\prime}{\mathbf{x}}_\alpha$ of the constituent φ^α will be substituted in the following by $\mathbf{v}_\alpha$, compare $(2.13)_1$.

Using the material time derivative (2.18) and the definition of the seepage velocity (2.19), the mass balances of the pore fluids φ^β, with $\beta = \{L, G\}$, can be rewritten with respect to the solid motion via

$$(\rho^\beta)'_S + \operatorname{grad} \rho^\beta \cdot \mathbf{w}_\beta + \rho^\beta \operatorname{div} (\mathbf{w}_\beta + \mathbf{v}_S) = 0 \,. \tag{3.5}$$

Sorting the terms and applying the divergence theorem (cf. Appendix A.2), viz.

$$(\rho^\beta)'_S + \underbrace{\operatorname{grad} \rho^\beta \cdot \mathbf{w}_\beta + \rho^\beta \operatorname{div} \mathbf{w}_\beta}_{\operatorname{div} (\rho^\beta \mathbf{w}_\beta)} + \rho^\beta \operatorname{div} \mathbf{v}_S = 0 \,, \tag{3.6}$$

yields with the definition of the partial density (2.8)

$$(n^\beta \rho^{\beta R})'_S + \operatorname{div} (n^\beta \rho^{\beta R} \mathbf{w}_\beta) + n^\beta \rho^{\beta R} \operatorname{div} \mathbf{v}_S = 0 \,. \tag{3.7}$$

According to (3.6), the gas mass balance reads

$$(\rho^G)'_S + \operatorname{div} (\rho^G \mathbf{w}_G) + \rho^G \operatorname{div} \mathbf{v}_S = 0 \,. \tag{3.8}$$

Assuming material incompressibility for the solid and liquid, compare (3.1), the mass balances of these constituents can further be reduced to volume balances, i. e.

$$\begin{aligned} &(n^S)'_S + n^S \operatorname{div} \mathbf{v}_S = 0 \,, \\ &(n^L)'_S + \operatorname{div} (n^L \mathbf{w}_L) + n^L \operatorname{div} \mathbf{v}_S = 0 \,. \end{aligned} \tag{3.9}$$

Remark: The solid volume balance can be integrated analytically over time, yielding a relation for the solidity n^S relative to the initial solidity n_0^S and the deformation gradient $\mathbf{F}_S$. Therefore, the material derivative of the Jacobian determinant is rewritten with the tensor calculus rules from Appendix A via

$$(\det \mathbf{F}_S)'_S = \operatorname{cof} \mathbf{F}_S \cdot (\mathbf{F}_S)'_S = \det \mathbf{F}_S \, \mathbf{F}_S^{T-1} \cdot \mathbf{L}_S \, \mathbf{F}_S = (\det \mathbf{F}_S) \operatorname{div} \mathbf{v}_S \,, \tag{3.10}$$

leading to

$$\frac{(n^S)'_S}{n^S} = -\operatorname{div} \mathbf{v}_S = -\frac{(\det \mathbf{F}_S)'_S}{\det \mathbf{F}_S} \quad \rightarrow \quad n^S = n_0^S \, (\det \mathbf{F}_S)^{-1} \,. \tag{3.11}$$

With the relation between the partial density and volume fraction (2.8), the definition (2.26) of the solid initial partial density, namely $\rho_0^S = (\det \mathbf{F}_S) \, \rho^S$, is recovered. □

3.2.2 Momentum balances

With the assumption of gravitational forces as uniform and constant body forces, the momentum balance $(2.53)_2$ of the constituent φ^α is given by

$$\rho^\alpha (\mathbf{v}_\alpha)'_\alpha = \operatorname{div} \mathbf{T}^\alpha + \rho^\alpha \mathbf{g} + \hat{\mathbf{p}}^\alpha \,. \tag{3.12}$$

Again, considering all balances relative to the solid motion via (2.18), the fluid momentum balances result in

$$\begin{aligned} \rho^L \big[(\mathbf{v}_L)'_S + (\operatorname{grad} \mathbf{v}_L) \, \mathbf{w}_L \big] &= \operatorname{div} \mathbf{T}^L + \rho^L \mathbf{g} + \hat{\mathbf{p}}^L \,, \\ \rho^G \big[(\mathbf{v}_G)'_S + (\operatorname{grad} \mathbf{v}_G) \, \mathbf{w}_G \big] &= \operatorname{div} \mathbf{T}^G + \rho^G \mathbf{g} + \hat{\mathbf{p}}^G \,. \end{aligned} \tag{3.13}$$

Furthermore, for the numerical studies in Chapters 4 and 5, it is convenient to consider the momentum balance of the overall aggregate instead of the solid one. Thereby, the complete load of the aggregate can be determined as a boundary term in the numerical treatment, allowing the individual constituents to hold as much of the external load as corresponds to their states of deformation and motion. The overall momentum balance is obtained by summation of all constituents' momentum balances[1]

$$\sum_\alpha \big[\rho^\alpha (\mathbf{v}_\alpha)'_\alpha \big] = \sum_\alpha \big[\operatorname{div} \mathbf{T}^\alpha + \rho^\alpha \mathbf{g} + \hat{\mathbf{p}}^\alpha \big] \,. \tag{3.14}$$

Finally, with restriction of the momentum production $(2.54)_4$ under the assumption of no mass exchanges between the constituents, yielding $\sum_\alpha \hat{\mathbf{p}}^\alpha = \mathbf{0}$, the overall momentum balance reads

$$\begin{aligned} \rho^S (\mathbf{v}_S)'_S + \rho^L \big[(\mathbf{v}_L)'_S + (\operatorname{grad} \mathbf{v}_L) \, \mathbf{w}_L \big] + \rho^G \big[(\mathbf{v}_G)'_S + (\operatorname{grad} \mathbf{v}_G) \, \mathbf{w}_G \big] \\ = \operatorname{div} (\mathbf{T}^S + \mathbf{T}^L + \mathbf{T}^G) + \rho \, \mathbf{g} \,. \end{aligned} \tag{3.15}$$

Hereby, ρ stands for the overall density, i. e. $\rho = \rho^S + \rho^L + \rho^G$, according to (2.9).

[1] Equally, the overall momentum balance can be derived from the momentum balance $(2.53)_1$. Considering $\rho \, \ddot{\mathbf{x}} = \sum_\alpha [\rho^\alpha \mathbf{x}''_\alpha - \operatorname{div} (\rho^\alpha \mathbf{d}_\alpha \otimes \mathbf{d}_\alpha) + \hat{\rho}^\alpha \mathbf{x}'_\alpha]$ and assuming no mass transfer leads with the restriction $(2.54)_2$ to the balance $\sum_\alpha [\rho^\alpha \mathbf{x}''_\alpha - \operatorname{div} (\rho^\alpha \mathbf{d}_\alpha \otimes \mathbf{d}_\alpha)] = \operatorname{div} [\sum_\alpha (\mathbf{T}^\alpha - \rho^\alpha \mathbf{d}_\alpha \otimes \mathbf{d}_\alpha)] + \rho \, \mathbf{g}$. This formulation finally yields $\sum_\alpha \rho^\alpha \mathbf{x}''_\alpha = \operatorname{div} [\sum_\alpha \mathbf{T}^\alpha] + \rho \, \mathbf{g}$, recovering (3.15).

3.2.3 Entropy inequality

The entropy inequality poses the basis of a thermodynamically consistent framework. Due to the assumption of isothermal processes and the restriction $(2.63)_4$, the Clausius-Duhem entropy inequality (2.69) can be simplified to the Clausius-Planck inequality:

$$\sum_{\alpha} \Big[\mathbf{T}^{\alpha} \cdot \mathbf{L}_{\alpha} - \rho^{\alpha} (\psi^{\alpha})'_{\alpha} - \hat{\mathbf{p}}^{\alpha} \cdot \mathbf{v}_{\alpha} - \hat{\rho}^{\alpha} (\psi^{\alpha} + \tfrac{1}{2}\, \mathbf{v}_{\alpha} \cdot \mathbf{v}_{\alpha}) \Big] \geq 0. \tag{3.16}$$

Since mass production is omitted here, (3.16) reduces further to

$$\sum_{\alpha} \Big[\mathbf{T}^{\alpha} \cdot \mathbf{L}_{\alpha} - \rho^{\alpha} (\psi^{\alpha})'_{\alpha} - \hat{\mathbf{p}}^{\alpha} \cdot \mathbf{v}_{\alpha} \Big] \geq 0. \tag{3.17}$$

Moreover, the solid momentum production can be reformulated with respect to the fluid constituents by exploiting the coupling relation $(2.54)_4$, viz.

$$\sum_{\alpha} \hat{\mathbf{p}}^{\alpha} = \mathbf{0} \quad \rightarrow \quad - \hat{\mathbf{p}}^{S} \cdot \mathbf{v}_{S} = (\hat{\mathbf{p}}^{L} + \hat{\mathbf{p}}^{G}) \cdot \mathbf{v}_{S} \,. \tag{3.18}$$

Thus, the entropy inequality can be rewritten as follows

$$\begin{aligned} &\mathbf{T}^{S} \cdot \mathbf{L}_{S} - \rho^{S} (\psi^{S})'_{S} + \mathbf{T}^{L} \cdot \mathbf{L}_{L} - \rho^{L} (\psi^{L})'_{L} - \hat{\mathbf{p}}^{L} \cdot \underbrace{(\mathbf{v}_{L} - \mathbf{v}_{S})}_{\mathbf{w}_{L}} + \\ &+ \mathbf{T}^{G} \cdot \mathbf{L}_{G} - \rho^{G} (\psi^{G})'_{G} - \hat{\mathbf{p}}^{G} \cdot \underbrace{(\mathbf{v}_{G} - \mathbf{v}_{S})}_{\mathbf{w}_{G}} \geq 0 \,. \end{aligned} \tag{3.19}$$

A further restriction stems from the saturation condition, (2.3). To include this mechanical condition in the thermodynamical process, it is convenient to consider its material time derivative with respect to the skeleton motion, namely

$$(n^{S} + n^{L} + n^{G})'_{S} = 0 \,. \tag{3.20}$$

Therein, the material time derivatives of the individual volume fractions relative to the solid motion can be recast with the mass balances (3.4) and under consideration of (2.18) to

$$\begin{aligned} (n^{S})'_{S} &= - n^{S} \mathrm{div}\, \mathbf{v}_{S} \,, \\ (n^{L})'_{S} &= - n^{L} \mathrm{div}\, \mathbf{v}_{L} - \mathrm{grad}\, n^{L} \cdot \mathbf{w}_{L} \,, \\ (n^{G})'_{S} &= \frac{1}{\rho^{GR}} \Big[- n^{G} (\rho^{GR})'_{G} - n^{G} \rho^{GR} \,\mathrm{div}\, \mathbf{v}_{G} \Big] - \mathrm{grad}\, n^{G} \cdot \mathbf{w}_{G} \,. \end{aligned} \tag{3.21}$$

Inserting (3.21) in (3.20) and multiplying with a Lagrangean parameter $\mathcal{P}$ leads to

$$\begin{aligned} &\mathcal{P} \Big\{ n^{S} \mathrm{div}\, \mathbf{v}_{S} + n^{L} \mathrm{div}\, \mathbf{v}_{L} + \mathrm{grad}\, n^{L} \cdot \mathbf{w}_{L} + \\ &+ \frac{1}{\rho^{GR}} \Big[n^{G} (\rho^{GR})'_{G} + n^{G} \rho^{GR} \mathrm{div}\, \mathbf{v}_{G} \Big] + \mathrm{grad}\, n^{G} \cdot \mathbf{w}_{G} \Big\} = 0 \,. \end{aligned} \tag{3.22}$$

The method of Lagrangean multipliers is a strategy to comprise conditions into a mathematical optimisation problem and has proven helpful for considering the saturation condition in the thermodynamical process, compare, e. g., Liu [176]. Thus, to ensure that the saturation condition is satisfied at any time and for arbitrary processes, (3.22) is added to the entropy inequality (3.19):

$$\begin{aligned}
&\mathbf{T}^S \cdot \mathbf{L}_S - \rho^S (\psi^S)'_S + \mathcal{P}\, n^S \operatorname{div} \mathbf{v}_S + \mathbf{T}^L \cdot \mathbf{L}_L - \rho^L (\psi^L)'_L - \\
&- (\hat{\mathbf{p}}^L - \mathcal{P} \operatorname{grad} n^L) \cdot \mathbf{w}_L + \mathcal{P}\, n^L \operatorname{div} \mathbf{v}_L + \mathbf{T}^G \cdot \mathbf{L}_G - \rho^G (\psi^G)'_G - \\
&- (\hat{\mathbf{p}}^G - \mathcal{P} \operatorname{grad} n^G) \cdot \mathbf{w}_G + \mathcal{P} \frac{n^G}{\rho^{GR}} (\rho^{GR})'_G + \mathcal{P}\, n^G \operatorname{div} \mathbf{v}_G \geq 0 \,.
\end{aligned} \tag{3.23}$$

As a result of the symmetry property of the partial stress tensors, see (3.3), the stress power $\mathbf{T}^\alpha \cdot \mathbf{L}_\alpha$ can be substituted by $\mathbf{T}^\alpha \cdot \mathbf{D}_\alpha$. Moreover, the divergence of the velocity can be reformulated with the relation (2.33), namely $\operatorname{div} \mathbf{v}_\alpha = \mathbf{I} \cdot \mathbf{L}_\alpha = \mathbf{I} \cdot \mathbf{D}_\alpha$. With this, the entropy inequality for the current model reads

$$\begin{aligned}
&\underbrace{\left(\mathbf{T}^S + \mathcal{P}\, n^S \mathbf{I}\right)}_{\mathbf{T}^S_E} \cdot \mathbf{D}_S - \rho^S (\psi^S)'_S + \underbrace{\left(\mathbf{T}^L + \mathcal{P}\, n^L \mathbf{I}\right)}_{\mathbf{T}^L_E} \cdot \mathbf{D}_L - \rho^L (\psi^L)'_L - \\
&- \underbrace{(\hat{\mathbf{p}}^L - \mathcal{P} \operatorname{grad} n^L)}_{\hat{\mathbf{p}}^L_E} \cdot \mathbf{w}_L + \underbrace{\left(\mathbf{T}^G + \mathcal{P}\, n^G \mathbf{I}\right)}_{\mathbf{T}^G_E} \cdot \mathbf{D}_G - \rho^G (\psi^G)'_G - \\
&- \underbrace{(\hat{\mathbf{p}}^G - \mathcal{P} \operatorname{grad} n^G)}_{\hat{\mathbf{p}}^G_E} \cdot \mathbf{w}_G + \mathcal{P} \frac{n^G}{\rho^{GR}} (\rho^{GR})'_G \geq 0 \,.
\end{aligned} \tag{3.24}$$

Therein, the so-called extra quantities are introduced according to the work of Truesdell & Noll [240]. This approach allows splitting the partial stresses $\mathbf{T}^\alpha$ and direct momentum productions $\hat{\mathbf{p}}^\alpha$ into an undetermined part resulting from the Lagrangean multiplier $\mathcal{P}$ and an extra term $(\cdot)_E$. One approach is to determine the constitutive relations for these extra terms, compare, e. g., Ehlers [84]. However, to improve clarity, the partial stresses and direct momentum productions will be split into equilibrium and non-equilibrium proportions for the constitutive approach in this monograph.

3.3 Evaluation of the entropy inequality

In the context of a continuum mechanical approach, the complete state of motion, as well as the initial conditions of the problem, are assumed to be known. For all other quantities that cannot directly be determined through the balance equations, reasonable and thermodynamically consistent constitutive relations must be found. However, the set of possible constitutive equations is not arbitrary but follows the principles of rational thermodynamics in analogy to the principles in the classical continuum mechanics of singlephasic materials, compare the work of Truesdell [239], Truesdell & Noll [240] and Truesdell & Toupin [241]. In the following, the principles are introduced and adapted for the current problem under study.

3.3.1 The basic thermodynamical principles

Identification of the constitutive variables The set $\mathcal{R}$ of undetermined response functions, which cannot be computed solely from the motion and balance relations, reads for the entropy inequality (3.24)

$$\mathcal{R} = \{\psi^S,\ \psi^L,\ \psi^G,\ \mathbf{T}^S,\ \mathbf{T}^L,\ \mathbf{T}^G,\ \hat{\mathbf{p}}^L,\ \hat{\mathbf{p}}^G,\ \mathcal{P}\}\,. \tag{3.25}$$

Following the *principle of determinism*, suitable constitutive equations must determine these yet undefined response functions.

Determination of the independent process variables The *principle of equipresence* states that the response functions can depend on the complete thermodynamical process, i. e. $\mathcal{R} = \mathcal{R}(\mathcal{V})$. In this context, Ehlers [86] introduces the fundamental set $\mathcal{V}$ of process variables for a general porous material via

$$\begin{aligned}\mathcal{V} =\{&\theta^\alpha,\ \operatorname{grad}\theta^\alpha,\ n^\beta,\ \operatorname{grad} n^\beta,\ \rho^{\alpha R},\ \operatorname{grad}\rho^{\alpha R},\ \mathbf{F}_S,\\ &\operatorname{Grad}_S \mathbf{F}_S,\ \mathbf{v}_\beta,\ \operatorname{Grad}_\beta \mathbf{v}_\beta,\ \mathbf{X}_\alpha\}\end{aligned} \tag{3.26}$$

As isothermal processes are considered in this monograph, the temperature θ^α and its gradient can be omitted as process variables.

Moreover, according to (2.3), (2.5), and (2.6), the volume fractions n^β can be computed via the solidity n^S and liquid saturation s^L. Therefore, n^β is replaced by solely the liquid saturation s^L in the set of process variables. Note that the solid volume fraction n^S is skipped as an independent process variable since it directly results from $\mathbf{F}_S$ through the integrated volume balance (3.11).

Furthermore, in the case of the material incompressible solid skeleton and pore liquid, the effective densities are constant, cf. (3.1), and are not considered further as variables.

In addition, the *principle of material frame indifference* states that the response functions must be independent of the observer's position. In that sense, the fluid velocities $\mathbf{v}_\beta$ are substituted by the seepage velocities $\mathbf{w}_\beta$ according to (2.19), and their gradients by the respective symmetric part $\mathbf{D}_\beta$ of the spatial velocity gradient, compare, e. g., the work of de Boer & Ehlers [40] and Ehlers [86].

The reference position $\mathbf{X}_\alpha$ plays a role as a process variable only in the case of inhomogeneities of the constituents φ^α in their initial state and can, therefore, be neglected here.

Note that $\mathcal{V}$ comprises the gradients of the respective basis variables, allowing the description of second-grade materials. However, within the *principle of local action*, the response functions for a material point $\mathcal{P}^\alpha$ of the current configuration only depend on the values of the process variables at and in the near vicinity of the material point $\mathcal{P}^\alpha$. Thus, the gradients of the process variables in (3.26) can be dropped, cf. Truesdell & Noll [240], Bowen [52, 53] and Ehlers [86].

Taking into account these considerations, the specific set $\mathcal{V}^1$ of independent process variables for the current model reads

$$\mathcal{V}^1 = \{s^L,\ \rho^{GR},\ \mathbf{F}_S,\ \mathbf{w}_\beta,\ \mathbf{D}_\beta,\ \phi^S,\ \operatorname{Grad}_S \phi^S\} \tag{3.27}$$

Note that to describe the fracture behaviour of the solid skeleton, a solid phase-field variable ϕ^S and its gradient $\mathrm{Grad}_S\,\phi^S$ have been added to the set $\mathcal{V}^1$ of process variables. Thereby, ϕ^S can be identified with a damage variable, compare Miehe *et al.* [190], while the crack-growth direction is represented by $\mathrm{Grad}_S\,\phi^S$.

Finally, Ehlers [80] introduced the *principle of phase separation*. This principle assumes *a priori* that the Helmholtz free energy of the constituent φ^α only depends on the non-dissipative variables, which are directly related to φ^α. The process variables $\mathbf{w}_\beta$ and $\mathbf{D}_\beta$ refer to dissipative quantities and are, therefore, omitted in the dependencies of the Helmholtz free energies. From this follows

$$\psi^S = \psi^S(\mathbf{F}_S,\, \phi^S,\, \mathrm{Grad}_S\,\phi^S)\,, \quad \psi^L = \psi^L(s^L)\,, \quad \psi^G = \psi^G(\rho^{GR})\,. \tag{3.28}$$

According to the *principle of material frame indifference*, the deformation gradient $\mathbf{F}_S$ can equally be expressed by the Green-Lagrangean strain tensor $\mathbf{E}_S$, cf. (2.29), for the Helmholtz solid free energy, viz.

$$\psi^S = \psi^S(\mathbf{E}_S,\, \phi^S,\, \mathrm{Grad}_S\,\phi^S)\,. \tag{3.29}$$

This results from the fact that the deformation gradient can be decomposed through a polar decomposition into a rigid body rotation and a stretch. Since the former is invariant to the observer's position, it does not affect the free energy. Consequently, ψ^S can be expressed via the stretch or, rather, the right Cauchy-Green deformation tensor $\mathbf{C}_S$, which in turn can be substituted by the Green-Lagrangean strain $\mathbf{E}_S$. The interested reader is referred to Ehlers [82, 86] and Wagner [243] and citations therein.

3.3.2 Thermodynamical restrictions for the model

The last principle, the *principle of dissipation*, provides the restrictions for the constitutive relations. Here, the procedure based on Coleman & Noll [65] is applied. An alternative exploitation of the entropy inequality is proposed by Liu & Müller [177]. It leads to basically identical results but is more demanding, which is why the procedure of Coleman & Noll is preferred here. A detailed discussion about this topic can be found, e. g., in the work of Bowen [51] and Ehlers [86].

First, the entropy inequality (3.24) is processed with the material time derivative of the free energies. According to the dependencies $(3.28)_{2,3}$ and (3.29), the derivatives $(\psi^\alpha)'_\alpha$ read

$$\begin{aligned}
(\psi^S)'_S &= \frac{\partial\psi^S}{\partial\mathbf{E}_S}\cdot(\mathbf{E}_S)'_S + \frac{\partial\psi^S}{\partial\phi^S}(\phi^S)'_S + \frac{\partial\psi^S}{\partial\mathrm{Grad}_S\phi^S}\cdot\mathrm{Grad}_S(\phi^S)'_S\,,\\
(\psi^L)'_L &= \frac{\partial\psi^L}{\partial s^L}(s^L)'_L\,,\\
(\psi^G)'_G &= \frac{\partial\psi^G}{\partial\rho^{GR}}(\rho^{GR})'_G\,.
\end{aligned} \tag{3.30}$$

The first addend of the time derivative of the solid free energy can be expressed by the velocity gradient according to (2.35):

$$\frac{\partial \psi^S}{\partial \mathbf{E}_S} \cdot (\mathbf{E}_S)'_S = \mathbf{F}_S \frac{\partial \psi^S}{\partial \mathbf{E}_S} \mathbf{F}_S^T \cdot \mathbf{D}_S \,. \tag{3.31}$$

Moreover, applying the divergence theorem (A.10) to the last term of $(3.30)_1$ gives

$$\frac{\partial \psi^S}{\partial \mathrm{Grad}_S \phi^S} \cdot \mathrm{Grad}_S (\phi^S)'_S = \mathrm{Div}_S \left(\frac{\partial \psi^S}{\partial \mathrm{Grad}_S \phi^S} (\phi^S)'_S \right) - (\phi^S)'_S \, \mathrm{Div}_S \left(\frac{\partial \psi^S}{\partial \mathrm{Grad}_S \phi^S} \right) . \tag{3.32}$$

In addition, rewriting the liquid saturation with (2.6) and applying the differentiation rule leads to

$$(s^L)'_L = \left(\frac{n^L}{n^F} \right)'_L = \frac{(n^L)'_L \, n^F - n^L \, (n^F)'_L}{(n^F)^2} = \frac{(n^L)'_L - s^L (n^F)'_L}{n^F} \,. \tag{3.33}$$

Also, using the saturation condition (2.3) and the reformulation of the material time derivative relative to the solid motion (2.18), $(n^F)'_L$ can be rewritten with respect to φ^S:

$$(n^F)'_L = (1 - n^S)'_L = -(n^S)'_L = -[(n^S)'_S + \mathrm{grad}\, n^S \cdot \mathbf{w}_L] \,, \tag{3.34}$$

whereby the derivative of the solid volume fraction is given by $(3.21)_1$. Furthermore, $(n^L)'_L$ can be substituted by the local mass balance (3.4) and simplified with the incompressibility assumption (3.1) to

$$(n^L)'_L = -n^L \, \mathrm{div}\, \mathbf{v}_L \,. \tag{3.35}$$

Given these reformulations, the material time derivative of the liquid saturation yields

$$\begin{aligned} (s^L)'_L &= \frac{1}{n^F} \big[- n^L \mathrm{div}\, \mathbf{v}_L + s^L (- n^S \mathrm{div}\, \mathbf{v}_S + \mathrm{grad}\, n^S \cdot \mathbf{w}_L) \big] \\ &= - s^L \underbrace{\mathrm{div}\, \mathbf{v}_L}_{\mathbf{D}_L \cdot \mathbf{I}} - s^L \frac{n^S}{n^F} \underbrace{\mathrm{div}\, \mathbf{v}_S}_{\mathbf{D}_S \cdot \mathbf{I}} + \frac{s^L}{n^F} \mathrm{grad}\, n^S \cdot \mathbf{w}_L \,. \end{aligned} \tag{3.36}$$

Finally, the specific entropy inequality for the current model inserting the material time

derivatives (3.30) of the free energies under consideration of the reformulations (3.31), (3.32) and (3.36) and sorting the terms reads

$$
\begin{aligned}
&\left[\mathbf{T}^S + n^S\Big(\mathcal{P} + \rho^{LR}\,(s^L)^2\,\frac{\partial \psi^L}{\partial s^L}\Big)\,\mathbf{I} - \rho^S \mathbf{F}_S\,\frac{\partial \psi^S}{\partial \mathbf{E}_S}\mathbf{F}_S^T\right] \cdot \mathbf{D}_S - \\
&- \rho^S\left[\frac{\partial \psi^S}{\partial \phi^S} - \mathrm{Div}_S\Big(\frac{\partial \psi^S}{\partial \mathrm{Grad}_S \phi^S}\Big)\right](\phi^S)'_S - \\
&- \rho^S\,\mathrm{Div}_S\Big(\frac{\partial \psi^S}{\partial \mathrm{Grad}_S \phi^S}\,(\phi^S)'_S\Big) + \\
&+ \left[\mathbf{T}^L + n^L\Big(\mathcal{P} + \rho^{LR}\,(s^L)\,\frac{\partial \psi^L}{\partial s^L}\Big)\,\mathbf{I}\right] \cdot \mathbf{D}_L - \\
&- \left[\hat{\mathbf{p}}^L - \mathcal{P}\,\mathrm{grad}\,n^L + \rho^{LR}\,(s^L)^2\,\frac{\partial \psi^L}{\partial s^L}\,\mathrm{grad}\,n^S\right] \cdot \mathbf{w}_L + \\
&+ \left[\mathbf{T}^G + n^G \mathcal{P}\,\mathbf{I}\right] \cdot \mathbf{D}_G - \left[\hat{\mathbf{p}}^G - \mathcal{P}\,\mathrm{grad}\,n^G\right] \cdot \mathbf{w}_G + \\
&+ n^G\left[\frac{\mathcal{P}}{\rho^{GR}} - \rho^{GR}\frac{\partial \psi^G}{\partial \rho^{GR}}\right](\rho^{GR})'_G \geq 0\,.
\end{aligned}
\tag{3.37}
$$

The Coleman-Noll procedure states that the entropy inequality (3.37) has to be fulfilled for all possible but fixed values of the process variables included in ψ^α and an arbitrary choice of their derivatives. Moreover, this approach distinguishes between the equilibrium and the dissipation (non-equilibrium) contributions of the entropy inequality. In that sense, also the stresses and momentum productions are split into equilibrium $(\cdot)_{EQ}$ and non-equilibrium $(\cdot)_{NEQ}$ terms:

$$
\begin{aligned}
\mathbf{T}^\alpha &= \mathbf{T}^\alpha_{EQ} + \mathbf{T}^\alpha_{NEQ}\,, \\
\hat{\mathbf{p}}^\alpha &= \hat{\mathbf{p}}^\alpha_{EQ} + \hat{\mathbf{p}}^\alpha_{NEQ}\,.
\end{aligned}
\tag{3.38}
$$

Since this model only considers a brittle-elastic solid skeleton, $\mathbf{T}^S_{NEQ} \equiv \mathbf{0}$ holds and the total partial solid stress results in

$$
\mathbf{T}^S \equiv \mathbf{T}^S_{EQ}\,. \tag{3.39}
$$

Equilibrium (reversible) parts

The equilibrium parts $(\cdot)_{EQ}$ of the entropy inequality (3.37) are found by transforming the inequality into an equality condition $\mathcal{D}_{EQ}$, viz.

$$\begin{aligned}
\mathcal{D}_{EQ} = &\left[\mathbf{T}^S_{EQ} + n^S\Big(\mathcal{P} + \rho^{LR}\,(s^L)^2\,\frac{\partial\psi^L}{\partial s^L}\Big)\,\mathbf{I} - \rho^S\,\mathbf{F}_S\,\frac{\partial\psi^S}{\partial\mathbf{E}_S}\mathbf{F}_S^T\right]\cdot\,\mathbf{D}_S - \\
&- \rho^S\,\mathrm{Div}_S\left(\frac{\partial\psi^S}{\partial\mathrm{Grad}_S\phi^S}\,(\phi^S)'_S\right) + \\
&+ \left[\mathbf{T}^L_{EQ} + n^L\Big(\mathcal{P} + \rho^{LR}\,(s^L)\,\frac{\partial\psi^L}{\partial s^L}\Big)\,\mathbf{I}\right]\cdot\,\mathbf{D}_L - \\
&- \left[\hat{\mathbf{p}}^L_{EQ} - \mathcal{P}\,\mathrm{grad}\,n^L + \rho^{LR}\,(s^L)^2\,\frac{\partial\psi^L}{\partial s^L}\,\mathrm{grad}\,n^S\right]\cdot\,\mathbf{w}_L + \\
&+ \left[\mathbf{T}^G_{EQ} + n^G\mathcal{P}\,\mathbf{I}\right]\cdot\,\mathbf{D}_G - \left[\hat{\mathbf{p}}^G_{EQ} - \mathcal{P}\,\mathrm{grad}\,n^G\right]\cdot\,\mathbf{w}_G + \\
&+ n^G\left[\frac{\mathcal{P}}{\rho^{GR}} - \rho^{GR}\frac{\partial\psi^G}{\partial\rho^{GR}}\right](\rho^{GR})'_G = 0\,.
\end{aligned} \tag{3.40}$$

To satisfy this latter, each addend has to fulfil the equality condition on its own. Particularly, the factors belonging to the arbitrary process variables have to vanish for arbitrary values of $\mathbf{D}_\alpha$, $\mathbf{w}_\beta$ and $(\rho^{GR})'_G$. It follows:

$$\begin{aligned}
\mathbf{0} &= \mathbf{T}^S_{EQ} + n^S\Big(\mathcal{P} + \rho^{LR}\,(s^L)^2\,\frac{\partial\psi^L}{\partial s^L}\Big)\,\mathbf{I} - \rho^S\,\mathbf{F}_S\,\frac{\partial\psi^S}{\partial\mathbf{E}_S}\mathbf{F}_S^T\,,\\
0 &= \mathrm{Div}_S\left(\frac{\partial\psi^S}{\partial\mathrm{Grad}_S\phi^S}\,(\phi^S)'_S\right),\\
\mathbf{0} &= \mathbf{T}^L_{EQ} + n^L\Big(\mathcal{P} + \rho^{LR}\,(s^L)\,\frac{\partial\psi^L}{\partial s^L}\Big)\,\mathbf{I}\,,\\
\mathbf{0} &= \hat{\mathbf{p}}^L_{EQ} - \mathcal{P}\,\mathrm{grad}\,n^L + \rho^{LR}\,(s^L)^2\,\frac{\partial\psi^L}{\partial s^L}\,\mathrm{grad}\,n^S\,,\\
\mathbf{0} &= \mathbf{T}^G_{EQ} + n^G\mathcal{P}\,\mathbf{I}\,,\\
\mathbf{0} &= \hat{\mathbf{p}}^G_{EQ} - \mathcal{P}\,\mathrm{grad}\,n^G\,,\\
0 &= \frac{\mathcal{P}}{\rho^{GR}} - \rho^{GR}\frac{\partial\psi^G}{\partial\rho^{GR}}\,.
\end{aligned} \tag{3.41}$$

The equilibrium restrictions (3.41) serve to determine the Lagrangean multiplier $\mathcal{P}$ and the equilibrium variables. In addition, the condition $(3.41)_2$ has to be considered separately. In equilibrium, it is intrinsically fulfilled with $(\phi^S)'_S = 0$. Beyond this, $(3.41)_2$ leads to a continuity equation for the term in bracket when $(\phi^S)'_S \neq 0$. Integrating the term over an arbitrary volumetric domain Ω_0 in the reference configuration and applying the Gaussian theorem yields

$$\int_{\Omega_0} \mathrm{Div}_S\left(\frac{\partial \psi^S}{\partial \mathrm{Grad}_S \phi^S}\,(\phi^S)'_S\right) \mathrm{d}V \;=\; \int_{\partial\Omega_0} \frac{\partial \psi^S}{\partial \mathrm{Grad}_S \phi^S}\,(\phi^S)'_S \cdot \mathbf{n}\,\mathrm{d}A = 0\,, \tag{3.42}$$

with $\partial\Omega_0$ the corresponding surface, while $\mathrm{d}V$ and $\mathrm{d}A$ are the volume and surface elements in the reference configuration, respectively. Considering closed surfaces, the equation holds when

$$\frac{\partial \psi^S}{\partial \mathrm{Grad}_S \phi^S} \cdot \mathbf{n} = 0\,, \tag{3.43}$$

for ϕ^S between zero and one, and $(\phi^S)'_S$ between zero and positive values. This equation will define the boundary condition for the phase-field evolution in the later numerical study, see Chapter 4.

Remark: Finally, note that the bracket term belonging to the phase-field derivative $(3.37)_2$ is not considered in the equilibrium condition (3.40). This term vanishes trivially in an equilibrium state with $(\phi^S)'_S = 0$. However, the evolution equation of $(\phi^S)'_S$ will be determined as a function of this term by means of the dissipation inequality since fracturing is an irreversible, dissipative process. □

Identification of the Lagrangean multiplier and equilibrium quantities

The Lagrangean multiplier $\mathcal{P}$ can be identified with the equilibrium condition $(3.41)_7$ as the gas pore pressure following Ehlers [85]:

$$\mathcal{P} := p^{GR} = (\rho^{GR})^2 \frac{\partial \psi^G}{\partial \rho^{GR}}\,, \tag{3.44}$$

yielding for the equilibrium gas stress

$$\mathbf{T}^G_{EQ} = -\,n^G\, p^{GR}\, \mathbf{I}\,. \tag{3.45}$$

In analogy, the equilibrium liquid stress is postulated to

$$\mathbf{T}^L_{EQ} =: -\,n^L\, p^{LR}\, \mathbf{I} \quad \text{with} \quad p^{LR} := p^{GR} + \rho^{LR} s^L \frac{\partial \psi^L}{\partial s^L}\,, \tag{3.46}$$

where p^{LR} is the liquid pressure. Here, it is convenient to introduce the pressure difference between the pore gas and the pore liquid as

$$p^D := p^{GR} - p^{LR} = -\rho^{LR} s^L \frac{\partial \psi^L}{\partial s^L}\,. \tag{3.47}$$

This pressure difference is comparable to the capillary pressure p^C in the vadose zone of unsaturated soil, cf. Bear [20], Fredlund & Rahardjo [111], Helmig [138] and Ehlers [85], among others. However, p^C is always positive in a capillary system, which restricts the gas pressure to be larger than or equal to the liquid pressure, compare, e. g., the work of Brooks & Corey [57] and van Genuchten [115]. In contrast, as the injection system of a fracking process needs a liquid pressure p^{LR} larger than or equal to the gas pressure p^{GR}, p^D can generally become negative. Subsection 3.4.2 will address this issue in detail.

Additionally, inserting (3.44) and $(3.46)_2$ in the equilibrium condition $(3.41)_1$ and considering the saturation condition (2.5), one obtains for the equilibrium solid stress

$$\mathbf{T}^S_{EQ} + n^S \big[\underbrace{(1-s^L)\, p^{GR} + s^L p^{LR}}_{=:\, p^{FR}} \big]\, \mathbf{I} = \rho^S\, \mathbf{F}_S\, \frac{\partial \psi^S}{\partial \mathbf{E}_S} \mathbf{F}_S^T \,. \tag{3.48}$$

Hereby, the overall pore pressure p^{FR} is given as the sum of the weighted effective fluid pressures $p^{\beta R}$ with the respective saturation s^β.

Remark: While p^{FR} is found here as a result of the Clausius-Planck inequality, this relation recovers Dalton's law of 1802 [69]. □

Introducing furthermore the effective solid stress $\mathbf{T}^S_{EF}$ as the stress portion that is obtained from the solid deformation, and considering (3.39), the solid (equilibrium) stress results in

$$\mathbf{T}^S \equiv \mathbf{T}^S_{EQ} = -\, n^S\, p^{FR}\, \mathbf{I} + \mathbf{T}^S_{EF} \quad \text{with} \quad \mathbf{T}^S_{EF} = \rho^S\, \mathbf{F}_S\, \frac{\partial \psi^S}{\partial \mathbf{E}_S} \mathbf{F}_S^T \,. \tag{3.49}$$

Thus, the equilibrium solid stress tensor splits into a weighted pore-pressure part and the effective stress for which an appropriate constitutive equation will be determined in the following section. The concept of effective stresses goes back to early investigations in geomechanics on saturated soils by Fillunger [105, 106] and von Terzaghi [235, 236], and matches the general definition of extra stresses formulated by Truesdell & Noll [240] in simpler systems, for example in purely liquid-saturated porous media. A historical review on the subject can be found, e. g., in the article of de Boer & Ehlers [42].

Moreover, inserting (3.44) and (3.47) in the equilibrium conditions $(3.41)_4$ and exploiting (2.6), (2.3) and the differentiation rule (A.10), leads for the equilibrium liquid momentum production $\hat{\mathbf{p}}^L_{EQ}$ to

$$\begin{aligned}
\hat{\mathbf{p}}^L_{EQ} &= p^{GR}\, \mathrm{grad}\, n^L - s^L p^D\, \mathrm{grad}\, n^S \\
&= p^{LR}\, \mathrm{grad}\, n^L + p^D \mathrm{grad}\, (s^L n^F) - s^L p^D\, \mathrm{grad}\, n^S \\
&= p^{LR}\, \mathrm{grad}\, n^L + p^D [s^L \mathrm{grad}\, n^F + n^F \mathrm{grad}\, s^L] - s^L p^D\, \mathrm{grad}\, n^S \\
&= p^{LR}\, \mathrm{grad}\, n^L + p^D n^F \mathrm{grad}\, s^L \,,
\end{aligned} \tag{3.50}$$

Finally, the equilibrium gas momentum production $\hat{\mathbf{p}}^G_{EQ}$ results with (3.44) in $(3.41)_6$ in

$$\hat{\mathbf{p}}^G_{EQ} = p^{GR}\, \mathrm{grad}\, n^G \,. \tag{3.51}$$

Summing-up of stresses and drag forces

Based on the above considerations, it is worth collecting the stresses and drag forces of all constituents. Given (3.38), (3.45), $(3.46)_1$ and $(3.49)_1$, the individual stresses of solid, liquid and gas read

$$\begin{aligned} \mathbf{T}^S &= -n^S\, p^{FR}\mathbf{I} + \mathbf{T}^S_{EF}\,, \\ \mathbf{T}^L &= -n^L\, p^{LR}\mathbf{I} + \mathbf{T}^L_{NEQ}\,, \\ \mathbf{T}^G &= -n^G\, p^{GR}\mathbf{I} + \mathbf{T}^G_{NEQ}\,. \end{aligned} \tag{3.52}$$

Besides, the drag forces of pore liquid and gas can be summarised by use of (3.50) and (3.51) towards

$$\begin{aligned} &\hat{\mathbf{p}}^L = p^{LR}\mathrm{grad}\, n^L + p^D n^F \mathrm{grad}\, s^L + \hat{\mathbf{p}}^L_{NEQ} \quad \text{and} \\ &\hat{\mathbf{p}}^G = p^{GR}\mathrm{grad}\, n^G + \hat{\mathbf{p}}^G_{NEQ}\,. \end{aligned} \tag{3.53}$$

Dissipation (non-equilibrium) parts

In contrast to the equilibrium equation (3.40), the dissipation inequality represents the total dissipation of the system. It is acquired by taking the remainder of (3.37) for the non-equilibrium, non-vanishing dissipation terms $\mathbf{T}^\beta_{NEQ}$, $\hat{\mathbf{p}}^\beta_{NEQ}$ and $(\phi^S)'_S$:

$$\begin{aligned} \mathcal{D}_{NEQ} = &\mathbf{T}^L_{NEQ} \cdot \mathbf{D}_L - \hat{\mathbf{p}}^L_{NEQ} \cdot \mathbf{w}_L + \mathbf{T}^G_{NEQ} \cdot \mathbf{D}_G - \hat{\mathbf{p}}^G_{NEQ} \cdot \mathbf{w}_G - \\ &- \rho^S \Big[\frac{\partial \psi^S}{\partial\, \phi^S} - \mathrm{Div}_S \frac{\partial \psi^S}{\partial(\mathrm{Grad}_S \phi^S)} \Big] (\phi^S)'_S \geq 0\,, \end{aligned} \tag{3.54}$$

Proceeding again from the Coleman-Noll approach, the above inequality is sufficiently fulfilled, if each of the single terms is positive on its own. Thus, exploiting the positive property of proportionality yields

$$\begin{aligned} &\mathbf{T}^L_{NEQ} \propto \mathbf{D}_L\,, \quad \hat{\mathbf{p}}^L_{NEQ} \propto -\mathbf{w}_L\,, \quad \mathbf{T}^G_{NEQ} \propto \mathbf{D}_G\,, \quad \hat{\mathbf{p}}^G_{NEQ} \propto -\mathbf{w}_G\,, \\ &(\phi^S)'_S \propto -\rho^S \Big[\frac{\partial \psi^S}{\partial\, \phi^S} - \mathrm{Div}_S \frac{\partial \psi^S}{\partial(\mathrm{Grad}_S \phi^S)} \Big]\,. \end{aligned} \tag{3.55}$$

3.4 Constitutive relations

In the following section, constitutive relations for the solid skeleton and the pore fluids are elaborated. The choice of the constitutive relations is not arbitrary but follows the physical behaviour of the constituents and must fulfil the restrictions (3.49) and (3.55) arising from the entropy inequality of the preceded section.

3.4.1 Fracturing solid skeleton

In hydraulic fracturing processes, a fracking fluid is pressed into the porous solid, which answers with tensile stresses forcing the onset and the development of fractures. Whether a fully saturated or a partially saturated medium is concerned, the fracturing itself is solely attached to the solid. The stored solid deformation and fracture energy, the effective solid stress and the phase-field evolution are presented in a geometric linear setting in what follows.

Linearisation

So far, all quantities have been introduced in a finite kinematic setting, compare Section 2.2. However, for the problem under study, assuming small solid deformations is common and convenient. In this sense, a geometric linearisation around the undeformed reference configuration simplifies the formulation of the kinematic and stress quantities. The interested reader of finite deformations in the context of the TPM is referred, for example, to the work of Eipper [99], Mahnkopf [180] and Markert [184].

According to Haupt [132], the deformations are considered small when the norm of the solid displacement gradient is small, viz.

$$\| \operatorname{Grad}_S \mathbf{u}_S \| \ll 1 \,. \tag{3.56}$$

Thus, expressing the solid material deformation gradient $\mathbf{F}_S$ via the solid's motion, one recognises that the solid material deformation gradient nearly equates to the identity tensor in the context of small deformations, viz.

$$\mathbf{F}_S = \frac{\partial \mathbf{x}}{\partial \mathbf{X}_S} = \frac{\partial (\mathbf{X}_S + \mathbf{u}_S)}{\partial \mathbf{X}_S} = \mathbf{I} + \operatorname{Grad}_S \mathbf{u}_S \,, \quad \rightarrow \quad \| \mathbf{F}_S - \mathbf{I} \| \ll 1 \,. \tag{3.57}$$

From this, linearising the Green-Lagrangean strain tensor $\mathbf{E}_S$, cf. (2.29), with regard to the solid displacement gradient and omitting the higher-order non-linear terms yields

$$(\mathbf{E}_S)_{\text{lin}} = \tfrac{1}{2} (\operatorname{Grad}_S \mathbf{u}_S + \operatorname{Grad}_S^T \mathbf{u}_S) \,. \tag{3.58}$$

Moreover, (3.57) implies that the referential and current configurations are close to each other, allowing the following approximations for the gradient and divergence operators:

$$\operatorname{Grad}_S (\cdot) \approx \operatorname{grad} (\cdot) \,, \quad \operatorname{Div}_S (\cdot) \approx \operatorname{div} (\cdot) \,, \tag{3.59}$$

This simplification leads to the final linearised form of the Green-Lagrangean strain tensor:

$$\boldsymbol{\varepsilon}_S := (\mathbf{E}_S)_{\text{lin}} = \tfrac{1}{2} (\operatorname{grad} \mathbf{u}_S + \operatorname{grad}^T \mathbf{u}_S) \,. \tag{3.60}$$

Regarding the effective solid stresses, the relation $(3.49)_2$ can be expressed in terms of the Kirchhoff stress tensor $\boldsymbol{\tau}_{EF}^S$ with (2.26) and (2.41), viz.

$$\underbrace{(\det \mathbf{F}_S)\, \mathbf{T}_{EF}^S}_{\boldsymbol{\tau}_{EF}^S} = \rho_0^S \, \mathbf{F}_S \, \frac{\partial \psi^S}{\partial \mathbf{E}_S} \mathbf{F}_S^T \,, \tag{3.61}$$

and further reformulated according to the second Piola-Kirchhoff stress tensor $\mathbf{S}^S_{EF}$, compare $(2.40)_2$, viz.

$$\boldsymbol{\tau}^S_{EF} = \mathbf{F}_S\,\mathbf{S}^S_{EF}\,\mathbf{F}_S^T \quad \rightarrow \quad \mathbf{S}^S_{EF} = \rho_0^S\,\frac{\partial \psi^S}{\partial \mathbf{E}_S}\,. \tag{3.62}$$

Introducing additionally the weighted Helmholtz free energy with the initial solid density as the solid stored energy W^S per bulk volume, i. e. $W^S := \rho_0^S\,\psi^S(\mathbf{E}_S, \phi^S, \mathrm{Grad}_S\,\phi^S)$, yields

$$\mathbf{S}^S_{EF} = \frac{\partial W^S}{\partial \mathbf{E}_S}\,. \tag{3.63}$$

Finally, the transport mechanisms are negligible in a geometric linear setting, compare (3.57). Thus, the stress tensors mentioned above coincide, leading to the linear solid effective stress

$$\boldsymbol{\sigma}^S_{EF} := (\mathbf{T}^S_{EF})_{\mathrm{lin}} = (\boldsymbol{\tau}^S_{EF})_{\mathrm{lin}} = (\mathbf{S}^S_{EF})_{\mathrm{lin}} = \frac{\partial W^S}{\partial \boldsymbol{\varepsilon}_S}\,, \tag{3.64}$$

with $W^S = W^S(\boldsymbol{\varepsilon}_S, \phi^S, \mathrm{grad}\,\phi^S)$.

Besides this, linearising the Jacobi determinant J_S and its inverse, cf. (2.23), with regard to the solid displacement gradient and neglecting the higher-order non-linear terms, yields with (3.59)

$$(J_S)_{\mathrm{lin}} = 1 + \mathrm{div}\ \mathbf{u}_S \quad \text{and} \quad (J_S^{-1})_{\mathrm{lin}} = 1 - \mathrm{div}\ \mathbf{u}_S\,. \tag{3.65}$$

Considering this, the solid partial density after (2.26) and the solid volume fraction (3.11) result in

$$\rho^S \approx \rho_0^S\,(1 - \mathrm{div}\,\mathbf{u}_S) \quad \text{and} \quad n^S \approx n_0^S\,(1 - \mathrm{div}\,\mathbf{u}_S)\,. \tag{3.66}$$

Finally, the boundary condition (3.43) and the thermodynamical restriction for the phase-field evolution $(3.55)_5$ simplify in a geometric linear setting with (3.59) to

$$\frac{\partial \psi^S}{\partial \mathrm{grad}\phi^S} \cdot \mathbf{n} = 0 \quad \text{and} \quad (\phi^S)'_S \propto -\rho^S \left[\frac{\partial \psi^S}{\partial\, \phi^S} - \mathrm{div}\frac{\partial \psi^S}{\partial(\mathrm{grad}\phi^S)}\right]. \tag{3.67}$$

Solid stored energy

Considering that a fracture is induced due to tension and not compression, Miehe *et al.* [190] proposed the stored energy for a pure solid based on the spectral decomposition of the strain, allowing for differentiation of a purely tensile and compression part, compare Section 2.5. Thereby, the solid strain tensor $\boldsymbol{\varepsilon}_S$ is decomposed relative to the sign of its eigenvalues ε_{Si} into positive and negative principle strains, viz.

$$\boldsymbol{\varepsilon}_S = \boldsymbol{\varepsilon}_S^+ + \boldsymbol{\varepsilon}_S^- \quad \text{with} \quad \begin{cases} \boldsymbol{\varepsilon}_S^+ = \sum\nolimits_i \dfrac{\varepsilon_{Si} + |\varepsilon_{Si}|}{2}\,\mathbf{n}_{Si} \otimes \mathbf{n}_{Si}\,, \\ \boldsymbol{\varepsilon}_S^- = \sum\nolimits_i \dfrac{\varepsilon_{Si} - |\varepsilon_{Si}|}{2}\,\mathbf{n}_{Si} \otimes \mathbf{n}_{Si}\,. \end{cases} \tag{3.68}$$

Therein, the plus/minus superscripts mark the positive/negative principal strains, and $\mathbf{n}_{Si}$ denotes the eigenvectors. Hence, the proposed formulation of Miehe *et al.* splits the

solid stored energy into an elastic tensile energy W^{S+}, an elastic compression energy W^{S-} and a fracture energy $G_c\,\Gamma^S$:

$$\begin{aligned} W^S(\boldsymbol{\varepsilon}_S,\, \phi^S,\, \mathrm{grad}\phi^S) = \left[(1-\phi^S)^2 + \eta_r^S\right] W^{S+}(\boldsymbol{\varepsilon}_S^+) + W^{S-}(\boldsymbol{\varepsilon}_S^-) + \\ + G_c\,\Gamma^S(\phi^S,\, \mathrm{grad}\phi^S)\,, \end{aligned}$$

$$\text{where} \quad \begin{cases} W^{S+}(\boldsymbol{\varepsilon}_S^+) &= \mu^S\big(\boldsymbol{\varepsilon}_S^+ \cdot \boldsymbol{\varepsilon}_S^+\big) + \dfrac{1}{2}\,\lambda^S\left(\dfrac{\mathrm{tr}\,\boldsymbol{\varepsilon}_S + |\mathrm{tr}\,\boldsymbol{\varepsilon}_S|}{2}\right)^2, \\ W^{S-}(\boldsymbol{\varepsilon}_S^-) &= \mu^S\big(\boldsymbol{\varepsilon}_S^- \cdot \boldsymbol{\varepsilon}_S^-\big) + \dfrac{1}{2}\,\lambda^S\left(\dfrac{\mathrm{tr}\,\boldsymbol{\varepsilon}_S - |\mathrm{tr}\,\boldsymbol{\varepsilon}_S|}{2}\right)^2, \\ \Gamma^S(\phi^S,\, \mathrm{grad}\phi^S) &= \dfrac{1}{2\epsilon}\,(\phi^S)^2 + \dfrac{\epsilon}{2}\,\mathrm{grad}\phi^S \cdot \mathrm{grad}\phi^S\,. \end{cases} \tag{3.69}$$

Therein, μ^S and λ^S denote the solid Lamé constants. The viscous stress resistant η_r^S represents a residual artificial stiffness of the solid skeleton, which prevents zero stiffness in a fully cracked zone. Furthermore, the fracture energy is composed of the critical energy release rate G_c of brittle solids and the crack-surface density function Γ^S. For a detailed discussion of the critical energy release rate in the model, the interested reader is referred to Wang *et al.* [247]. The crack-surface density function Γ^S depends on the phase-field variable ϕ^S, its gradient and the internal length-scale parameter ϵ, which is responsible for the thickness of the fractured zone. Note that the phase-field variable only affects the stored tensile energy and the fracture energy in (3.69).

Solid effective stress

Inserting the proposed formula of the solid stored energy (3.69) into the linearised restriction resulting from the equilibrium part of the entropy inequality (3.64), the linearised solid effective stress reads

$$\begin{aligned} \boldsymbol{\sigma}_{EF}^S = \left[(1-\phi^S)^2 + \eta_r^S\right]\left[2\mu^S\boldsymbol{\varepsilon}_S^+ + \lambda^S\left(\frac{\mathrm{tr}\,\boldsymbol{\varepsilon}_S + |\mathrm{tr}\,\boldsymbol{\varepsilon}_S|}{2}\right)\mathbf{I}\right] + \\ + 2\mu^S\boldsymbol{\varepsilon}_S^- + \lambda^S\left(\frac{\mathrm{tr}\,\boldsymbol{\varepsilon}_S - |\mathrm{tr}\,\boldsymbol{\varepsilon}_S|}{2}\right)\mathbf{I}\,. \end{aligned} \tag{3.70}$$

With this formulation, the stiffness of the fractured solid skeleton decreases only in tension direction with an evolving phase field.

Evolution of the phase-field variable

The proportionality request of the dissipation relation $(3.67)_2$ for the phase-field evolution $(\phi^S)'_S$ can be satisfied by a linear dependency following Ehlers & Luo [93], i. e.

$$(\phi^S)'_S = -\frac{1}{M}\left[\frac{\partial W^S}{\partial \phi^S} - \mathrm{div}\left(\frac{\partial W^S}{\partial \mathrm{grad}\phi^S}\right)\right]. \tag{3.71}$$

Therein, M is introduced as a non-negative mobility parameter responsible for the dissipation upon stable crack propagation, compare Kuhn & Müller[2] [164]. Under consideration of the formulated solid stored energy (3.69), the evolution equation for the phase-field variable can be determined as

$$(\phi^S)'_S = \frac{1}{M}\left[2(1-\phi^S)\,W^{S+} - G_c\Big(\frac{\phi^S}{\epsilon} - \epsilon\,\mathrm{div}\,\mathrm{grad}\phi^S\Big)\right] \tag{3.72}$$

with

$$\mathrm{grad}\,\phi^S \cdot \mathbf{n} = 0 \tag{3.73}$$

as the corresponding boundary condition according to the restriction $(3.67)_1$.

To avoid a singularity caused by a zero-value denominator, the evolution equation (3.72) is reformulated to:

$$M(\phi^S)'_S = 2(1-\phi^S)\,W^{S+} - G_c\Big(\frac{\phi^S}{\epsilon} - \epsilon\,\mathrm{div}\,\mathrm{grad}\phi^S\Big)\,. \tag{3.74}$$

Remark: In Ehlers & Luo [93], the mobility parameter M has been explained physically as a viscosity parameter. There, it was found that in case of M larger than 10^6 Pa s, while W^{S+} and G_c/ϵ are in the range of $10^6 - 10^7$ J/m^3, an increase of M results in a delay of crack nucleation and propagation. However, the mobility parameter can also be understood as a purely numerical parameter that has a stabilising effect on the computation, also compare Miehe *et al.* [193] for a monolithic solution and Miehe *et al.* [190] for a staggered solution of a purely solid fracturing process. □

3.4.2 Fluid pressure

The following subsections present the constitutive relations for a partially saturated porous material, where two immiscible fluid phases percolate the fracturing solid skeleton. The constitutive relations concern the interaction between the fluids themselves and the interaction forces between the fluid phases and the solid. Multiphasic flow processes in intact porous material are discussed in detail, for example, in the work of Bear [20], Hassanizadeh & Gray [129, 130], Helmig [138] and Ehlers *et al.* [92]. Moreover, a detailed description of the liquid behaviour in a fully saturated fracturing porous media can be found, e. g., in Luo [178].

As the two fluid phases are considered immiscible, they occupy different pore volumes of the porous material and are separated on the microscale by a mobile interface. They exhibit, accordingly, different pressures. At this interface, the molecular cohesion within and adhesion between the phases cause surface tension without external load. The related displacement of the fluids in the pore space responds to capillary effects at the microscale. The following briefly introduces it before considering the resulting effects on the macroscale. Finally, the pressure behaviour during a dynamic injection will be discussed.

[2] In Kuhn & Müller [164], the mobility parameter is the inverse of M in (3.71)-(3.74).

Capillarity on the microscale

A pore can be considered a vertical tube in an idealised representation on the microscale, compare Figure 3.1. In the case of a liquid-gas mixture in the pore space, the solid molecules attract the liquid molecules at the interfacial area due to adhesive forces. By this, the liquid displaces the gas and wets the solid. Due to the surface tension, the interfacial area curves, here with a circular cross-section with an angle ω, see Figure 3.1, and involves a spontaneous pressure drop.

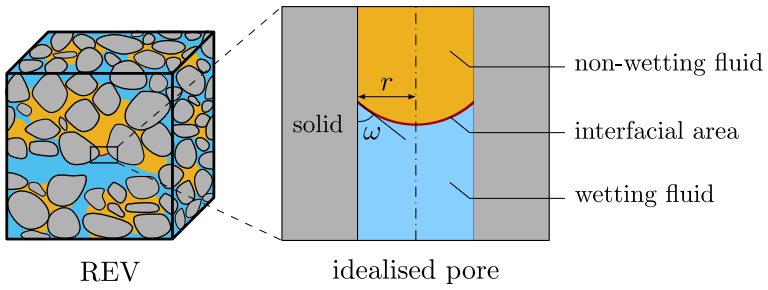

Figure 3.1: *Depiction of an idealised pore at the microscale.*

According to their characteristics, the fluid with an acute angle to the solid is termed the wetting fluid, here the liquid, and the fluid with an obtuse angle is referred to as non-wetting fluid, here the gas. The (always positive) pressure difference between the non-wetting and the wetting pressures, p^{nw} and p^{w}, respectively, is termed microscopic capillary pressure p^{c}. It can directly be related to the surface tension γ_s and the tube's radius r via

$$p^{c} := p^{nw} - p^{w} = \frac{2\,\gamma_s\,\cos\omega}{r}\,. \tag{3.75}$$

Note for clarity that the superscripts for microscopic values are lowercase letters, and those for macroscopic values are capital letters. For a complete overview of capillary and wettability effects at the microscale, the reader is referred, e. g., to the work of Bear [20], Hassanizadeh & Gray [129, 130], Helmig [138] and Blunt [36] and citations therein.

The Young-Laplace equation (3.75) states equilibrium in pressure between the two sides of the interface at the pore scale. Analogously, the macroscopic phase-pressure difference captures the capillary effects on the macroscale. This pressure is always measured at equilibrium and cannot represent dynamic processes. Since an injection, as it is considered for hydraulic fracturing, poses a highly dynamic process, a modified description of the pressure difference is needed in this case. In the following paragraph, (equilibrium) capillarity at the macroscale is first discussed, and then, in a further paragraph, a modified description of the pressure within dynamic injection processes is proposed.

Capillarity on the macroscale

The phase-pressure difference p^{C} at equilibrium on the macroscale, also named the macroscopic capillary pressure, is defined in analogy to (3.75) as the pressure difference between

the effective gas pore pressure p^{GR} and the effective liquid pore pressure p^{LR}, viz.

$$p^C := p^{GR} - p^{LR} \,. \tag{3.76}$$

The dependence of the microscopic capillary pressure on the surface tension and interface curvature in (3.75) is then expressed on the macroscale in a relation between the phase-pressure difference, the saturation and the geometry of the pores, compare Brooks & Corey [58]. There are many experimental and empirical approaches to determine this relationship specific to the system's properties, for example, the combination of the three phases, the temperature, the grain size distribution, and the hysteresis of the process's direction (drainage or imbibition), to name a few. An overview of the different approaches and their applicability can be found, e. g., in the work of Sheta [223]. One important aspect here is that all states of the pressure-difference-saturation models are equilibrium states. In particular, the laboratory techniques, which involve changing fluid saturation in small increments, ensure that the saturation level remains stable, allowing enough time for equilibrium. Among the best-known empirical approaches for liquid-gas systems are those of Brooks & Corey [57] and van Genuchten [115]. Both models deal with the effective saturation $s^L_{\text{eff.}}$, defined as

$$s^L_{\text{eff.}} = \frac{s^L - s^L_{\text{r}}}{1 - s^L_{\text{r}} - s^G_{\text{r}}} \tag{3.77}$$

for $s^L_{\text{r}} \leq s^L \leq 1 - s^G_{\text{r}}$, see, e. g., Mualem [198]. Therein, s^L_{r} and s^G_{r} are the residual liquid and gas saturations, respectively, and stand for the saturation portions above which the respective fluid becomes mobile. Note that Brooks & Corey assumed that $s^G_{\text{r}} = 0$, see also the work of Corey [66]. A discussion of the different definitions of effective saturation can be found, for example, in the textbook of Helmig [138].

Brooks & Corey [57] established a function between the slope of the effective saturation's logarithmic curve and the phase-pressure difference's logarithm, leading to

$$s^L_{\text{eff.}}(p^C) = \left[\frac{p_d}{p^C}\right]^{\lambda} \quad \text{for} \quad p^C \geq p_d \quad \rightarrow \quad p^C(s^L_{\text{eff.}}) = p_d \, [s^L_{\text{eff.}}]^{-\frac{1}{\lambda}} \,, \tag{3.78}$$

with $\lambda > 0$ the pore size distribution factor and p_d the displacement pressure. Therein, λ has a small value for a porous medium with a wide range of pore sizes and a large value for a porous medium with a uniform pore size. Moreover, Brooks & Corey described p_d as the approximate minimum of the capillary pressure at which a continuous gas phase exists in the porous medium during drainage.

Besides this, van Genuchten [115] formulated the macroscopic capillary-pressure-saturation function with respect to the definition of the effective saturation (3.77) as follows

$$s^L_{\text{eff.}}(p^C) = [1 + (\alpha_G \, p^C)^n]^{-m} \quad \text{for} \quad p^C > 0 \quad \rightarrow \quad p^C(s^L_{\text{eff.}}) = \frac{1}{\alpha_G} \left[(s^L_{\text{eff.}})^{-\frac{1}{m}} - 1\right]^{\frac{1}{n}} \tag{3.79}$$

with the pore space geometry parameters α_G, m and n determined based on experimental data.

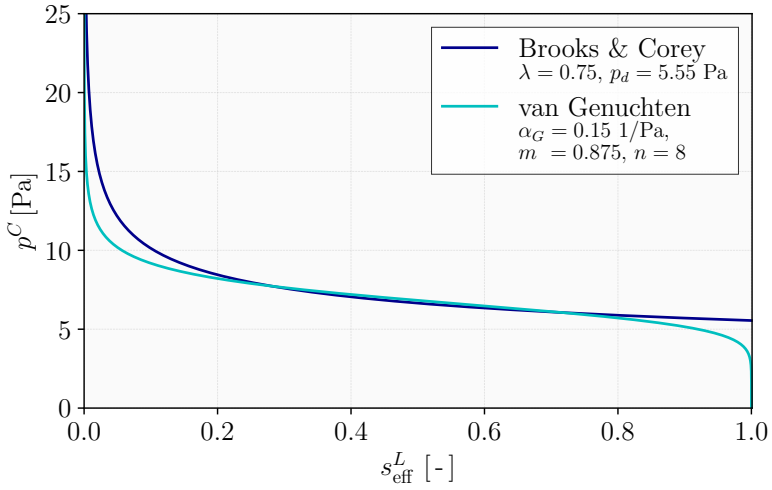

Figure 3.2: *Phase-pressure difference-saturation curve with respect to the Brooks-Corey [57] and van Genuchten [115] model. Parameters after Lenhard et al. [171].*

Remark: Lenhard *et al.* [171] derived correlations between Brooks & Corey's and van Genuchten's model parameters. □

The two models are depicted in Figure 3.2. In the case of a spontaneous drainage process, the (positive) pressure difference increases, and the gas displaces the liquid through the pore space, by which the liquid saturation decreases. In contrast, in the case of a spontaneous imbibition process, the pressure difference decreases, and the liquid displaces the gas.

Remark: When successive imbibition and drainage processes occur, the macroscopic capillary-pressure-saturation curve undergoes hysteresis effects. These latter are omitted here as no recurring imbibition and drainage processes are regarded in this monograph. However, concepts with hysteresis effects can be found, e. g., in the work of Mualem [198], Kool & Parker [161] and Lenhard [170]. For an overview of this topic, the interested reader is referred to Bear [20], Helmig [138] and Blunt [36], among others. □

Injection process

In fracturing processes, the liquid is injected into the porous solid domain. In this case, no equilibrium state is achieved. This is a decisive difference compared to the capillary effects described in the previous paragraphs. In order to capture the significance of the dynamic process, Manthey [182] discussed, based on a dimensional analysis, the dominating forces related to the viscous, dynamic and equilibrium (capillary) effects within multiphasic systems. The dynamic effects dominate with increasing flow velocity and decreasing length scale of a system. Therefore, in the case of hydraulic fracturing, where high liquid velocities are reached, the dynamic process of the liquid injection is the system's driving force and needs to be considered in detail. While the pressure-difference-saturation relation was unique for equilibrium conditions, it is no longer the case when dynamic processes are

considered. Particularly, the pressure-difference-saturation relation becomes a function of the rate-dependent behaviour of the saturation. Different approaches, experimental and theoretical, have been developed to capture this dependence. Most of them, e. g., Stauffer [230], Kalaydjian [152] and Hassanizadeh *et al.* [126], suggest the difference between a dynamic and an equilibrium capillary pressure, p^C_{dyn} and p^C, respectively, as a linear function of the rate of change of saturation, viz.

$$p^C_{\text{dyn}} - p^C(s^L_{\text{eff}}) = -\tau \frac{\partial s^L_{\text{eff}}}{\partial t} \,, \tag{3.80}$$

where τ is the damping coefficient. This latter has to be carefully determined by methodical or laboratory studies. Manthey [182] found out that the relationship between the difference in capillary pressure and the rate of saturation change is non-linear at low rates of saturation change. The complexity of such dynamic processes is high and can not be represented in conventional hydromechanical equations. Here, the change of equilibrium and dynamic processes will be represented by a mathematical sign change in the pressure-difference-saturation relation $p^D(s^L)$, whereby the equilibrium and dynamic capillary pressure are united in the pressure term $p^D = p^C \cup p^C_{\text{dyn}}$. Thus, in order to include both equilibrium and dynamic processes in one single simplified function, the liquid free energy is introduced *a priori* as

$$\psi^L(s^L) = \frac{a}{\rho^{LR}} \left[\frac{b}{s^L} + c \ln \left(\frac{s^L}{1 - s^L} \right) - d \ln s^L \right] , \tag{3.81}$$

such that with (3.47) the pressure difference reads

$$p^D(s^L) = -\rho^{LR} s^L \frac{\partial \psi^L}{\partial s^L} = a \left[\frac{b}{s^L} - \frac{c}{1 - s^L} + d \right] . \tag{3.82}$$

The fitting constants a, b, c and d allow an adjustment in the above equations. Finally, the curve of $p^D(s^L)$ describes an asymptotic function satisfying equilibrium capillary effects for $p^D \geq 0$, while a dynamic injection is described in the range of $p^D < 0$, compare Figure 3.3. In the present context, the switch between capillary effects and dynamic injection, where $p^{GR} = p^{LR}$ holds, has been set at $s^L = 0.7$. This state will also be the initial state for all numerical examples of hydraulic fracturing in Chapter 5. On the left side of this starting point, equilibrium capillary effects hold, where the gas can displace the liquid (drainage) or *vice versa* (imbibition). Thereby, $p^{GR} > p^{LR}$ is valid. On the other hand, in this model, the liquid displaces the mobile gas during a dynamic liquid injection with $p^{LR} > p^{GR}$. Note that the pressure-difference-saturation function restricts $s^L \neq \{0, 1\}$ and implicitly includes residual liquid and gas saturations.

Remark: Similar curves at the pore level can be found in petroleum engineering for water-oil mixtures, see, e. g., Amott [13], Anderson [14], Kovscek *et al.* [163], Blunt [35, 36], Øren *et al.* [205], Dixit *et al.* [77], Al-Futaisi & Patzek [2], among others. However, the change from the "spontaneous displacement" to the "forced injection" processes (where the water pressure exceeds the oil pressure) is correlated with a wettability change of the water and oil. In this monograph, no wettability changes are present. □

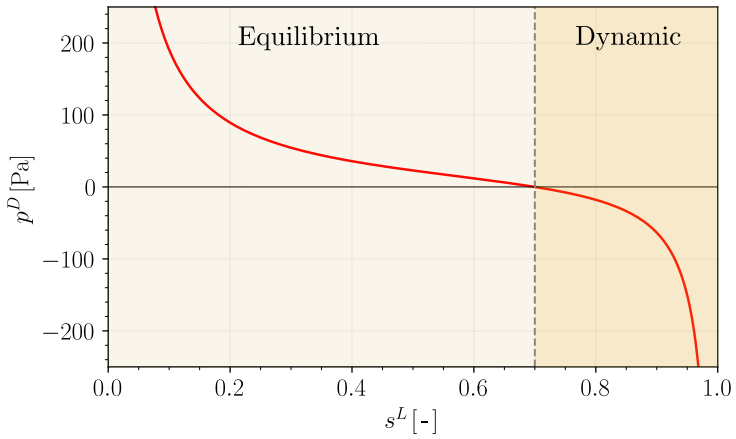

Figure 3.3: *Pressure-difference function p^D over liquid saturation s^L with following values: $p^D = 0$ [Pa] at $s^L = 0.7$ [-] and $a = 5 \cdot 10^{-3}$ [Pa], $b = 4\,000.5$ [-], $c = 1\,714.5$ [-] and $d = 0$ [-].*

Considering Figure 3.3, the capillary suction − and therewith the gas pressure − is relatively low compared to the liquid pressure during the injection process, which is in the range of MPa. For this reason, some contributions neglect the role of capillary suction during the injection process, e. g., Heider & Sun [137]. However, since this thesis aims to study in detail the interaction among the fluid phases during the hydraulic crack propagation, the pressure-difference-saturation function plays a significant role here. This effect will be shown in the numerical examples in Chapter 5, Section 5.2.

3.4.3 Fluid flow

Based on the restrictions arising from the dissipation inequality $(3.55)_{1-4}$, the non-equilibrium momentum productions and frictional fluid stresses, $\hat{\mathbf{p}}^{\beta}_{NEQ}$ and $\mathbf{T}^{\beta}_{NEQ}$, are assumed proportional to either the seepage velocities $\mathbf{w}_\beta$ or the fluid velocity gradients $\mathbf{D}_\beta$, respectively. Following the work of Ehlers & Luo [93, 94], these quantities are introduced via

$$\hat{\mathbf{p}}^{\beta}_{NEQ} = -(1-\phi^S)^2 (n^\beta)^2 \frac{\gamma^{\beta R}}{K^\beta_r}\, \mathbf{w}_\beta\,, \quad \mathbf{T}^{\beta}_{NEQ} = 2(\phi^S)^2 n^\beta \mu^{\beta R} \mathbf{D}_\beta\,, \tag{3.83}$$

where $\gamma^{\beta R} = \rho^{\beta R}|\mathbf{g}|$ is the specific weight of φ^β and $\mu^{\beta R}$ the effective shear viscosity of the pore fluids. Moreover, K^β_r defines the relative fluid conductivity and will be introduced in the next subsection.

By inclusion of ϕ^S in the above equations, the pore fluids undergo a transition between a Darcy-type flow in the unbroken porous-media domain with $\phi^S = 0$, governed by the drag forces $\hat{\mathbf{p}}^{\beta}_{NEQ}$, and a Navier-Stokes flow in fully broken zones with $\phi^S = 1$, governed by the frictional Newton terms $\mathbf{T}^{\beta}_{NEQ}$. A detailed derivation of these limit states is shown in Appendix B.2. This result is in line with the observations of Beavers & Joseph [21], who investigated the transition zone of pore liquids between a porous-media flow and a free flow, compare also Ehlers & Luo [94] and Luo [178].

However, more than this consideration is required when geological materials are regarded. Notably, in naturally grown soil and rock, not only open but also closed fractures occur. The fractured zones might close again, or there might even be closed precracks due to the amount of confining stresses caused by the load of the upper layers of the stratum. In these cases, the fluids permeate the fractured but closed domain by a Darcy-type flow, like in the surrounding unbroken porous material. This is in contradiction to (3.83), where the evolution of a fracture with growing values of ϕ^S is interpreted as a fracture opening. While this might not be of interest in the frame of standard solid mechanics, it matters strongly when porous media are concerned. As a result and in order to distinguish between open and closed cracks, Ehlers & Luo [94] introduced another variable into this constitutive approach, namely the crack-opening indicator $\mathcal{I}$ (COI). Since an enlarging pore space is an indicator for open fractures and n^F is growing when n^S is shrinking through positive values of $\operatorname{div}\mathbf{u}_S$, compare (2.3) and $(3.66)_2$, the COI takes the binary values zero or one as follows:

$$\mathcal{I} = \begin{cases} 1\text{: for increasing porosity } n^F > n_0^F \text{ with } \operatorname{div}\mathbf{u}_S > 0\,, \\ 0\text{: for decreasing or constant porosity } n^F \leq n_0^F \text{ with } \operatorname{div}\mathbf{u}_S \leq 0\,, \end{cases} \tag{3.84}$$

where n_0^F is the initial porosity. Embedding the COI in the relations (3.83) through

$$\hat{\mathbf{p}}^\beta_{NEQ} = -[1-\mathcal{I}+\mathcal{I}(1-\phi^S)^2](n^\beta)^2\,\frac{\gamma^{\beta R}}{K_r^\beta}\,\mathbf{w}_\beta\,, \quad \mathbf{T}^\beta_{NEQ} = 2\,\mathcal{I}(\phi^S)^2 n^\beta \mu^{\beta R}\mathbf{D}_\beta\,, \tag{3.85}$$

leads to the properties:

Table 3.1: *Hydraulic fracturing and flow in porous media depending on ϕ^S and $\mathcal{I}$ after [94]*

Phase field ϕ^S	COI $\mathcal{I}$	Description	Flow type
0	1	intact solid with enlarging pores	Darcy
0	0	intact solid with shrinking pores	Darcy
1	1	fractured solid with open cracks	Navier-Stokes
1	0	fractured solid with closed cracks	Darcy

Thus, for an intact porous material with $\phi^S = 0$, the extra momentum productions dominate the fluid flow and yield a Darcy-type flow, regardless of the porosity evolution, i. e. $\mathcal{I} = \{0, 1\}$. Nevertheless, in the case of fully broken material with $\phi^S = 1$, two states are distinguished through $\mathcal{I}$. On the one hand, the frictional forces $\operatorname{div}\mathbf{T}^\beta_{NEQ}$ govern the fluid flows and follow the Navier-Stokes equation when $\mathcal{I} = 1$. On the other hand, when $\mathcal{I} = 0$, the broken domain behaves like an intact one, and the fluid flows follow the Darcy law again. Between these cases, when $0 < \phi^S < 1$, the phase-field variable determines the transition between these flow types.

A full description of the introduction and applicability of the COI can be found in the work of Ehlers & Luo [94] and Luo [178].

3.4.4 Fluid conductivity

When multiple fluid phases are present in the pore space, they interfere with each other's flow behaviour. Therefore, the drag forces $\hat{\mathbf{p}}^{\beta}_{NEQ}$ included in $(3.83)_1$ and $(3.85)_1$ depend on relative fluid conductivities K^{β}_r, which are related to the standard hydraulic conductivities K^{β} through relative permeability factors κ^{β}_r:

$$K^{\beta}_r := \kappa^{\beta}_r K^{\beta} \,. \tag{3.86}$$

Note that K^{β} is also known as Darcy permeability and governs the permeating behaviour of a single fluid (liquid or gas) under fully saturated conditions. It is defined in $[\mathrm{m}^3/(\mathrm{m}^2\,\mathrm{s})]$, in short $[\mathrm{m/s}]$. The dimensionless relative permeability factors regulate the permeability of the particular fluid φ^{β} by its saturation in the pore space, viz. $\kappa^{\beta}_r = \kappa^{\beta}_r(s^{\beta})$. Through the relation (2.5), both saturation variables can be expressed over the liquid saturation s^L, leading to $\kappa^{\beta}_r = \kappa^{\beta}_r(s^L)$. The dependence of the relative permeability on the saturation was already recognised experimentally in soil science and petroleum engineering in the 1930s, cf. Richards [211], Muskat *et al.* [200] and Leverett [172], among others. Since then, many empirical approaches have been developed to determine the relative permeability factors, compare, e. g., the work of Ahmed [1] and Sheta [223] for an overview of these relations. Among the most prominent concepts is the Brooks-Corey approach [57]. Brooks & Corey substituted their capillary-pressure-saturation relation (3.78) into the capillary tube model after Burdine[3] [60], leading to the following formulation for the relative permeability factors

$$\kappa^L_r = [s^L]^{\frac{2+3\lambda}{\lambda}} \quad \text{and} \quad \kappa^G_r = (1-s^L)^2\,[\,1-(s^L)^{\frac{2+\lambda}{\lambda}}\,]\,. \tag{3.87}$$

Remark: Strictly speaking, Brooks & Corey formulated this relation for the effective liquid saturation s^L_{eff} instead of s^L, cf. (3.77). However, since residual saturations are implicit in the asymptotic curve of the pressure-difference-saturation function, compare Figure 3.3, s^L_{eff} has been replaced by s^L here. □

Figure 3.4 displays the permeability factors κ^L_r and κ^G_r as a function of s^L for a poorly sorted and a well-sorted soil, with $\lambda = 1$ and $\lambda = 3$, respectively, according to Brooks & Corey [57]. Generally speaking, when the saturation increases, the fluid displaces the other fluid phase and takes up more space, which allows the particular fluid to flow more easily. This phenomenon is reflected in the relative permeability factor, which increases until one with the saturation. Conversely, when the saturation falls below a certain threshold, in other words, when the amount of interconnected fluid particles decreases towards zero, κ^{β}_r vanishes, and the system is impermeable for the particular fluid constituent.

Remark: The increase of the relative permeability factor in the range of lower saturations is more decisive for the pore gas than for the pore liquid. This difference is because the liquid, as the wetting phase here, prefers to fill the smaller pores. There, the flow conditions are more difficult than in the larger pores, where the pore gas, the non-wetting

[3] Therein, the porous medium is modelled via several parallel capillary tubes with different cross-sections (pore sizes) perpendicular to the direction of flow and constant cross-sections in the direction of flow. In contrast, the van Genuchten model [115] for the relative permeability factors is based on Mualem's capillary tube model with variable pore size in both directions, cf. Mualem [198].

phase, is mainly located. This behaviour is accentuated in the case of poorly sorted soil, compare the dashed to the solid line in Figure 3.4. □

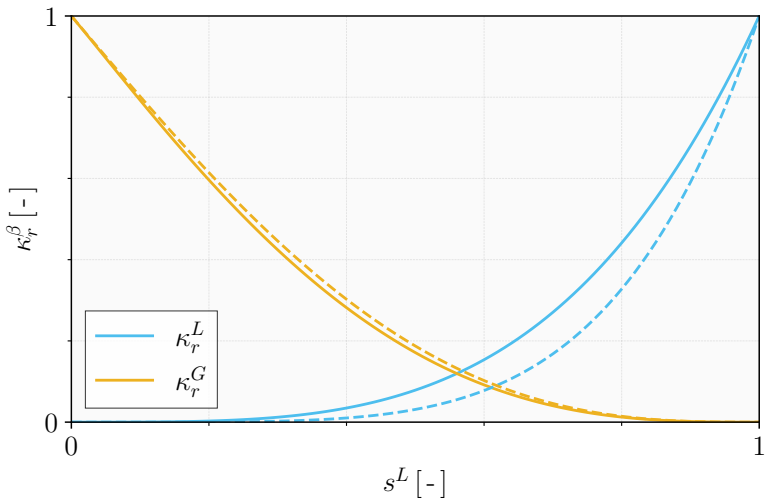

Figure 3.4: *Relative permeability factors after Brooks & Corey [57] as a function of the liquid saturation s^L for poorly sorted soil ($\lambda = 1$, dashed line) and well-sorted soil ($\lambda = 3$, solid line).*

Note that different flow behaviours can occur at the same saturation depending on whether wetting or drying is in process. Accordingly, similar to the hysteresis effect in capillarity, history effects on saturation may also occur for relative permeabilities. An overview of the different hysteresis models can be found, e. g., in the work of Sheta [223]. In this monograph, no hysteresis will be considered.

While K^β describes the conductivity behaviour of a single fluid under fully saturated conditions, K^β can be related to the intrinsic solid permeability K^S through

$$\frac{K^S}{\mu^{\beta R}} = \frac{K^\beta}{\gamma^{\beta R}} \tag{3.88}$$

with K^S in [m^2] and $\mu^{\beta R}$ in [Pa s], compare Ehlers [88]. The deformation-dependent solid intrinsic permeability is defined following Eipper [99] via

$$K^S := \left(\frac{1 - n^S}{1 - n_0^S} \right)^\kappa K_0^S \,. \tag{3.89}$$

Therein, K_0^S stands for the initial solid permeability in the reference configuration, and $\kappa > 0$ is a material parameter adjusting the dependency of the permeability on the solid deformation. In this monograph, κ is chosen as one. Note that K^S can be a tensorial quantity $\mathbf{K}^S$ in non-isotropic permeability circumstances. The interested reader on this topic is referred, e. g., to the work of Markert [185] and citations therein. Further information on permeability estimations in porous media with regular structure can be found in Wagner *et al.* [245].

3.4.5 Pore gas density

As the pore gas has been assumed to represent an ideal gas following Boyle's law, it can be described by the free-energy function

$$\psi^G(\rho^{GR}) = R^G\theta \ln \rho^{GR}\,, \quad \text{such that} \quad p^{GR} = R^G\theta\rho^{GR}\,, \tag{3.90}$$

where (3.44) has been used. In the above equations, R^G is the specific gas constant and θ the absolute temperature after Kelvin, which is assumed constant in this study. Note that the absolute values can be employed as excess values relative to the atmospheric pressure p_{atm}. In that sense, the absolute gas pressure p^{GR} is defined as the sum of the atmospheric pressure with a mean value (at sea level) of approximately $p_{\text{atm}} = 101\,325\,\text{Pa}$ and the gas excess pressure p^{GR}_{excess}, viz.

$$p^{GR} = p^{GR}_{\text{excess}} + p_{\text{atm}}\,, \tag{3.91}$$

such that the gas excess pressure reads

$$p^{GR}_{\text{excess}} = R^G\theta\rho^{GR} - p_{\text{atm}}\,. \tag{3.92}$$

From this, the following relation holds for the gas density:

$$\rho^{GR} = \frac{p^{GR}_{\text{excess}}}{R^G\theta} + \rho^{GR}_{\text{atm}} \quad \text{with} \quad \rho^{GR}_{\text{atm}} = \frac{p_{\text{atm}}}{R^G\theta}\,. \tag{3.93}$$

In order to simplify the appearance of the following equations, the term p^{GR}_{excess} is substituted by the term p^{GR} in the numerical study, such that

$$p^{GR} := p^{GR}_{\text{excess}}\,. \tag{3.94}$$

It should be noted that, as p^{GR} is defined as excess pressure, the same is applied to the liquid pressure p^{LR}.

3.5 Closure problem for the fully coupled system

Finally, this section summarises the previous constitutive modelling of the coupled TPM model with an embedded phase-field approach to fracture. The closure problem is detailed for the partially saturated porous material, and the governing equations for the biphasic, fully saturated porous material are outlined.

3.5.1 Triphasic material

The governing equations for the numerical computation of the triphasic problem under study can be taken from Table 3.2. Therein, the momentum balances have been taken from (3.13) and (3.15), and the mass and volume balances from (3.8) and $(3.9)_2$, respectively. These equations together with the phase-field evolution equation (3.72), the constitutive

relations and the initial and boundary conditions define the strong form of the initial-boundary-value problem resulting in a system of 12 scalar differential equations that have to be solved in a monolithic manner. Note that the solid displacement-velocity relation does not count here, as it is solved locally in order to reduce the order of time derivatives of the solid motion from second to first order.

As mentioned, the overall momentum balance has been included instead of the solid momentum balance here. This choice is due to the fact that the overall external load can only be placed onto the overall surface, while a distribution to the individual constituents remains a result of deformations, velocities and stiffnesses of the constituents. Concerning the corresponding numerical solution derived in the next chapter, the primary variables for this coupled system are chosen as the solid displacement $\mathbf{u}_S$, the solid, liquid and gas velocities, $\mathbf{v}_S$, $\mathbf{v}_L$ and $\mathbf{v}_G$, the liquid saturation s^L, the gas pressure p^{GR} and the phase-field variable ϕ^S, respective to the equations in Table 3.2. Moreover, all temporal changes are considered with respect to the skeleton motion, making use of the seepage velocities $\mathbf{w}_\beta = \mathbf{v}_\beta - \mathbf{v}_S$, with $\beta = \{L, G\}$.

Table 3.2: *Summary of the governing partial differential equations in their strong forms of the partially saturated model.*

Solid displacement-velocity relation

$$(\mathbf{u}_S)'_S = \mathbf{v}_S$$

Overall momentum balance

$$\rho^S (\mathbf{v}_S)'_S + \rho^L \left[(\mathbf{v}_L)'_S + (\mathrm{grad}\mathbf{v}_L)\, \mathbf{w}_L \right] + \rho^G \left[(\mathbf{v}_G)'_S + (\mathrm{grad}\mathbf{v}_G)\, \mathbf{w}_G \right] = \mathrm{div}\,(\boldsymbol{\sigma}^S_{EF} + \mathbf{T}^L_{NEQ} + \mathbf{T}^G_{NEQ} - p^{FR}\mathbf{I}) + \rho\,\mathbf{g}$$

Liquid momentum balance

$$\rho^L \left[(\mathbf{v}_L)'_S + (\mathrm{grad}\mathbf{v}_L)\, \mathbf{w}_L \right] = \mathrm{div}\,\mathbf{T}^L_{NEQ} + \rho^L \mathbf{g} + \hat{\mathbf{p}}^L_{NEQ} - n^L \mathrm{grad}\, p^{LR} + p^D n^F \mathrm{grad} s^L$$

Gas momentum balance

$$\rho^G \left[(\mathbf{v}_G)'_S + (\mathrm{grad}\mathbf{v}_G)\, \mathbf{w}_G \right] = \mathrm{div}\,\mathbf{T}^G_{NEQ} + \rho^G \mathbf{g} + \hat{\mathbf{p}}^G_{NEQ} - n^G \mathrm{grad}\, p^{GR}$$

Liquid volume balance

$$(n^L)'_S + n^L \mathrm{div}\,(\mathbf{u}_S)'_S + \mathrm{div}\,(n^L\, \mathbf{w}_L) = 0$$

Gas mass balance

$$(\rho^G)'_S + \rho^G \mathrm{div}\,(\mathbf{u}_S)'_S + \mathrm{div}\,(\rho^G \mathbf{w}_G) = 0$$

Phase-field evolution equation

$$(\phi^S)'_S = \frac{1}{M}\Big[\, 2(1-\phi^S)\, W^{S+} - G_c \Big(\frac{\phi^S}{\epsilon} - \epsilon\, \mathrm{div}\,\mathrm{grad}\,\phi^S \Big) \Big]$$

In the following, the secondary equations are summarised. This set of coupled equations is the basis for the numerical implementation.

First, the volume fractions are defined through the integrated solid volume balance (3.11), the condition (2.3) and the saturation definition (2.6):

$$\begin{aligned} n^S &= n_0^S\,(1-\operatorname{div}\mathbf{u}_S)\,, \\ n^F &= 1-n^S\,, \\ n^L &= s^L\,n^F\,, \\ n^G &= (1-s^L)\,n^F\,. \end{aligned} \tag{3.95}$$

Besides the gas pore pressure, which is a primary variable, the fluid pressures are given by

$$\begin{aligned} p^D &= p^D(s^L)\,, \text{ depending on the specific problem,} \\ p^{LR} &= p^{GR}-p^D\,, \\ p^{FR} &= s^L\,p^{LR}+(1-s^L)\,p^{GR}\,. \end{aligned} \tag{3.96}$$

Therein, the pressure-difference-saturation relation depends on the specific problem. Moreover, the solid and liquid phases are assumed incompressible, with $\rho^{SR} \equiv$ const. and $\rho^{LR} \equiv$ const., while the gas density reads

$$\rho^{GR} = \frac{p^{GR}}{R^G\theta}+\rho^{GR}_{\text{atm}} \quad \text{with} \quad \rho^{GR}_{\text{atm}}=\frac{p_{\text{atm}}}{R^G\theta}\,. \tag{3.97}$$

The elastic strain tensor can be computed based on the solid displacement and split to

$$\boldsymbol{\varepsilon}_S=\boldsymbol{\varepsilon}_S^+ + \boldsymbol{\varepsilon}_S^- \quad \text{with} \quad \begin{cases} \boldsymbol{\varepsilon}_S^+ = \sum\nolimits_i \dfrac{\varepsilon_{Si}+|\varepsilon_{Si}|}{2}\,\mathbf{n}_{Si}\otimes\mathbf{n}_{Si}\,, \\ \boldsymbol{\varepsilon}_S^- = \sum\nolimits_i \dfrac{\varepsilon_{Si}-|\varepsilon_{Si}|}{2}\,\mathbf{n}_{Si}\otimes\mathbf{n}_{Si}\,, \end{cases} \tag{3.98}$$

with ε_{Si} the eigenvalues and $\mathbf{n}_{Si}$ the eigenvectors of the strain tensor $\boldsymbol{\varepsilon}_S$. From this and the phase-field (primary) variable, the linearised solid stress tensor yields

$$\begin{aligned} \boldsymbol{\sigma}^S_{EF} = &\Big[(1-\phi^S)^2+\eta_r^S\Big]\left[2\mu^S\boldsymbol{\varepsilon}_S^+ + \lambda^S\left(\frac{\operatorname{tr}\boldsymbol{\varepsilon}_S+|\operatorname{tr}\boldsymbol{\varepsilon}_S|}{2}\right)\mathbf{I}\right]+ \\ &+2\mu^S\boldsymbol{\varepsilon}_S^- + \lambda^S\left(\frac{\operatorname{tr}\boldsymbol{\varepsilon}_S-|\operatorname{tr}\boldsymbol{\varepsilon}_S|}{2}\right)\mathbf{I}\,. \end{aligned} \tag{3.99}$$

The momentum productions and frictional fluid stresses read

$$\begin{aligned} \hat{\mathbf{p}}^\beta_{NEQ} &= -[1-\mathcal{I}+\mathcal{I}(1-\phi^S)^2](n^\beta)^2\,\frac{\gamma^{\beta R}}{K_r^\beta}\,\mathbf{w}_\beta\,, \\ \mathbf{T}^\beta_{NEQ} &= 2\,\mathcal{I}(\phi^S)^2 n^\beta\mu^{\beta R}\mathbf{D}_\beta\,, \end{aligned} \tag{3.100}$$

whereby the relative permeabilities are calculated by

$$K_r^\beta = \kappa_r^\beta K^\beta = \kappa_r^\beta\frac{\gamma^{\beta R}K^S}{\mu^{\beta R}} \tag{3.101}$$

with the intrinsic solid permeability

$$K^S = \left(\frac{1-n^S}{1-n_0^S}\right) K_0^S , \tag{3.102}$$

and the relative permeability factors according to Brooks & Corey [57], namely

$$\kappa_r^L = [s^L]^{\frac{2+3\lambda}{\lambda}} \quad \text{and} \quad \kappa_r^G = (1-s^L)^2 \,[\,1-(s^L)^{\frac{2+\lambda}{\lambda}}\,] . \tag{3.103}$$

Finally, with the equations of Table 3.2 and the constitutive setting summarised above, the continuum-mechanical problem is closed for the partially saturated case.

3.5.2 Reduction to biphasic material

Regarding a fully saturated porous material, only one single fluid fills the pore space. This fluid is usually a materially incompressible pore liquid. In this case, the liquid saturation s^L reduces to one, and the pressure-difference-saturation condition becomes unnecessary. Moreover, the governing equations simplify, such that the gas balances of mass and momentum vanish. For convenience, the reduced set of governing equations is listed in Table 3.3. For a complete description of the theoretical and numerical treatment of fully saturated porous media combined with the phase-field approach to fracture, the interested reader is referred to Ehlers & Luo [93, 94], Luo [178], Ehlers & Wagner [98] and Appendix C.2.

Table 3.3: *Summary of the reduced set of governing equations in their strong forms of the fully saturated model.*

Solid displacement-velocity relation

$$(\mathbf{u}_S)'_S = \mathbf{v}_S$$

Overall momentum balance

$$\rho^S (\mathbf{v}_S)'_S + \rho^L \big[(\mathbf{v}_L)'_S + (\mathrm{grad}\mathbf{v}_L)\,\mathbf{w}_L \big] = \mathrm{div}\,(\boldsymbol{\sigma}^S_{EF} + \mathbf{T}^L_{NEQ} - p^{LR}\,\mathbf{I}) + \rho\,\mathbf{g}$$

Liquid momentum balance

$$\rho^L \big[(\mathbf{v}_L)'_S + (\mathrm{grad}\mathbf{v}_L)\,\mathbf{w}_L \big] = \mathrm{div}\,\mathbf{T}^L_{NEQ} + \rho^L \mathbf{g} + \hat{\mathbf{p}}^L_{NEQ} - n^L \mathrm{grad}\,p^{LR}$$

Liquid volume balance

$$(n^L)'_S + n^L \mathrm{div}\,(\mathbf{u}_S)'_S + \mathrm{div}\,(n^L\,\mathbf{w}_L) = 0$$

Phase-field evolution equation

$$(\phi^S)'_S = \frac{1}{M}\Big[\, 2(1-\phi^S)\,W^{S+} - G_c\Big(\frac{\phi^S}{\epsilon} - \epsilon\,\mathrm{div}\,\mathrm{grad}\,\phi^S\Big)\Big]$$

Chapter 4:
Numerical Treatment

The governing equations of the closure problem must be fulfilled simultaneously at each point of the considered domain occupied by the mixture body. Solving this system of partial differential equations analytically is not possible for arbitrary problems. Therefore, the domain is discretised in space and time, and the set of equations is solved numerically for the discretised domain. A typical numerical technique in engineering applications is the Finite-Element Method (FEM). Therein, the problem is divided into smaller subdomains called finite elements, and a global system of equations is formed by assembling the equations from all the elements. This system represents the entire problem domain and can be solved numerically to obtain approximate solutions for the unknowns within the domain. A comprehensive overview of this method is given, e. g., in Bathe [19], Braess [54], Zienkiewicz & Taylor [260]. For the solution of multiphasic problems within the FEM framework, Eipper [99], Ellsiepen [100], and Ammann [11] set up the fundamentals for the numerical tool PANDAS. This solver is particularly suitable for treating strongly coupled problems and proceeds from a monolithic solution of the complete system of partial differential equations.

This chapter encompasses the numerical implementation of the triphasic porous media model to fracture within PANDAS. The weak formulations of the governing equations are derived, and the spatial and temporal discretisation are introduced. After that, particular numerical treatments are outlined concerning the fracturing problem such as the implementation of the irreversibility condition and the definition of pre-fractured areas.

4.1 Finite-Element Method

The governing equations of Table 3.2 together with the initial and boundary conditions define the strong form of the initial-boundary-value problem (IBVP). As mentioned in the previous chapter, the set of primary variables used in this monograph consists of the solid velocity $\mathbf{v}_S$ belonging to the overall momentum balance, the liquid and gas velocities, $\mathbf{v}_L$ and $\mathbf{v}_G$, corresponding to the fluid momentum balances of pore liquid and pore gas, the liquid saturation s^L corresponding to the liquid volume balance, the gas pressure p^{GR} corresponding to the gas mass balance, and the phase-field variable ϕ^S corresponding to the phase-field evolution equation. Moreover, the solid displacement $\mathbf{u}_S$ corresponds to the displacement-velocity relation $(\mathbf{u}_S)'_S = \mathbf{v}_S$ in order to reduce the set of partial differential equations from second to first order in time. Summarising the variables in an abstract vector $\boldsymbol{u}$ leads to

$$\boldsymbol{u}(\mathbf{x}, t) = [\mathbf{u}_S \ \mathbf{v}_S \ \mathbf{v}_L \ \mathbf{v}_G \ s^L \ p^{GR} \ \phi^S]^T . \tag{4.1}$$

Remark: This set of primary variables has been chosen based on the specific IBVP computed in Chapter 5 and assures a robust solution scheme. For other IBVP, another combination of primary variables for the liquid volume and gas mass balance might be appropriate, such as p^{LR} and p^{GR}, compare, e. g., Helmig [138]. A detailed discussion on the choice of primary variables for multiphase flow in porous media can be found in Wu & Forsyth [255]. □

To build the particular IBVP, initial conditions for the primary variables need to be specified, i. e.

$$\boldsymbol{u}(\mathbf{x}, t_0) = \boldsymbol{u}_0(\mathbf{x})\,. \tag{4.2}$$

Moreover, the boundaries $\partial\Omega$ of the spatial domain Ω are split into Dirichlet (essential) boundaries $\partial\Omega_D$ and Neumann (natural) boundaries $\partial\Omega_N$. For any arbitrary boundary, either a Dirichlet boundary condition or a Neumann boundary condition has to be defined exclusively for each primary variable in order to have a unique solution of the equation:

$$\begin{aligned}
\partial\Omega_{\mathbf{v}_S} &= \partial\Omega_D^{\mathbf{v}_S} \cup \partial\Omega_N^{\bar{\mathbf{t}}}, & \emptyset &= \partial\Omega_D^{\mathbf{v}_S} \cap \partial\Omega_N^{\bar{\mathbf{t}}},\\
\partial\Omega_{\mathbf{v}_L} &= \partial\Omega_D^{\mathbf{v}_L} \cup \partial\Omega_N^{\bar{\mathbf{t}}^L}, & \emptyset &= \partial\Omega_D^{\mathbf{v}_L} \cap \partial\Omega_N^{\bar{\mathbf{t}}^L},\\
\partial\Omega_{\mathbf{v}_G} &= \partial\Omega_D^{\mathbf{v}_G} \cup \partial\Omega_N^{\bar{\mathbf{t}}^G}, & \emptyset &= \partial\Omega_D^{\mathbf{v}_G} \cap \partial\Omega_N^{\bar{\mathbf{t}}^G},\\
\partial\Omega_{s^L} &= \partial\Omega_D^{s^L} \cup \partial\Omega_N^{\bar{v}^L}, & \emptyset &= \partial\Omega_D^{s^L} \cap \partial\Omega_N^{\bar{v}^L},\\
\partial\Omega_{p^{GR}} &= \partial\Omega_D^{p^{GR}} \cup \partial\Omega_N^{\bar{v}^G}, & \emptyset &= \partial\Omega_D^{p^{GR}} \cap \partial\Omega_N^{\bar{v}^G},\\
\partial\Omega_{\phi^S} &= \partial\Omega_D^{\phi^S} \cup \partial\Omega_N^{\bar{v}^{\phi^S}}, & \emptyset &= \partial\Omega_D^{\phi^S} \cap \partial\Omega_N^{\bar{v}^{\phi^S}}.
\end{aligned} \tag{4.3}$$

Therein, the Dirichlet boundary conditions define the exact value of the primary variable on the boundary, while the Neumann boundary conditions address the flux of the primary variable over the respective boundary. The fluxes $\{\bar{\mathbf{t}},\, \bar{\mathbf{t}}^L,\, \bar{\mathbf{t}}^G,\, \bar{v}^L,\, \bar{v}^G,\, \bar{v}^{\phi^S}\}$ on the Neumann boundaries will be specified in Subsection 4.1.1. Finally, note that no boundary statement for the solid displacement-velocity relation has been listed. Although the solid displacement-velocity relation will be discretised in space to determine the solid displacement, it does not involve a Neumann boundary, see Subsection 4.1.1.

The ansatz (trial) functions of the primary variables (4.2) read

$$\begin{aligned}
\mathcal{A}^{\mathbf{u}_S}(t) &:= \{\ \mathbf{u}_S \in \mathcal{H}^1(\Omega)^d \ :\ \mathbf{u}_S(\mathbf{x}) = \bar{\mathbf{u}}_S(\mathbf{x}, t) \ \text{ on } \partial\Omega_D^{\mathbf{u}_S}\ \},\\
\mathcal{A}^{\mathbf{v}_S}(t) &:= \{\ \mathbf{v}_S \in \mathcal{H}^1(\Omega)^d \ :\ \mathbf{v}_S(\mathbf{x}) = \bar{\mathbf{v}}_S(\mathbf{x}, t) \ \text{ on } \partial\Omega_D^{\mathbf{v}_S}\ \},\\
\mathcal{A}^{\mathbf{v}_L}(t) &:= \{\ \mathbf{v}_L \in \mathcal{H}^1(\Omega)^d \ :\ \mathbf{v}_L(\mathbf{x}) = \bar{\mathbf{v}}_L(\mathbf{x}, t) \ \text{ on } \partial\Omega_D^{\mathbf{v}_L}\ \},\\
\mathcal{A}^{\mathbf{v}_G}(t) &:= \{\ \mathbf{v}_G \in \mathcal{H}^1(\Omega)^d \ :\ \mathbf{v}_G(\mathbf{x}) = \bar{\mathbf{v}}_G(\mathbf{x}, t) \ \text{ on } \partial\Omega_D^{\mathbf{v}_G}\ \},\\
\mathcal{A}^{s^L}(t) &:= \{\ s^L \in \mathcal{H}^1(\Omega) \ :\ s^L(\mathbf{x}) = \bar{s}^L(\mathbf{x}, t) \ \text{ on } \partial\Omega_D^{s^L}\ \},\\
\mathcal{A}^{p^{GR}}(t) &:= \{\ p^{GR} \in \mathcal{H}^1(\Omega) \ :\ p^{GR}(\mathbf{x}) = \bar{p}^{GR}(\mathbf{x}, t) \text{ on } \partial\Omega_D^{p^{GR}}\ \},\\
\mathcal{A}^{\phi^S}(t) &:= \{\ \phi^S \in \mathcal{H}^1(\Omega) \ :\ \phi^S(\mathbf{x}) = \bar{\phi}^S(\mathbf{x}, t) \ \text{ on } \partial\Omega_D^{\phi^S}\ \},
\end{aligned} \tag{4.4}$$

with $d \in \{1,2,3\}$ as the spatial dimension of the problem. The ansatz functions are chosen from the Sobolev space $\mathcal{H}^1(\Omega)^d$ in order to ensure the square-integrability of their first derivative on Ω (cf. Braess [54]). The respective test (weighting) functions are given by

$$\begin{aligned}
\mathcal{T}^{\mathbf{u}_S} &:= \{\ \delta\mathbf{u}_S \in \mathcal{H}^1(\Omega)^d \ :\ \delta\mathbf{u}_S(\mathbf{x}) = \mathbf{0} \text{ on } \partial\Omega_D^{\mathbf{u}_S}\ \}\,,\\
\mathcal{T}^{\mathbf{v}_S} &:= \{\ \delta\mathbf{v}_S \in \mathcal{H}^1(\Omega)^d \ :\ \delta\mathbf{v}_S(\mathbf{x}) = \mathbf{0} \text{ on } \partial\Omega_D^{\mathbf{v}_S}\ \}\,,\\
\mathcal{T}^{\mathbf{v}_L} &:= \{\ \delta\mathbf{v}_L \in \mathcal{H}^1(\Omega)^d \ :\ \delta\mathbf{v}_L(\mathbf{x}) = \mathbf{0} \text{ on } \partial\Omega_D^{\mathbf{v}_L}\ \}\,,\\
\mathcal{T}^{\mathbf{v}_G} &:= \{\ \delta\mathbf{v}_G \in \mathcal{H}^1(\Omega)^d \ :\ \delta\mathbf{v}_G(\mathbf{x}) = \mathbf{0} \text{ on } \partial\Omega_D^{\mathbf{v}_G}\ \}\,,\\
\mathcal{T}^{s^L} &:= \{\ \delta s^L \in \mathcal{H}^1(\Omega) \ :\ \delta s^L(\mathbf{x}) = 0 \text{ on } \partial\Omega_D^{s^L}\ \}\,,\\
\mathcal{T}^{p^{GR}} &:= \{\ \delta p^{GR} \in \mathcal{H}^1(\Omega) \ :\ \delta p^{GR}(\mathbf{x}) = 0 \text{ on } \partial\Omega_D^{p^{GR}}\ \}\,,\\
\mathcal{T}^{\phi^S} &:= \{\ \delta\phi^S \in \mathcal{H}^1(\Omega) \ :\ \delta\phi^S(\mathbf{x}) = 0 \text{ on } \partial\Omega_D^{\phi^S}\ \}\,.
\end{aligned} \tag{4.5}$$

Note that on the Dirichlet boundary, the ansatz functions satisfy the Dirichlet boundary conditions, viz. $\boldsymbol{u}(\mathbf{x},t) = \bar{\boldsymbol{u}}(\mathbf{x},t)$, while the test functions vanish, viz. $\delta\boldsymbol{u}(\mathbf{x}) = \mathbf{0}$.

4.1.1 Governing equations in their weak formulation

Since it is not possible to solve the governing equations at each material point of the domain, the equations are handled in an integral manner and no longer point-wise at each material point. In that sense, the set of local governing equations of Table 3.2 is recast in a weak (global) form $\mathcal{G}_{\boldsymbol{u}}$. Therefore, the governing equations in their strong form are multiplied with the respective test functions $\delta\boldsymbol{u}$ and integrated over the domain Ω.

For example, the solid displacement-velocity relation reads in its weak form:

$$\mathcal{G}_{\mathbf{u}_S}(\boldsymbol{u}, \delta\mathbf{u}_S) \equiv \int_\Omega [\,(\mathbf{u}_S)'_S - \mathbf{v}_S\,] \cdot \delta\mathbf{u}_S = 0\,. \tag{4.6}$$

Moreover, to introduce the (natural) Neumann boundary, particular volume integrals are transformed into surface integrals by applying the Gaussian theorem.

By this, the weak form of the overall momentum balance reads

$$\begin{aligned}
\mathcal{G}_{\mathbf{v}_S}(\boldsymbol{u}, \delta\mathbf{v}_S) \equiv &\int_\Omega \left[\,\rho^S(\mathbf{v}_S)'_S + \rho^L(\mathbf{v}_L)'_S + \rho^G(\mathbf{v}_G)'_S\,\right] \cdot \delta\mathbf{v}_S \,\mathrm{d}v +\\
&+ \int_\Omega \left[\,\rho^L(\operatorname{grad}\mathbf{v}_L)\,\mathbf{w}_L + \rho^G(\operatorname{grad}\mathbf{v}_G)\,\mathbf{w}_G\,\right] \cdot \delta\mathbf{v}_S \,\mathrm{d}v +\\
&+ \int_\Omega \left(\,\boldsymbol{\sigma}^S_{EF} + \mathbf{T}^L_{NEQ} + \mathbf{T}^G_{NEQ} - p^{FR}\,\mathbf{I}\,\right) \cdot \operatorname{grad}\delta\mathbf{v}_S \, dv -\\
&- \int_\Omega \rho\,\mathbf{g} \cdot \delta\mathbf{v}_S \mathrm{d}v - \int_{\partial\Omega^{\bar{\mathbf{t}}}_N} \bar{\mathbf{t}} \cdot \delta\mathbf{v}_S \,\mathrm{d}a = 0\,,
\end{aligned} \tag{4.7}$$

with $\bar{\mathbf{t}} := \left(\boldsymbol{\sigma}^S_{EF} + \mathbf{T}^L_{NEQ} + \mathbf{T}^G_{NEQ} - p^{FR}\,\mathbf{I}\right)\mathbf{n}$ as the stress vector acting on the Neumann boundary $\partial\Omega^{\bar{\mathbf{t}}}_N$ of the overall mixture. Thereby, the applied surface load acts on the overall surface, such that the portion of the load carried by each constituent has not to be specified. In analogy, the weak forms of the liquid and gas momentum balances result in

$$\begin{aligned}
\mathcal{G}_{\mathbf{v}_L}(\boldsymbol{u}, \delta\mathbf{v}_L) \equiv & \int_\Omega \left[\, \rho^L (\mathbf{v}_L)'_S + \rho^L (\mathrm{grad}\mathbf{v}_L)\, \mathbf{w}_L \,\right] \cdot\, \delta\mathbf{v}_L \,\mathrm{d}v + \\
& + \int_\Omega \left(\, \mathbf{T}^L_{NEQ} - n^L p^{LR}\,\mathbf{I}\,\right) \cdot\, \mathrm{grad}\delta\mathbf{v}_L \,\mathrm{d}v - \\
& - \int_\Omega \left(p^{LR}\mathrm{grad}\, n^L + \rho^L\, \mathbf{g} + \hat{\mathbf{p}}^L_{NEQ} + p^D n^F \mathrm{grad} s^L\right) \cdot\, \delta\mathbf{v}_L \,\mathrm{d}v - \\
& - \int_{\partial\Omega^{\bar{\mathbf{t}}L}_N} \bar{\mathbf{t}}^L \,\cdot\, \delta\mathbf{v}_L \,\mathrm{d}a = 0\,,
\end{aligned} \tag{4.8}$$

$$\begin{aligned}
\mathcal{G}_{\mathbf{v}_G}(\boldsymbol{u}, \delta\mathbf{v}_G) \equiv & \int_\Omega \left[\, \rho^G (\mathbf{v}_G)'_S + \rho^G (\mathrm{grad}\,\mathbf{v}_G)\mathbf{w}_G \,\right] \cdot\, \delta\mathbf{v}_G \,\mathrm{d}v \,+ \\
& + \int_\Omega \left(\, \mathbf{T}^G_{NEQ} - \, n^G p^{GR}\,\mathbf{I}\,\right) \cdot\, \mathrm{grad}\,\delta\mathbf{v}_G \,\mathrm{d}v - \\
& - \int_\Omega \left(p^{GR}\mathrm{grad}\, n^G + \rho^G\, \mathbf{g} + \hat{\mathbf{p}}^G_{NEQ}\,\right) \cdot\, \delta\mathbf{v}_G \,\mathrm{d}v - \\
& - \int_{\partial\Omega^{\bar{\mathbf{t}}G}_N} \bar{\mathbf{t}}^G \,\cdot\, \delta\mathbf{v}_G \,\mathrm{d}a = 0\,,
\end{aligned} \tag{4.9}$$

with $\bar{\mathbf{t}}^L = \left(\mathbf{T}^L_{NEQ} - n^L p^{LR}\,\mathbf{I}\right)\mathbf{n}$ and $\bar{\mathbf{t}}^G = \left(\mathbf{T}^G_{NEQ} - n^G p^{GR}\,\mathbf{I}\right)\mathbf{n}$ the external forces of the liquid and gas, respectively. Note that $\mathbf{T}^\beta_{NEQ}$ included in $\bar{\mathbf{t}}^\beta$ usually vanishes and only comes into play when the pore fluids are connected to an external shear flow. The weak formulation of the liquid volume balance and the gas mass balance read

$$\begin{aligned}
\mathcal{G}_{s^L}(\boldsymbol{u}, \delta s^L) \equiv & \int_\Omega \left\{\, \left[\, (n^L)'_S + n^L \mathrm{div}\,\mathbf{v}_S \right] \delta s^L - n^L \mathbf{w}_L \cdot \mathrm{grad}\delta s^L \,\right\} \mathrm{d}v + \\
& + \int_{\partial\Omega^{\bar{v}L}_N} \bar{v}^L \delta s^L \,\mathrm{d}a = 0\,,
\end{aligned} \tag{4.10}$$

$$\begin{aligned}
\mathcal{G}_{p^{GR}}(\boldsymbol{u}, \delta p^{GR}) \equiv & \int_\Omega \left[\, \rho^{GR} (n^G)'_S + n^G (\rho^{GR})'_S + n^G \rho^{GR} \mathrm{div}\,(\mathbf{u}_S)'_S \right] \delta p^{GR} \,\mathrm{d}v - \\
& - \int_\Omega n^G \rho^{GR} \mathbf{w}_G \cdot \mathrm{grad}\delta p^{GR} \,\mathrm{d}v + \int_{\partial\Omega^{\bar{v}G}_N} \rho^{GR}\, \bar{v}^G\, \delta p^{GR} \,\mathrm{d}a = 0\,.
\end{aligned} \tag{4.11}$$

Therein, $\bar{v}^L = n^L \mathbf{w}_L \cdot \mathbf{n}$ and $\bar{v}^G = n^G \mathbf{w}_G \cdot \mathbf{n}$ denote the fluid volume effluxes over the Neumann boundaries $\partial\Omega_N^{\bar{v}^L}$ and $\partial\Omega_N^{\bar{v}^G}$, respectively.

Combining the weak formulations of the fluid momentum balances, (4.8) and (4.9), with the volume and mass balances, (4.10) and (4.11), respectively, may lead to numerical problems when modelling an injection process. The reason is that impermeability for the liquid and gas flow requires $\bar{v}_L = 0$ and $\bar{v}_G = 0$ for the liquid volume balance (4.10) and the gas mass balance (4.11), the former with an exception at the liquid injection point. At the same time, the momentum balances of liquid and gas require a no-flow condition in the form of $\mathbf{n} \cdot \delta\mathbf{v}_\beta = 0$ at these edges with the exception at the notch, where the liquid pressure p^{LR} has to be applied in such a way that it physically fits the flow resistance of the liquid volume injection $\bar{v}^L$ included in the surface term of (4.10). As the liquid and gas pressures are coupled through the pressure difference p^D after (3.47) and the pore pressure p^{FR} after (3.48), the liquid boundary-pressure term $\bar{p}^{LR}$ has to fulfil the condition $\bar{p}^{LR} = p^{LR}$ with p^{LR} as a function of the primary variables $\mathbf{u}_S$ through $\mathbf{v}_S$, s^L and p^{GR} obtained from the internal solution of the problem. Problems like this can only be solved successfully using a weakly imposed implicit boundary condition, compare, for example, Ehlers & Acartürk [89] and citations therein. This procedure, however, causes a lot of computational effort and should therefore be avoided.

Instead of using an implicit boundary condition, the pressure terms p^{LR} and p^{GR} included in (4.8) and (4.9) are taken back from the surface integral and re-integrated into the volume integrals. This results in a rearranged liquid momentum balance:

$$\begin{aligned}\mathcal{G}_{\mathbf{v}_L}(\boldsymbol{u}, \delta\mathbf{v}_L) \equiv & \int_\Omega [\, \rho^L (\mathbf{v}_L)'_S + \rho^L (\operatorname{grad}\mathbf{v}_L)\, \mathbf{w}_L \,] \cdot \delta\mathbf{v}_L \, \mathrm{d}v + \int_\Omega \mathbf{T}^L_{NEQ} \cdot \operatorname{grad}\delta\mathbf{v}_L \, \mathrm{d}v + \\ & + \int_\Omega n^L \operatorname{grad} p^{LR} \cdot \delta\mathbf{v}_L \, \mathrm{d}v - \int_\Omega (\rho^L \, \mathbf{g} + \hat{\mathbf{p}}^L_{NEQ} + p^D n^F \operatorname{grad} s^L) \cdot \delta\mathbf{v}_L \, \mathrm{d}v - \\ & - \int_{\partial\Omega_N^{\bar{\mathbf{t}}^L}} \bar{\mathbf{t}}^L \cdot \delta\mathbf{v}_L \, \mathrm{d}a = 0 \,, \qquad \text{with} \quad \bar{\mathbf{t}}^L = \mathbf{T}^L_{NEQ}\, \mathbf{n} \,,\end{aligned} \tag{4.12}$$

and a rearranged gas momentum balance:

$$\begin{aligned}\mathcal{G}_{\mathbf{v}_G}(\boldsymbol{u}, \delta\mathbf{v}_G) \equiv & \int_\Omega [\, \rho^G (\mathbf{v}_G)'_S + \rho^G (\operatorname{grad}\mathbf{v}_G) \mathbf{w}_G \,] \cdot \delta\mathbf{v}_G \, \mathrm{d}v + \int_\Omega \mathbf{T}^G_{NEQ} \cdot \operatorname{grad}\delta\mathbf{v}_G \, \mathrm{d}v + \\ & + \int_\Omega n^G \operatorname{grad} p^{GR} \cdot \delta\mathbf{v}_G \, \mathrm{d}v - \int_\Omega (\rho^G \, \mathbf{g} + \hat{\mathbf{p}}^G_{NEQ}\,) \cdot \delta\mathbf{v}_G \, \mathrm{d}v - \\ & - \int_{\partial\Omega_N^{\bar{\mathbf{t}}^G}} \bar{\mathbf{t}}^G \cdot \delta\mathbf{v}_G \, \mathrm{d}a = 0 \,, \qquad \text{with} \quad \bar{\mathbf{t}}^G = \mathbf{T}^G_{NEQ}\, \mathbf{n} \,,\end{aligned} \tag{4.13}$$

thus substituting the momentum balances (4.8) and (4.9).

This procedure might be unconventional, but it works, as the equations are simply rearranged. This can be seen from a proof of concept included in the Appendix C.1, where a consolidation problem of a triphasic medium of solid, liquid and gas is computed by use of (4.7)-(4.14) and by substituting (4.8) and (4.9) through the above-rearranged equations (4.12) and (4.13), respectively. As the set of equations is highly coupled, the pressure boundary condition is not lost but is still active through the pore pressure p^{FR} included in the surface integral of the overall momentum balance (4.7). As p^{FR} also depends on the unknown boundary term $p^{LR} = \bar{p}^{LR}$, the solution profits from the fact that a Dirichlet boundary condition can be used by setting the test function $\mathbf{n} \cdot \delta\mathbf{v}_S$ normal to the boundary to zero, such that p^{FR} can freely attune.

Finally, the weak formulation of the phase-field evolution equation results in

$$\begin{aligned} \mathcal{G}_{\phi^S}(\boldsymbol{u}, \delta\phi^S) \equiv & \int_\Omega [\, M(\phi^S)'_S - 2(1-\phi^S)W^{S+} + \frac{G_c}{\epsilon}\phi^S \,]\, \delta\phi^S \,\mathrm{d}v + \\ & + \int_\Omega G_c\, \epsilon\, \mathrm{grad}\, \phi^S \cdot \mathrm{grad}\, \delta\phi^S \,\mathrm{d}v - \\ & - \int_{\partial\Omega_N^{\bar{v}^{\phi^S}}} \bar{v}^{\phi^S}\, \delta\phi^S \mathrm{d}a = 0\,, \quad \text{with} \quad \bar{v}^{\phi^S} = G_c\, \epsilon\, \mathrm{grad}\, \phi^S \cdot \mathbf{n}\,. \end{aligned} \tag{4.14}$$

Note that in order to satisfy the condition (3.73) resulting from the entropy equality, i. e. $\mathrm{grad}\, \phi^S \cdot \mathbf{n} = 0$, the phase-field variable efflux $\bar{v}^{\phi^S}$ has to vanishes on all boundaries $\Omega_N^{\bar{v}^{\phi^S}}$.

For completeness, the numerical treatment for fracturing fully saturated porous media is given in Luo [178] and summarised in Appendix C.2.

Finally, the problem to solve can be formulated by

$$\text{Find} \quad \boldsymbol{u} \in \mathcal{A}^{\boldsymbol{u}}(t) \quad \text{such that} \quad \boldsymbol{\mathcal{G}}_{\boldsymbol{u}}(\boldsymbol{u}, \delta\boldsymbol{u}) = \mathbf{0} \quad \forall\, \delta\boldsymbol{u} \in \mathcal{T}^{\boldsymbol{u}}\,, \quad t \in [t_0, T]\,. \tag{4.15}$$

In order to solve this problem numerically for any time t, the domain is discretised in space and time in the following.

4.1.2 Discretisation in space

In the framework of the FEM, the continuous domain Ω of the overall body $\mathcal{B}$ is discretised into the domain Ω^h with E non-overlapping finite elements Ω_e:

$$\Omega \approx \Omega^h = \bigcup_{e=1}^{E} \Omega_e\,, \tag{4.16}$$

compare also Figure 4.1. Each finite element is formed with connected nodal points P^j, denoted as nodes. Thereby, adjacent elements share the same nodes and connections. The entire set of N nodes and their connections forms the finite-element mesh.

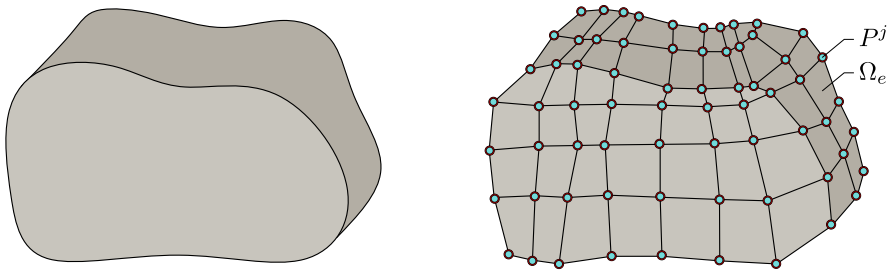

continuous domain Ω approximated domain Ω^h

Figure 4.1: *Sketch of the spatial discretisation of a continuous domain* Ω.

Also, the weak formulations (4.7)-(4.14) have to be discretised in space. Therefore, the primary variables $\boldsymbol{u}$ are approximated with the discrete ansatz (approximation) functions $\boldsymbol{u}^h$ as follows

$$
\begin{aligned}
\mathbf{u}_S(\mathbf{x},t) &\approx \mathbf{u}_S^h(\mathbf{x},t) = \bar{\mathbf{u}}_S^h(\mathbf{x},t) + \sum_{j=1}^{N} \mathbf{Q}^j_{\mathbf{u}_S}(\mathbf{x})\,\mathbf{u}_S^j(t) &&\in \mathcal{A}^{\mathbf{u}_S\,h}(t)\,,\\
\mathbf{v}_S(\mathbf{x},t) &\approx \mathbf{v}_S^h(\mathbf{x},t) = \bar{\mathbf{v}}_S^h(\mathbf{x},t) + \sum_{j=1}^{N} \mathbf{Q}^j_{\mathbf{v}_S}(\mathbf{x})\,\mathbf{v}_S^j(t) &&\in \mathcal{A}^{\mathbf{v}_S\,h}(t)\,,\\
\mathbf{v}_L(\mathbf{x},t) &\approx \mathbf{v}_L^h(\mathbf{x},t) = \bar{\mathbf{v}}_L^h(\mathbf{x},t) + \sum_{j=1}^{N} \mathbf{Q}^j_{\mathbf{v}_L}(\mathbf{x})\,\mathbf{v}_L^j(t) &&\in \mathcal{A}^{\mathbf{v}_L\,h}(t)\,,\\
\mathbf{v}_G(\mathbf{x},t) &\approx \mathbf{v}_G^h(\mathbf{x},t) = \bar{\mathbf{v}}_G^h(\mathbf{x},t) + \sum_{j=1}^{N} \mathbf{Q}^j_{\mathbf{v}_G}(\mathbf{x})\,\mathbf{v}_G^j(t) &&\in \mathcal{A}^{\mathbf{v}_G\,h}(t)\,,\\
s^L(\mathbf{x},t) &\approx s^{L\,h}(\mathbf{x},t) = \bar{s}^{L\,h}(\mathbf{x},t) + \sum_{j=1}^{N} Q^j_{s^L}(\mathbf{x})\,s^{L\,j}(t) &&\in \mathcal{A}^{s^L\,h}(t)\,,\\
p^{GR}(\mathbf{x},t) &\approx p^{GR\,h}(\mathbf{x},t) = \bar{p}^{GR\,h}(\mathbf{x},t) + \sum_{j=1}^{N} Q^j_{p^{GR}}(\mathbf{x})\,p^{GR\,j}(t) &&\in \mathcal{A}^{p^{GR}\,h}(t)\,,\\
\phi^S(\mathbf{x},t) &\approx \phi^{S\,h}(\mathbf{x},t) = \bar{\phi}^{S\,h}(\mathbf{x},t) + \sum_{j=1}^{N} Q^j_{\phi^S}(\mathbf{x})\,\phi^{S\,j}(t) &&\in \mathcal{A}^{\phi^S\,h}(t)\,.
\end{aligned}
\tag{4.17}
$$

Therein, $\{\mathbf{u}_S^j\,,\mathbf{v}_S^j\,,\mathbf{v}_G^j\,,\mathbf{v}_G^j\,,s^{L\,j},\,p^{GR\,j},\,\phi^{S\,j}\}$ are the unknown nodal quantities at the finite-element node P^j, also termed degrees of freedom (DOF) of the system, and N is the total number of nodes. Moreover, $\{\mathbf{Q}^j_{\mathbf{u}_S}\,,\mathbf{Q}^j_{\mathbf{v}_S}\,,\mathbf{Q}^j_{\mathbf{v}_L}\,,\mathbf{Q}^j_{\mathbf{v}_G}\,,Q^j_{s^L}\,,Q^j_{p^{GR}}\,,Q^j_{\phi^S}\}$ are the global basis functions. Note that the basis functions of the displacement and velocities are vectorial quantities, i. e. $\mathbf{Q}^j_{\mathbf{u}_S} = [Q^j_{\mathbf{u}_{S1}}\,,\ldots\,,Q^j_{\mathbf{u}_{Sd}}]^T$ and $\mathbf{Q}^j_{\mathbf{v}_\alpha} = [Q^j_{\mathbf{v}_{\alpha 1}}\,,\ldots\,,Q^j_{\mathbf{v}_{\alpha d}}]^T$, respectively. Note furthermore that the discrete ansatz functions satisfy the discrete Dirichlet boundary conditions $\{\bar{\mathbf{u}}_S^h\,,\bar{\mathbf{v}}_S^h\,,\bar{\mathbf{v}}_G^h\,,\bar{\mathbf{v}}_G^h\,,\bar{s}^{L\,h},\,\bar{p}^{GR\,h},\,\bar{\phi}^{S\,h}\}$.

The corresponding test functions read

$$\begin{aligned}
\delta\mathbf{u}_S(\mathbf{x}) &\approx \delta\mathbf{u}_S^h(\mathbf{x}) = \sum_{j=1}^{N} \mathbf{Q}^j_{\mathbf{u}_S}(\mathbf{x})\,\delta\mathbf{u}_S^j \in \mathcal{T}^{\mathbf{u}_S\,h}\,,\\
\delta\mathbf{v}_S(\mathbf{x}) &\approx \delta\mathbf{v}_S^h(\mathbf{x}) = \sum_{j=1}^{N} \mathbf{Q}^j_{\mathbf{v}_S}(\mathbf{x})\,\delta\mathbf{v}_S^j \in \mathcal{T}^{\mathbf{v}_S\,h}\,,\\
\delta\mathbf{v}_L(\mathbf{x}) &\approx \delta\mathbf{v}_L^h(\mathbf{x}) = \sum_{j=1}^{N} \mathbf{Q}^j_{\mathbf{v}_L}(\mathbf{x})\,\delta\mathbf{v}_L^j \in \mathcal{T}^{\mathbf{v}_L\,h}\,,\\
\delta\mathbf{v}_G(\mathbf{x}) &\approx \delta\mathbf{v}_G^h(\mathbf{x}) = \sum_{j=1}^{N} \mathbf{Q}^j_{\mathbf{v}_G}(\mathbf{x})\,\delta\mathbf{v}_G^j \in \mathcal{T}^{\mathbf{v}_G\,h}\,,\\
\delta s^L(\mathbf{x}) &\approx \delta s^{L\,h}(\mathbf{x}) = \sum_{j=1}^{N} Q^j_{s^L}(\mathbf{x})\,\delta s^{L\,j} \in \mathcal{T}^{s^L\,h}\,,\\
\delta p^{GR}(\mathbf{x}) &\approx \delta p^{GR\,h}(\mathbf{x}) = \sum_{j=1}^{N} Q^j_{p^{GR}}(\mathbf{x})\,\delta p^{GR\,j} \in \mathcal{T}^{p^{GR}\,h}\,,\\
\delta\phi^S(\mathbf{x}) &\approx \delta\phi^{S\,h}(\mathbf{x}) = \sum_{j=1}^{N} Q^j_{\phi^S}(\mathbf{x})\,\delta\phi^{S\,j} \in \mathcal{T}^{\phi^S\,h}
\end{aligned} \tag{4.18}$$

with $\delta\boldsymbol{u}^h$ as the discretised test functions. Here, following the Bubnov-Galerkin method, the same basis functions $\{\mathbf{Q}^j_{\mathbf{u}_S}, \mathbf{Q}^j_{\mathbf{v}_S}, \mathbf{Q}^j_{\mathbf{v}_L}, \mathbf{Q}^j_{\mathbf{v}_G}, Q^j_{s^L}, Q^j_{p^{GR}}, Q^j_{\phi^S}\}$ are applied both to the ansatz and test functions. Besides this, it is also possible to define different basis functions for the ansatz and test spaces. This more general approach called the Petrov-Galerkin method is relevant, e. g., in the context of numerical stabilisation techniques, compare also Ehlers *et al.* [91].

Remark: As stated in (4.17), the basis functions only depend on the position $\mathbf{x}$ while the degrees of freedom only depend on the time t. Therefore, the DOF can be mapped by the basis functions at any position inside the discrete domain, allowing the evaluation of physical quantities besides the nodes P^j. A detailed view on the basis functions can be found in Ellsiepen [100], Ammann [11] and Rempler [210], among others. □

In addition, the test functions $\delta\boldsymbol{u}^h$ have to satisfy the concept of Partition-of-Unity, stating that the basis functions sum up to one for every point $\mathbf{x} \in \Omega^h$ and vanish at all other nodes.

Thus, the space-discrete system to solve can be formulated as

$$\text{Find} \quad \boldsymbol{u}^h \in \mathcal{A}^{\boldsymbol{u}\,h}(t) \quad \text{such that} \quad \boldsymbol{\mathcal{G}}^h_{\boldsymbol{u}}(\boldsymbol{u}^h, \delta\boldsymbol{u}^h) = \mathbf{0} \quad \forall\, \delta\boldsymbol{u}^h \in \mathcal{T}^{\boldsymbol{u}\,h}\,, \quad t \in [t_0, T]\,, \tag{4.19}$$

for a given set of Neumann boundary conditions at any time t. In order to account for the strong coupling of the system, see Section 3.5, the spatially discretised problem (4.19) is solved monolithically within PANDAS. Therefore, all DOF are approximated simultaneously.

Finding suitable ansatz functions is one of the difficulties within such a mixed finite-element formulation. From a mathematical point of view, the set of ansatz functions has to fulfil the inf-sup condition (also called Ladyshenskaya-Babuška-Brezzi (LBB) condition) or the patch test to ensure a stable solution, compare, e. g., Zienkiewicz *et al.* [259], Brezzi & Fortin [55] and Hughes [146]. A more mechanical approach considers the overall momentum balance (cf. Table 3.2). There, the partial stresses and the pore pressure constitute the overall stress from which the divergence has to be computed. As the partial stresses $\boldsymbol{\sigma}^S_{EF}$, $\mathbf{T}^L_{NEQ}$, $\mathbf{T}^G_{NEQ}$ are obtained from the gradient of the solid displacement $\mathbf{u}_S$ and the gradients of the fluid velocities $\mathbf{v}_L$ and $\mathbf{v}_G$, respectively, their approximations need to be one order higher than the pore pressure p^{FR}, which is linearly determined by the saturation s^L and the gas pressure p^{GR}. Thus, quadratic shape functions are chosen for the solid displacement and the constituent's velocities, and linear ones for the saturation, the gas pressure and the phase-field variable. This choice of quadratic and linear shape functions yields the usage of an element type denoted as an extended Taylor-Hood element from the serendipity family of quadrilateral elements, depicted in Figure 4.2. The original Taylor-Hood element was introduced in the work of Taylor & Hood [234] and Hood & Taylor [143]. Note that original Taylor-Hood elements fulfil the inf-sup condition and lead to numerical stability and accuracy, compare the work of Bercovier & Pironneau [27] and Brezzi & Fortin [55] for a mathematical proof for the original 2-d and Stenberg [233] for the 3-d element.

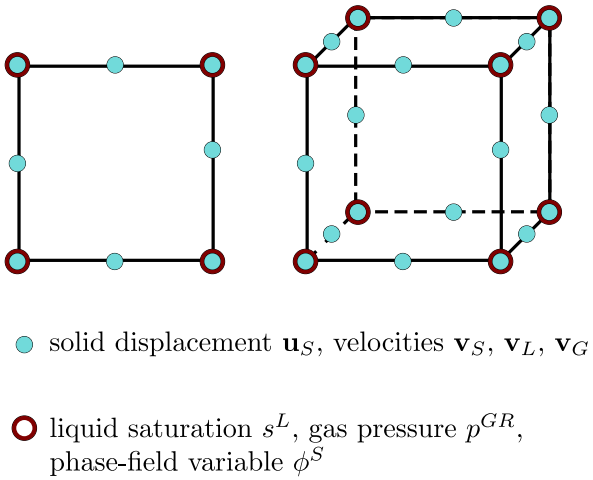

Figure 4.2: *Extended plane (2-d) and hexahedral (3-d) Taylor-Hood elements.*

Moreover, the numerical integration of the weak balance equations is carried out locally at a reference element. The results are then mapped from the local coordinates of the reference element to the global (physical) coordinates with the Gauss quadrature method. Thereby, an isoparametric concept is applied, where the basis functions correspond to the geometry functions. The interested reader in the geometry transformation between the reference and global elements and in the numerical integration is referred, e. g., to the work of Hughes [146] and Mardal & Langtangen [183].

Finally, to enable a compact formulation of the coupled problem, the nodal unknowns of

each primary variable are brought together in abstract vectors, viz.

$$\begin{aligned}
\mathbf{u}_S &:= [\mathbf{u}_S^1 \dots \mathbf{u}_S^N]^T , \\
\mathbf{v}_S &:= [\mathbf{v}_S^1 \dots \mathbf{v}_S^N]^T , \\
\mathbf{v}_L &:= [\mathbf{v}_L^1 \dots \mathbf{v}_L^N]^T , \\
\mathbf{v}_G &:= [\mathbf{v}_G^1 \dots \mathbf{v}_G^N]^T , \\
\mathbf{s}^L &:= [s^{L\,1} \dots s^{L\,N}]^T , \\
\mathbf{p}^{GR} &:= [p^{GR\,1} \dots p^{GR\,N}]^T , \\
\boldsymbol{\phi}^S &:= [\phi^{S\,1} \dots \phi^{S\,N}]^T ,
\end{aligned} \tag{4.20}$$

and then collected in a global vector of unknowns $\boldsymbol{y} \in \mathbb{R}^{\mathrm{DOF}}$, with DOF the total number of degrees of freedom:

$$\boldsymbol{y} := [\mathbf{u}_S \, \mathbf{v}_S \, \mathbf{v}_L \, \mathbf{v}_G \, \mathbf{s}^L \, \mathbf{p}^{GR} \, \boldsymbol{\phi}^S]^T . \tag{4.21}$$

Moreover, the material time derivative of the vector of unknowns with respect to the solid skeleton is expressed for convenience through $(\boldsymbol{y})'_S = \dot{\boldsymbol{y}}$. This leads to the compact formulation of the space-discrete system of coupled equations:

$$\boldsymbol{\mathcal{F}}(t, \boldsymbol{y}, \dot{\boldsymbol{y}}) \equiv \boldsymbol{\mathcal{G}}_{\boldsymbol{u}}^h(t, \boldsymbol{y}, \dot{\boldsymbol{y}}) \equiv \boldsymbol{\mathcal{D}}\dot{\boldsymbol{y}} + \boldsymbol{\mathcal{K}}\boldsymbol{y} - \boldsymbol{f} \stackrel{!}{=} \boldsymbol{0} , \tag{4.22}$$

with $\boldsymbol{f}$ as the general external load vector. The global damping and stiffness matrices, $\boldsymbol{\mathcal{D}}$ and $\boldsymbol{\mathcal{K}}$, respectively, are defined as follows

$$\begin{aligned}
\boldsymbol{\mathcal{G}}_{\boldsymbol{u}}^h = & \underbrace{\begin{bmatrix}
\boldsymbol{I} & 0 & 0 & 0 & 0 & 0 & 0 \\
0 & \boldsymbol{D}_{22} & \boldsymbol{D}_{23} & \boldsymbol{D}_{24} & 0 & 0 & 0 \\
0 & 0 & \boldsymbol{D}_{33} & 0 & 0 & 0 & 0 \\
0 & 0 & 0 & \boldsymbol{D}_{44} & 0 & 0 & 0 \\
0 & 0 & 0 & 0 & \boldsymbol{D}_{55} & 0 & 0 \\
0 & 0 & 0 & 0 & \boldsymbol{D}_{65} & \boldsymbol{D}_{66} & 0 \\
0 & 0 & 0 & 0 & 0 & 0 & \boldsymbol{D}_{77}
\end{bmatrix}}_{\boldsymbol{\mathcal{D}}} \dot{\boldsymbol{y}} + \\
& + \underbrace{\begin{bmatrix}
0 & -\mathbf{I} & 0 & 0 & 0 & 0 & 0 \\
\boldsymbol{K}_{21} & \boldsymbol{K}_{22} & \boldsymbol{K}_{23} & \boldsymbol{K}_{24} & \boldsymbol{K}_{25} & \boldsymbol{K}_{26} & \boldsymbol{K}_{27} \\
0 & \boldsymbol{K}_{32} & \boldsymbol{K}_{33} & 0 & \boldsymbol{K}_{35} & \boldsymbol{K}_{36} & \boldsymbol{K}_{37} \\
0 & \boldsymbol{K}_{42} & 0 & \boldsymbol{K}_{44} & \boldsymbol{K}_{45} & \boldsymbol{K}_{46} & \boldsymbol{K}_{47} \\
\boldsymbol{K}_{51} & \boldsymbol{K}_{52} & \boldsymbol{K}_{53} & 0 & \boldsymbol{K}_{55} & 0 & 0 \\
0 & \boldsymbol{K}_{62} & 0 & \boldsymbol{K}_{64} & \boldsymbol{K}_{65} & \boldsymbol{K}_{66} & 0 \\
0 & 0 & 0 & 0 & 0 & 0 & \boldsymbol{K}_{77}
\end{bmatrix}}_{\boldsymbol{\mathcal{K}}} \boldsymbol{y} = \boldsymbol{f} .
\end{aligned} \tag{4.23}$$

Note that the individual matrices $\boldsymbol{D}_{ij}$ and $\boldsymbol{K}_{ij}$ can contain coupling terms, non-coupled terms, and zeros.

4.2 Discretisation in time

The space-discrete system (4.23) is still time-continuous and needs to be discretised in time for the numerical solution. Therefore, time-discretisation schemes discretise the time domain into a sequence of time steps, and the solution is approximated at each time step. In this monograph, the time-discretisation method will only be briefly introduced. For more details on time-discretisation methods used in the context of coupled systems, the work of Ehlers & Ellsiepen [90], Diebels *et al.* [75] and Ellsiepen [100] are recommended.

Here, a finite difference scheme is applied to approximate the time. Thereby, the numerical solution only depends on the previous time step, i. e. the current time step is defined as $\Delta t_n = t_n - t_{n-1} > 0$, with t_n the current time and t_{n-1} the time of the previous time step. By considering the solid displacement-velocity relation (4.6), the inertia terms of the momentum balances are computed via the derivative of the respective velocity. Therewith, the system (4.23) is of first order in time. Hence, the implicit (backward) Euler method can be applied from the implicit Runge-Kutta (IRK) time-stepping algorithms available in PANDAS. This algorithm is unconditionally stable and can handle stiff equations and large time steps without numerical instability. However, computationally expensive efforts are taken into account compared to explicit methods. Note that a semi-explicit-implicit splitting scheme is also possible in PANDAS, compare, e. g., Markert *et al.* [187] and Heider [133].

Within the implicit Euler method, the temporal change of the solution vector, namely $\dot{\boldsymbol{y}}_n$, at the current time t_n reads

$$\dot{\boldsymbol{y}}_n = \frac{\boldsymbol{y}_n - \boldsymbol{y}_{n-1}}{\Delta t_n} = \frac{\Delta \boldsymbol{y}_n}{\Delta t_n} \quad \text{with} \quad \boldsymbol{y}_n = \boldsymbol{y}_{n-1} + \Delta \boldsymbol{y}_n \,. \tag{4.24}$$

Therein, the Taylor series expansion is truncated after the linear terms. The differential-algebraic equation system (4.22) can then be evaluated at the current time t_n by

$$\boldsymbol{\mathcal{F}}_n(t, \boldsymbol{y}_n, \dot{\boldsymbol{y}}_n(\boldsymbol{y}_n)) =: \boldsymbol{R}_n \stackrel{!}{=} \boldsymbol{0} \,, \tag{4.25}$$

introducing the nonlinear functional $\boldsymbol{R}_n$. This latter is solved iteratively by applying the Newton-Raphson method. In this sense, the residual tangent (Jacobian matrix) is required. For the problem under study, it is not possible to use a numerical tangent since it leads to unstable solutions. Therefore, the tangent at the current Newton iteration step k is defined analytically via

$$\boldsymbol{J}_n^k = \frac{\mathrm{d}\boldsymbol{R}_n^k}{\mathrm{d}\Delta \boldsymbol{y}_n^k} = \frac{1}{\Delta t_n^k} \frac{\partial \boldsymbol{\mathcal{F}}_n^k}{\partial \dot{\boldsymbol{y}}_n^k}\bigg|_{\boldsymbol{z}} + \frac{\partial \boldsymbol{\mathcal{F}}_n^k}{\partial \boldsymbol{y}_n^k}\bigg|_{\boldsymbol{z}} \,, \tag{4.26}$$

with $\boldsymbol{z} = (t_n^k,\ \boldsymbol{y}_n^k,\ \dot{\boldsymbol{y}}_n^k)$ as the current set of arguments. Therein, $\boldsymbol{\mathcal{D}}_n^k = \partial \boldsymbol{\mathcal{F}}_n^k / \partial \dot{\boldsymbol{y}}_n^k$ represents the damping matrix and $\boldsymbol{\mathcal{K}}_n^k = \partial \boldsymbol{\mathcal{F}}_n^k / \partial \boldsymbol{y}_n^k$ the stiffness matrix after analytical linearisation, respectively. After updating the solution vector $\boldsymbol{y}_n^{k+1} = \boldsymbol{y}_n^k + \Delta \boldsymbol{y}_n^k$, the procedure is iterated via the next Newton step until the norm of the residual is below a predefined tolerance, i. e. $\left\| \boldsymbol{R}_n^{k+1} \right\| < \varepsilon_{\mathrm{tol.}}$.

For the numerical solution procedure, the generalised minimal residual method (GMRES) of Saad & Schultz [213] with an incomplete LU preconditioner is applied in PANDAS. If no convergence can be achieved, time adaptivity starts, and the time-step control reduces the step size. For more details on the time adaptivity scheme in PANDAS, the interested reader is referred to Ellsiepen [100].

4.3 Solid fracturing process

For the consideration of solid fracturing, supplementary numerical treatments are necessary. In what follows, the procedure to ensure the irreversibility of the fracturing process and the implementation of initial cracks is outlined.

4.3.1 Irreversibility of the fracturing process

Since the solid skeleton involved in fracking cannot self-heal, the fracturing process is irreversible. In order to capture this characteristic, the fracture evolution must always be positive or zero, such that

$$(\phi^S)'_S \;=\; \max\left\{ \frac{1}{M}\left[2(1-\phi^S)\, W^{S+} - G_c\big(\frac{\phi^S}{\epsilon} - \epsilon\, \mathrm{div}\, \mathrm{grad}\, \phi^S\big)\right] , \, 0 \right\} \geq 0\,. \tag{4.27}$$

Therefore, Miehe *et al.* [190] introduced a local history field $\mathcal{H}$ of the maximum stored tensile energy W^{S+} for the numerical implementation, viz.

$$\mathcal{H} = \max_{t \geq t_0} W^{S+}\,. \tag{4.28}$$

In the numerical treatment, the history variable for the current time step t_n is defined through

$$\mathcal{H} := \mathcal{H}(\mathbf{x}, t_n) = \begin{cases} W^{S+}(\boldsymbol{\varepsilon}_S^+) & \text{for } W^{S+}(\boldsymbol{\varepsilon}_S^+) > \mathcal{H}_{n-1} \\ \mathcal{H}_{n-1} & \text{otherwise}\,, \end{cases} \tag{4.29}$$

with $\mathcal{H}_{n-1}$ the history variable at the previous time step. Thereby, $\mathcal{H}$ comprises the maximum tensile strain attained in the deformation history and is responsible for crack propagation. A detailed description of the implementation scheme for a staggered solution for a purely solid phase-field fracture with a history field can be found, e. g., in Miehe *et al.* [190] and Hofacker [140].

Finally, the evolution equation (3.72) is rewritten as

$$(\phi^S)'_S = \frac{1}{M}\Big[2(1-\phi^S)\mathcal{H} - G_c\Big(\frac{\phi^S}{\epsilon} - \epsilon\, \mathrm{div}\, \mathrm{grad}\, \phi^S\Big)\Big]\,, \tag{4.30}$$

leading to the weak form

$$\begin{aligned} \mathcal{G}_{\phi^S}(\boldsymbol{u}, \delta\phi^S) \equiv & \int_\Omega \big[\, M(\phi^S)'_S - 2(1-\phi^S)\mathcal{H} + \frac{G_c}{\epsilon}\phi^S \,\big]\, \delta\phi^S \,\mathrm{d}v + \\ & + \int_\Omega G_c\, \epsilon\, \mathrm{grad}\, \phi^S \cdot \mathrm{grad}\, \delta\phi^S \,\mathrm{d}v - \int_{\Omega_N^{\bar{v}^{\phi^S}}} \bar{v}^{\phi^S}\, \delta\phi^S \mathrm{d}a = 0\,. \end{aligned} \tag{4.31}$$

4.3.2 Defining pre-fractured areas

There are two possibilities to define pre-fractured areas in a numerical setting. On the one hand, they can be included by modelling a discrete crack in the mesh geometry. On the other hand, for the phase-field model to fracture, an initial crack can be defined by exploiting the term in brackets of (4.30), also compare Borden *et al.* [46][1]. This latter approach is advantageous since initial cracks can be defined as mesh independently in the whole domain. With $\phi^S = 1$ in fully pre-fractured zones, and, as ϕ^S cannot grow further, leading to $(\phi^S)'_S = 0$ and $\operatorname{grad}\phi^S = \mathbf{0}$, (4.30) yields

$$(\phi^S)'_S = 0 = \frac{1}{M}\left[2(1-\phi^S)\mathcal{H} - G_c\Big(\frac{\phi^S}{\epsilon} - \epsilon\operatorname{div}\mathbf{0}\Big)\right]\Big|_{\phi^S=1} . \tag{4.32}$$

Following this, the term in brackets can be solved with respect to $\mathcal{H}$ yielding

$$\mathcal{H}_0 = \frac{G_c\,\phi^S}{2\,\epsilon(1-\phi^S)} \tag{4.33}$$

with $\mathcal{H}_0$ as the initial value of $\mathcal{H}$ for pre-fractured areas. As $\mathcal{H}_0$ would grow to infinity at $\phi^S = 1$, ϕ^S is usually set approximatively to one, i. e. $\phi^S \approx 1$.

[1] Note that Borden *et al.* [46] consider the double length-scale parameter $2\epsilon = c$, compare also (2.71), which results in a factor of 4 in the work of Borden *et al.* instead of 2 in (4.33).

Chapter 5:
Numerical Examples

This chapter presents representative numerical simulations to show the capabilities and advantages of the material model proposed in Chapter 3 and the numerical scheme presented in Chapter 4. The simulations focus on different scenarios of partially saturated porous material with application to hydraulic fracturing to examine the occurring processes. First, the model is verified on consistency regarding the multiphasic character of the porous material and the material's response to fracture. Then, proceeding from a quasi-two-dimensional hydraulic fracturing simulation of a single crack, the coupled behaviour of the solid skeleton and the interaction of the fluid phases are examined in detail. It is extended to three dimensions to show the full scope of the model. Finally, two kinds of heterogeneities are assessed: global ones caused by confining stresses and local ones induced by inhomogeneous material properties.

5.1 Model consistency

For the presented model of hydraulic fracturing in partially saturated porous media, two complex phenomena are considered: the porous material's multiphasic behaviour with the specific interaction of the fluids in the pore space and the fracturing problem. In order to verify both phenomena, two numerical examples are presented in the following section. The first example deals with the capillary behaviour of the fluids in the pore space. Therefore, a leaking problem is computed and compared to experimental data. The second numerical example aims to verify the fracturing process. For it, a crack in an infinite, impermeable elastic medium under pressure is modelled and verified to the linear elastic fracture mechanic's solution.

5.1.1 Liakopoulos' leaking problem

A common problem in validating the constitutive setting of a triphasic model for partially saturated soil is the drainage of a soil column. Therefore, the well-documented leaking problem of Liakopoulos [175] is modelled, and the obtained numerical results are compared to the experimental ones. Further numerical solutions to this problem can be found, e. g., in the work of Gawin *et al.* [113, 114], Jommi *et al.* [151], Schrefler & Scotta [220], Ehlers *et al.* [92] and Cajuhi *et al.* [61].

In 1964, Liakopoulos published his experimental study of the leaking of a soil column in his PhD thesis [175]. The experiment comprised a one-meter-high impermeable vessel filled with fine Del Monte sand. In an independent experiment, Liakopoulos determined the initial porosity to 29.75% and the bulk density to 1 724 g/cm^3 for the particular sand. The pressure at the top and bottom of the sample corresponded to atmospheric pressure, i. e. $p_{\text{atm.}} = 101\,325\,\text{Pa}$. Moreover, the sample's sides and bottom were rigid, and no

vertical load was applied on the top. First, a constant liquid flow through the column was imposed in the initial step to saturate the sand. Then, in a second step, the top and bottom of the cylindrical vessel were opened, inducing air to flow in and out and water to drain due to the gravitational forces. The experimentally measured outflow rate at the bottom of the soil column is presented in Figure 5.6.

Table 5.1: *Material parameters for the Liakopoulos leaking problem.*

Parameter	Symbol	Value	Parameter	Symbol	Value
Lamé constants	μ^S	$4.64 \cdot 10^5$ Pa	Effective liquid viscosity	μ^{LR}	10^{-3} Pa s
	λ^S	$1.857 \cdot 10^6$ Pa	Effective gas viscosity	μ^{GR}	$1.8 \cdot 10^{-5}$ Pa s
Intrinsic permeability	K^S	$4.5 \cdot 10^{-13}$ m^2	Specific gas constant	R^G	287.17 Nm/(kg K)
Initial porosity	n_0^F	0.2975 [-]	Temperature	θ	293.15 K
Initial liquid saturation	s_0^L	0.999 [-]	van Genuchten parameter	α_{vG}	$2 \cdot 10^{-5}$ 1/Pa
Effective solid density	ρ^{SR}	2 000 kg/m^3	van Genuchten parameter	m	1.03 [-]
Effective liquid density	ρ^{LR}	1 000 kg/m^3	van Genuchten parameter	n	1.5 [-]
Atmospheric gas density	ρ^{GR}_{atm}	1.246 kg/m^3	Pore-size distribution factor	λ	3 [-]
Gravitation value	g	9.806 m/s^2	Residual liquid saturation	s^L_{r}	0.2 [-]

In his thesis, Liakopoulos did not define all the material parameters needed to compute the leaking problem. In particular, the parameters for the solid skeleton were not specified further. As the European Network ALERT Geomaterials framework used the Liakopoulos problem as a benchmark for multiphasic flow in porous media, the group completed the list of material parameters, see Jommi *et al.* [151] and Klubertanz *et al.* [160]. The relevant parameters are listed in Table 5.1.

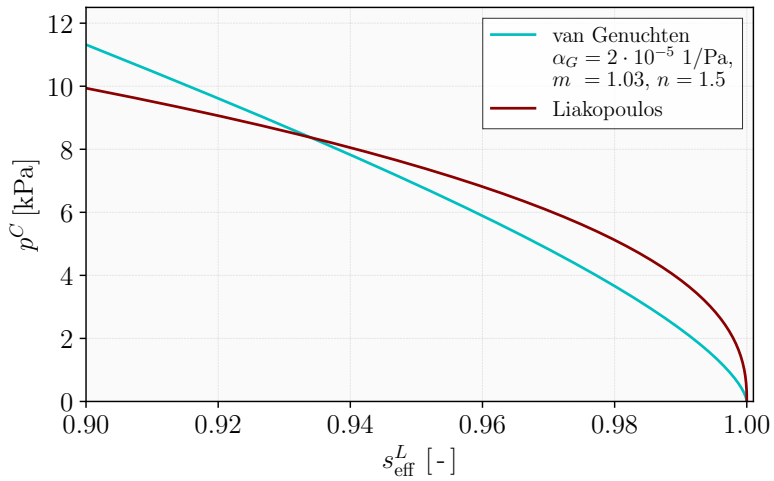

Figure 5.1: *Capillary-pressure-saturation curve with respect to the van Genuchten model [115] and Liakopoulos [175].*

Moreover, in this thesis, the van Genuchten model [115] is adopted for the pressure-difference-saturation condition, given in (3.79), and the Brooks-Corey model [57] for the

relative permeability factors, given in (3.87). Figure 5.1 depicts the related pressure-difference-saturation curve. The corresponding van Genuchten parameters α_G, m, and n are chosen according to Ehlers *et al.* [92]. The pore size distribution factor λ, which plays a role in the calculation of the relative permeability factors after Brooks & Corey [57], is set to $\lambda = 3$ according to Gawin *et al.* [113]. This value corresponds to well-sorted soil, as is the Del Monte sand. Next, the residual saturation is set to $s_{\mathrm{r}}^L = 0.2$ for the liquid and $s_{\mathrm{r}}^L = 0.0$ for the gas. The final set of material parameters is given in Table 5.1.

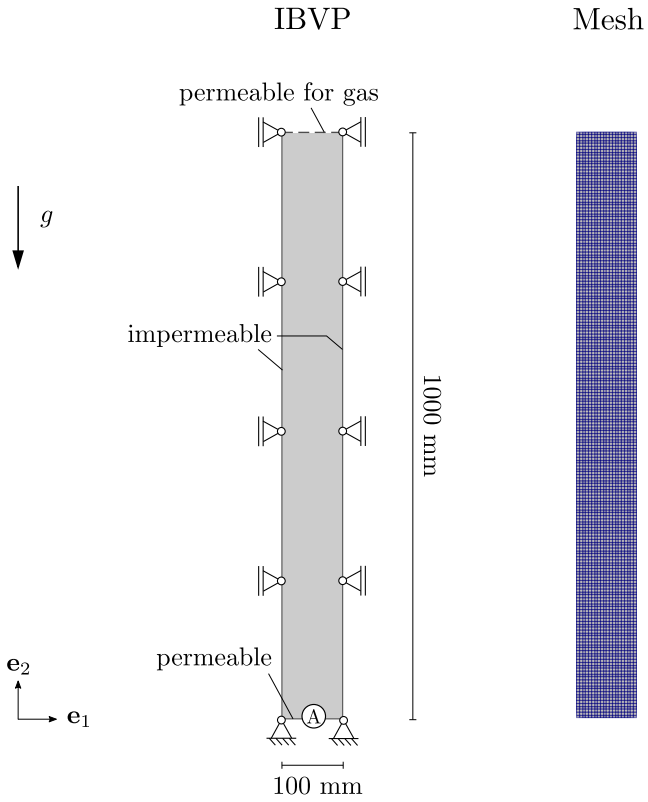

Figure 5.2: *Geometry and boundary conditions for the Liakopoulos leaking problem.*

Since Liakopoulos' experiment is rotationally symmetric, the numerical simulation is carried out in a quasi two-dimensional setting. For the present computation, a regular mesh of 4 000 elements is used, whereby the mesh length of one element comprises $h = 5\,\mathrm{mm}$. In order to reduce the effort in time, a simplified quasi-static triphasic model without a phase field is used for the computation. Thereby, only the balances for the overall momentum, the liquid volume and the gas mass are considered. The set of primary variables reduces consequently to the solid displacement $\mathbf{u}_S$, the effective liquid saturation s_{eff}^L and the effective gas pressure p^{GR}. An overview of the relevant balances is given in Appendix C.3. The initial conditions are set to atmospheric pressure for both fluids, leading to the effective gas pressure $p_0^{GR} = 0\,\mathrm{Pa}$ and the liquid saturation $s_{\mathrm{eff}}^L(t = t_0) = s_0^L = 1$. Since this latter condition would lead to numerical instability caused by an infinity tangent of the pressure-difference-saturation relation, the initial liquid saturation is finally fixed at $s_0^L = 0.999$. Furthermore, for the volume and mass balances of the fluid phases, (C.8) and (C.9), respectively, Neumann boundary conditions equal to zero are chosen for

the sides of the model, reproducing the impermeable vessel, i. e. $\bar{v}^L = 0\,\mathrm{m}^3/(\mathrm{m}^2\,\mathrm{s})$ and $\bar{v}^G = 0\,\mathrm{m}^3/(\mathrm{m}^2\,\mathrm{s})$. For the top and bottom edges, the experimental setting is fulfilled for the gas by the Dirichlet condition $\bar{p}^{GR} = 0\,\mathrm{Pa}$, allowing the gas to flow arbitrarily. For the bottom boundary, atmospheric pressure is also assumed for the liquid phase, i. e. $\bar{p}^{LR} = 0\,\mathrm{Pa}$. According to the definition of the capillary pressure after the van Genuchten model (3.79), this condition corresponds to a saturation equal to one. Thus, the Dirichlet boundary condition $\bar{s}^L_{\mathrm{eff}} = 0.999$ is set at the bottom of the column, enabling an unhindered liquid flow. At last, as no water flows in, the Neumann condition at the top boundary is $\bar{v}^L = 0\,\mathrm{m}^3/(\mathrm{m}^2\mathrm{s})$. Figure 5.2 sketches the applied boundary conditions and employed mesh.

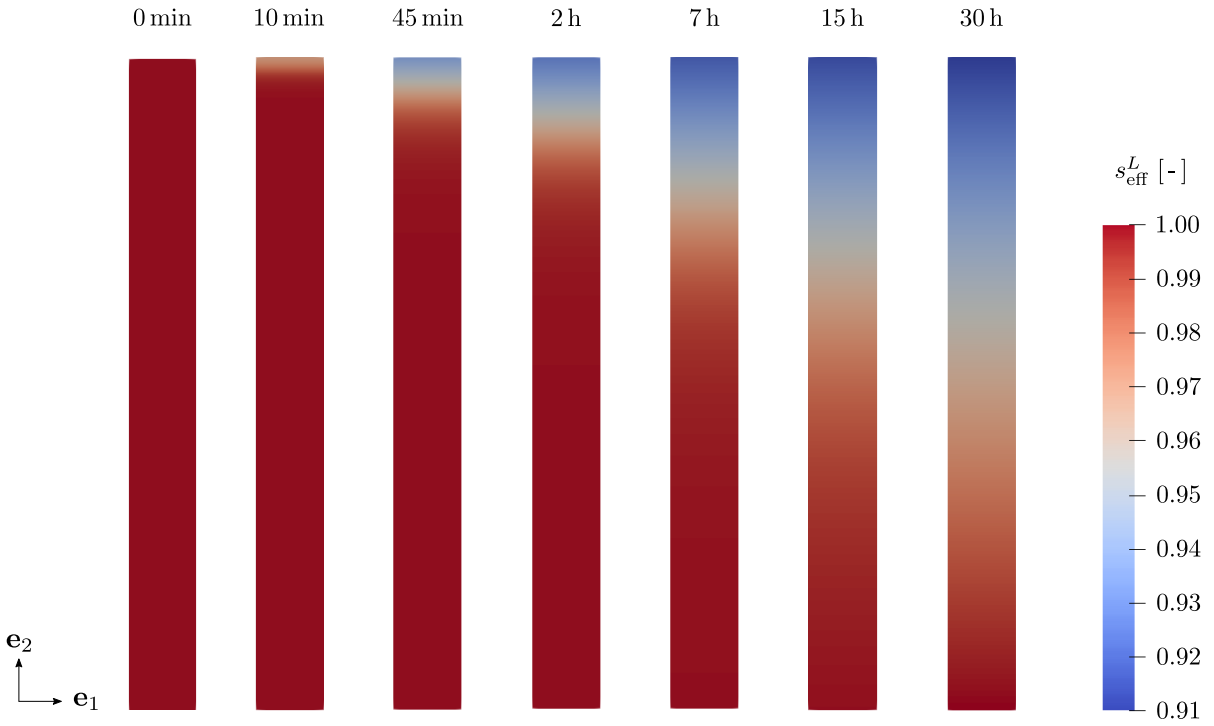

Figure 5.3: *Development of the liquid saturation during the draining process.*

As a result of the gravitational forces, the liquid drains off at the bottom of the sand column. However, some liquid is retained relative to the capillary effects in the pore space. The temporal development of the saturation variable s^L_{eff} is shown in Figure 5.3 and Figure 5.4. The saturation profile over the height is in agreement with other numerical computations, compare, e. g., Gawin *et al.* [113], Ehlers *et al.* [92] and Cajuhi *et al.* [61].

While the liquid leaks out, the gas undergoes a pressure suction before equilibrium with the atmospheric pressure. The distribution of the effective gas pressure over the height for different time values is depicted in Figure 5.5. The maximal gas-pressure suction of $p^{GR} = -6000\,\mathrm{Pa}$ is reached at a time $t = 45\,\mathrm{min}$. These values are in accordance with the numerical results of Ehlers *et al.* [92]. However, the gas suction is significantly lower than predicted by Gawin *et al.* [113] and Lewis & Schrefler [173]. The choice of pressure-difference-saturation relation can explain this discrepancy. The two latter groups consider the pressure-difference-saturation relation obtained experimentally by Liakopoulos [175]

for $s^L_{\text{eff}} \geq 0.91$, also depicted in Figure 5.1. Above a saturation of 0.934, the experimentally captured capillary pressure of Liakopoulos exceeds the predicted capillary pressure of the considered van Genuchten model (depicted in blue in the same figure). For this reason, the gas pressure after Liakopoulos' model surpasses the gas pressure of the considered model here. After approximately 150 h, the gas pressure reaches the atmospheric pressure, and the system is in equilibrium.

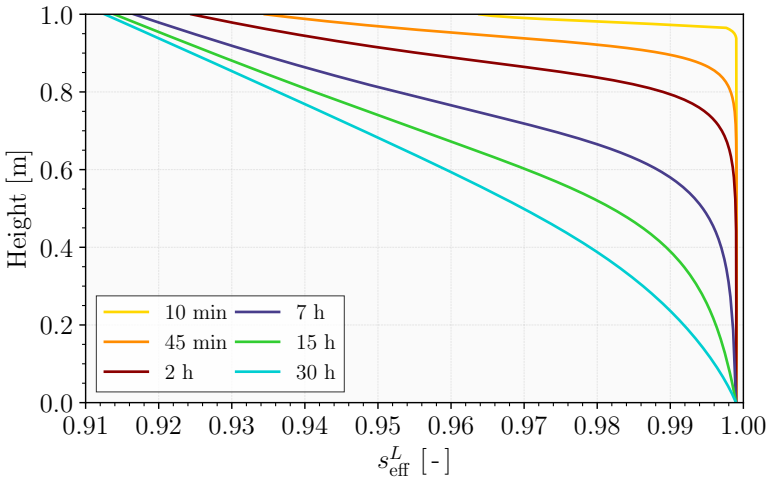

Figure 5.4: *Effective liquid saturation over the height of the sand column for different time spots.*

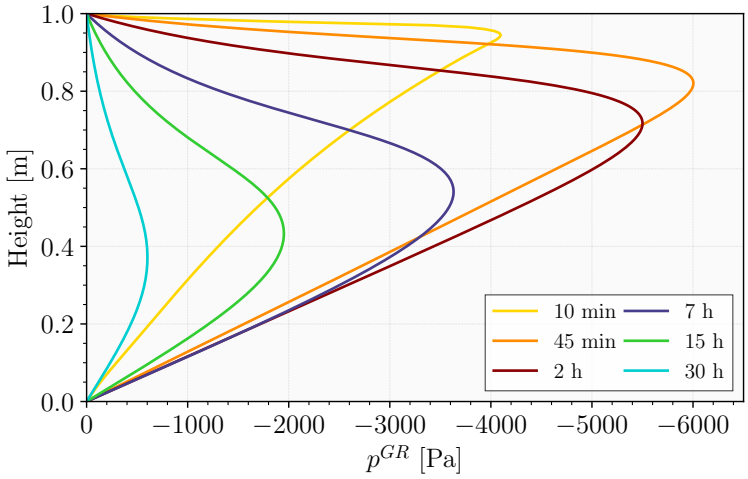

Figure 5.5: *Effective gas pressure over the height of the sand column for different time spots.*

Finally, Figure 5.6 presents the numerical results of the water outflow rate over time at point A (cf. Figure 5.2) compared to the experimental measurements from Liakopoulos [175]. At the beginning of the draining process, the numerical computation fits the experimental results quite well. The initial vertical outflow rate counts $n^L\, w_{L2} = 5 \cdot 10^{-6}\,\text{m}^3/(\text{m}^2\text{s}) = 0.03\,\text{cm/min}$. After one hour of leaking, the computation overestimates the liquid outflow compared to the experimental measurements. Besides imprecision in the experimental measurements, one possible source of discrepancy is the chosen

pressure-difference-saturation relation. Since the considered van Genuchten model underestimates the capillary pressure for s_{eff}^{L} compared to Liakopoulos experimental results, cf. Figure 5.1, the outflow is overestimated for the further course of the leaking process. At last, the presented model predicts the final distribution adequately.

Overall, the current model yields reasonable results concerning the interaction of the fluid phases in the pore space depending on the considered pressure-difference-saturation relation and the determination of the relative permeabilities.

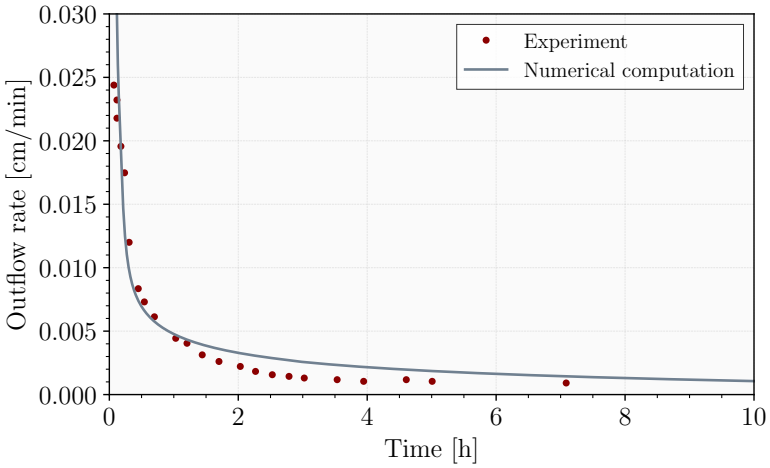

Figure 5.6: *Outflow rate at the bottom of the sand column versus time according to the experimental measurements of Liakopoulos [174] and the numerical results at point A.*

5.1.2 Linear-elastic fracture mechanics

In order to verify the PANDAS code with respect to fracturing, a typical problem of the linear elastic fracture mechanics (LEFM) is modelled and compared to the specific analytical solution of the LEFM.

Here, a central straight crack of length $2a$ is subjected to uniformly distributed tensile stresses σ in an infinite plate, see Figure 5.7 (left). This load state corresponds to a mode I crack with a symmetric crack opening normal to the crack plane according to Irwin [148]. Considering early approaches to this problem in fracture mechanics, compare, for example, Griffith [120, 121] and Sneddon [225], the critical tensile stress σ_c for crack propagation is given by

$$\sigma_c = \sqrt{\frac{2E_l\gamma_s}{\pi a}}\,, \tag{5.1}$$

where $E_l = E$ in the plain stress and $E_l = E/(1-\nu^2)$ in the plain strain case, with E the Young's modulus, ν the Poisson ration, γ_s the surface tension of the solid material and a the half-crack length. Besides this, Irwin [148, 149] correlates the surface tension γ_s with the critical energy release rate G_c and fracture thoughness K_{Ic} under mode I, via

$$G_c = \frac{K_{Ic}^2}{E_l} = 2\gamma_s\,. \tag{5.2}$$

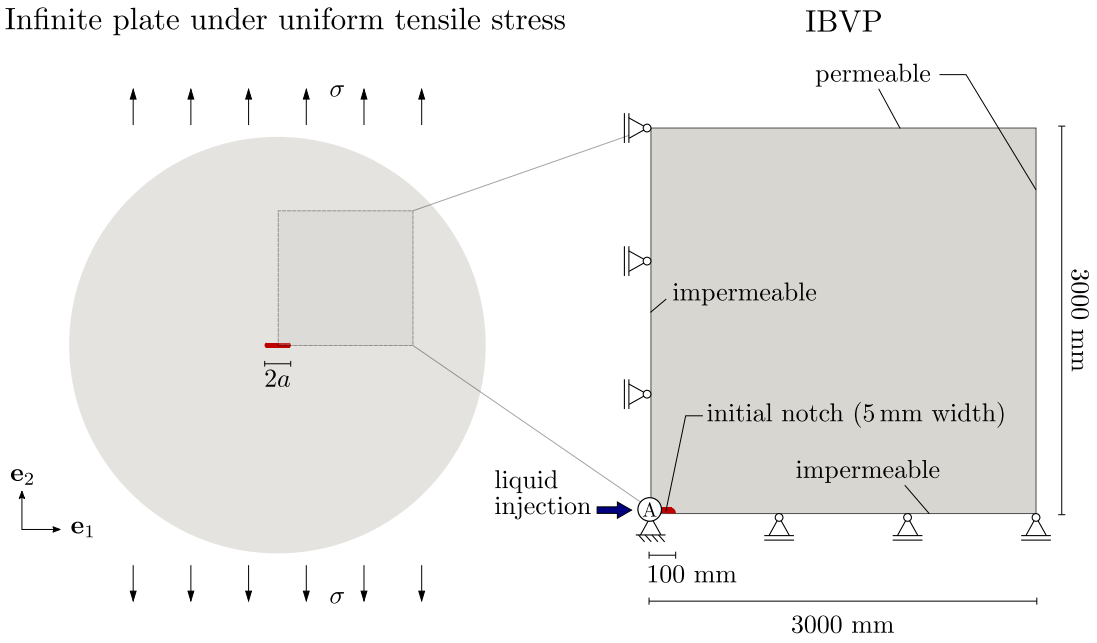

Figure 5.7: *Single crack under tensile stress (left) and geometry of the corresponding initial-boundary-value problem (right).*

A detailed description of this relation can be found, for example, in the work of Yarema [257] and Gross & Seelig [122]. Under consideration of (5.2), the crack propagates when the tensile stress exceeds the critical value

$$\sigma_c = \sqrt{\frac{E_l\, G_c}{\pi a}}\,. \tag{5.3}$$

Wilson & Landis [249] adopted this analytical critical stress to verify their poroelastic model with an embedded phase field, considering a pressurised crack under plane-strain conditions. They enhanced (5.3) with the phase-field length-scale parameter ϵ, thus obtaining a dimensionless relation for the critical pore pressure p_c for crack propagation:

$$\frac{p_c}{\sigma_0} = \sqrt{\frac{\epsilon}{\pi a}} \quad \text{with} \quad \sigma_0 = \sqrt{\frac{E_l\, G_c}{\epsilon}}\,. \tag{5.4}$$

The analytical solution of the LEFM for the problem under study was elaborated for purely elastic, brittle solid material. Therefore, the fully saturated model outlined in Subsection 3.5.2 and Appendix C.2 is used for the following numerical problem and the permeability is set to $K^S = 10^{-15}\,\mathrm{m}^2$, such that the material is very close to the impermeable state. The complete set of material parameters is listed in Table 5.2.

The IBVP follows the example of Wilson & Landis [249] and is sketched in Figure 5.7 (right). The initial crack half-length is set to $a = 100\,\mathrm{mm}$. The inflow rate amounts $\bar{v}^L = 5 \cdot 10^{-3}\, t\,\mathrm{m/s}$ at the crack center, where t is the current time. The right and bottom edges are impermeable and fixed, while the right and top edges are permeable.

Table 5.2: *Material parameters for the LEFM problem.*

Parameter	Symbol	Value	Parameter	Symbol	Value
Lamé constants	μ^S	$8.077 \cdot 10^{10}$ Pa	Effective liquid density	ρ^{LR}	$1\,000\,\mathrm{kg/m^3}$
	λ^S	$1.211 \cdot 10^{11}$ Pa	Effective liquid viscosity	μ^{LR}	10^{-3} Pa s
Intrinsic permeability	K^S	$1.0 \cdot 10^{-15}\,\mathrm{m^2}$	Crack resistance	G_c	2 700 Pa m
Initial porosity	n_0^F	0.20 [-]	Length-scale parameter	ϵ	0.01 m
Effective solid density	ρ^{SR}	$3\,000\,\mathrm{kg/m^3}$	Residual stiffness	η_r^S	0.001 [-]

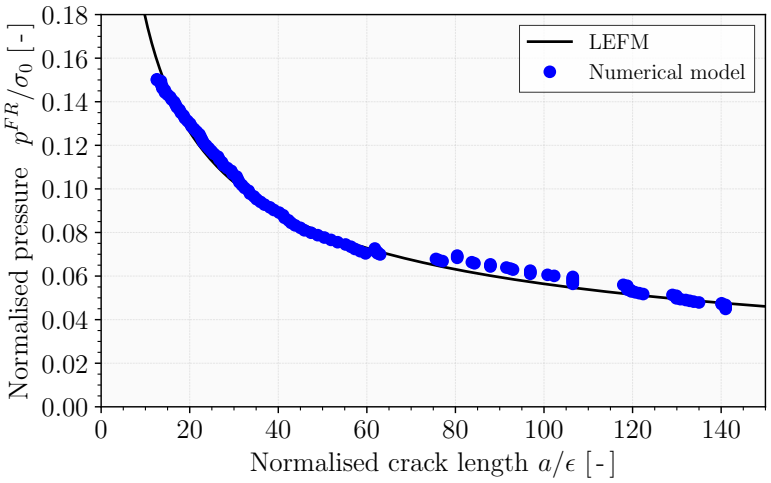

Figure 5.8: *Normalised pore pressure p^{FR}/σ_0 at point A over the normalised crack length a/ϵ.*

As an outcome, the normalised pore pressure p^{FR}/σ_0 at point A (compare Figure 5.7) is plotted over the normalised crack length a/ϵ in Figure 5.8. The numerical results are very close to the exact solution of the LEFM with $p_c = p^{FR}$ in (5.4).

5.2 Coupled hydraulic fracturing process in partially saturated porous media

The following numerical study shows a hydraulically induced crack propagation in a partially saturated porous material, where the coupling between the solid, the liquid and the gas and the fracturing process are considered in detail. Table 5.3 lists the material parameters that have been used. Moreover, the interaction between the pore fluids follows the pressure-difference-saturation function $p^D(s^L)$ after (3.82) with $a = 5 \cdot 10^{-3}$ Pa, $b = 4\,000.5$, $c = 1\,714.5$ and $d = 0$, as displayed in Figure 3.3.

5.2.1 Initial-boundary-value problem in quasi-two dimensions

First, the computation is carried out in a three-dimensional setting with no solid deformations and no fluid fluxes perpendicular to the $\mathbf{e}_1$-$\mathbf{e}_2$-plane, yielding a quasi-two-dimensional procedure. Figure 5.9 (left) exhibits the geometry and boundary conditions of the model.

Table 5.3: *Material parameters for the coupled hydraulic fracturing problem.*

Parameter	Symbol	Value	Parameter	Symbol	Value
Lamé constants	μ^S	$8.077 \cdot 10^{10}$ Pa	Effective liquid viscosity	μ^{LR}	10^{-3} Pa s
	λ^S	$1.211 \cdot 10^{11}$ Pa	Effective gas viscosity	μ^{GR}	$1.8 \cdot 10^{-5}$ Pa s
Intrinsic permeability	K^S	$1.0 \cdot 10^{-14}$ m^2	Specific gas constant	R^G	287.17 Nm/(kg K)
Initial porosity	n_0^F	0.20 [-]	Temperature	θ	283 K
Initial liquid saturation	s_0^L	0.7 [-]	Crack resistance	G_c	2 700 Pa m
Effective solid density	ρ^{SR}	3 000 kg/m^3	Length-scale parameter	ϵ	0.01 m
Effective liquid density	ρ^{LR}	1 000 kg/m^3	Residual stiffness	η_r^S	0.001 [-]
Atmospheric gas density	ρ_{atm}^{GR}	1.246 kg/m^3	Pore-size distribution factor	λ	3 [-]

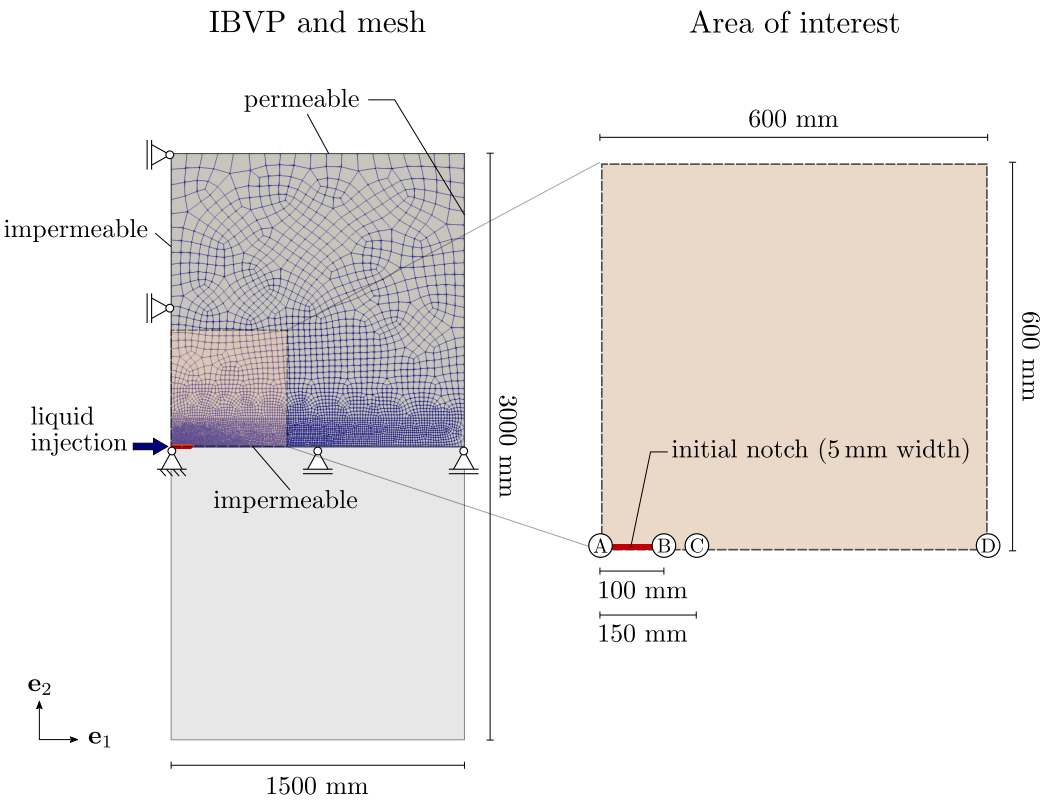

Figure 5.9: *Geometry and mesh (left) of the initial-boundary-value problem of the hydraulic fracturing problem with an area of interest as detail of the numerical computation (right).*

A fracking process is typically a problem of the underground that could either be considered a half-space or a restricted domain. Proceeding from the latter, the size of the system under study is relevant for the influence of the liquid- and gas-flow behaviour on the overall solution. Accordingly, the larger the control area is chosen, the more fluid must be moved. When a liquid is injected into a fully liquid-saturated domain, the pore space expands such that a part of the additional liquid can be stored. However, another part leaves the domain towards the external environment while the total solid and liquid bodies are displaced. Enlarging the domain under study also includes an enlargement of

the liquid body. As a result, when a larger liquid body has to be moved by the injection process, this leads to increasing resistance in the entire area, such that the pore pressure rises faster at the same amount of injected fluid in a time span compared to a smaller area that could have been used. In the unsaturated case, this process is basically the same. However and as a result of the compressibility of the pore gas, the injection pressure leads to a strong compression of the gaseous volume, such that more liquid has to be injected into the unsaturated domain compared to the fully saturated domain in order to obtain the same frack. At the same time, the fracking liquid displaces the pore gas out of the fractured area. In order to reduce the influence of the domain boundary on the computation of the fracking process, the domain of interest with a length and width of 0.6 m is embedded in an environment with an edge length of 1.5 m, compare Figure 5.9. With the material-parameter set of Table 5.3, the computed domain has proven large enough such that the boundary conditions do not influence the results obtained for the area under discussion.

Due to the system's symmetry, only the upper part is considered. This part is based on 158 746 DOF and 5 751 elements with an element size h of $2\,\mathrm{mm} \leq h \leq 80\,\mathrm{mm}$. Particularly, the mesh has been chosen fine in the vicinity of the initial notch and in areas where the crack is expected to propagate ($2\,\mathrm{mm} \leq h \leq 5\,\mathrm{mm}$) and coarser elsewhere, see Figure 5.9 (left). The domain is fixed at the left and lower edges. As a result, the displacements are constrained normally to the bearing directions. The upper and right edges of the model are fully permeable at atmospheric pressure, whereas the left and lower edges are impermeable. At the beginning of the computation, atmospheric pressure not only holds along the boundary but is also prescribed for the liquid and gas pressures in the porous domain. The initial liquid saturation is set to 70%.

In the first step of the following computation, an initial crack is imposed on the left edge of the system by applying an initial pseudo-elastic energy according to relation (4.33), such that $\mathcal{H}_0 = 134.865\,\mathrm{MJ/m^3}$ corresponding to a phase field of $\phi^S = 0.999$ with the given parameters of Table 5.3. Additionally, the end of the initial crack is rounded to prevent artificial singularities that sharp edges may cause. In the second step, a liquid flow is injected at the initial notch with an increasing flow rate of $\bar{v}^L = 5 \cdot 10^{-3}\, t\,\mathrm{m^3/(m^2 s)}$. Gravitational forces are neglected, as well as the non-equilibrium frictional gas stresses $\mathbf{T}^G_{NEQ}$.

The driving force of the crack propagation is the pressure field induced by the liquid injection. Based on the pore pressure, tensile stresses in the porous solid grow, such that the stored tensile energy W^{S+} grows and the fracture evolves. Figure 5.10 shows the phase field, the pore pressure and the liquid saturation at different time steps during the fracturing process. As a result of the isotropic permeability of the solid with constant K^S, the injected liquid initially induces a more or less radial distribution of the pore pressure p^{FR} until the crack starts to evolve, thus inducing a reduction of the fracture resistance. With increasing pore pressure also the liquid saturation grows, partly leading to a nearly complete displacement of the pore gas.

To better understand the highly coupled situation during fracking, the fracturing solid skeleton is examined first, before the interaction between the solid and the pore fluids is discussed in detail.

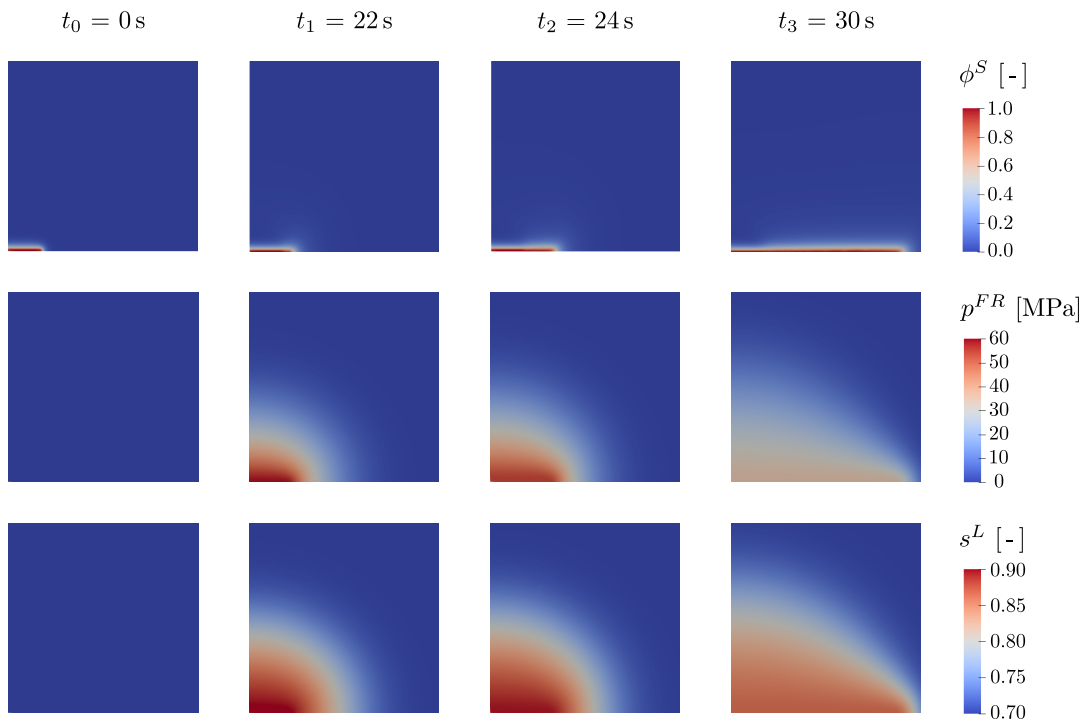

Figure 5.10: *Evolution of the phase-field variable, the pore pressure and the liquid saturation during the fracking process.*

5.2.2 Fracturing solid skeleton

Based on the constitutive setting of the solid skeleton and the phase-field variable, the coupled deformation and fracturing process is uniquely controlled by the solid stored energy W^S and consequences thereof, compare (3.69). However, the liquid injection and the coupled fluid flow in the entire domain induce these terms. To track the development of the total stored energy W^S and its effective tensile elastic and fracture contributions, W_e^{S+} and $G_c\Gamma^S$, respectively, consider Figure 5.11. There, these energies are displayed at point C of Figure 5.9, together with the values of the phase field ϕ^S and its time derivative $(\phi^S)'_S$. The effective tensile energy W_e^{S+} is defined as $W_e^{S+} = [(1-\phi^S)^2 + \eta_r^S]W^{S+}$. Note that the solid material at point C is in front of the initial crack and, therefore, unaffected by the fracture energy at time t_0.

During the liquid injection, the strain field evolves, and with it, the effective tensile elastic energy W_e^{S+}, see the black dotted line. With the growth of W^{S+} as the strain-depending part of W_e^{S+}, the phase-field evolution $(\phi^S)'_S$ also increases after (4.27). Unlike a sharp crack, the phase-field approach to fracture allows for a transition zone between the intact case with $\phi^S = 0$ and the fully broken case with $\phi^S = 1$. As a result, the material undergoes an irreversible damage process between these bounding states. The phase-field variable grows from zero to one with its increasing derivative, see the solid red and brown lines in Figure 5.11. In addition, the crack energy $G_c\Gamma^S$ rises driven by the phase field and its gradient according to $(3.69)_4$, compare the dashed black line.

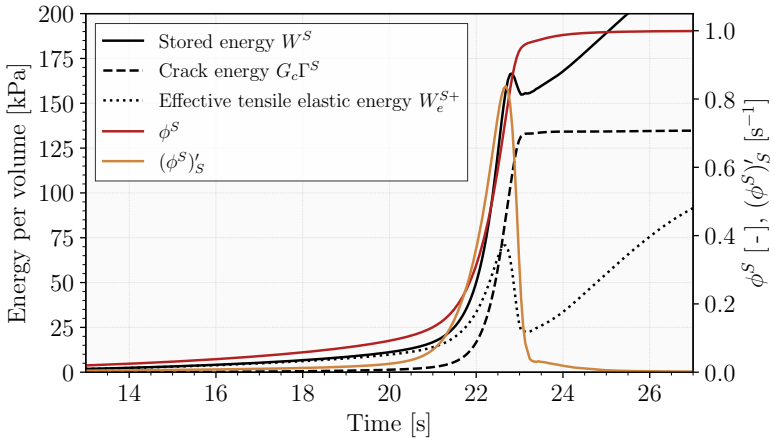

Figure 5.11: *Temporal development of the stored solid energy and its contributions, and the phase field and its derivative, all values at point C of Figure 5.9 in front of the initial crack tip.*

At a certain point, here around $t = 22.6\,\mathrm{s}$, the damage in the material reaches an amount where the bonding forces of the material cannot stand more strains. In the constitutive model, the factor $(1-\phi^S)^2$ of the effective elastic energy describes this stiffness loss between the undamaged and broken state. This factor becomes so tiny that W_e^{S+} decreases, even if the strains are still growing due to the injection. Consequently, also the phase-field evolution $(\phi^S)'_S$ shrinks until it finally reaches zero. Note that the condition $(\phi^S)'_S \geq 0$ is fulfilled at any time to guarantee an irreversible fracturing process, cf. Subsection 4.3.1. Once $(\phi^S)'_S$ has reached zero, ϕ^S has grown up to one, and the material is entirely broken. Moreover, the fracture energy is at its maximum, corresponding to $G_c\Gamma^S \approx G_c/2\epsilon = 135\,\mathrm{kPa}$. At this point, the energy released during the crack propagation correlates to the energy necessary for the fracturing process. Finally, note that the effective elastic tensile energy is adjusted with a residual stiffness η_r^S to prevent zero stiffness values. As a result of η_r^S, both the effective elastic energy W_e^{S+} and the total stored energy W^S formally increase again, even at $\phi^S = 1$.

5.2.3 Fluid interaction in the fracturing process

After initiating the fracturing process at t_0, the liquid fills the initial crack and saturates the region around it at the beginning of the injection until time $t_1 = 22\,\mathrm{s}$, compare Figure 5.10. As the saturation s^L reaches 0.9 in the centre of this area, the gas is mainly driven out of the domain due to the increasing pressure. When the evolving fracture opens, the newly gained "vacant" space fills with fluids, particularly liquid, since the liquid is continuously injected into the notch at the left edge of the crack. As a further result of the initiation of the crack propagation, the saturation in the fracture nearly remains at $s^L = 0.9$, see Figure 5.10 (time t_2) and Figure 5.12 (solid blue line). However, since the pore gas cannot flow out rapidly enough, it is compressed in front of the crack, compare the solid yellow line in Figure 5.12. Note that the gas could escape more quickly if a smaller boundary value area is selected. In this latter case, there would be a lower gas overpressure in front of the crack. After a while, the injection rate and the amount of liquid in the surrounding area are insufficient to saturate the newly created crack space. In

turn, the gas expands in the crack while the gas pressure decreases, compare Figure 5.12 (dashed yellow line). This pressure drop initiates a reverse gas flow from the surrounding area into the fracture. Thus, the liquid saturation decreases, cf. Figure 5.10 (time t_3) and Figure 5.12 (dashed blue line), and the accessible amount of gas fills the crack. This phenomenon slows down crack propagation.

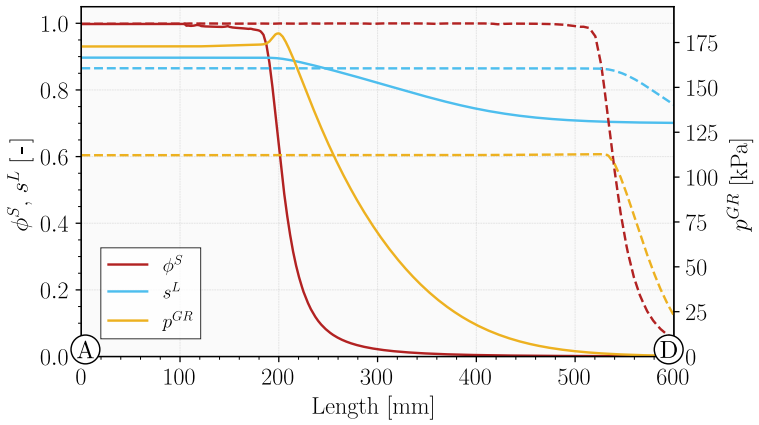

Figure 5.12: *Phase-field variable, liquid saturation and effective gas pressure over the length of the specimen (point A to D) at time $t_2 = 24\,\mathrm{s}$ (solid lines) and $t_3 = 30\,\mathrm{s}$ (dashed lines).*

5.2.4 The gas phase as a retardant of the fracturing process

To analyse the influence of the degree of saturation on the fracturing process in detail, three partially saturated (PS) models with different pressure-difference-saturation functions are examined. The corresponding curves are depicted in Figure 5.13, where the red curve (PS, case 2) corresponds to the previous example (Subsections 5.2.2 and 5.2.3). Together with two further pressure-difference-saturation curves (PS, cases 1 and 3), the partially saturated situation is compared to a fully saturated setting, where the material parameters and the boundary conditions remain the same as before. For this latter model, the numerical treatment is introduced in Appendix C.2.

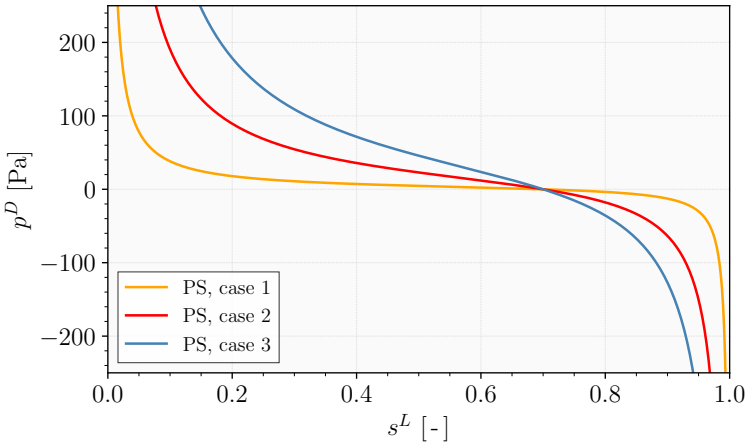

Figure 5.13: *Pressure-difference functions over liquid saturation for the three partially saturated (PS) cases.*

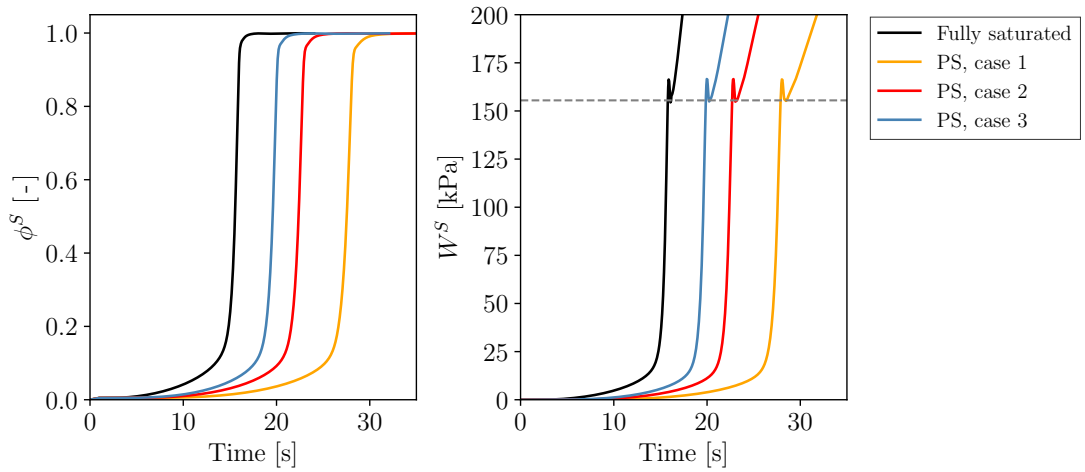

Figure 5.14: *Temporal development of the phase field (left) and the stored energy (right) at point C in front of the initial crack tip. The horizontal dashed line depicts the crack energy of* $W^S_{\text{crack}} = 156\,kPa$.

In this comparison, Figure 5.14 displays the temporal development of the phase-field variable ϕ^S and the stored energy W^S in front of the initial crack tip (point C in Figure 5.9) for both the partially and the fully saturated situations. From this figure and the following Figure 5.15, it is seen that the crack evolves earlier for the fully saturated model than for the three partially saturated ones. Nevertheless, the stored energy $W^S_{\text{crack}} = 156\,\text{kPa}$ necessary for the crack propagation is the same for all models, no matter whether or not the models are considered fully or partially saturated or, as in the latter case, what pressure-difference-saturation function is chosen, see the right image of Figure 5.14. Although the pore fluids trigger the fracking process, the fracturing itself is solely attached to the solid. This insight is consistent with the constitutive setting, where the solid strain energy W^S includes the fracture energy $G_c\Gamma^S$, compare (3.69). Concerning the peak of the W^S curves in Figure 5.14, the reader is referred to the arguments in Subsection 5.2.2.

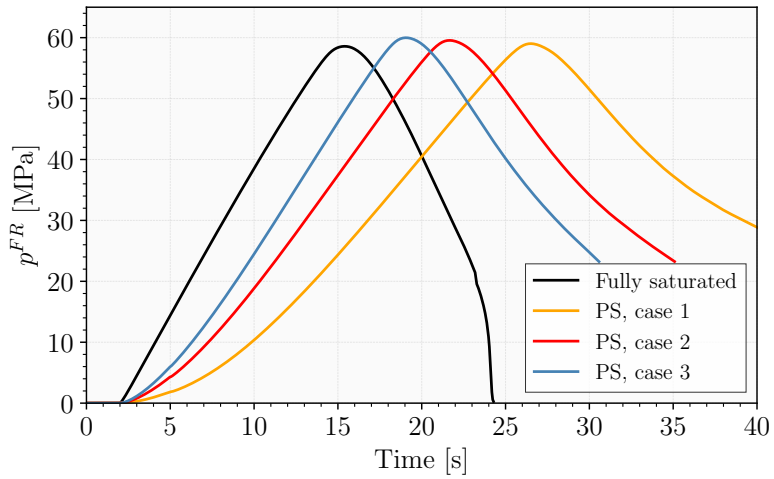

Figure 5.15: *Temporal development of the pore pressure* p^{FR} *at the initial crack tip (point B).*

Furthermore, the delay in crack propagation of the partially saturated models compared to the fully saturated one can be related to the mutual interaction of the fluid phases. As was shown in Subsection 5.2.3, the liquid displaces the gas at the beginning of the injection and compresses it when the resistance becomes too high. This interaction between the pore liquid and the pore gas causes a decrease in the overall pore pressure. Figure 5.15 illustrates this phenomenon by exhibiting the pore pressure over time at the initial crack tip (point B in Figure 5.9) for the different models. It is seen that the increase in pore pressure is lower for the partially saturated models than for the fully saturated case.

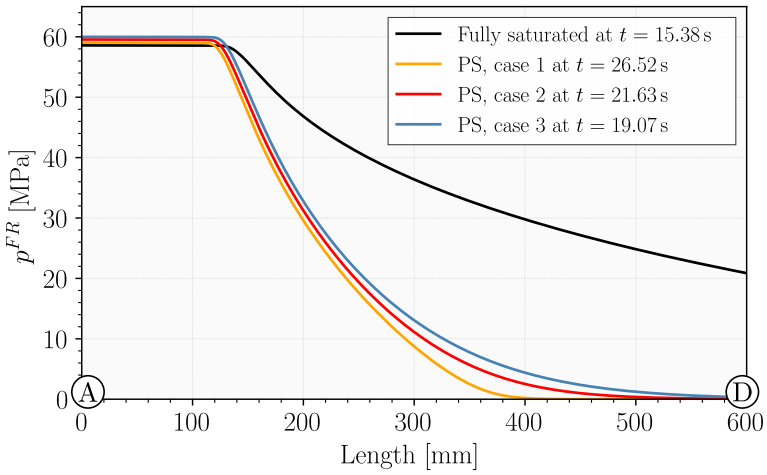

Figure 5.16: *Pore-pressure fields over the length of the specimen (point A to D) at the respective time of the initial crack evolution.*

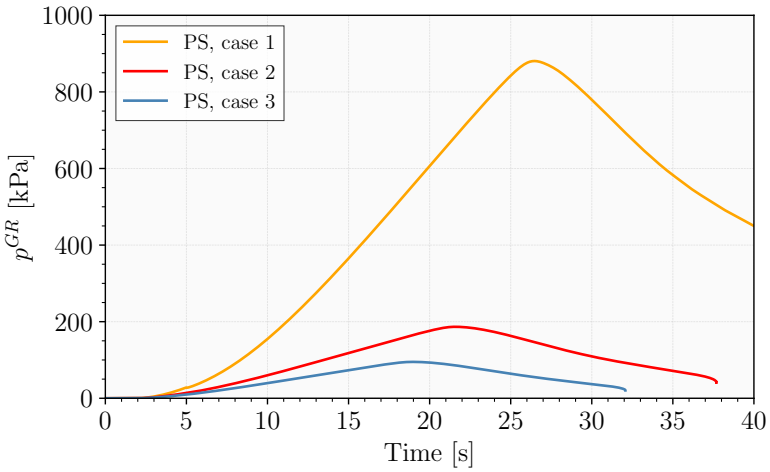

Figure 5.17: *Temporal development of the effective gas pressure p^{GR} at the initial crack tip (point B).*

Moreover, Figure 5.16 plots the pore-pressure distribution from point A to point D at the time of the first crack propagation for the different models. Here, the pressure in front of the initial crack presents higher values for the fully saturated than for the partially saturated models. In the latter cases, the gas compression affects the effective pore pressure in the whole domain, such that the crack evolves later. This effect is highlighted by a

comparison of the three partially saturated cases: the more the gas is compressed (case 1 vs case 3 as shown in Figure 5.17), the more the pore-pressure growth is delayed, and the lower the pressure field is around the crack (Figure 5.15 and Figure 5.16), the later evolves the fracture.

Finally, the mutual interaction of the pore fluids and, notably, the compressibility of the pore gas hinder the crack propagation in the partially saturated porous medium compared to the same fracturing process in a fully saturated one. Therefore, it is essential to include the interplay of the pore fluids in the fracturing process when dealing with hydraulically induced fractures in solids.

5.2.5 Coupled fracturing process in three dimensions

The following numerical example shows the coupled process of dynamic hydraulic fracturing in three dimensions, revealing the possibilities of the realised three-dimensional implementation for partially saturated porous media. The geometry, boundary conditions and mesh configuration are depicted in Figure 5.18. A three-dimensional IBVP for hydraulic fracturing of fully saturated porous material can be found in Ehlers & Luo [94].

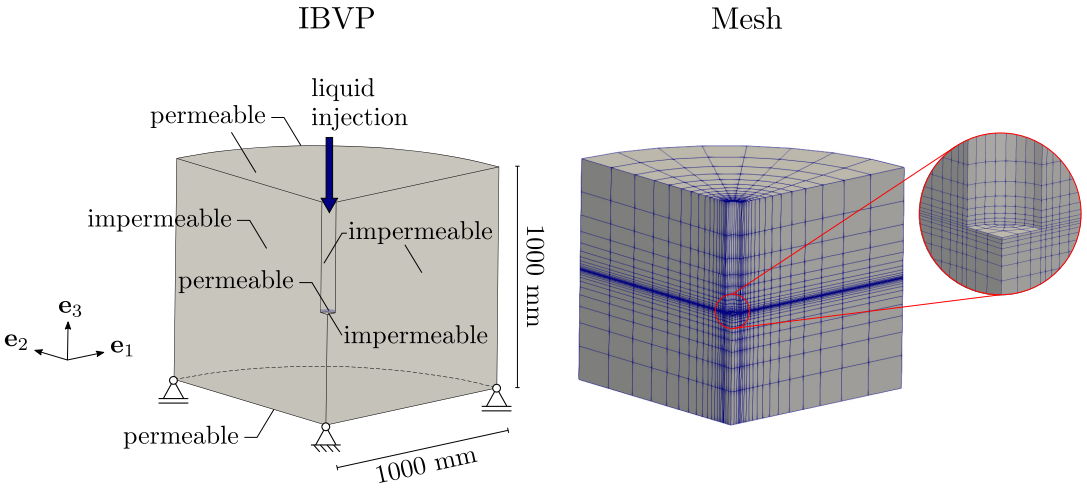

Figure 5.18: *Geometry (left) and mesh (right) of the three-dimensional initial-boundary-value problem of hydraulic fracturing.*

A quarter of a cylindrical specimen with a radius and height of one meter is fixed on its bottom surface. The system is fully axial-symmetric and counts 2 850 elements. The mesh is refined in the expected crack areas, see Figure 5.18, right. The liquid injection with an increasing flow rate of $\bar{v}^L = 20 \cdot 10^{-3}\, t\, \mathrm{m}^3/(\mathrm{m}^2\mathrm{s})$ is carried out through a borehole of 0.0445 m radius. The borehole is fixed in the normal direction and only permeable at the bottom edge. The system's bottom, top and outer circular surfaces are permeable for both fluids, whereas the symmetry surfaces ($\mathbf{e}_1$- and $\mathbf{e}_2$-plane, respectively) are impermeable. Atmospheric pressure is set at the beginning of the computation, and the initial porosity is $n_0^F = 0.015$, while the length-scale parameter amounts $\epsilon = 0.005\,\mathrm{m}$. All the other material parameters follow the previous example, cf. Table 5.3. The pressure-difference-saturation

curve is given in (3.82) and depicted in Figure 3.3. Finally, note that no initial notch is defined.

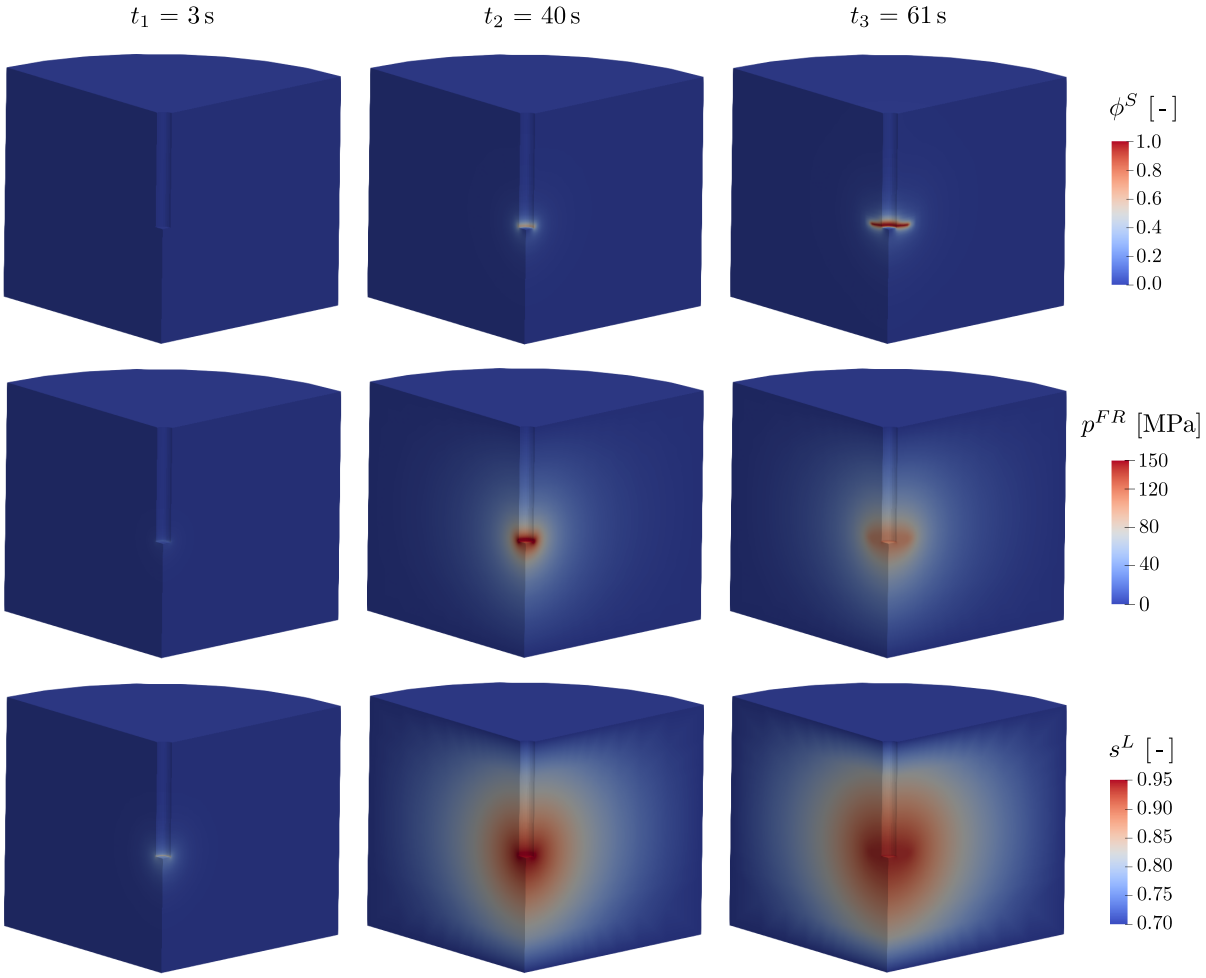

Figure 5.19: *Evolution of the phase-field variable, the pore pressure and the liquid saturation.*

Figure 5.19 displays the crack propagation, pore pressure field and saturation evolution for different time steps. At the beginning of the computation, the phase-field variable states zero for the whole domain. As the pressure at the bottom of the borehole augments, the phase field increases to one, and the crack propagation starts. This development shows the ability of the phase-field method to model crack initiation. At time $t = 55\,\mathrm{s}$, the crack propagates from the borehole bottom as a quarter circle surface, see also Figure 5.21. The pore pressure evolves more or less radially in the crack direction, similar to the quasi-two-dimensional computation in Subsection 5.2.1. Also, the liquid saturation exhibits a more or less radial distribution around the notch. The IBVP was chosen large enough that the boundary conditions do not affect the calculation at time $t_3 = 61\,\mathrm{s}$. Selecting a larger area in the future would be advantageous to study further crack propagation.

The fluid behaviour examined in detail in Section 5.2 for the quasi-two-dimensional setting is recovered for the fully three-dimensional case. Figure 5.20 displays the gas pressure. The gas is compressed in the surrounding, particularly in front of the evolving crack. This compression is accompanied by an expansion of the gas particles in the crack, resulting in

gas reflux to the crack. This phenomenon can be observed in Figure 5.21, where the liquid and gas streamlines are illustrated for a detailed area of 250 mm × 250 mm × 300 mm. In contrast, the incompressible liquid flows through the crack towards the permeable surfaces.

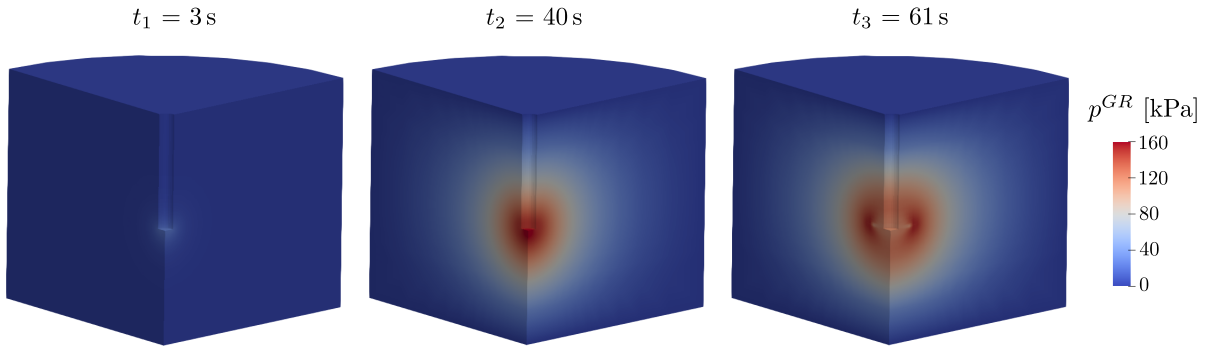

Figure 5.20: *Evolution of the effective gas pore pressure.*

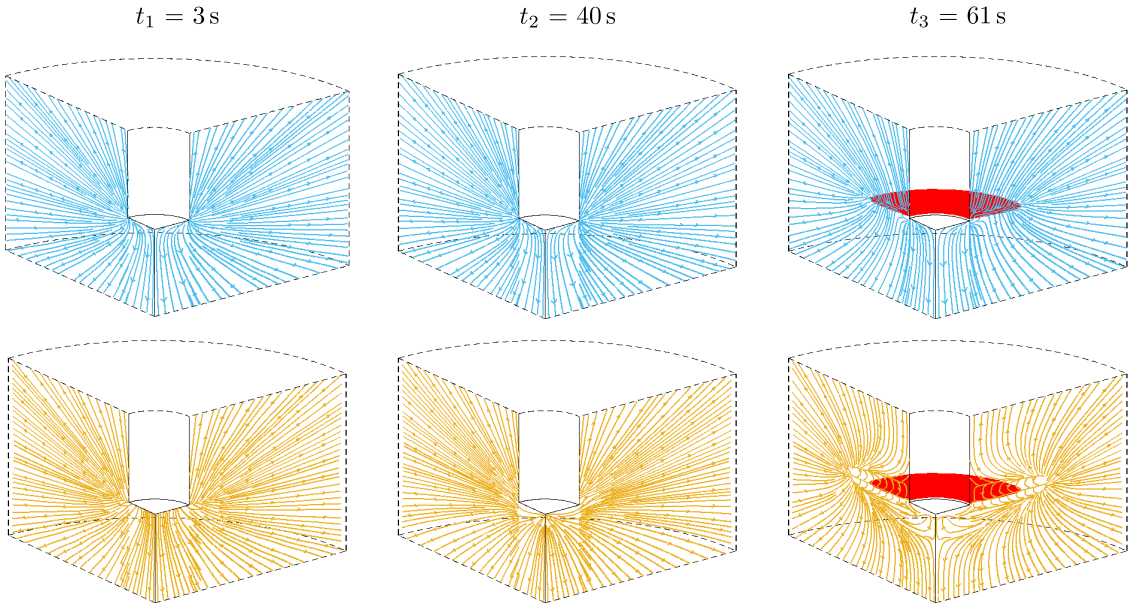

Figure 5.21: *Streamlines of the liquid (top) and gas (bottom) flow with crack evolution (red) for the detailed area 250 mm×250 mm×300 mm.*

Finally, the three-dimensional computation reproduces and confirms the results of the quasi-two-dimensional computation. However, a fully three-dimensional boundary value problem causes enormous computational effort. For instance, the present example has taken 52 days on a single core of a standard computer with 32 GB RAM. The following studies are, hence, carried out on quasi-two-dimensional numerical examples with plain strain and flow.

5.3 Fracturing porous media under confining stresses

When dealing with soil and rock, it is essential to consider confining stresses. In nature, rocks under *in situ* conditions are subjected to the pressure of the gravitational loading of overlying rocks, tectonic or even thermal stresses. In the near-surface, also topographic anomalies or geological discontinuities can trigger stresses. The confining stresses influence the fracturing process, as they present a constraint for the deformation process and can, additionally, open or close fractures. Both effects will be treated in the following section.

5.3.1 Influence of confining pressures on a single crack

The following numerical example extends the previous quasi-two-dimensional investigations of Section 5.2, compare Figure 5.9, with confining stresses. Figure 5.22 displays the current boundary conditions. The applied mesh is depicted in Figure 5.9 (left).

The computation starts by applying the same initial pseudo-elastic energy as in the previous example to generate the initial crack (step 1). Then, displacements are applied to yield confining stresses (step 2). Here, use is made of $\Delta u_1 > \Delta u_2$ with $\Delta u_1 / \Delta u_2 = 12.5$. The displacements are generated by increasing $v_{S1} = 0.15\,\mathrm{mm/s}$ and $v_{S2} = 0.012\,\mathrm{mm/s}$ within the next 10 s. After 600 s, the time-dependent drainage process of both fluids is accomplished and the pressure field remains constant (step 3). Finally, in the fourth step, liquid is injected at the left side of the precrack with the same initial conditions and at the same flow rate of $\bar{v}_L = 5 \cdot 10^{-3}\,t\,\mathrm{m}^3/(\mathrm{m}^2\mathrm{s})$, compare Subsection 5.2.1.

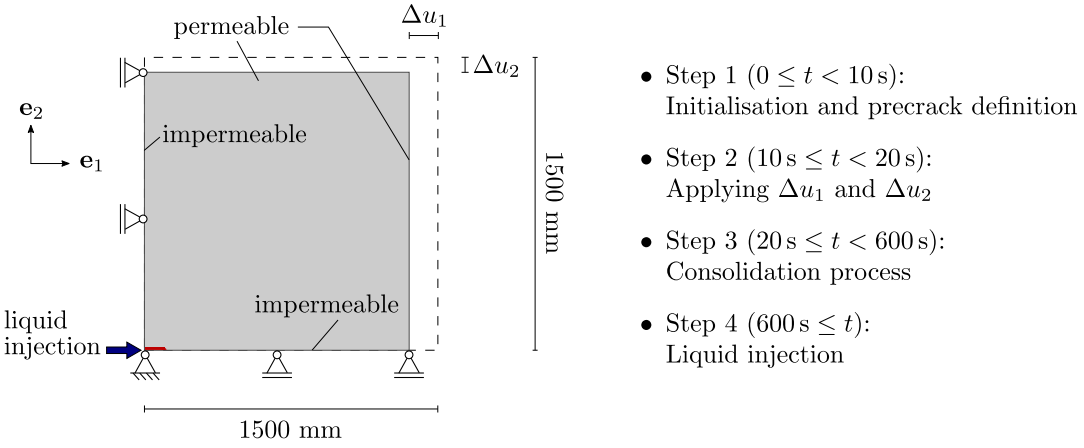

Figure 5.22: *Geometry and loading history of the initial-boundary-value problem of the fracking process under confining stresses.*

Figure 5.23 shows the evolution of the phase field at the deformed body, where a dashed red line indicates the undeformed geometry. As before, only a detailed area of 0.6 m × 0.6 m (cf. Figure 5.9, right) is displayed. The deformation is scaled by a factor of 150. It is seen that the crack evolves later than in the comparable model without confining

stresses, compare Figure 5.10 in Subsection 5.2.1. Note that the injection in the present example starts at $t = 600\,\mathrm{s}$ instead of $t = 0$ as in Subsection 5.2.1.

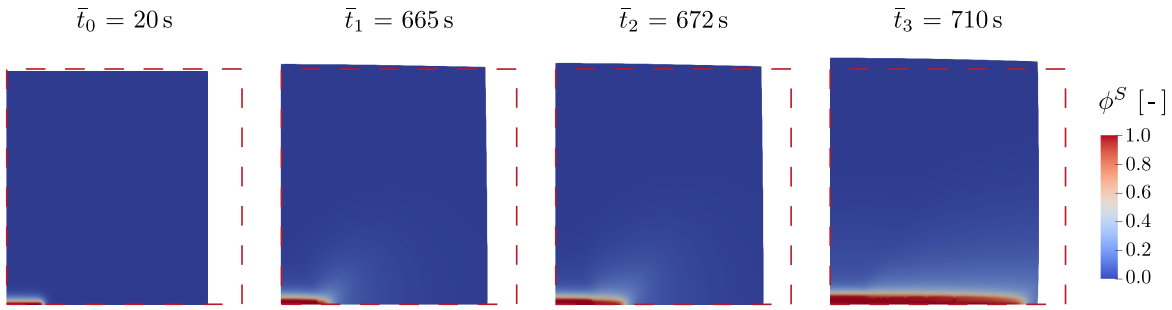

Figure 5.23: *Evolution of the phase-field variable at the deformed skeleton (scaled by a factor of 150) during the fracking process. The dashed red line sketches the initial configuration.*

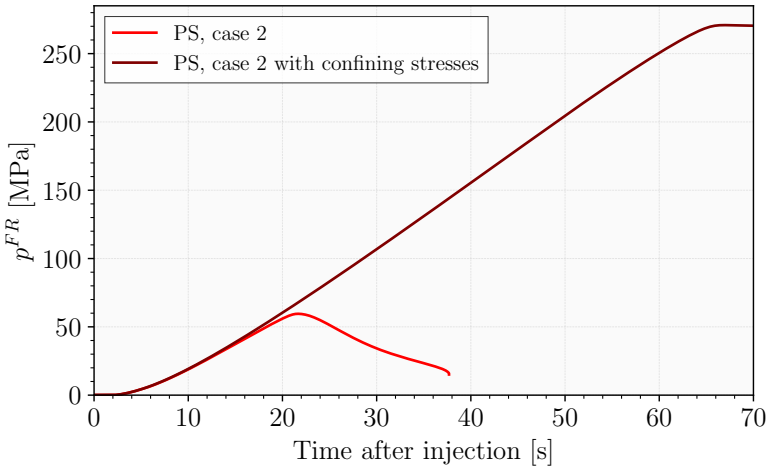

Figure 5.24: *Temporal development of the effective pore pressure at the initial crack tip (point B) with and without confining stresses after the liquid injection.*

The temporal evolution of the effective pore pressure starting at the initiation of the liquid injection for both models with and without confining stresses is displayed in Figure 5.24. As shown in the previous section, the fluid interaction, especially the gas compressibility, controls the pore-pressure growth. Therefore, the pore-pressure increase is the same for both boundary-value problems. However, in the current example, the confining stresses compress the pore space, thus hindering the undisturbed evolution of solid tensile strains. Instead, the pore-pressure increase resulting from the injection process must overcome the confining conditions to enable the necessary strain field and, therewith, the energy evolution necessary for crack propagation. As a result, the maximum pore pressure is higher than in the unconfined model, and the solid material breaks later under confining stresses than without. Nevertheless, the required stored energy for crack propagation is the same for both models, namely $W^S_{\mathrm{crack}} = 156\,\mathrm{kPa}$. This is consistent with the previous analysis, compare Figure 5.14.

5.3.2 Open and closed fractures

Confining stresses do not only slow down the crack propagation but may also yield hydraulically closed fractures. This feature will be discussed by introducing two initially closed cracks, compare Figure 5.25. Two numerical examples with different displacement ratios of Δu_1 to Δu_2, namely example 1 with $\Delta u_1/\Delta u_2 = 2.5$ at $v_{S1} = 0.03\,\mathrm{mm/s}$ and $v_{S2} = 0.012\,\mathrm{mm/s}$, and example 2 with $\Delta u_1/\Delta u_2 = 12.5$ at $v_{S1} = 0.15\,\mathrm{mm/s}$ and $v_{S2} = 0.012\,\mathrm{mm/s}$, are chosen, using the same ratios as have been investigated by Ehlers & Luo [94].

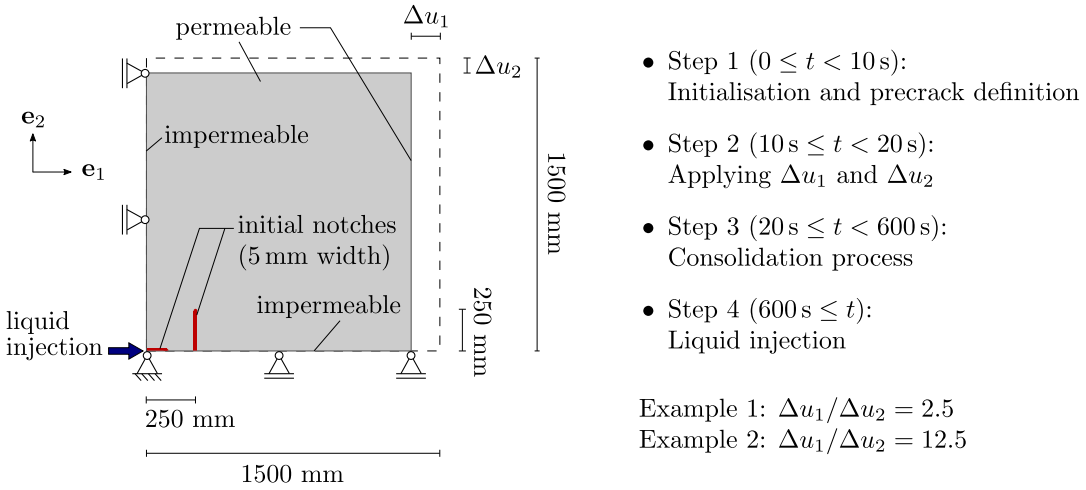

Figure 5.25: *Geometry and loading history of the initial-boundary-value problem of the fracking process under confining stresses (examples 1 and 2) with two initial precracks.*

Figures 5.26 and 5.27 show the area of interest for the examples 1 and 2, where the phase field ϕ^S, the effective pore pressure p^{FR} and the liquid saturation s^L are displayed at different time steps of the fracking process. As has been expected, the fractures evolve differently depending on the ratio of the confining stresses. Although the area is compressed in both directions, both initial precracks remain open in the case of example 1. In the case of example 2, however, the horizontal compression is so strong that the vertical precrack is closed. This can be seen from Figure 5.28, where the divergence of the solid displacement $\mathbf{u}_S$ is exhibited. As $\operatorname{div}\mathbf{u}_S > 0$ is the criterion for open or opening cracks, $\operatorname{div}\mathbf{u}_S \le 0$ is the criterion for closed or closing cracks, compare the crack-opening indicator $\mathcal{I}$ from (3.84).

In the case of example 1, both precracks are open with $\operatorname{div}\mathbf{u}_S > 0$ and thus $\mathcal{I} = 1$. In addition, the fracture has evolved at $t = 675\,\mathrm{s}$ at positive $\operatorname{div}\mathbf{u}_S$ at the top of the vertical precrack by wing-like fractures under an angle of approximately 40° to the right. As a result of the fracture opening, the Darcy-type flow in the porous domain has changed towards a Navier-Stokes-type flow in the open fractures. This switch is displayed in Figure 5.29, where the liquid velocity profile is shown for the wing-like fracture. The transition zone regulates the velocity between the two extreme states of Darcy-type and free flow. The corresponding liquid and gas streamlines can be seen in Figure 5.30. It is also seen from Figure 5.26 that the pore pressure increases around both cracks and the evolving fracture, and that the saturation field likewise follows the crack pattern.

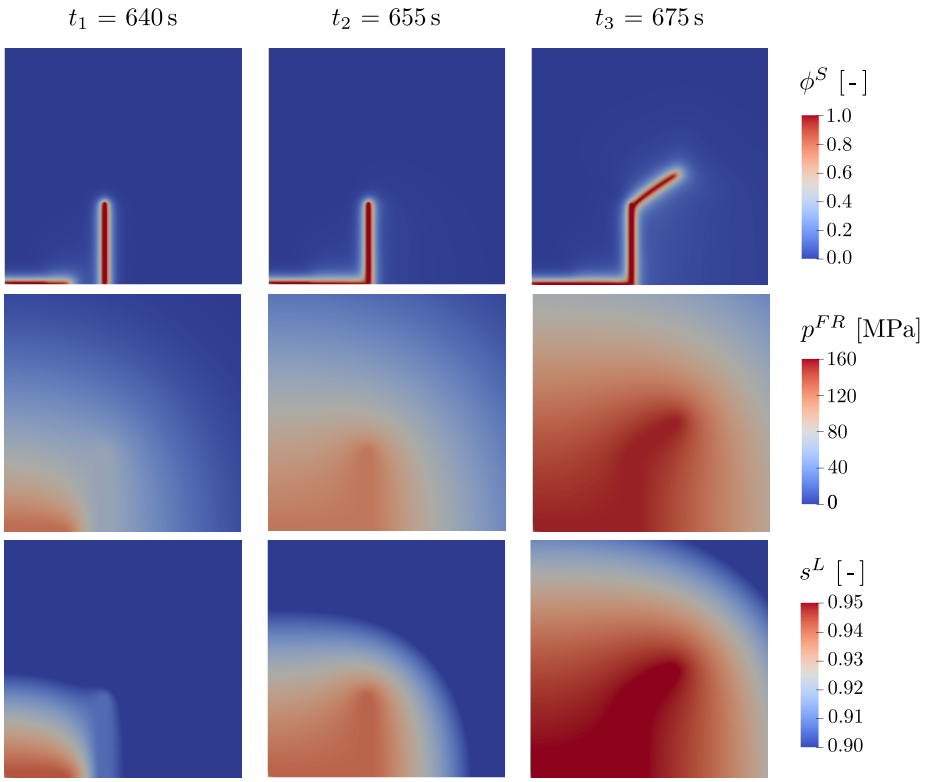

Figure 5.26: *Evolution of the phase field, pore pressure and saturation for example 1.*

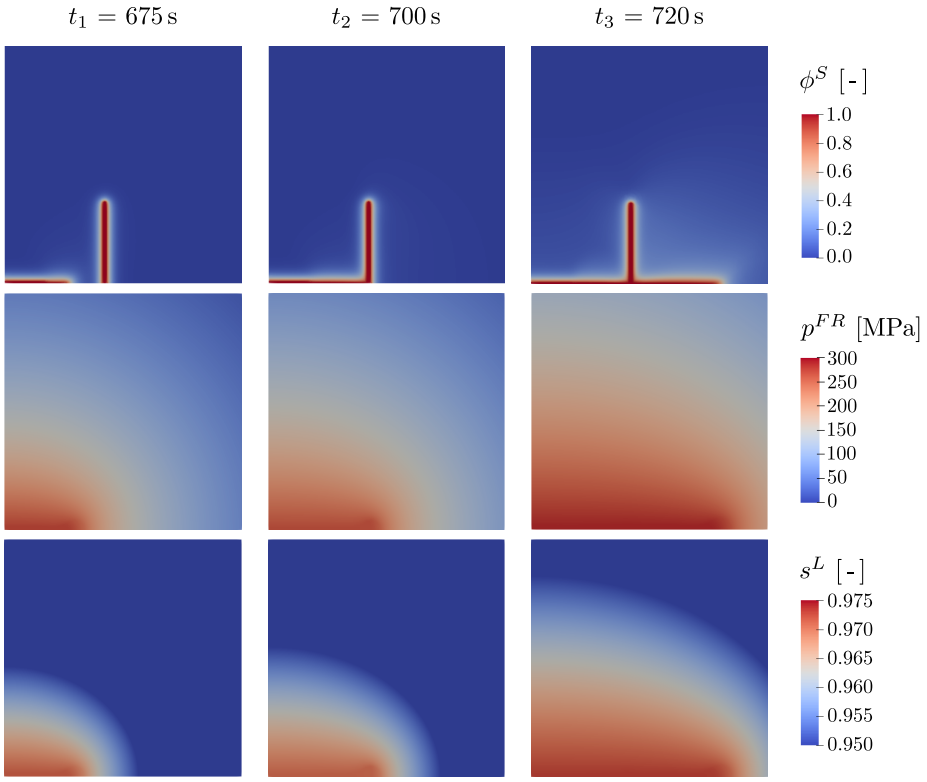

Figure 5.27: *Evolution of the phase field, pore pressure and saturation for example 2.*

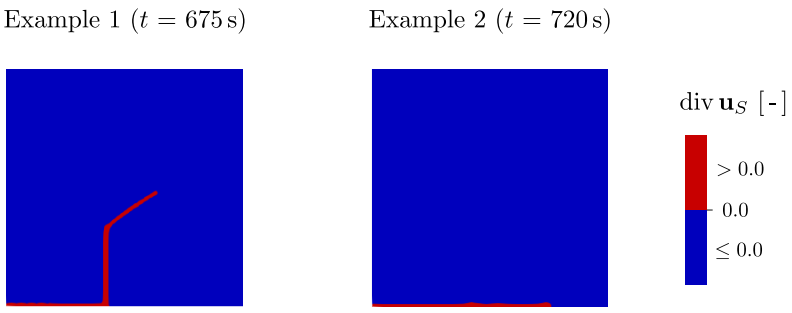

Figure 5.28: *Divergence of the solid displacement for example 1 at time $t = 675$ s and for example 2 at time $t = 720$ s.*

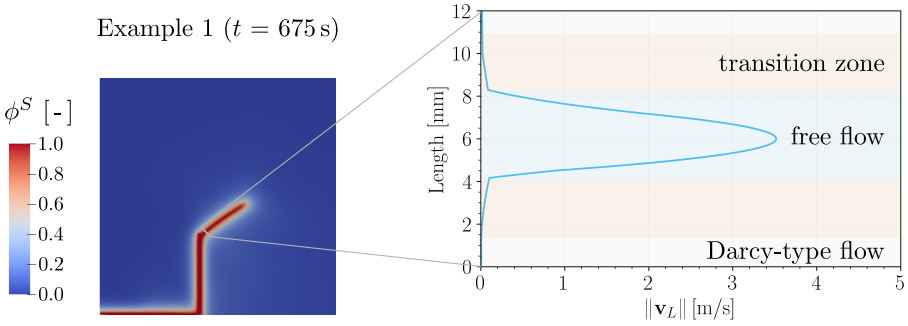

Figure 5.29: *Liquid velocity profile in the wing-like fracture for example 1 at time $t = 675$ s.*

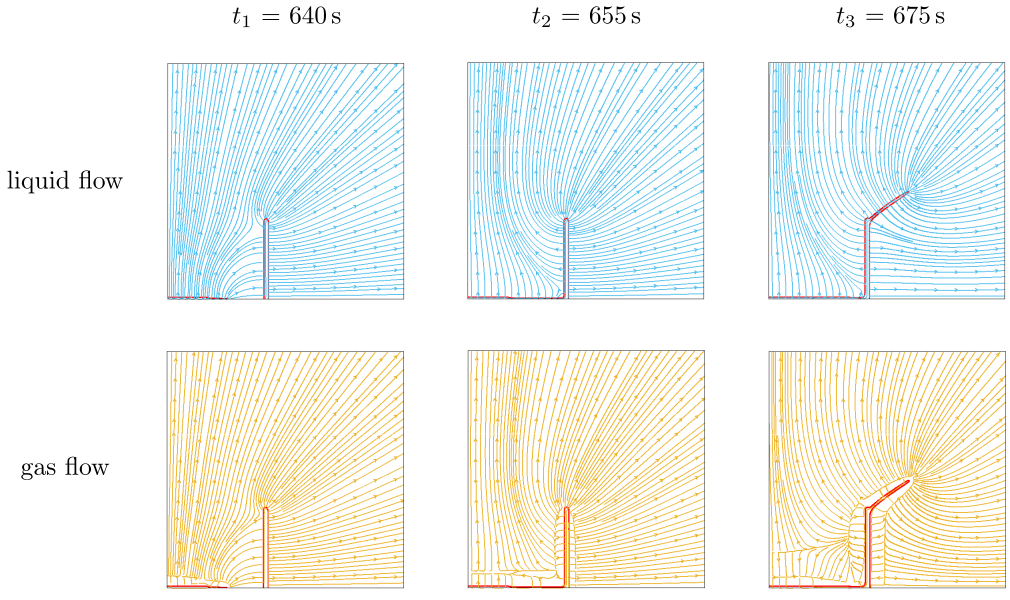

Figure 5.30: *Streamlines of the liquid and gas flow for example 1 during the fracking process under confining stresses with two initial precracks.*

In the case of example 2, the ratio of Δu_1 to Δu_2 is much higher, such that also the horizontal confining stress is much higher than in example 1. Thus, the vertical precrack remains almost closed, compare Figure 5.28. As a result, the whole area is under compression with $\operatorname{div} \mathbf{u}_S \leq 0$ and thus $\mathcal{I} = 0$ except for the horizontal precrack and the

evolving fracture in horizontal direction. As a result, Darcy-type flow can be observed in the whole area without the horizontal fracture, where the flow type has changed towards Navier-Stokes-type flow, also compare Figure 5.31. Here, it is also seen from the liquid and gas streamlines that the whole domain behaves like a porous medium without fractures except for the horizontal crack. Comparing these results with those of Figure 5.27, one again recognises that the fracturing process only touches the horizontal precrack with expectable consequences for the pore pressure and the liquid saturation.

Finally, the gas streamlines included in Figures 5.30 and 5.31 exhibit gas reflux due to the gas expansion in the crack. Similar to the computation with only one initial crack, compare Subsection 5.2.3, this reverse gas flow into the crack slows down the fracture evolution compared to a fully saturated model.

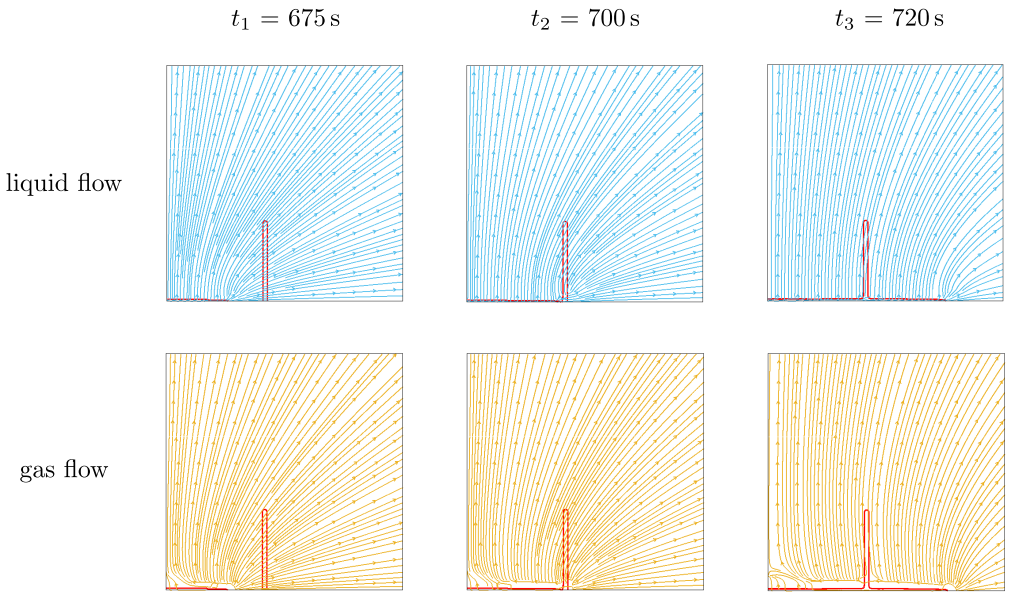

Figure 5.31: *Streamlines of the liquid and gas flow for example 2 during the fracking process under confining stresses with two initial precracks.*

5.4 Hydraulic fracturing in heterogeneous porous media

So far, the dynamic hydraulic fracturing problem has been evaluated for homogeneous porous media. However, natural porous materials exhibit material heterogeneities. In this sense, the inclusion of location-dependent material parameters is derived here. In contrast to stochastic phase-field modelling approaches, such as in Gerasimov *et al.* [117], a deterministic ansatz is studied. Thereby, predefined imperfection areas, as well as statistical fields of geomechanical properties, are considered. The main focus is discussing the impact of local heterogeneities in porous media on crack evolution and path. Here, a triphasic porous material is considered. Local heterogeneities in a biphasic porous material are discussed, for example, in Wagner *et al.* [246].

5.4.1 Consideration of material imperfection domains

First, a numerical example with a homogeneous domain is compared with a two-zone model containing a stiffer, predefined (rectangular) imperfection area.

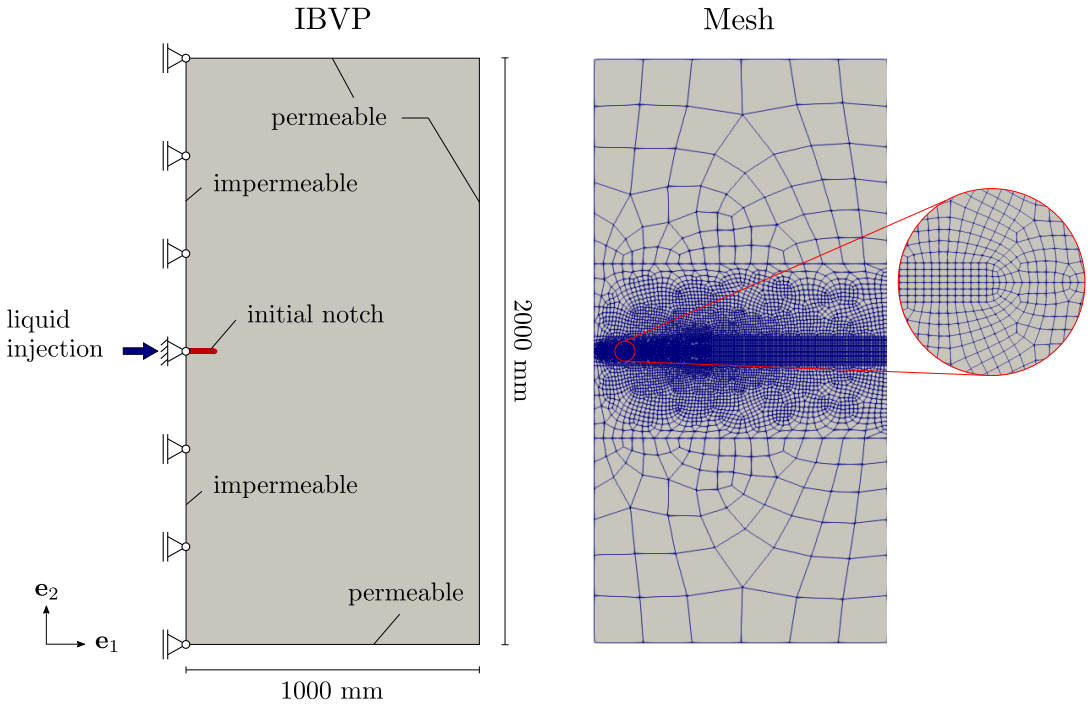

Figure 5.32: *Sketch of the initial-boundary-value problem (left) and finite-element mesh (right).*

Figure 5.32 (left) shows the basic two-dimensional initial-boundary-value problem. The initial and boundary conditions are comparable to those of the numerical model in Section 5.2. The considered domain of 1 m in length and 2 m in height is impermeable on its left and permeable on all the other edges. In the middle of the left edge, an initial notch of 100 mm length and 10 mm height is imposed via the initial pseudo-elastic energy $\mathcal{H}_0 = 134.865\,\mathrm{MJ/m^3}$, compare (4.33). A liquid flow is injected with an increasing flow rate of $\bar{v}^L = 5 \cdot 10^{-3}\,t\,\mathrm{m^3/(m^2 s)}$, where t is the current time. The model is mechanically fixed at the left edge of the initial notch and constrained in normal direction on the whole left edge. The other three edges, the bottom, the right and the top, are free to move. Thereby, the boundary conditions induce a symmetric system in the $\mathbf{e}_2$-direction. The gravitational forces and frictional gas forces are neglected. Moreover, note that no external forces are imposed on the system to avoid an influence on crack propagation despite the local heterogeneities of the material properties. The material parameters are the same as in Section 5.2 and listed in Table 5.3. Regarding the spatial discretisation of the model, a symmetric mesh with 8 848 two-dimensional elements is chosen with a refined central area of the domain, see Figure 5.32 (right).

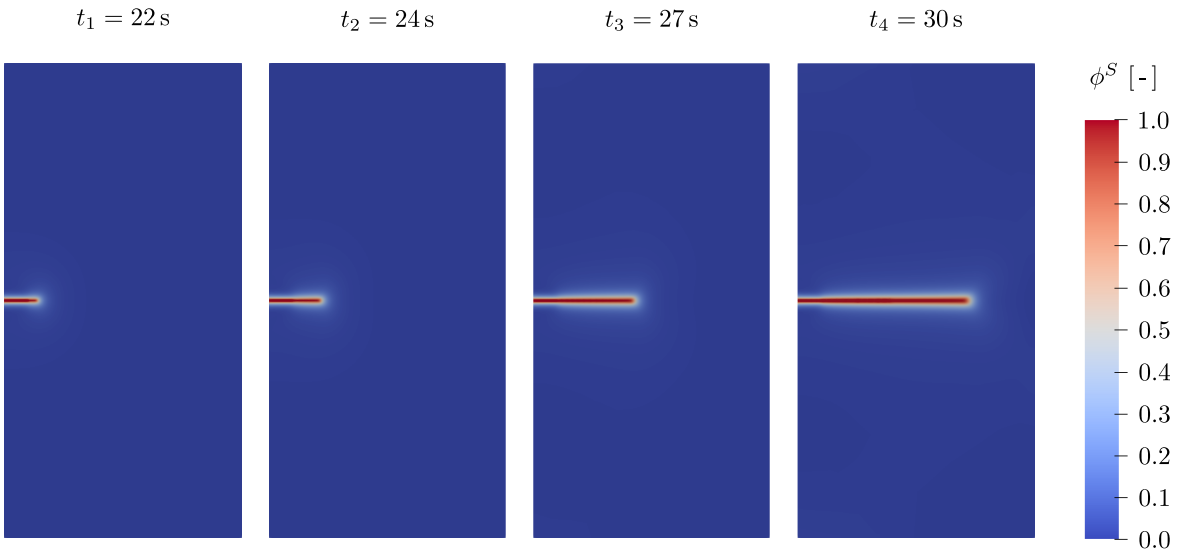

Figure 5.33: *Crack propagation in the homogeneous model at different time steps.*

In the case of a homogeneous model with constant material parameters in the whole area, i. e. using the Lamé constants from Table 5.3, the crack evolves horizontally through the model until reaching the right edge at time $t = 31.3\,\mathrm{s}$. Figure 5.33 shows the evolution of the phase-field variable for the homogeneous model.

In the next step, a rectangular area of $600\,\mathrm{mm} \times 100\,\mathrm{mm}$ is predefined in the direction of the crack propagation to model a two-zone domain. There, the Lamé constant λ^S is prescribed as a hundred times higher than in the rest of the model, see Figure 5.34. Note that the transition between the two areas is rather sharp. Such a material composition can be motivated, e. g., by layered rocks.

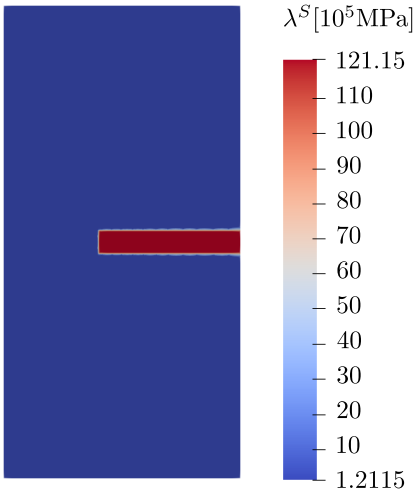

Figure 5.34: *Distribution of the Lamé constant λ^S in the idealised heterogeneous (two-zone) model.*

As can be seen in Figure 5.35, where the phase-field evolution for this latter model is depicted, the crack splits into two branches in order to circumvent the stiffer area. Moreover, the crack branches reach the right edge later than in the homogeneous model, compare

Figure 5.33 and Figure 5.35, time t_4. Once the stiffer area is bypassed, the crack straightens towards the permeable right edge. The system is still symmetric due to the choice of the ideal (symmetric) problem. Note that the computation is carried out in a dynamic setting. However, caused by the local heterogeneity of the ideal material inclusion, the crack would split even in a fully quasi-static setting.

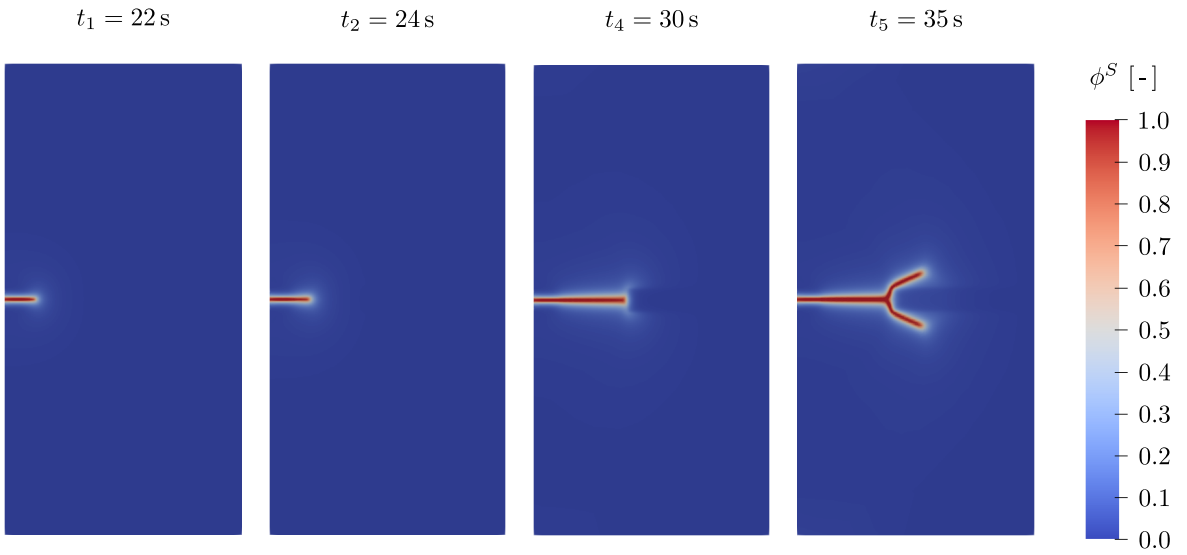

Figure 5.35: *Crack propagation in the two-zone model at different time steps.*

In analogy to the numerical examples of Sections 5.2 and 5.3, the gas is compressed around the branching crack, see Figure 5.36. This compression causes gas reflux into the crack while the liquid strictly flows to the permeable boundaries.

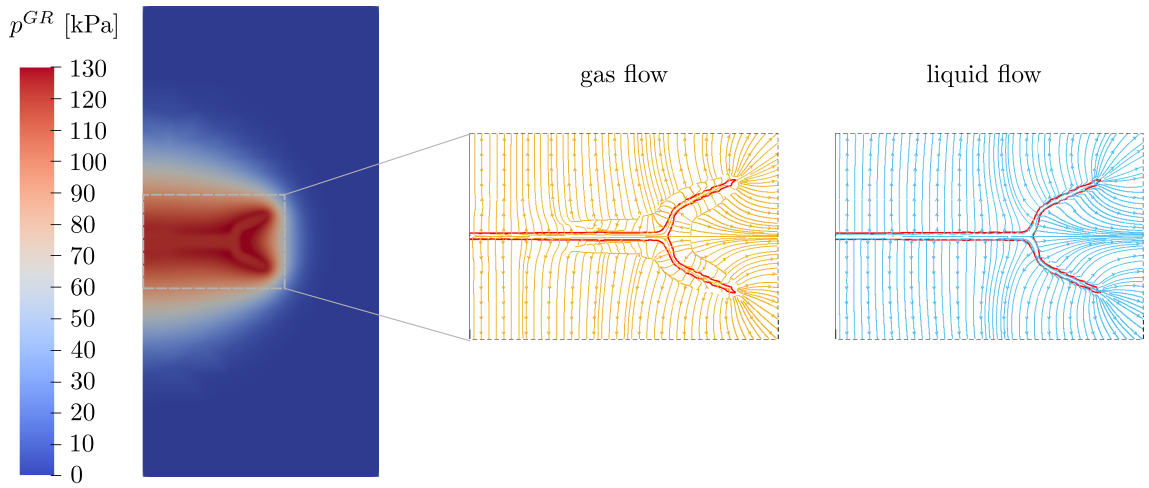

Figure 5.36: *Gas pressure (left) and fluid streamlines (right) in the idealised heterogeneous (two-zone) model at time $t_5 = 35\,\mathrm{s}$.*

5.4.2 Statistical fields of geomechanical properties

In the following, a further generalisation of predefined zones of material imperfections, discussed in the previous subsection, towards a statistical distribution of geomechanical parameters is carried out. To start with, a normal distribution with possible enhancement towards more complex distributions is used. Since the statistical fields of the solid properties induce spatially varying local stresses, an influence on the crack path is expected.

Statistical definition of a parameter

To generate random realisations of material parameters, a Gaussian variogram is assumed, compare, e. g., Kitanidis [159]. Similar to the previous example, the focus is here on a statistical distribution of the Lamé constant λ^S. In this regard, the distribution of λ^S satisfies the following Gaussian variogram

$$\begin{aligned} &p_{\mathrm{G}}(\lambda^S) = (2\pi)^{\frac{N_v}{2}} |\boldsymbol{\Sigma}|^{\frac{1}{2}} \exp\left(\tfrac{1}{2}\boldsymbol{\mu}^T \boldsymbol{\Sigma}^{-1} \boldsymbol{\mu}\right) \\ &\text{with} \quad \Sigma_{ij} = \sigma^2 \left\{1 - \exp[-(|\mathbf{x}_i - \mathbf{x}_j|/\ell)^2]\right\} . \end{aligned} \tag{5.5}$$

Thereby, $\boldsymbol{\mu}$ contains at each entry the mean value μ of the field, N_v represents the number of discretisation points, and $\boldsymbol{\Sigma}$ stands for the covariance matrix with coefficients Σ_{ij}. Moreover, σ^2 signifies the variance of the field, $\mathbf{x}_i$ and $\mathbf{x}_j$ are the vectors describing the positions of discretisation points, and ℓ is the so-called statistical length-scale parameter, also termed correlation length. This latter determines the spatial variance of the material parameter. Particularly, the smaller ℓ is chosen, the more significant is the variance of λ^S to the next point, whereas, conversely, the larger ℓ is chosen, the smaller is the change to the next point, see Figure 5.38. In particular, the parameters shown in Table 5.4 are used in this work. The corresponding normal distribution, which is fulfilled at each material point, is depicted in Figure 5.37. The generation of random material parameter fields is implemented on a regular grid using MATLAB. In addition, a customised algorithm is implemented after Wagner [243] in PANDAS to assign the spatially dependent material parameters. The approach is briefly introduced in Appendix C.4.

Table 5.4: *Statistical parameters.*

Parameter	Symbol	Value
Mean value	μ	$5.05 \cdot 10^{11}\,\mathrm{Pa}$
Standard deviation	σ	$1.65 \cdot 10^{11}\,\mathrm{Pa}$
Correlation lengths	ℓ	$7, 70, 140, 700\,\mathrm{mm}$
Number of discretisation points	N_v	120

On the influence of a statistical distribution of the first Lamé constant

To study the influence of statistical fields of geomechanical properties, the IBVP of Subsection 5.4.1 is now studied for different random distributions of the Lamé constant λ^S.

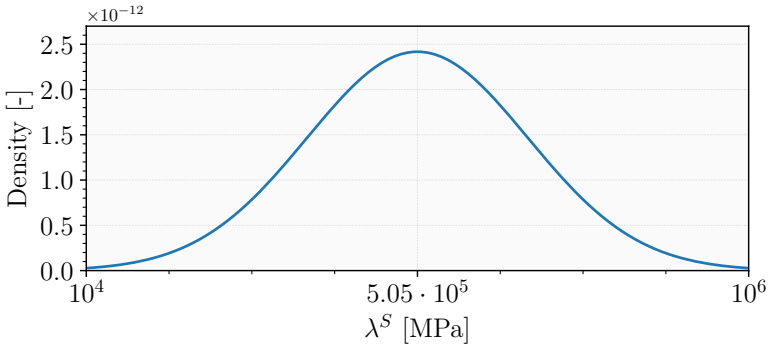

Figure 5.37: *Density curve of the Lamé constant λ^S.*

The geostatistical fields are considered in terms of the definition and implementation described above and in Appendix C.4. The mean value, which is chosen around five times higher than the Lamé constant from Table 5.3, and the standard derivation are the same for all of the following examples, see Table 5.4. Only the statistical length-scale parameter is varied, namely to 7 mm (model 1), 70 mm (model 2), 140 mm (model 3) and 700 mm (model 4). This choice results in different structures of the Lamé-constant variations with the same (global) statistic distribution, see Figure 5.38.

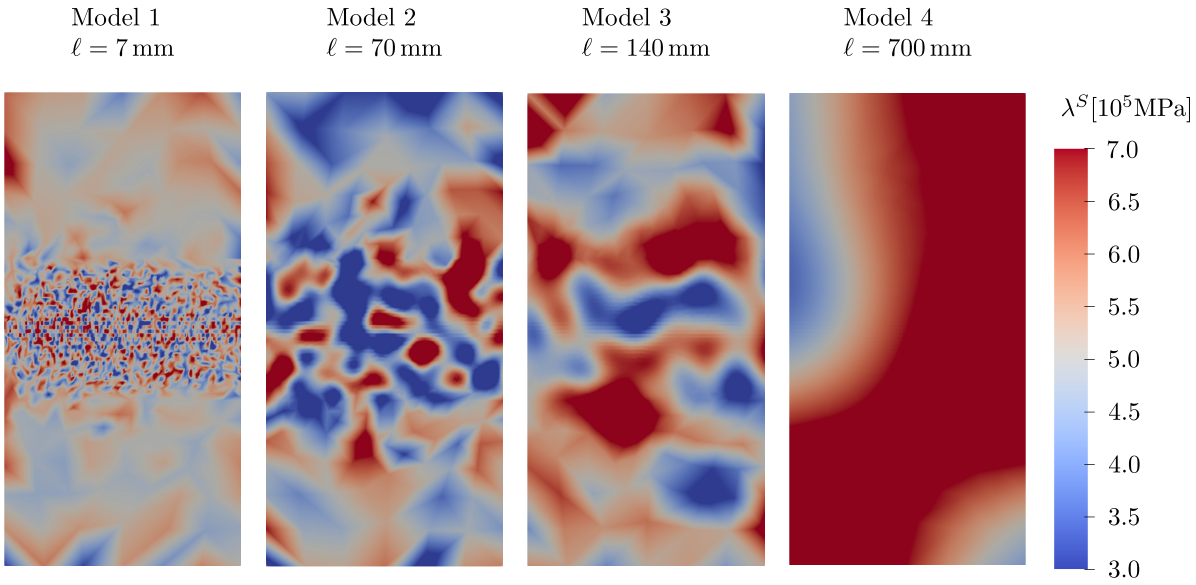

Figure 5.38: *Distribution of the Lamé constant λ^S for four different heterogeneous models using a Gaussian variogram.*

Each sample structure can be related to the microstructure of a specific porous material, namely with many smaller (model 1) or a few larger (model 4) areas with higher or lower stiffness, respectively. Note that the smeared λ^S-variation in the upper and lower parts of model 1 is due to the coarser mesh in these areas, see Figure 5.32 (right), since the influence radius for the weighting of the material parameter (i. e. the voxel information) depends on the individual element size, compare Appendix C.4.

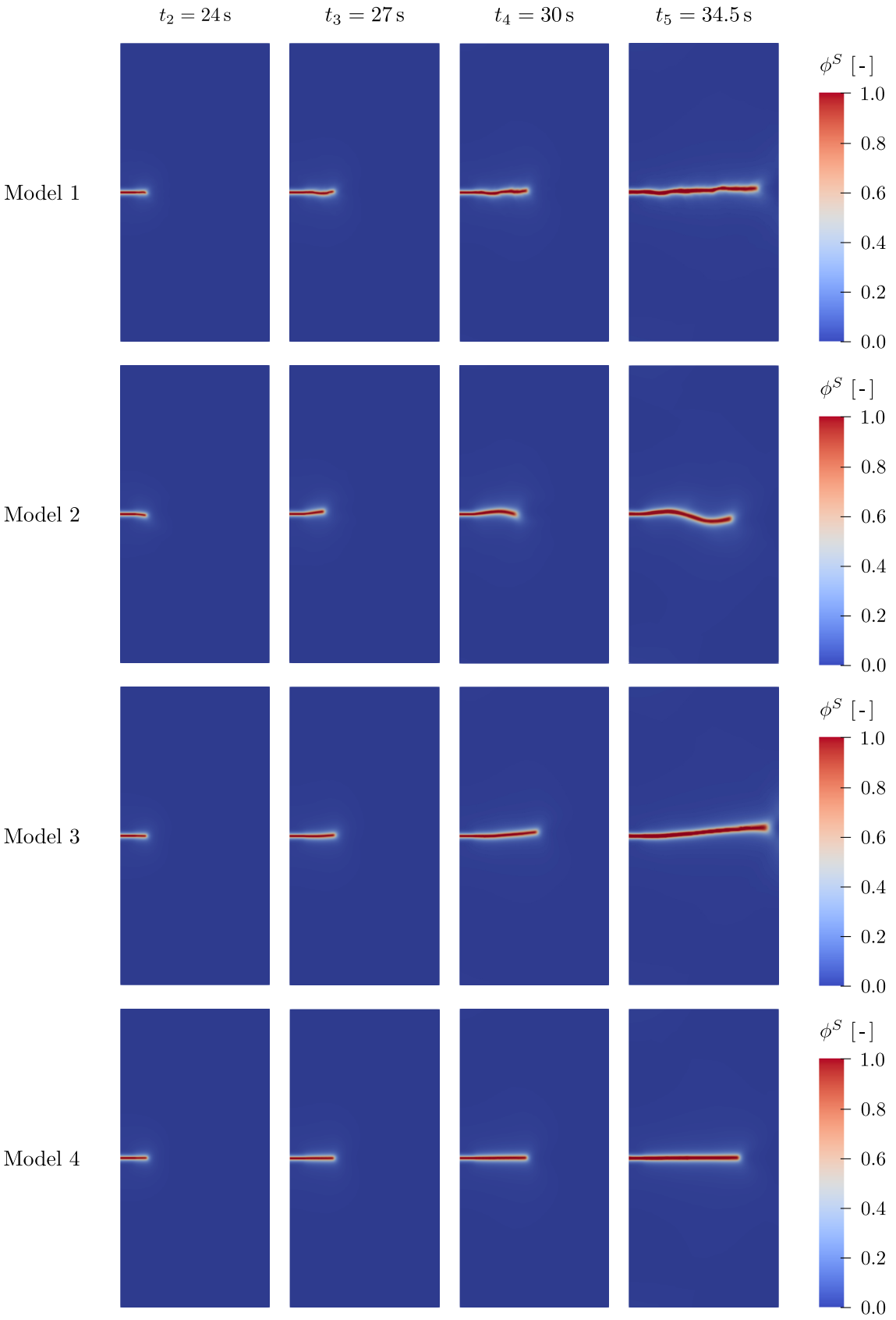

Figure 5.39: *Crack propagation for the four heterogeneous models at different time steps.*

Figure 5.39 shows the crack evolution for each model at intermediate time steps before the crack reaches the right edge. In model 1, the statistical length-scale parameter ℓ is chosen small, and the heterogeneities are in the order of a few elements. Physically, the crack always follows the path with the lowest resistance. Consequently, the crack evolves not straight horizontally to the right edge in model 1 but interferes with the material parameter variations and shows many fluctuations. Since the variations in the properties are very local in this model, the disturbed crack path is compensated such that the crack as a whole hits the right edge more or less in the centre.

The most significant deflection of the crack path is visible in model 2 and model 3. Here, the statistical length-scale parameter is chosen to be moderate such that the inclusions are in the order of magnitude of the initial notch length. As a result, the crack bypasses the areas of greater stiffness and winds around these inclusions, creating a wave-like crack field, see Figure 5.39 (model 2, model 3). To emphasise this phenomenon, Figure 5.40 shows the crack path in black colour (for $\phi^S \geq 0.85$) over the distribution of the Lamé constant at time $t_5 = 34.5\,\mathrm{s}$. It can be seen that the crack is deflected by the areas with higher stiffness.

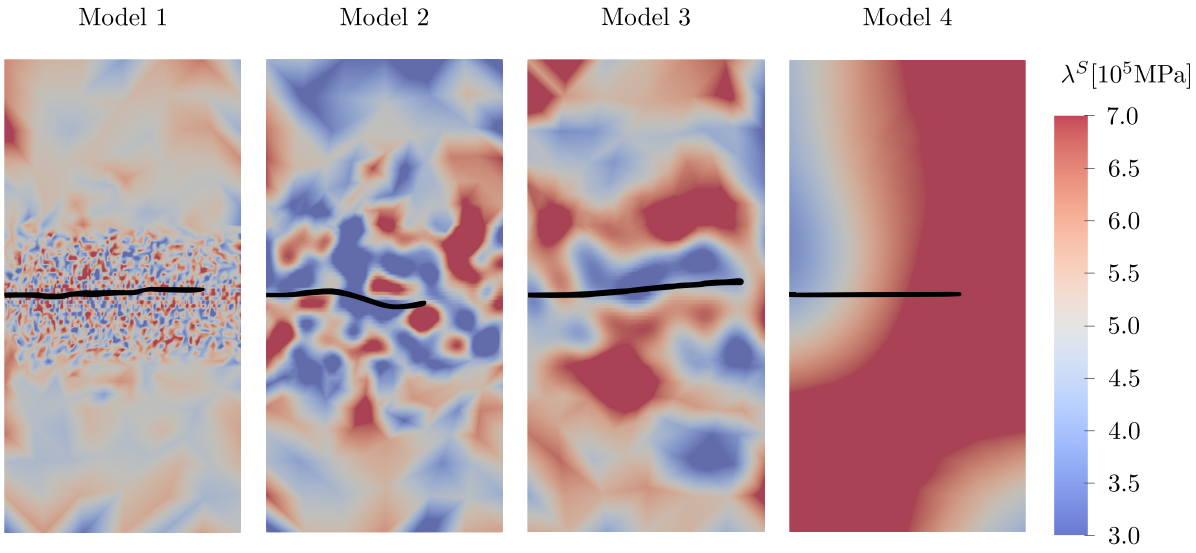

Figure 5.40: *Crack paths in black colour ($\phi^S \geq 0.85$) and distribution of the Lamé constant λ^S at time $t_5 = 34.5\,s$ for the four heterogeneous models.*

Finally, the correlation length is set to 700 mm in model 4, corresponding approximately to the half-domain width. Here, the heterogeneous inclusions are large in comparison to the notch dimensions. The crack evolves more or less horizontally, as in the case of the homogeneous model, even though there is a large area of higher stiffness in front of the crack, similar to the idealised two-zone model from Subsection 5.4.1. However, the crack path differs significantly from the two-zone model, where the crack branches. This different behaviour is caused by the transition characteristics from softer to stiffer areas. The transition is rather sharp in the two-zone model, causing the crack branching, whereas the transition in model 4 is relatively smooth, without a significant stiffness change at the crack tip. Moreover, the difference in stiffness values is more significant in the two-zone

model than in model 4. As a result, the crack slows down for the latter case but stays on its original path and does not turn in a different direction.

Figure 5.41 displays the crack evolution for three statistical distributions with the same correlation length to show the randomness of each statistical field. The crack path is depicted in black colour ($\phi^S \geq 0.85$) and the distribution of the Lamé constant in the back. Example 1 corresponds to the results of model 2 of the previous figures. Even if all statistical properties are the same for the three examples, the local assignment of the stiffer areas varies, and so does the crack path. This insight shows that the crack propagation does not depend only on the choice of the correlation length but is specific to each statistical field.

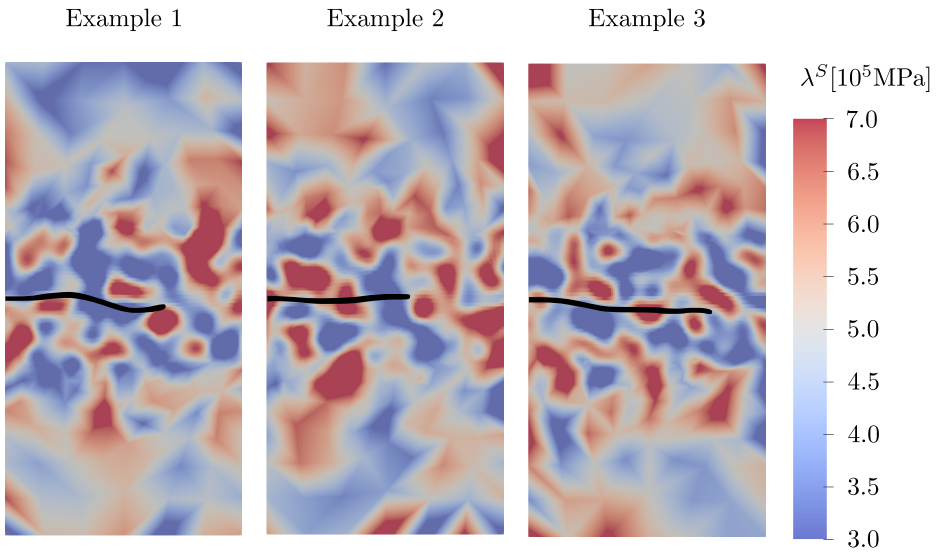

Figure 5.41: *Crack paths in black ($\phi^S \geq 0.85$) and distribution of the Lamé constant λ^S at time $t_5 = 34.5\,s$ for three examples with the same correlation length $\ell = 70$ mm (model 2).*

In conclusion, an effect on the crack path is identified in models with minor and moderate length-scale parameters caused by the local variations of elastic stiffness properties representing a heterogeneous porous solid skeleton. Moreover, each statistical field yields an exclusive crack path.

Chapter 6:
Summary and Outlook

6.1 Summary

Hydraulic fracturing has raised concerns regarding environmental and health risks, such as groundwater contamination, air pollution and microseismic activities. Understanding the ongoing processes of fluid-driven fractures in porous media is crucial to minimise risks and prevent these hazards. This thesis enlarged the knowledge of dynamic processes of brittle fracturing in unsaturated porous media. A continuum-mechanical model for partially saturated porous media was developed, which includes the possibility of describing hydraulically driven fracturing processes. The model is thermodynamically consistent, resulting in a highly coupled system of partial differential equations solved monolithically.

Based on the Theory of Porous Media (TPM), the model consists of a brittle, materially incompressible elastic solid with two immiscible pore fluids, an incompressible liquid and a compressible gas, both percolating the interconnected pore space. The TPM considers an individual motion function and a set of balance equations for every constituent, coupled to each other by production terms. In the context of hydraulic fracturing, this approach enabled coupling the solid deformation to the fluid pressure. The TPM model was enhanced by the phase-field approach to fracture to describe fluid-driven fracturing processes. The phase field yields diffuse interfaces between broken and unbroken material and prevents discontinuities during the fracturing process. Since a crack is solely induced under tension and not compression, the phase field reduced only the tensile part of the solid stiffness in this monograph. Therefore, a spectral decomposition was applied to split the solid strain into positive and negative values and distinguish between tension and compression. Moreover, a history variable, responsible for the phase field's evolution as it covers the maximum tensile energy obtained in the deformation process, was used in this model. Although the phase-field evolution is solid-based, the interaction of the pore fluids strongly influences the fracturing behaviour. This interaction was examined in depth within the scope of this thesis. A constitutive relation for the pressure difference between liquid and gas described as a function of the liquid saturation was developed for the particular problem. Since hydraulic fracturing is a highly dynamic process, the standard hydromechanical relations for capillary effects valid in an equilibrium state do not apply to this model. A specific constitutive relation was proposed to encompass the equilibrium (capillary) behaviour with a positive pressure difference and the dynamic fluid reaction with a negative pressure difference. Using this relation, both the dynamic behaviour near the crack and injection as well as the capillary effects in the distant vicinity of the crack were considered in the overall process. Furthermore, the crack-opening-indicator was included in the constitutive setting of the fluid phases. This additional scalar variable distinguishes between an hydraulically open and closed crack. Depending on these two states, the liquid flow switches between a Darcy-flow regime in the intact porous medium

and a Navier–Stokes regime in fully broken zones.

The coupled partial-differential-equations system was solved monolithically using the Finite-Element code PANDAS. The numerical scheme consisted of the pore fluids' volume/mass and momentum balances, the overall momentum balance adding all individual momentum balances, and the phase-field evolution. Instead of transferring the pressure terms of the fluid momentum balances towards the boundary, they were left in the volume integral. Nevertheless, these terms are still active at the boundary as they are considered within the boundary term of the overall momentum balance. This procedure has massive numerical advantages when injection processes are computed since different boundary conditions have to be coupled.

Based on this procedure, several numerical examples were investigated. First, the model of fluid interaction under equilibrium and the solid fracturing process were verified with experimental and analytical results, respectively. Then, proceeding from a single crack, the fracturing behaviour of the solid skeleton was examined in detail. For this purpose, the stored solid energy was split into components, and the effect of crack propagation on the different proportions was analysed. In the same example, the mutual interaction of the fluids during the fracking process was also assessed. Gas pressure compression at the crack tip and subsequent gas reflux into the crack area were identified. By comparing fully to partially saturated models, it was shown that the presence of pore gas primarily hinders the fracturing process. This deceleration was attributed to the slower build-up of pore pressure caused by the gas compressibility.

A second group of numerical examples displayed more realistic scenarios by assessing two types of heterogeneities in partially saturated porous media. First, global heterogeneities induced by external loads were evaluated. Such a consideration is essential as soils and rocks in nature are often subjected to external stresses, such as overlying rock loads, tectonic forces, or thermal stresses. In this context, two initial cracks – one horizontal and one vertical – were applied to the specimen, accompanied by different ratios of horizontal to vertical displacements. Both initial fractures opened in the first of these examples, so the fluids dominantly searched their flow directions along these cracks. In contrast, an increase in the displacement ratio hydraulically closed the vertical fracture in the second example, and the fluid flow exhibited a flow behaviour without taking notice of the closed crack. The gas reflux observed in the single-notch model was recovered in both cases.

The second type of heterogeneity considered variations within the porous structure by including location-dependent material parameters. This model introduced predefined regions of higher stiffness, namely variations of the elastic Lamé constant, to simulate material imperfections. Crack branching caused by this latter was observed. The model was furthermore improved by implementing statistical fields of geomechanical properties. Numerical examples with different statistical correlation lengths were compared to study the influence of material variations. As a result, an effect of the statistical fields on the crack evolution was made out. The spatially varying local stresses caused characteristic deviations in the crack path.

In conclusion, this thesis applied the phase-field approach to fracture within the Theory of Porous Media to address fully dynamic fracturing problems in partially saturated

porous media. The presented methodical and numerical model holds promise for various applications.

6.2 Future aspects

At this stage, the proposed triphasic TPM model can describe partially saturated porous material, where a liquid and a gaseous pore fluid percolate the solid skeleton pore space, with particular application to dynamic hydraulic fracturing processes. The theoretically developed and numerically implemented model already allowed the study of the interaction of fluids and the effect of heterogeneities in the fracturing process. Nevertheless, there exist several (unresolved) issues that require further consideration.

First, the presented model considers equilibrium and dynamic effects for the fluid interaction in the pore space and distinguishes between Darcy and Navier-Stokes flow within the intact and broken areas, respectively, for the liquid phase. However, the frictional gas stresses have been neglected in the numerical examples, resulting in a Darcy-type flow in the whole domain for the gas phase. This assumption is justifiable since the effective gas viscosity is two orders of magnitude smaller than the liquid one in the specific problem. Nevertheless, if the interaction of the two phases in the pore space has to be studied in detail, it would be advantageous also to resolve the gas stresses.

A further step towards a more realistic model concerns the model's dimension. The numerical examples were proposed in quasi-two and axial-symmetric three dimensions at this stage. One step towards a more realistic view of the fracturing process in nature is to compute fully non-symmetric three-dimensional numerical examples. However, this comes along with an enormous computational effort. In this context, particular attention must be paid to the mesh to achieve results in a realistic time period. Notably, the mesh has to be chosen very fine around the crack tip to resolve the transition between broken and intact material with respect to the length-scale parameter, while it can be chosen large in the surrounding areas. An adaptive mesh refinement would be advantageous for fully non-symmetric three-dimensional numerical examples. With this approach, the mesh could adaptively refine solely at the crack tip and widen in the surrounding, saving valuable computational costs. Besides mesh adaptivity, an extension towards a parallelisation scheme for the monolithic solution of the partial differential equations is promising to save computational efforts. In this context, combining PANDAS with the commercial Finite-Element tool Abaqus is promising, compare Schenke [217].

Up to now, two types of heterogeneities were considered separately. On the one hand, global heterogeneities arising from loading conditions and, on the other hand, local inhomogeneities in the porous structure were examined. Regarding this latter case, hydraulic parameters, such as porosity and permeability, could be considered apart from the mechanical parameters. Moreover, the pressure-difference-saturation relation could also be varied in a more complex system. In addition, the crack path deviation due to statistical variation of the material parameters was only discussed so far. A further step in this matter could be the quantification of these deviations. Finally, a mix of both heterogeneity types could be evaluated to improve the understanding of heterogeneities on

the fracturing behaviour in a more general manner. In particular, the question of which inhomogeneity type is decisive for a crack path deviation when both are active could be assessed.

Last, also drying-induced fractures play a role in unsaturated media besides fluid-driven fractures. In this case, the fractures result from drying shrinkage. Particularly, the solid stresses are coupled not only with the phase field but also with the saturation. For example, Cajuhi *et al.* [61] linked the fracture energy to the water content, directly connected to the liquid saturation. Furthermore, Heider & Sun [137] coupled the solid free energy to the phase field and the pressure suction, which is, in turn, linked to the saturation. In both cases, desiccation induces stiffness loss, which can foster or lead to fracture. These aspects could be further considered in the presented model to assess drying-induced in addition to hydraulic fractures.

Appendix A:
Selected relations of tensor calculus

This appendix section offers a condensed set of essential rules for vector and tensor operations. For a more extensive discussion, the reader is referred to the vector- and tensor script of the Institute of Applied Mechanics (Chair of Continuum Mechanics) at the University of Stuttgart, cf. Ehlers [79], which is partly based on the fundamental textbook of de Boer [37].

A.1 Tensor algebra

For the following considerations arbitrary **placeholders** are introduced, viz.:

$$\begin{array}{lll} \{\alpha, \beta\} & \in \mathbb{R} & : \text{scalars (zero-order tensors) as rational quantities,} \\ \{\mathbf{a}, \mathbf{b}, \mathbf{c}\} & \in \mathcal{V}^3 & : \text{vectors (first-order tensors) of the proper} \\ & & \quad \text{Euklidian 3-d vector space } \mathcal{V}^3, \\ \{\mathbf{A}, \mathbf{B}, \mathbf{C}\} & \in \mathcal{V}^3 \otimes \mathcal{V}^3 & : \text{tensors (of second order) of the corresponding} \\ & & \quad \text{dyadic product space } \mathcal{V}^3 \otimes \mathcal{V}^3. \end{array}$$

Collected rules for **products** of second-order tensors with scalars or vectors:

$$\begin{array}{rcll} \alpha\,(\beta\,\mathbf{A}) & = & (\alpha\,\beta)\,\mathbf{A} & : \text{associative law} \\ \mathbf{A}\,(\alpha\,\mathbf{a}) & = & \alpha(\mathbf{A}\,\mathbf{a}) \;=\; (\alpha\,\mathbf{A})\,\mathbf{a} & : \text{associative law} \\ (\alpha+\beta)\,\mathbf{A} & = & \alpha\,\mathbf{A} + \beta\,\mathbf{A} & : \text{distributive law} \\ \alpha\,(\mathbf{A}+\mathbf{B}) & = & \alpha\,\mathbf{A} + \alpha\,\mathbf{B} & : \text{distributive law} \\ \mathbf{A}\,(\mathbf{a}+\mathbf{b}) & = & \mathbf{A}\,\mathbf{a} + \mathbf{A}\,\mathbf{b} & : \text{distributive law} \\ (\mathbf{A}+\mathbf{B})\,\mathbf{a} & = & \mathbf{A}\,\mathbf{a} + \mathbf{B}\,\mathbf{a} & : \text{distributive law} \\ \alpha\,\mathbf{A} & = & \mathbf{A}\,\alpha & : \text{commutative law} \\ \mathbf{a} & = & \mathbf{A}\,\mathbf{b} & : \text{linear mapping} \\ \mathbf{I}\,\mathbf{a} & = & \mathbf{a} & : \mathbf{I} : \text{identical element (linear mapping)} \\ \mathbf{0}\,\mathbf{a} & = & \mathbf{0} & : \mathbf{0} : \text{zero element (linear mapping)} \end{array} \tag{A.1}$$

Collected rules for **scalar (inner) products** of tensors:

$$\begin{array}{rcll} (\alpha\,\mathbf{A})\cdot\mathbf{B} & = & \mathbf{A}\cdot(\alpha\,\mathbf{B}) = \alpha\,(\mathbf{A}\cdot\mathbf{B}) & : \text{associative law} \\ \mathbf{A}\cdot(\mathbf{B}+\mathbf{C}) & = & \mathbf{A}\cdot\mathbf{B} + \mathbf{A}\cdot\mathbf{C} & : \text{distributive law} \\ \mathbf{A}\cdot\mathbf{B} & = & \mathbf{B}\cdot\mathbf{A} & : \text{commutative law} \\ \mathbf{A}\cdot\mathbf{B} & = & 0 \quad \forall\ \mathbf{A}\,, \text{ if } \mathbf{B} \equiv \mathbf{0} & \\ \mathbf{A}\cdot\mathbf{A} & > & 0 \quad \forall\ \mathbf{A} \neq \mathbf{0} & \end{array} \tag{A.2}$$

Collected rules for **tensor products** of second-order tensors:

$$\begin{aligned}
\alpha\,(\mathbf{A}\,\mathbf{B}) &= (\alpha\,\mathbf{A})\,\mathbf{B} = \mathbf{A}\,(\alpha\,\mathbf{B}) && : \text{associate law}\\
(\mathbf{A}\,\mathbf{B})\,\mathbf{a} &= \mathbf{A}\,(\mathbf{B}\,\mathbf{a}) && : \text{associate law}\\
(\mathbf{A}\,\mathbf{B})\,\mathbf{C} &= \mathbf{A}\,(\mathbf{B}\,\mathbf{C}) && : \text{associate law}\\
\mathbf{A}\,(\mathbf{B}+\mathbf{C}) &= \mathbf{A}\,\mathbf{B}+\mathbf{A}\,\mathbf{C} && : \text{distributive law}\\
(\mathbf{A}+\mathbf{B})\,\mathbf{C} &= \mathbf{A}\,\mathbf{C}+\mathbf{B}\,\mathbf{C} && : \text{distributive law}\\
\mathbf{A}\,\mathbf{B} &\neq \mathbf{B}\,\mathbf{A} && : \textbf{no} \text{ commutative law}\\
\mathbf{I}\,\mathbf{A} &= \mathbf{A}\,\mathbf{I} = \mathbf{A} && : \mathbf{I} : \text{identical element (linear mapping)}\\
\mathbf{0}\,\mathbf{A} &= \mathbf{A}\,\mathbf{0} = \mathbf{0} && : \mathbf{0} : \text{zero element (linear mapping)}
\end{aligned} \tag{A.3}$$

Collected rules for **transposed** and **inverse** second-order tensors:

$$\begin{aligned}
(\mathbf{a}\otimes\mathbf{b})^T &= (\mathbf{b}\otimes\mathbf{a}) & \mathbf{A}^{-1} &= (\det\mathbf{A})^{-1}\,(\operatorname{cof}\mathbf{A})^T\\
(\alpha\,\mathbf{A})^T &= \alpha\,\mathbf{A}^T & \rightarrow\ \mathbf{A}^{-1} &\text{ exists if } \det\mathbf{A}\neq 0\\
(\mathbf{A}\,\mathbf{B})^T &= \mathbf{B}^T\mathbf{A}^T & &\\
\mathbf{a}\cdot(\mathbf{B}\,\mathbf{b}) &= (\mathbf{B}^T\mathbf{a})\cdot\mathbf{b} & \mathbf{A}\,\mathbf{A}^{-1} &= \mathbf{A}^{-1}\,\mathbf{A} = \mathbf{I}\\
\mathbf{A}\cdot(\mathbf{B}\,\mathbf{C}) &= (\mathbf{B}^T\mathbf{A})\cdot\mathbf{C} & (\mathbf{A}^{-1})^T &= (\mathbf{A}^T)^{-1} =: \mathbf{A}^{T-1}\\
(\mathbf{A}+\mathbf{B})^T &= \mathbf{A}^T+\mathbf{B}^T & (\mathbf{A}\,\mathbf{B})^{-1} &= \mathbf{B}^{-1}\mathbf{A}^{-1}
\end{aligned} \tag{A.4}$$

The computation rules of the **determinant** and the **cofactor** are given via

$$\begin{aligned}
\det\mathbf{A} &= \tfrac{1}{6}\,(\mathbf{A}\divideontimes\mathbf{A})\cdot\mathbf{A} = \tfrac{1}{6}\,(\operatorname{tr}\mathbf{A})^3 - \tfrac{1}{2}\,(\operatorname{tr}\mathbf{A})\,(\mathbf{A}^T\cdot\mathbf{A}) + \tfrac{1}{3}\,(\mathbf{A}\mathbf{A})^T\cdot\mathbf{A}\\
\operatorname{cof}\mathbf{A} &= \tfrac{1}{2}\,\mathbf{A}\divideontimes\mathbf{A}\,, \quad \text{where} \quad \operatorname{cof}\mathbf{A} = \tfrac{1}{2}\,(a_{ik}\,a_{no}\,e_{inj}\,e_{kop})\,(\mathbf{e}_j\otimes\mathbf{e}_p) =: \overset{+}{a}_{jp}\,(\mathbf{e}_j\otimes\mathbf{e}_p)
\end{aligned}$$

can be evaluated using (A.7) and index notation. Thus, the coefficient matrix $\overset{+}{a}_{jp}$ contains at each position $(\,\cdot\,)_{jp}$ the corresponding subdeterminant, e. g., $\overset{+}{a}_{11} = a_{22}\,a_{33} - a_{23}\,a_{32}$.

Collected rules for the **determinant** and the **inverse** of second-order tensors:

$$\begin{aligned}
(\operatorname{cof}\mathbf{A})^T &= \operatorname{cof}\mathbf{A}^T & \det(\operatorname{cof}\mathbf{A}) &= (\det\mathbf{A})^2\\
\det\mathbf{A}^T &= \det\mathbf{A} & \det\mathbf{A}^{-1} &= (\det\mathbf{A})^{-1}\\
\det(\mathbf{A}\,\mathbf{B}) &= \det\mathbf{A}\,\det\mathbf{B} & \det(\mathbf{A}+\mathbf{B}) &= \det\mathbf{A} + \operatorname{cof}\mathbf{A}\cdot\mathbf{B} +\\
\det(\alpha\,\mathbf{A}) &= \alpha^3\,\det\mathbf{A} & &\quad + \mathbf{A}\cdot\operatorname{cof}\mathbf{B} + \det\mathbf{B}\\
\det\mathbf{I} &= 1 & &
\end{aligned} \tag{A.5}$$

Collected rules for the **trace** operator of second-order tensors:

$$\begin{aligned}
\operatorname{tr}\mathbf{A} &= \mathbf{A}\cdot\mathbf{I} & \operatorname{tr}(\alpha\,\mathbf{A}) &= \alpha\,\operatorname{tr}\mathbf{A}\\
\operatorname{tr}(\mathbf{a}\otimes\mathbf{b}) &= \mathbf{a}\cdot\mathbf{b} & \operatorname{tr}\mathbf{A}^T &= \operatorname{tr}\mathbf{A}\\
\operatorname{tr}(\mathbf{A}\,\mathbf{B}) &= \operatorname{tr}(\mathbf{B}\,\mathbf{A}) & \operatorname{tr}(\mathbf{A}\,\mathbf{B}\,\mathbf{C}) &= \operatorname{tr}(\mathbf{B}\,\mathbf{C}\,\mathbf{A})\\
&= \mathbf{A}\cdot\mathbf{B}^T = \mathbf{A}^T\cdot\mathbf{B} & &= \operatorname{tr}(\mathbf{C}\,\mathbf{A}\,\mathbf{B})
\end{aligned} \tag{A.6}$$

In index notation, the properties of the permutation tensor are given, viz.:

$$\overset{3}{\mathbf{E}} = e_{ijk}\,(\mathbf{e}_i \otimes \mathbf{e}_j \otimes \mathbf{e}_k) \qquad \text{with the "permutation symbol" } e_{ijk}$$

$$e_{ijk} = \begin{cases} 1 & : \text{even permutation} \\ -1 & : \text{odd permutation} \\ 0 & : \text{double indexing} \end{cases} \longrightarrow \begin{cases} e_{123} = e_{231} = e_{312} = 1 \\ e_{321} = e_{213} = e_{132} = -1 \\ \text{all remaining } e_{ijk} \text{ vanish} \end{cases} \tag{A.7}$$

A.2 Tensor analysis

The **product rule** of derivatives of products of functions:

$$(\mathbf{a} \otimes \mathbf{b})' = \mathbf{a}' \otimes \mathbf{b} + \mathbf{a} \otimes \mathbf{b}' \qquad \text{and} \qquad (\mathbf{A}\,\mathbf{B})' = \mathbf{A}'\,\mathbf{B} + \mathbf{A}\,\mathbf{B}' \tag{A.8}$$

Collected **derivatives** of tensors and their invariants:

$$\begin{aligned} \frac{\partial \mathbf{A}}{\partial \mathbf{A}} &= (\mathbf{I} \otimes \mathbf{I})^{23}_{T} = \overset{4}{\mathbf{I}} & \frac{\partial\, \mathrm{tr}\mathbf{A}}{\partial \mathbf{A}} &= \mathbf{I} \\ \frac{\partial \mathbf{A}^T}{\partial \mathbf{A}} &= (\mathbf{I} \otimes \mathbf{I})^{24}_{T} & \frac{\partial\, \det \mathbf{A}}{\partial \mathbf{A}} &= \mathrm{cof}\,\mathbf{A} = (\det \mathbf{A})\,\mathbf{A}^{T-1} \\ \frac{\partial \mathbf{A}^{-1}}{\partial \mathbf{A}} &= -\,(\mathbf{A}^{-1} \otimes \mathbf{A}^{T-1})^{23}_{T} & \frac{\partial\, \mathrm{cof}\,\mathbf{A}}{\partial \mathbf{A}} &= \det \mathbf{A}\,[(\mathbf{A}^{T-1} \otimes \mathbf{A}^{T-1}) - \\ & & & \quad -\,(\mathbf{A}^{T-1} \otimes \mathbf{A}^{T-1})^{24}_{T}] \end{aligned} \tag{A.9}$$

Selected computation rules for the **gradient** and the **divergence** operators:

$$\begin{aligned} \mathrm{grad}(\alpha\,\beta) &= \alpha\,\mathrm{grad}\beta + \beta\,\mathrm{grad}\alpha & \mathrm{div}\,(\mathbf{a} \otimes \mathbf{b}) &= \mathbf{a}\,\mathrm{div}\,\mathbf{b} + (\mathrm{grad}\mathbf{a})\,\mathbf{b} \\ \mathrm{grad}(\alpha\,\mathbf{b}) &= \mathbf{b} \otimes \mathrm{grad}\alpha + \alpha\,\mathrm{grad}\mathbf{b} & \mathrm{div}\,(\alpha\,\mathbf{B}) &= \mathbf{B}\,\mathrm{grad}\alpha + \alpha\,\mathrm{div}\,\mathbf{B} \\ \mathrm{grad}(\alpha\,\mathbf{B}) &= \mathbf{B} \otimes \mathrm{grad}\alpha + \alpha\,\mathrm{grad}\mathbf{B} & \mathrm{div}\,(\mathbf{A}\,\mathbf{b}) &= (\mathrm{div}\,\mathbf{A}^T) \cdot \mathbf{b} + \mathbf{A}^T \cdot \mathrm{grad}\mathbf{b} \\ \mathrm{div}\,(\alpha\,\mathbf{b}) &= \mathbf{b} \cdot \mathrm{grad}\alpha + \alpha\,\mathrm{div}\,\mathbf{b} & \mathrm{div}\left(\frac{\mathbf{b}}{\alpha}\right) &= \frac{1}{\alpha}\,\mathrm{div}\,\mathbf{b} - \frac{1}{\alpha^2}\,\mathbf{b} \cdot \mathrm{grad}\alpha \end{aligned} \tag{A.10}$$

Appendix B: Mechanical supplements

B.1 Spectral decomposition of the strain tensor

This section briefly introduces the spectral decomposition of the strain tensor. For a detailed discussion of this topic, the interested reader is referred, e. g., to Ehlers [79], Markert [184] and Luo [178].

First, the eigenvalue problem is evaluated for the linearised solid strain tensor $\boldsymbol{\varepsilon}_S$ via

$$\boldsymbol{\varepsilon}_S \;=\; \sum_{i=1}^{3} \varepsilon_{Si}\, \mathbf{n}_{Si} \otimes \mathbf{n}_{Si} \;\;\leftrightarrow\;\; (\boldsymbol{\varepsilon}_S - \varepsilon_S\, \mathbf{I})\, \mathbf{n}_S \;=\; \mathbf{0} \tag{B.1}$$

where $\varepsilon_{Si} \in \mathbb{R}^+$ (for $i = 1,2,3$) denote the real and positive eigenvalues of the positive definite strain tensor $\boldsymbol{\varepsilon}_S$. If there are corresponding non-trivial orthogonal eigenvectors $\mathbf{n}_{Si} \neq \mathbf{0}$, the eigenvalue problem (B.1) can be solved via the characteristic polynomial

$$\det\left(\boldsymbol{\varepsilon}_S - \varepsilon_S\, \mathbf{I}\right) = \varepsilon_S^3 - I_{S1}\, \varepsilon_S^2 + I_{S2}\, \varepsilon_S - I_{S3} = 0\,. \tag{B.2}$$

Therein, the principal invariants are defined in terms of the strain tensor as

$$\begin{aligned} I_{S1} &= \operatorname{tr} \boldsymbol{\varepsilon}_S &&= \boldsymbol{\varepsilon}_S \cdot \mathbf{I}\,, \\ I_{S2} &= \operatorname{tr}\left(\operatorname{cof} \boldsymbol{\varepsilon}_S\right) &&= \tfrac{1}{2}[(\operatorname{tr} \boldsymbol{\varepsilon}_S)^2 - \operatorname{tr}(\boldsymbol{\varepsilon}_S\, \boldsymbol{\varepsilon}_S)]\,, \\ I_{S3} &= \det \boldsymbol{\varepsilon}_S\,. \end{aligned} \tag{B.3}$$

Moreover, the principal invariants are related to the eigenvalues through

$$\begin{aligned} I_{S1} &= \varepsilon_{S1} + \varepsilon_{S2} + \varepsilon_{S3}\,, \\ I_{S2} &= \varepsilon_{S1}\, \varepsilon_{S2} + \varepsilon_{S2}\, \varepsilon_{S3} + \varepsilon_{S3}\, \varepsilon_{S1}\,, \\ I_{S3} &= \varepsilon_{S1}\, \varepsilon_{S2}\, \varepsilon_{S3}\,. \end{aligned} \tag{B.4}$$

Finally, splitting the strain tensor according to the sign of its eigenvalues leads to

$$\boldsymbol{\varepsilon}_S = \boldsymbol{\varepsilon}_S^+ + \boldsymbol{\varepsilon}_S^- \;\; \text{with} \;\; \begin{cases} \boldsymbol{\varepsilon}_S^+ = \sum\nolimits_i \dfrac{\varepsilon_{Si} + |\varepsilon_{Si}|}{2}\, \mathbf{n}_{Si} \otimes \mathbf{n}_{Si}\,, \\ \boldsymbol{\varepsilon}_S^- = \sum\nolimits_i \dfrac{\varepsilon_{Si} - |\varepsilon_{Si}|}{2}\, \mathbf{n}_{Si} \otimes \mathbf{n}_{Si}\,. \end{cases} \tag{B.5}$$

B.2 Fluid flow state in the unbroken and broken case

In this section, the fluid flow is specified for the two extreme states of unbroken and broken material. On the one hand, regarding the limit case of intact material when $\phi^S = 0$, the

frictional stresses $\mathbf{T}^{\beta}_{NEQ}$ vanish, and the non-equilibrium momentum productions yield according to $(3.83)_1$

$$\hat{\mathbf{p}}^{\beta}_{NEQ} = -(n^{\beta})^2 \frac{\gamma^{\beta R}}{K^{\beta}_r}\,\mathbf{w}_{\beta} \quad \text{for } \phi^S = 0\,. \tag{B.6}$$

Considering the fluid momentum balances (3.13) under creeping-flow conditions, i. e. $(\mathbf{v}_{\beta})'_{\beta} \approx \mathbf{0}$ and $\operatorname{grad}\mathbf{v}_{\beta} \approx \mathbf{0}$, and inserting the relations for the total, equilibrium and non-equilibrium quantities (3.38), (3.45), $(3.46)_1$, (3.50), (3.51) and (B.6), leads with the differentiation rule (A.10) for the pore liquid to

$$\begin{aligned}
\mathbf{0} &= \operatorname{div}\mathbf{T}^{L}_{EQ} + \rho^{L}\,\mathbf{g} + \hat{\mathbf{p}}^{L}_{EQ} + \hat{\mathbf{p}}^{L}_{NEQ} \\
&= \operatorname{div}\left(-\,n^{L}\,p^{LR}\,\mathbf{I}\right) + n^{L}\rho^{LR}\mathbf{g} + p^{LR}\operatorname{grad} n^{L} + p^{D}n^{F}\operatorname{grad} s^{L} - (n^{L})^2\frac{\gamma^{LR}}{K^{L}_r}\,\mathbf{w}_{L} \\
&= -\,n^{L}\operatorname{grad} p^{LR} + n^{L}\rho^{LR}\,\mathbf{g} + p^{D}n^{F}\operatorname{grad} s^{L} - (n^{L})^2\frac{\gamma^{LR}}{K^{L}_r}\,\mathbf{w}_{L} \\
\rightarrow \quad n^{L}\mathbf{w}_{L} &= -\frac{K^{L}_r}{\gamma^{LR}}\left(\operatorname{grad} p^{LR} - \rho^{LR}\,\mathbf{g} - \frac{p^{D}}{s^{L}}\operatorname{grad} s^{L}\right)
\end{aligned} \tag{B.7}$$

and in analogy for the pore gas to

$$\begin{aligned}
\mathbf{0} &= \operatorname{div}\mathbf{T}^{G}_{EQ} + \rho^{G}\,\mathbf{g} + \hat{\mathbf{p}}^{G}_{EQ} + \hat{\mathbf{p}}^{G}_{NEQ} \\
&= \operatorname{div}\left(-\,n^{G}\,p^{GR}\,\mathbf{I}\right) + n^{G}\rho^{GR}\mathbf{g} + p^{GR}\operatorname{grad} n^{G} - (n^{G})^2\frac{\gamma^{GR}}{K^{G}_r}\,\mathbf{w}_{G} \\
&= -\,n^{G}\operatorname{grad} p^{GR} + n^{G}\rho^{GR}\,\mathbf{g} - (n^{G})^2\frac{\gamma^{GR}}{K^{G}_r}\,\mathbf{w}_{G} \\
\rightarrow \quad n^{G}\mathbf{w}_{G} &= -\frac{K^{G}_r}{\gamma^{GR}}\left(\operatorname{grad} p^{GR} - \rho^{GR}\,\mathbf{g}\right)
\end{aligned} \tag{B.8}$$

Thus, for $\phi^S = 0$, Darcy-like filter velocities $n^{L}\mathbf{w}_{L}$ and $n^{G}\mathbf{w}_{G}$ are recovered, compare Darcy [70]. Note that the liquid filter velocity contains a term with the saturation gradient, which is not included in the original Darcy filter law.

On the other hand, the non-equilibrium momentum productions $\hat{\mathbf{p}}^{\beta}_{NEQ}$ vanish for the limit case $\phi^S = 1$, and the frictional stresses $\mathbf{T}^{\beta}_{NEQ}$ read

$$\mathbf{T}^{\beta}_{NEQ} = 2\,n^{\beta}\mu^{\beta R}\,\mathbf{D}_{\beta} \quad \text{for } \phi^S = 1\,. \tag{B.9}$$

Including this formulation in the fluid momentum balances (3.13) and considering the relations (3.38), (3.45), $(3.46)_1$, (3.50), (3.51) and (B.9), yields for the pore liquid

$$\begin{aligned}
\rho^{L}(\mathbf{v}_{L})'_{L} &= \operatorname{div}\left(\mathbf{T}^{L}_{EQ} + \mathbf{T}^{L}_{NEQ}\right) + \rho^{L}\,\mathbf{g} + \hat{\mathbf{p}}^{L}_{EQ} \\
&= \operatorname{div}\left(-\,n^{L}\,p^{LR}\,\mathbf{I} + 2\,n^{L}\mu^{LR}\,\mathbf{D}_{L}\right) + \rho^{L}\mathbf{g} + p^{LR}\operatorname{grad} n^{L} + p^{D}n^{F}\operatorname{grad} s^{L} \\
&= \operatorname{div}\left(2\,n^{L}\mu^{LR}\,\mathbf{D}_{L}\right) - n^{L}\operatorname{grad} p^{LR} + \rho^{L}\,\mathbf{g} + p^{D}n^{F}\operatorname{grad} s^{L}
\end{aligned} \tag{B.10}$$

and for the pore gas

$$\begin{aligned} \rho^G (\mathbf{v}_G)'_G &= \operatorname{div}(\mathbf{T}^G_{EQ} + \mathbf{T}^G_{NEQ}) + \rho^G \mathbf{g} + \hat{\mathbf{p}}^G_{EQ} \\ &= \operatorname{div}(-n^G p^{GR} \mathbf{I} + 2\, n^G \mu^{GR} \mathbf{D}_G) + \rho^G \mathbf{g} + p^{GR} \operatorname{grad} n^G \\ &= \operatorname{div}(2\, n^G \mu^{GR} \mathbf{D}_G) - n^G \operatorname{grad} p^{GR} + \rho^G \mathbf{g}\,, \end{aligned} \tag{B.11}$$

similar to the Navier-Stokes equation of a single, incompressible Newtonian fluid. Note that here as well, the liquid balance additionally includes a term with the saturation gradient, arising from the interaction of the two fluids in the pore space.

Appendix C: Complement numerical treatment

C.1 Proof of concept of rearranged weak fluid-momentum formulations

As a proof of concept for the numerical treatment of partially saturated porous media either by use of (4.7)-(4.14) (standard formulation) or by substituting (4.8) and (4.9) with (4.12) and (4.13) (rearranged formulation), the well-known consolidation problem is considered. Table C.1 lists the material parameters for the current problem.

Table C.1: *Material parameters for the consolidation problem.*

Parameter	Symbol	Value	Parameter	Symbol	Value
Lamé constants	μ^S	$5.58 \cdot 10^6$ Pa	Atmospheric gas density	ρ^{GR}_{atm}	$1.246\,\text{kg/m}^3$
	λ^S	$8.37 \cdot 10^6$ Pa	Effective liquid viscosity	μ^{LR}	$10^{-3}\,\text{Pa s}$
Intrinsic permeability	K^S	$1.0 \cdot 10^{-11}\,\text{m}^2$	Effective gas viscosity	μ^{GR}	$1.8 \cdot 10^{-5}\,\text{Pa s}$
Initial porosity	n^F_0	0.33 [-]	Specific gas constant	R^G	$287.17\,\text{Nm/(kg K)}$
Initial liquid saturation	s^L_0	0.7 [-]	Temperature	θ	283 K
Effective solid density	ρ^{SR}	$3\,000\,\text{kg/m}^3$	Pore-size distribution factor	λ	3 [-]
Effective liquid density	ρ^{LR}	$1\,000\,\text{kg/m}^3$			

The geometry and boundary conditions are shown in Figure C.1, where the load $q = 15\,\text{MPa}$ substitutes a building wished in place within 5 s onto partially saturated soil. The left, bottom and right edges are impermeable and fixed. The top edge is divided into three parts: the left and right parts (dashed lines) are permeable, while the middle part is impermeable and loaded. The system is discretised with a regular mesh of 200 elements.

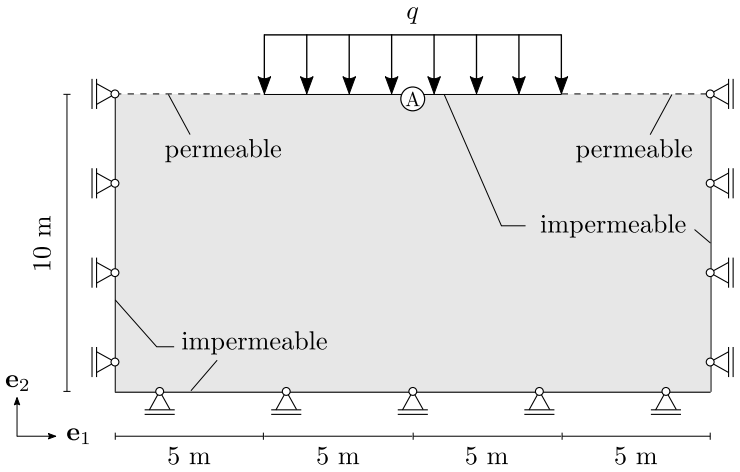

Figure C.1: *Sketch of the IBVP of the consolidation problem.*

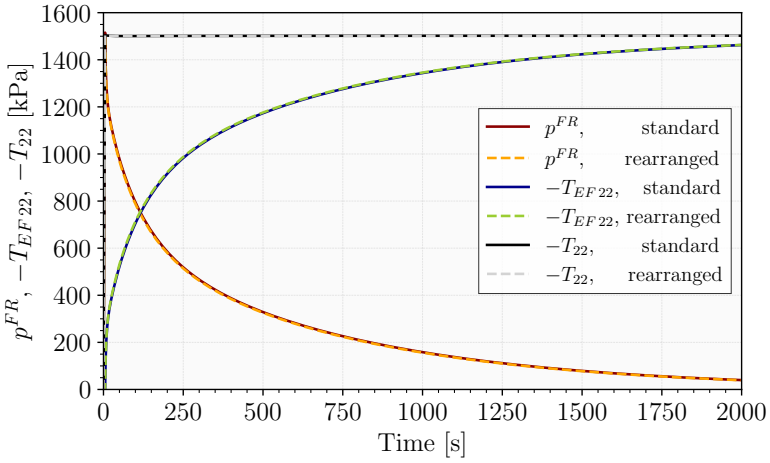

Figure C.2: *Temporal development of the pore pressure and vertical stresses at point A.*

After having applied the external load, this latter is kept constant until the end of the consolidation process. For both models, standard and modified, Figure C.2 shows the effective pore pressure p^{FR} and the negative values of the effective vertical stress $T_{EF\,22}$ at point A together with the negative values of the total vertical stress T_{22} as the sum of both. During the application of the external load within the first 5 seconds of the consolidation process, there is a sudden vertical displacement of 0.3 m at point A due to the compressibility of the pore gas, compare Figure C.3.

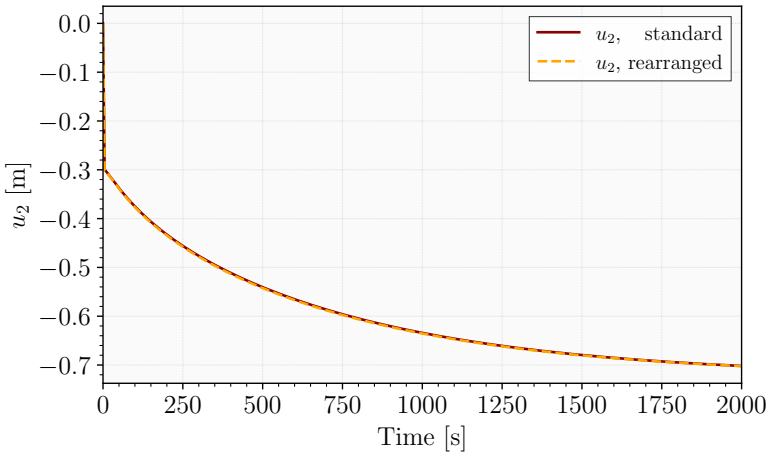

Figure C.3: *Temporal development of the vertical displacement at point A.*

This leads to a fast pore-pressure relaxation starting from 15 MPa at $t = 5$ s together with a first buildup of the effective stress. Once this has happened, the proper consolidation process initiates, where the pore fluids are squeezed out of the domain, while the solid deforms with a shrinking pore space. Further on, this leads to an ongoing but slower relaxation of the pore pressure accompanied by a corresponding buildup of the effective stress until the pore pressure vanishes and the total load is carried by the soil alone, thus marking the end of the consolidation process.

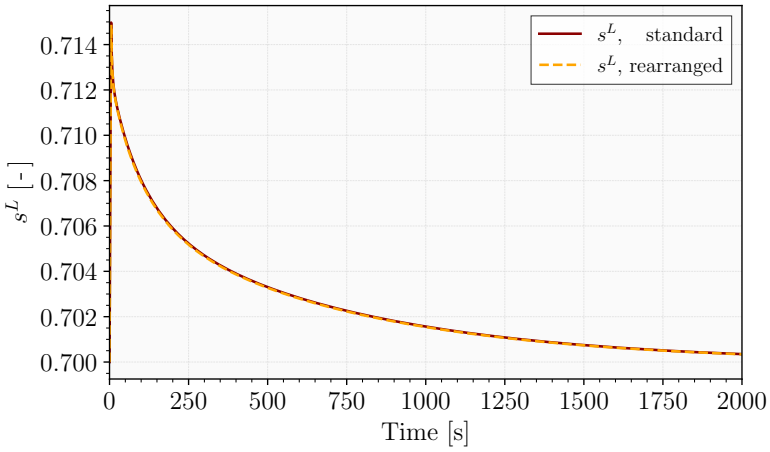

Figure C.4: *Temporal development of the liquid saturation at point A.*

Figure C.4 exhibits further details at point A, displaying the evolving liquid saturation. According to the pressure jump of Figure C.2, the liquid saturation increases in the first 5 seconds and decreases thereafter until the consolidation process has finished.

As a result of this proof of concept, it can be stated that both the standard and the rearranged numerical formulations lead to exactly the same computational results, thus justifying the numerical procedure used for treating fracking processes in partially saturated porous media.

C.2 Governing equations of the biphasic model

A detailed numerical treatment for this biphasic model can be found in Luo [178]. There, the primary variables are the solid displacement $\mathbf{u}_S$ corresponding to the displacement-velocity relation, the solid velocity $\mathbf{v}_S$ belonging to the overall momentum balance, the liquid velocity $\mathbf{v}_L$ corresponding to the momentum balance of the pore liquid, the effective pore pressure p^{LR} corresponding to the liquid volume balance, and the phase-field variable ϕ^S corresponding to the phase-field evolution equation. Summarising the primary variables of the biphasic model in an abstract vector $\boldsymbol{u}_1$ leads to

$$\boldsymbol{u}_1(\mathbf{x},t) = [\mathbf{u}_S,\, \mathbf{v}_S,\, \mathbf{v}_L,\, p^{LR},\, \phi^S]^T\,. \tag{C.1}$$

With this set $\boldsymbol{u}_1(\mathbf{x},t)$, the governing equations of Table 3.3 read in their weak form:

Overall momentum balance:

$$\begin{aligned}\mathcal{G}_{\mathbf{v}_S}(\boldsymbol{u}_1,\delta\mathbf{v}_S) \equiv \int_\Omega \left[\,\rho^S(\mathbf{v}_S)'_S + \rho^L(\mathbf{v}_L)'_S + \rho^L(\operatorname{grad}\mathbf{v}_L)\,\mathbf{w}_L\,\right]\cdot\delta\mathbf{v}_S\,\mathrm{d}v + \\ + \int_\Omega \left(\boldsymbol{\sigma}^S_{EF} + \mathbf{T}^L_{NEQ} - p^{LR}\,\mathbf{I}\right)\cdot\operatorname{grad}\delta\mathbf{v}_S\,dv - \int_\Omega \rho\,\mathbf{g}\cdot\delta\mathbf{v}_S\mathrm{d}v - \\ - \int_{\delta\Omega^{\tilde{\mathbf{t}}}_N} \tilde{\mathbf{t}}\cdot\delta\mathbf{v}_S\,\mathrm{d}a = 0\,, \qquad \text{with} \quad \tilde{\mathbf{t}} := \left(\boldsymbol{\sigma}^S_{EF} + \mathbf{T}^L_{NEQ}\right)\mathbf{n} - p^{LR}\,\mathbf{n}\,,\end{aligned} \tag{C.2}$$

Liquid momentum balance:

$$\begin{aligned}\mathcal{G}_{\mathbf{v}_L}(\boldsymbol{u}_1,\delta\mathbf{v}_L) \equiv \int_\Omega [\,\rho^L(\mathbf{v}_L)'_S + \rho^L(\mathrm{grad}\mathbf{v}_L)\,\mathbf{w}_L\,]\cdot\delta\mathbf{v}_L\,\mathrm{d}v + \int_\Omega \mathbf{T}^L_{NEQ}\cdot\,\mathrm{grad}\delta\mathbf{v}_L\,\mathrm{d}v + \\ + \int_\Omega n^L\mathrm{grad}\,p^{LR}\cdot\,\delta\mathbf{v}_L\,\mathrm{d}v - \int_\Omega(\rho^L\,\mathbf{g}+\hat{\mathbf{p}}^L_{NEQ})\cdot\,\delta\mathbf{v}_L\,\mathrm{d}v - \\ - \int_{\Omega^{\bar{\mathbf{t}}^L}_N}\bar{\mathbf{t}}^L\,\cdot\,\delta\mathbf{v}_L\,\mathrm{d}a = 0\,,\qquad \text{with}\quad \bar{\mathbf{t}}^L=\mathbf{T}^L_{NEQ}\,\mathbf{n}\,,\end{aligned} \tag{C.3}$$

Liquid volume balance:

$$\begin{aligned}\mathcal{G}_{p^{LR}}(\boldsymbol{u}_1,\delta p^{LR}) \equiv \int_\Omega \mathrm{div}\,\mathbf{v}_S\,\delta p^{LR}\,\mathrm{d}v\; - \int_\Omega n^L\mathbf{w}_L\cdot\mathrm{grad}\delta p^{LR}\,\mathrm{d}v + \\ + \int_{\Omega^{\bar{v}^L}_N}\bar{v}^L\delta p^{LR}\,\mathrm{d}a = 0\,,\qquad \text{with}\quad \bar{v}^L = n^L\mathbf{w}_L\cdot\mathbf{n}\,,\end{aligned} \tag{C.4}$$

Phase-field evolution equation:

$$\begin{aligned}\mathcal{G}_{\phi^S}(\boldsymbol{u}_1,\delta\phi^S) \equiv \int_\Omega [\,M(\phi^S)'_S - 2(1-\phi^S)\mathcal{H} + \frac{G_c}{\epsilon}\phi^S\,]\,\delta\phi^S\,\mathrm{d}v + \int_\Omega G_c\,\epsilon\,\mathrm{grad}\,\phi^S\cdot\,\mathrm{grad}\,\delta\phi^S\,\mathrm{d}v - \\ - \int_{\Omega^{\bar{v}^{\phi^S}}_N}\bar{v}^{\phi^S}\,\delta\phi^S\mathrm{d}a = 0\,,\quad \text{with}\quad \bar{v}^{\phi^S} = G_c\,\epsilon\,\mathrm{grad}\,\phi^S\cdot\,\mathbf{n}\,.\end{aligned} \tag{C.5}$$

C.3 Excerpt of the numerical treatment of the quasi-static triphasic model without fracture

For the simplified triphasic model, no dynamic or fracturing processes need to be taken into account. Thus, the set of primary variables for the quasi-static triphasic model can be reduced to the solid displacement $\mathbf{u}_S$, the effective liquid saturation s^L_{eff} and the effective gas pressure p^{GR}, viz.

$$\boldsymbol{u}_2(\mathbf{x},t) = [\mathbf{u}_S,\, s^L_{\mathrm{eff}},\, p^{GR}]^T\,. \tag{C.6}$$

Moreover, the viscous effective stresses of the fluid components are negligible compared to the fluid extra momentum productions, compare Ehlers *et al.* [91]. In addition, the fluid velocities are computed based on Darcy's filter law. A complete overview of the mechanical model can be found, e. g., in Ehlers [85]. The corresponding weak formulations of the governing equations for the quasi-static model are finally given by

Overall momentum balance:

$$\begin{aligned}\mathcal{G}_{\mathbf{u}_S}(\boldsymbol{u}_2, \delta\mathbf{u}_S) \equiv \int_\Omega \left(\boldsymbol{\sigma}_{EF}^S - p^{FR}\mathbf{I} \right) \cdot \operatorname{grad} \delta\mathbf{u}_S \, dv - \int_\Omega \rho\, \mathbf{g} \cdot \delta\mathbf{u}_S \mathrm{d}v - \\ - \int_{\delta\Omega_N^{\tilde{\mathbf{t}}}} \tilde{\tilde{\mathbf{t}}} \cdot \delta\mathbf{u}_S \, \mathrm{d}a = 0\,, \qquad \text{with} \quad \tilde{\tilde{\mathbf{t}}} := \left(\boldsymbol{\sigma}_{EF}^S - p^{FR}\mathbf{I} \right) \mathbf{n}\,,\end{aligned} \tag{C.7}$$

Liquid volume balance:

$$\begin{aligned}\mathcal{G}_{s_{\mathrm{eff}}^L}(\boldsymbol{u}_2, \delta s_{\mathrm{eff}}^L) \equiv \int_\Omega \left[(n^L)'_S + n^L \operatorname{div} \mathbf{v}_S \right] \delta s_{\mathrm{eff}}^L \, \mathrm{d}v - \int_\Omega n^L \mathbf{w}_L \cdot \operatorname{grad} \delta s_{\mathrm{eff}}^L \, \mathrm{d}v + \\ + \int_{\Omega_N^{\bar{v}^L}} \bar{v}^L \delta s_{\mathrm{eff}}^L \, \mathrm{d}a = 0\,, \qquad \text{with} \quad \bar{v}^L = n^L \mathbf{w}_L \cdot \mathbf{n}\,,\end{aligned} \tag{C.8}$$

Gas mass balance:

$$\begin{aligned}\mathcal{G}_{p^{GR}}(\boldsymbol{u}_2, \delta p^{GR}) \equiv \int_\Omega \left[\rho^{GR} (n^G)'_S + n^G (\rho^{GR})'_S + n^G \rho^{GR} \operatorname{div} (\mathbf{u}_S)'_S \right] \delta p^{GR} \, \mathrm{d}v - \\ - \int_\Omega n^G \rho^{GR} \mathbf{w}_G \cdot \operatorname{grad} \delta p^{GR} \, \mathrm{d}v + \int_{\Omega_N^{\bar{v}^G}} \rho^{GR} \, \bar{v}^G \, \delta p^{GR} \, \mathrm{d}a = 0 \\ \text{with} \quad \bar{v}^G = n^G \mathbf{w}_G \cdot \mathbf{n}\,.\end{aligned} \tag{C.9}$$

Note that only the arguments and the weak formulation of the overall momentum balance changes compared to (4.7), (4.10) and (4.11).

C.4 Assignment of spatially dependent material parameters

A customised algorithm is used for the assignment of the arbitrary heterogeneous parameter fields onto the meshing grid. In general, the spatial discretisation of the meshing grid is independent of material parameter data, given here in a regular distribution (Figure C.5). It is often sufficient that each integration point K_G is basically equipped with the spatially closest material parameter data for a suitable spatial fit (Figure C.5, green circle). However, a mismatch of integration points (Figure C.5, red circle) combined with (sparse) data can cause inaccurate results. In this regard, a customised algorithm after Wagner [243] is implemented and provides a suitable averaging process to allocate and store the material parameter information at each integration point K_G in a preceding calculation step for the subsequent numerical simulation. Thereby, a (scalar-valued) material

parameter μ^{K_G} is linearly weighted at the considered integration point K_G, viz.:

$$\mu^{K_G} = \frac{\sum_{\mathrm{n}} \mu^{\mathrm{data,n}}\, w^{\mathrm{data,n}}}{\sum_{\mathrm{n}} w^{\mathrm{data,n}}} \tag{C.10}$$

with $w^{\mathrm{data,n}} = 1 - d^{\mathrm{data,n}}/R_{K_G}$. Therein, $d^{\mathrm{data,n}}$ is the spatial distance of the material parameter data to the considered K_G within a certain (influence) radius R_{K_G} for K_G, see Figure C.5. The superscript n is used to label the included material data points. The considered surrounding of K_G can either be chosen constant for the overall domain or location-dependent on the individual element size.

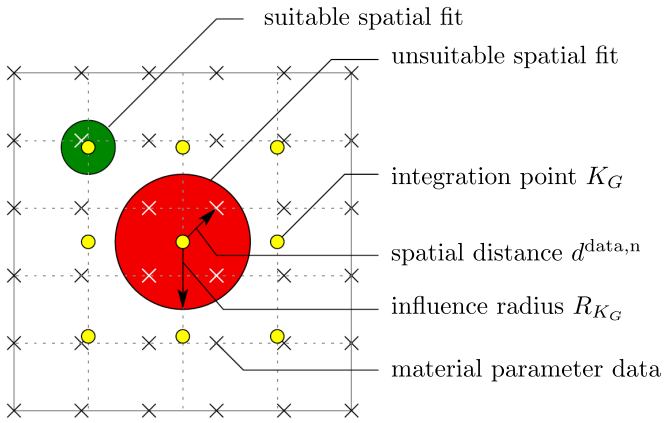

Figure C.5: *Two-dimensional example of material-parameter assignment onto the integration points from Wagner [243].*

Bibliography

[1] Ahmed, T.: *Reservoir Engineering Handbook*. 5th edition, Gulf Professional Publishing 2019.

[2] Al-Futaisi, A. & Patzek, T. W.: Impact of wettability alteration on two-phase flow characteristics of sandstones: A quasi-static description. *Water Resources Research* **39** (2003), 1042, 13 pages.

[3] Alessi, R.; Ambati, M.; Gerasimov, T.; Vidoli, S. & De Lorenzis, L.: Comparison of phase-field models of fracture coupled with plasticity. In Oñate, E.; Peric, D.; de Souza Neto, E. & Chiumenti, M. (eds.): *Advances in Computational Plasticity: A Book in Honour of D. Roger J. Owen*. Springer International Publishing, Cham 2018, pp. 1–21.

[4] Alessi, R.; Vidoli, S. & De Lorenzis, L.: A phenomenological approach to fatigue with a variational phase-field model: The one-dimensional case. *Engineering Fracture Mechanics* **190** (2018), 53–73.

[5] Altenbach, H.: *Kontinuumsmechanik: Einführung in die materialunabhängigen und materialabhängigen Gleichungen*. Springer-Verlag, Berlin 2012.

[6] Ambati, M. & De Lorenzis, L.: Phase-field modeling of brittle and ductile fracture in shells with isogeometric NURBS-based solid-shell elements. *Computer Methods in Applied Mechanics and Engineering* **312** (2016), 351–373.

[7] Ambati, M.; Gerasimov, T. & De Lorenzis, L.: Phase-field modeling of ductile fracture. *Computational Mechanics* **55** (2015), 1017–1040.

[8] Ambati, M.; Gerasimov, T. & De Lorenzis, L.: A review on phase-field models of brittle fracture and a new fast hybrid formulation. *Computational Mechanics* **55** (2015), 383–405.

[9] Ambati, M.; Kruse, R. & De Lorenzis, L.: A phase-field model for ductile fracture at finite strains and its experimental verification. *Computational Mechanics* **57** (2016), 149–167.

[10] Ambrosio, L. & Tortorelli, V. M.: Approximation of functional depending on jumps by elliptic functional via Γ-convergence. *Communications on Pure and Applied Mathematics* **43** (1990), 999–1036.

[11] Ammann, M.: *Parallel Finite Element Simulations of Localization Phenomena in Porous Media*. Dissertation thesis, Report No. II-11 of the Institute of Applied Mechanics (CE), University of Stuttgart 2005.

[12] Amor, H.; Marigo, J.-J. & Maurini, C.: Regularized formulation of the variational brittle fracture with unilateral contact: Numerical experiments. *Journal of the Mechanics and Physics of Solids* **57** (2009), 1209–1229.

[13] Amott, E.: Observations relating to the wettability of porous rock. *Petroleum Transactions, AIME* **216** (1959), 156–162.

[14] Anderson, W. G.: Wettability literature survey - Part 4: Effects of wettability on capillary pressure. *Journal of Petroleum Technology* **39** (1987), 1283–1300.

[15] Aranson, I.; Kalatsky, V. & Vinokur, V.: Continuum field description of crack propagation. *Physical Review Letters* **85** (2000), 118–121.

[16] Bamber, A. M.; Hasanali, S. H.; Nair, A. S.; Watkins, S. M.; Vigil, D. I.; Van Dyke, M.; McMullin, T. S. & Richardson, K.: A systematic review of the epidemiologic literature assessing health outcomes in populations living near oil and natural gas operations: study quality and future recommendations. *International Journal of Environmental Research and Public Health* **16** (2019), 2123, 20 pages.

[17] Banks, D.; Odling, N. E.; Skarphagen, H. & Rohr-Torp, E.: Permeability and stress in crystalline rocks. *Terra Nova* **8** (1996), 223–235.

[18] Barenblatt, G. I.: The mathematical theory of equilibrium cracks in brittle fracture. *Advances in Applied Mechanics* **7** (1962), 55–129.

[19] Bathe, K. J.: *Finite-Elemente-Methoden*. 2nd edition, Springer-Verlag, Berlin 2002.

[20] Bear, J.: *Hydraulics of Groundwater*. Dover Publications, Mineola (NY) 1979.

[21] Beavers, G. S. & Joseph, D. D.: Boundary conditions at a naturally permeable wall. *Journal of Fluid Mechanics* **30** (1967), 197–207.

[22] Bedford, A. & Drumheller, D.: Theories of immiscible and structured mixtures. *International Journal of Engineering Science* **21** (1983), 863–960.

[23] Belytschko, T. & Black, T.: Elastic crack growth in finite elements with minimal remeshing. *International Journal for Numerical Methods in Engineering* **45** (1999), 601–620.

[24] Belytschko, T.; Loehnert, S. & Song, J.-H.: Multiscale aggregating discontinuities: A method for circumventing loss of material stability. *International Journal for Numerical Methods in Engineering* **73** (2008), 869–894.

[25] Bennethum, L. S. & Cushman, J. H.: Multiscale, hybrid mixture theory for swelling systems – I: Balance laws. *International Journal of Engineering Science* **34** (1996), 125–145.

[26] Bennethum, L. S. & Cushman, J. H.: Multiscale, hybrid mixture theory for swelling systems – II: Constitutive theory. *International Journal of Engineering Science* **34** (1996), 147–169.

[27] Bercovier, M. & Pironneau, O.: Error estimates for finite element method solution of the Stokes problem in the primitive variables. *Numerische Mathematik* **33** (1979), 211–224.

[28] Berre, I.; Doster, F. & Keilegavlen, E.: Flow in fractured porous media: A review of conceptual models and discretization approaches. *Transport in Porous Media* **130** (2019), 215–236.

[29] Bidier, S.: *From Particle Mechanics to Micromorphic Continua*. Dissertation thesis, Report No. II-36 of the Institute of Applied Mechanics (CE), University of Stuttgart 2019.

[30] Bilgen, C. & Weinberg, K.: A phase-field approach to pneumatic fracture with anisotropic crack resistance. *International Journal of Fracture* **232** (2021), 135–151.

[31] Biot, M. A.: General theory of three-dimensional consolidation. *Journal of Applied Physics* **12** (1941), 155–164.

[32] Biot, M. A.: Theory of elasticity and consolidation for a porous anisotropic solid. *Journal of Applied Physics* **26** (1955), 182–185.

[33] Biot, M. A. & Willis, D. G.: The elastic coefficients of the theory of consolidation. *Journal of Applied Mechanics* **24** (1957), 594–601.

[34] Birdsell, D. T.; Rajaram, H. & Lackey, G.: Imbibition of hydraulic fracturing fluids into partially saturated shale. *Water Resources Research* **51** (2015), 6787–6796.

[35] Blunt, M. J.: Pore level modeling of the effects of wettability. *Society of Petroleum Engineers Journal* **2** (1997), 494–510.

[36] Blunt, M. J.: *Multiphase Flow in Permeable Media: A Pore-Scale Perspective*. Cambridge University Press 2017.

[37] de Boer, R.: *Vektor- und Tensorrechnung für Ingenieure*. Springer-Verlag, Berlin 1982.

[38] de Boer, R.: Highlights in the historical development of the porous media theory: toward a consistent macroscopic theory. *Applied Mechanics Reviews* **49** (1996), 201–262.

[39] de Boer, R.: *Theory of Porous Media.* Springer-Verlag, Berlin 2000.

[40] de Boer, R. & Ehlers, W.: *Theorie der Mehrkomponentenkontinua mit Anwendungen auf bodenmechanische Probleme*. Forschungsberichte aus dem Fachbereich Bauwesen, Heft 40, Universität-GH-Essen 1986.

[41] de Boer, R. & Ehlers, W.: A historical review of the formulation of porous media theories. *Acta Mechanica* **74** (1988), 1–8.

[42] de Boer, R. & Ehlers, W.: The development of the concept of effective stresses. *Acta Mechanica* **83** (1990), 77–92.

[43] de Boer, R. & Ehlers, W.: Uplift, friction and capillarity: three fundamental effects for liquid-saturated porous solids. *International Journal of Solids and Structures* **26** (1990), 43–57.

[44] Borden, M. J.; Hughes, T. J.; Landis, C. M.; Anvari, A. & Lee, I. J.: A phase-field formulation for fracture in ductile materials: Finite deformation balance law derivation, plastic degradation, and stress triaxiality effects. *Computer Methods in Applied Mechanics and Engineering* **312** (2016), 130–166.

[45] Borden, M. J.; Hughes, T. J.; Landis, C. M. & Verhoosel, C. V.: A higher-order phase-field model for brittle fracture: Formulation and analysis within the isogeometric analysis framework. *Computer Methods in Applied Mechanics and Engineering* **273** (2014), 100–118.

[46] Borden, M. J.; Verhoosel, C. V.; Scott, M. A.; Hughes, T. J. & Landis, C. M.: A phase-field description of dynamic brittle fracture. *Computer Methods in Applied Mechanics and Engineering* **217-220** (2012), 77–95.

[47] de Borst, R. & Verhoosel, C. V.: Gradient damage vs phase-field approaches for fracture: Similarities and differences. *Computer Methods in Applied Mechanics and Engineering* **312** (2016), 78–94.

[48] Bouchard, P.-O.; Bay, F. & Chastel, Y.: Numerical modelling of crack propagation: automatic remeshing and comparison of different criteria. *Computer Methods in Applied Mechanics and Engineering* **192** (2003), 3887–3908.

[49] Bourdin, B. & Francfort, G. A.: Past and present of variational fracture. *SIAM News* **52** (2019).

[50] Bourdin, B.; Francfort, G. A. & Marigo, J.-J.: Numerical experiments in revisited brittle fracture. *Journal of the Mechanics and Physics of Solids* **48** (2000), 797–826.

[51] Bowen, R. M.: Theory of mixtures. In Eringen, A. C. (ed.): *Continuum Physics, Vol. 3.* Academic Press, New York 1976, pp. 1–127.

[52] Bowen, R. M.: Incompressible porous media models by use of the theory of mixtures. *International Journal of Engineering Science* **18** (1980), 1129–1148.

[53] Bowen, R. M.: Compressible porous media models by use of the theory of mixtures. *International Journal of Engineering Science* **20** (1982), 697–735.

[54] Braess, D.: *Finite Elemente: Theorie, schnelle Löser und Anwendungen in der Elastizitätstheorie.* Springer-Verlag, Berlin 1992.

[55] Brezzi, F. & Fortin, M.: *Mixed and Hybrid Finite Element Methods.* Springer-Verlag, New York 1991.

[56] Brinkman, H. C.: A calculation of the viscous force exerted by a flowing fluid on a dense swarm of particles. *Flow, Turbulence and Combustion* **1** (1949), 27–34.

[57] Brooks, R. H. & Corey, A. T.: Hydraulic properties of porous media. In *Hydrology Papers No. 3*. Colorado State University, Fort Collins 1964, 37 pages.

[58] Brooks, R. H. & Corey, A. T.: Properties of porous media affecting fluid flow. *Journal of the Irrigation and Drainage Division* **92** (1966), 61–88.

[59] Bruner, K. R. & Smosna, R. A.: *A Comparative Study of the Mississippian Barnett Shale, Fort Worth Basin, and Devonian Marcellus Shale, Appalachian Basin*. US Department of Energy, National Energy Technology Laboratory 2011.

[60] Burdine, N. T.: Relative permeability calculations from pore size distribution data. *Journal of Petroleum Technology* **5** (1953), 71–78.

[61] Cajuhi, T.; Sanavia, L. & De Lorenzis, L.: Phase-field modeling of fracture in variably saturated porous media. *Computational Mechanics* **61** (2018), 299–318.

[62] Carrara, P.; Ambati, M.; Alessi, R. & De Lorenzis, L.: A framework to model the fatigue behavior of brittle materials based on a variational phase-field approach. *Computer Methods in Applied Mechanics and Engineering* **361** (2020), 112731, 45 pages.

[63] Chadwick, P.: *Continuum Mechanics: Concise Theory and Problems*. Dover Publications, Mineola (NY) 1999.

[64] Chukwudozie, C.; Bourdin, B. & Yoshioka, K.: A variational phase-field model for hydraulic fracturing in porous media. *Computer Methods in Applied Mechanics and Engineering* **347** (2019), 957–982.

[65] Coleman, B. D. & Noll, W.: The thermodynamics of elastic materials with heat conduction and viscosity. *Archive of Rational Mechanics and Analysis* **13** (1963), 167–178.

[66] Corey, A. T.: The interrelation between gas and oil relative permeabilities. *Producers Monthly* **19** (1954), 38–41.

[67] Coussy, O.: *Poromechanics*. John Wiley & Sons 2004.

[68] Coussy, O.; Dormieux, L. & Detournay, E.: From mixture theory to Biot's approach for porous media. *International Journal of Solids and Structures* **35** (1998), 4619–4635.

[69] Dalton, J.: Essay IV. On the expansion of elastic fluids by heat. *Memoirs of the Literary and Philosophical Society of Manchester* **5** (1802), 595–602.

[70] Darcy, H.: *Les fontaines publiques de la ville de Dijon*. Victor Dalmont, Paris 1856.

[71] Delesse, M.: Pour déterminer la composition des roches. *Annales des mines, 4 séries* **13** (1848), 379–388.

[72] Detournay, E. & Cheng, A. H.-D.: Fundamentals of poroelasticity. In Fairhurst, C. (ed.): *Analysis and Design Methods*. Pergamon, Oxford 1993, pp. 113–171.

[73] Diebels, S.: *Mikropolare Zweiphasenmodelle: Formulierung auf der Basis der Theorie Poröser Medien*. Habilitation thesis, Report No. II-4 of the Institute of Applied Mechanics (CE), University of Stuttgart 2000.

[74] Diebels, S. & Ehlers, W.: On fundamental concepts of multiphase micropolar materials. *Technische Mechanik* **16** (1996), 77–88.

[75] Diebels, S.; Ellsiepen, P. & Ehlers, W.: Error-controlled Runge-Kutta time integration of a viscoplastic hybrid two-phase model. *Technische Mechanik* **19** (1999), 19–27.

[76] Diehl, P.; Lipton, R.; Wick, T. & Tyagi, M.: A comparative review of peridynamics and phase-field models for engineering fracture mechanics. *Computational Mechanics* **69** (2022), 1259–1293.

[77] Dixit, A. B.; Buckley, J.; McDougall, S. R. & Sorbie, K. S.: Empirical measures of wettability in porous media and the relationship between them derived from pore-scale modelling. *Transport in Porous Media* **40** (2000), 27–54.

[78] Dugdale, D. S.: Yielding of steel sheets containing slits. *Journal of the Mechanics and Physics of Solids* **8** (1960), 100–104.

[79] Ehlers, W.: *Vector and Tensor Calculus: An Introduction*. Release 2018, Institute of Applied Mechanics, Chair of Continuum Mechanics, University of Stuttgart, URL `https://www.mib.uni-stuttgart.de/en/institute/team/Ehlers-00001/`.

[80] Ehlers, W.: On thermodynamics of elasto-plastic porous media. *Archives of Mechanics* **41** (1989), 73–93.

[81] Ehlers, W.: Compressible, incompressible and hybrid two-phase models in porous theories. In Angel, Y. C. (ed.): *Anisotropy and Inhomogeneity in Elasticity and Plasticity*. The American Society of Mechanical Engineers, New York 1993, Vol. 158, pp. 25–38.

[82] Ehlers, W.: Constitutive equations for granular materials in geomechanical context. In Hutter, K. (ed.): *Continuum Mechanics in Environmental Sciences and Geophysics*. Springer-Verlag, Wien 1993, CISM Courses and Lectures No. 337, pp. 313–402.

[83] Ehlers, W.: Grundlegende Konzepte in der Theorie Poröser Medien. *Technische Mechanik* **16** (1996), 63–76.

[84] Ehlers, W.: Foundations of multiphasic and porous materials. In Ehlers, W. & Bluhm, J. (eds.): *Porous Media: Theory, Experiments and Numerical Applications*. Springer-Verlag, Berlin 2002, pp. 3–86.

[85] Ehlers, W.: Challenges of porous media models in geo-and biomechanical engineering including electro-chemically active polymers and gels. *International Journal of Advances in Engineering Sciences and Applied Mathematics* **1** (2009), 1–24.

[86] Ehlers, W.: *Poröse Medien – ein kontinuumsmechanisches Modell auf der Basis der Mischungstheorie*. Nachdruck der Habilitationsschrift aus dem Jahre 1989 (Forschungsbericht aus dem Fachbereich Bauwesen der Universität-GH-Essen, Heft 47, Essen 1989), Report No. II-22 of the Institute of Applied Mechanics (CE), University of Stuttgart 2012.

[87] Ehlers, W.: Porous media in the light of history. In Stein, E. (ed.): *The History of Theoretical, Material and Computational Mechanics – Mathematics Meets Mechanics and Engineering. Lecture Notes in Applied Mathematics and Mechanics (LAMM), Vol. 1*. Springer-Verlag, Berlin, Heidelberg 2014, pp. 211–227.

[88] Ehlers, W.: Darcy, Forchheimer, Brinkman and Richards: Classical hydromechanical equations and their significance in the light of the TPM. *Archive of Applied Mechanics* **92** (2020), 619–639.

[89] Ehlers, W. & Acartürk, A.: The role of weakly imposed Dirichlet boundary conditions for numerically stable computations of swelling phenomena. *Computational Mechanics* **43** (2009), 545–557.

[90] Ehlers, W. & Ellsiepen, P.: PANDAS: Ein FE-System zur Simulation von Sonderproblemen der Bodenmechanik. In Wriggers, P.; Meißner, U.; Stein, E. & Wunderlich, W. (eds.): *Finite Elemente in der Baupraxis: Modellierung, Berechnung und Konstruktion*. Ernst & Sohn, Berlin 1998, pp. 391–400.

[91] Ehlers, W.; Ellsiepen, P.; Blome, P.; Mahnkopf, D. & Markert, B.: *Theoretische und numerische Studien zur Lösung von Rand- und Anfangswertproblemen in der Theorie Poröser Medien, Abschlußbericht zum DFG-Forschungsvorhaben Eh 107/6-2*. Bericht Nr. 99-II-1 aus dem Institut für Mechanik (Bauwesen), Universität Stuttgart 1999.

[92] Ehlers, W.; Graf, T. & Ammann, M.: Deformation and localization analysis of partially saturated soil. *Computer Methods in Applied Mechanics and Engineering* **193** (2004), 2885–2910.

[93] Ehlers, W. & Luo, C.: A phase-field approach embedded in the Theory of Porous Media for the description of dynamic hydraulic fracturing. *Computer Methods in Applied Mechanics and Engineering* **315** (2017), 348–368.

[94] Ehlers, W. & Luo, C.: A phase-field approach embedded in the Theory of Porous Media for the description of dynamic hydraulic fracturing, Part II: The crack-opening indicator. *Computer Methods in Applied Mechanics and Engineering* **341** (2018), 429–442.

[95] Ehlers, W. & Markert, B.: On the viscoelastic behaviour of fluid-saturated porous materials. *Granular Matter* **2** (2000), 153–161.

[96] Ehlers, W. & Markert, B.: A linear viscoelastic biphasic model for soft tissues based on the Theory of Porous Media. *ASME Journal of Biomechechanical Engineering* **123** (2001), 418–424.

[97] Ehlers, W.; Morrison, M.; Schröder, P.; Stöhr, D. & Wagner, A.: Multiphasic modelling and computation of metastatic lung-cancer cell proliferation and atrophy in brain tissue based on experimental data. *Biomechanics and Modeling in Mechanobiology* **21** (2022), 277–315.

[98] Ehlers, W. & Wagner, A.: Modelling and simulation methods applied to coupled problems in porous-media mechanics. *Archive of Applied Mechanics* **89** (2019), 609–628.

[99] Eipper, G.: *Theorie und Numerik finiter elastischer Deformationen in fluidgesättigten porösen Festkörpern*. Disseration thesis, Report No. II-1 of the Institute of Applied Mechanics (CE), University of Stuttgart 1998.

[100] Ellsiepen, P.: *Zeit- und ortsadaptive Verfahren angewandt auf Mehrphasenprobleme poröser Medien*. Disseration thesis, Report No. II-3 of the Institute of Applied Mechanics (CE), University of Stuttgart 1999.

[101] Ellsworth, W. L.: Injection-induced earthquakes. *Science* **341** (2013), 1225942, 7 pages.

[102] Engelder, T.: Capillary tension and imbibition sequester frack fluid in Marcellus gas shale. *Proceedings of the National Academy of Sciences* **109** (2012), E3625, 1 page.

[103] Engelder, T.; Cathles, L. M. & Bryndzia, L. T.: The fate of residual treatment water in gas shale. *Journal of Unconventional Oil and Gas Resources* **7** (2014), 33–48.

[104] Eurich, L.: *A quasi-double-porosity thermo-hydro-mechanical model with application to plant tissues*. Disseration thesis, Report No. II-38 of the Institute of Applied Mechanics (CE), University of Stuttgart 2021.

[105] Fillunger, P.: Der Auftrieb in Talsperren. *Österreichische Wochenschrift für den öffentlichen Baudienst* **19** (1913), 532–556; 567–570.

[106] Fillunger, P.: Versuche über die Zugfestigkeit bei allseitigem Wasserdruck. *Österreichische Wochenschrift für den öffentlichen Baudienst* **29** (1915), 443–448.

[107] Finkel, M. L. & Hays, J.: The implications of unconventional drilling for natural gas: A global public health concern. *Public Health* **127** (2013), 889–893.

[108] Forchheimer, P.: Wasserbewegung durch Boden. *Zeitschrift des Vereines Deutscher Ingenieure* **49** (1901), 1736–1741.

[109] Francfort, G. A. & Marigo, J.-J.: Revisiting brittle fracture as an energy minimization problem. *Journal of the Mechanics and Physics of Solids* **46** (1998), 1319–1342.

[110] Frank, U. & Barkley, N.: Remediation of low permeability subsurface formations by fracturing enhancement of soil vapor extraction. *Journal of Hazardous Materials* **40** (1995), 191–201.

[111] Fredlund, D. G. & Rahardjo, H.: *Soil Mechanics for Unsaturated Soils*. John Wiley & Sons, New York 1993.

[112] Fu, P.; Settgast, R. R.; Hao, Y.; Morris, J. P. & Ryerson, F. J.: The influence of hydraulic fracturing on carbon storage performance. *Journal of Geophysical Research: Solid Earth* **122** (2017), 9931–9949.

[113] Gawin, D.; Schrefler, B. A. & Galindo, M.: Thermo-hydro-mechanical analysis of partially saturated porous materials. *Engineering Computations* **13** (1996), 113–143.

[114] Gawin, D.; Simoni, L. & Schrefler, B. A.: Numerical model for hydro-mechanical behaviour in deformable porous media: A benchmark problem. *Computer Methods and Advances in Geomechanics* (1997), 1143–1148.

[115] van Genuchten, M. T.: A closed-form equation for predicting the hydraulic conductivity of unsaturated soils. *Soil Science Society of America Journal* **44** (1980), 892–898.

[116] Gerasimov, T. & De Lorenzis, L.: A line search assisted monolithic approach for phase-field computing of brittle fracture. *Computer Methods in Applied Mechanics and Engineering* **312** (2016), 276–303.

[117] Gerasimov, T.; Römer, U.; Vondřejc, J.; Matthies, H. G. & De Lorenzis, L.: Stochastic phase-field modeling of brittle fracture: Computing multiple crack patterns and their probabilities. *Computer Methods in Applied Mechanics and Engineering* **372** (2020), 113353, 29 pages.

[118] Ginzburg, V. L. & Landau, L. D.: On the theory of superconductivity. *Zhurnal Eksperimentalnoi I Theoreticheskoi Fiziki* **20** (1950), 1064–1082.

[119] Graf, T.: *Multiphasic Flow Processes in Deformable Porous Media under Consideration of Fluid Phase Transitions*. Dissertation thesis, Report No. II-17 of the Institute of Applied Mechanics (CE), University of Stuttgart 2008.

[120] Griffith, A. A.: The phenomena of rupture and flow in solids. *Philosophical Transactions of the Royal Society of London. Series A, Containing Papers of a Mathematical or Physical Character* **221** (1921), 163–198.

[121] Griffith, A. A.: The Theory of Rupture. In *Proceedings of the First International Conference on Applied Mechanics*, Delft 1924, pp. 55–63.

[122] Gross, D. & Seelig, T.: *Fracture Mechanics with an Introduction to Micromechanics*. 3rd edition, Springer International Publishing, Cham 2018.

[123] Gurtin, M. E.: *An Introduction to Continuum Mechanics*. Academic Press, New-York 1982.

[124] Häberle, K.: *Fluid-phase Transitions in a Multiphasic Model of CO2 Sequestration into Deep Aquifers: A Fully Coupled Analysis of Transport Phenomena and Solid Deformation*. Dissertation thesis, Report No. II-34 of the Institute of Applied Mechanics (CE), University of Stuttgart 2017.

[125] Hakim, V. & Karma, A.: Laws of crack motion and phase-field models of fracture. *Journal of the Mechanics and Physics of Solids* **57** (2009), 342–368.

[126] Hassanizadeh, S. M.; Celia, M. A. & Dahle, H. K.: Dynamic effect in the capillary pressure–saturation relationship and its impacts on unsaturated flow. *Vadose Zone Journal* **1** (2002), 38–57.

[127] Hassanizadeh, S. M. & Gray, W. G.: General conservation equations for multi-phase systems: 1. Averaging procedure. *Advances in Water Resources* **2** (1979), 131–144.

[128] Hassanizadeh, S. M. & Gray, W. G.: General conservation equations for multi-phase systems: 2. Mass, momenta, energy, and entropy equations. *Advances in Water Resources* **2** (1979), 191–203.

[129] Hassanizadeh, S. M. & Gray, W. G.: Mechanics and thermodynamics of multiphase flow in porous media including interphase boundaries. *Advances in Water Resources* **13** (1990), 169–186.

[130] Hassanizadeh, S. M. & Gray, W. G.: Thermodynamic basis of capillary pressure in porous media. *Water Resources Research* **29** (1993), 3389–3405.

[131] Haupt, P.: Foundation of Continuum Mechanics. In Hutter, K. (ed.): *Continuum Mechanics in Environmental Sciences and Geophysics*. Springer-Verlag, Wien 1993, CISM Courses and Lectures No. 337, pp. 1–77.

[132] Haupt, P.: *Continuum Mechanics and Theory of Materials*. Springer-Verlag, Berlin, Heidelberg 2000.

[133] Heider, Y.: *Saturated Porous Media Dynamics with Application to Earthquake Engineering*. Dissertation thesis, Report No. II-25 of the Institute of Applied Mechanics (CE), University of Stuttgart 2012.

[134] Heider, Y.: A review on phase-field modeling of hydraulic fracturing. *Engineering Fracture Mechanics* **253** (2021), 107881, 30 pages.

[135] Heider, Y. & Markert, B.: A phase-field modeling approach of hydraulic fracture in saturated porous media. *Mechanics Research Communications* **80** (2017), 38–46.

[136] Heider, Y.; Reiche, S.; Siebert, P. & Markert, B.: Modeling of hydraulic fracturing using a porous-media phase-field approach with reference to experimental data. *Engineering Fracture Mechanics* **202** (2018), 116–134.

[137] Heider, Y. & Sun, W.: A phase field framework for capillary-induced fracture in unsaturated porous media: Drying-induced vs. hydraulic cracking. *Computer Methods in Applied Mechanics and Engineering* **359** (2020), 112647, 29 pages.

[138] Helmig, R.: *Multiphase Flow and Transport Processes in the Subsurface: A Contribution to the Modeling of Hydrosystems*. Springer-Verlag, Berlin, Heidelberg 1997.

[139] Henry, H. & Levine, H.: Dynamic instabilities of fracture under biaxial strain using a phase field model. *Physical Review Letters* **93** (2004), 105504, 4 pages.

[140] Hofacker, M.: *A thermodynamically consistent phase field approach to fracture*. Dissertation thesis, University of Stuttgart, Institute of Applied Mechanics (CE) (2014).

[141] Holian, B. L. & Ravelo, R.: Fracture simulations using large-scale molecular dynamics. *Physical Review B* **51** (1995), 11275–11288.

[142] Holzapfel, G. A.: *Nonlinear Solid Mechanics: A Continuum Approach for Engineering*. Wiley, Chichester 2000.

[143] Hood, P. & Taylor, C.: Navier-Stokes equations using mixed interpolation. In Oden, J. T.; Zienkiewicz, O. C.; Gallagher, R. H. & Taylor, C. (eds.): *Finite Element Methods in Flow Problems*. UAH Press, Huntsville, Alabama 1974, pp. 121–132.

[144] Howarth, R. W.; Ingraffea, A. & Engelder, T.: Should fracking stop? *Nature* **477** (2011), 271–275.

[145] Huerta, N. J.; Cantrell, K. J.; White, S. K. & Brown, C. F.: Hydraulic fracturing to enhance injectivity and storage capacity of CO2 storage reservoirs: Benefits and risks. *International Journal of Greenhouse Gas Control* **100** (2020), 103105, 12 pages.

[146] Hughes, T. J. R.: *The Finite Element Method: Linear Static and Dynamic Finite Element Analysis*. Dover Publications, New York 2000.

[147] Inglis, C. E.: Stresses in a plate due to the presence of cracks and sharp corners. *Transactions of the Royal Institution of Naval Architects* **55** (1913), 219–230.

[148] Irwin, G.: Fracture. In Flügge, S. (ed.): *Handbuch der Physik*. Springer, Berlin 1958, Vol. 6, pp. 551–590.

[149] Irwin, G. R.: Analysis of stresses and strains near the end of a crack traversing a plate. *Journal of Applied Mechanics* **24** (1957), 361–364.

[150] Jackson, R. B.; Vengosh, A.; Darrah, T. H.; Warner, N. R.; Down, A.; Poreda, R. J.; Osborn, S. G.; Zhao, K. & Karr, J. D.: Increased stray gas abundance in a subset of drinking water wells near Marcellus shale gas extraction. *Proceedings of the National Academy of Sciences* **110** (2013), 11250–11255.

[151] Jommi, C.; Vaunat, J.; Gens, A.; Gawin, D. & Schrefler, B. A.: Multiphase flow in porous media: A numerical benchmark. *NAFEMS, Proceedings of the 6th International Conference* **2** (1997), 1338–1349.

[152] Kalaydjian, F.: A macroscopic description of multiphase flow in porous media involving spacetime evolution of fluid/fluid interface. *Transport in Porous Media* **2** (1987), 537–552.

[153] Karajan, N.: *An Extended Biphasic Description of the Inhomogeneous and Anisotropic Intervertebral Disc*. Dissertation, Report No. II-19 of the Institute of Applied Mechanics (CE), University of Stuttgart 2009.

[154] Karma, A.; Kessler, D. A. & Levine, H.: Phase-field model of mode III dynamic fracture. *Physical Review Letters* **87** (2001), 045501, 4 pages.

[155] Katsube, N. & Carroll, M.: The modified mixture theory for fluid-filled porous materials: Theory. *Journal of Applied Mechanics* **54** (1987), 35–40.

[156] Kelly, P. D.: A reacting continuum. *International Journal of Engineering Science* **2** (1964), 129–153.

[157] Kerr, R. A.: Learning how to not make your own earthquakes. *Science* **335** (2012), 1436–1437.

[158] Kiendl, J.; Ambati, M.; De Lorenzis, L.; Gomez, H. & Reali, A.: Phase-field description of brittle fracture in plates and shells. *Computer Methods in Applied Mechanics and Engineering* **312** (2016), 374–394.

[159] Kitanidis, P. K.: *Introduction to Geostatistics: Applications in Hydrogeology*. Cambridge University Press 1997.

[160] Klubertanz, G.; Laloui, L. & Vulliet, L.: Numerical modeling of unsaturated porous media as a two and three phase medium: A comparison. *Computer Methods and Advances in Geomechanics* **2** (1997), 1159–1164.

[161] Kool, J. & Parker, J. C.: Development and evaluation of closed-form expressions for hysteretic soil hydraulic properties. *Water Resources Research* **23** (1987), 105–114.

[162] Kopaničáková, A.; Kothari, H. & Krause, R.: Nonlinear field-split preconditioners for solving monolithic phase-field models of brittle fracture. *Computer Methods in Applied Mechanics and Engineering* **403** (2023), 115733, 31 pages.

[163] Kovscek, A.; Wong, H. & Radke, C.: A pore-level scenario for the development of mixed wettability in oil reservoirs. *American Institute of Chemical Engineers Journal* **39** (1993), 1072–1085.

[164] Kuhn, C. & Müller, R.: A continuum phase field model for fracture. *Engineering Fracture Mechanics* **77** (2010), 3625–3634.

[165] Kuhn, C. & Müller, R.: A phase field model for fracture. *Proceedings in Applied Mathematics and Mechanics* **8** (2008), 10223–10224.

[166] Kuhn, C.; Schlüter, A. & Müller, R.: On degradation functions in phase field fracture models. *Computational Materials Science* **108** (2015), 374–384.

[167] Lancioni, G. & Royer-Carfagni, G.: The variational approach to fracture mechanics. A practical application to the French *Panthéon* in Paris. *Journal of Elasticity* **95** (2009), 1–30.

[168] Lecampion, B.; Bunger, A. & Zhang, X.: Numerical methods for hydraulic fracture propagation: A review of recent trends. *Journal of Natural Gas Science and Engineering* **49** (2018), 66–83.

[169] Leichsenring, P.; Serdas, S.; Wallmersperger, T.; Bluhm, J. & Schröder, J.: Electrochemical aspects of IPMCs within the framework of the theory of porous media. *Smart Materials and Structures* **26** (2017), 045004, 14 pages.

[170] Lenhard, R.: Measurement and modeling of three-phase saturation-pressure hysteresis. *Journal of Contaminant Hydrology* **9** (1992), 243–269.

[171] Lenhard, R.; Parker, J. & Mishra, S.: On the correspondence between Brooks-Corey and van Genuchten models. *Journal of Irrigation and Drainage Engineering* **115** (1989), 744–751.

[172] Leverett, M. C.: Flow of oil-water mixtures through unconsolidated sands. *Transactions of the AIME* **132** (1939), 149–171.

[173] Lewis, R. W. & Schrefler, B. A.: *The Finite Element Method in the Static and Dynamic Deformation and Consolidation of Porous Media*. John Wiley & Sons 1998.

[174] Liakopoulos, A. C.: Theoretical solution of the gravity drainage problem. *Journal of Hydraulic Research* **2** (1964), 50–74.

[175] Liakopoulos, A. C.: *Transient flow through unsaturated porous media*. Dissertation thesis, University of California, Berkeley (1964).

[176] Liu, I.-S.: Method of Lagrange multipliers for exploitation of entropy principle. *Archive for Rational Mechanics and Analysis* **46** (1972), 131–148.

[177] Liu, I.-S. & Müller, I.: Thermodynamics of mixtures of fluids. In Truesdell, C. (ed.): *Rational Thermodynamics*. 2nd edition, Springer-Verlag, New York 1984, pp. 264–285.

[178] Luo, C.: *A Phase-Field Model Embedded in the Theory of Porous Media with Application to Hydraulic Fracturing*. Dissertation thesis, Report No. II-35 of the Institute of Applied Mechanics (CE), University of Stuttgart 2019.

[179] Luo, C.; Sanavia, L. & De Lorenzis, L.: Phase-field modeling of drying-induced cracks: Choice of coupling and study of homogeneous and localized damage. *Computer Methods in Applied Mechanics and Engineering* **410** (2023), 115962, 26 pages.

[180] Mahnkopf, D.: *Lokalisierung fluidgesättigter poröser Festkörper bei finiten elastoplastischen Deformationen*. Dissertation thesis, Report No. II-5 of the Institute of Applied Mechanics (CE), University of Stuttgart 2000.

[181] Malvern, L. E.: *Introduction to the Mechanics of a Continuous Medium*. Prentice-Hall International, Englewood Cliffs (NJ) 1969.

[182] Manthey, S.: *Two-phase flow processes with dynamic effects in porous media - parameter estimation and simulation*. Dissertation thesis, University of Stuttgart, Institute for Modelling Hydraulic and Environmental Systems (2006).

[183] Mardal, K.-A. & Langtangen, H.: Mixed finite elements. In Langtangen, H. P. & Tveito, A. (eds.): *Advanced Topics in Computational Partial Differential Equations: Numerical Methods and Diffpack Programming*. Springer-Verlag, Berlin, Heidelberg 2003, pp. 153–197.

[184] Markert, B.: *Porous Media Viscoelasticity with Application to Polymeric Foams*. Dissertation thesis, Report No. II-12 of the Institute of Applied Mechanics (CE), University of Stuttgart 2005.

[185] Markert, B.: A constitutive approach to 3-d nonlinear fluid flow through finite deformable porous continua. *Transport in Porous Media* **70** (2007), 427–450.

[186] Markert, B. & Heider, Y.: Coupled multi-field continuum methods for porous media fracture. In Mehl, M.; Bischoff, M. & Schäfer, M. (eds.): *Recent Trends in Computational Engineering-CE2014*. Springer International Publishing, Cham 2015, pp. 167–180.

[187] Markert, B.; Heider, Y. & Ehlers, W.: Comparison of monolithic and splitting solution schemes for dynamic porous media problems. *International Journal for Numerical Methods in Engineering* **82** (2010), 1341–1383.

[188] Mauthe, S. & Miehe, C.: Hydraulic fracture in poro-hydro-elastic media. *Mechanics Research Communications* **80** (2017), 69–83.

[189] Miehe, C.; Hofacker, M.; Schänzel, L.-M. & Aldakheel, F.: Phase field modeling of fracture in multi-physics problems. Part II. Coupled brittle-to-ductile failure criteria and crack propagation in thermo-elastic–plastic solids. *Computer Methods in Applied Mechanics and Engineering* **294** (2015), 486–522.

[190] Miehe, C.; Hofacker, M. & Welschinger, F.: A phase field model for rate-independent crack propagation: Robust algorithmic implementation based on operator splits. *Computer Methods in Applied Mechanics and Engineering* **199** (2010), 2765–2778.

[191] Miehe, C. & Mauthe, S.: Phase field modeling of fracture in multi-physics problems. Part III. Crack driving forces in hydro-poro-elasticity and hydraulic fracturing of fluid-saturated porous media. *Computer Methods in Applied Mechanics and Engineering* **304** (2016), 619–655.

[192] Miehe, C.; Mauthe, S. & Teichtmeister, S.: Minimization principles for the coupled problem of Darcy–Biot-type fluid transport in porous media linked to phase field modeling of fracture. *Journal of the Mechanics and Physics of Solids* **82** (2015), 186–217.

[193] Miehe, C.; Welschinger, F. & Hofacker, M.: Thermodynamically consistent phase-field models of fracture: Variational principles and multi-field FE implementations. *International Journal for Numerical Methods in Engineering* **83** (2010), 1273–1311.

[194] Mikelić, A.; Wheeler, M. F. & Wick, T.: A phase-field method for propagating fluid-filled fractures coupled to a surrounding porous medium. *Multiscale Modeling and Simulation* **13** (2015), 367–398.

[195] Mikelić, A.; Wheeler, M. F. & Wick, T.: Phase-field modeling of a fluid-driven fracture in a poroelastic medium. *Computational Geoscience* **19** (2015), 1171–1195.

[196] Mikelić, A.; Wheeler, M. F. & Wick, T.: A quasi-static phase-field approach to pressurized fractures. *Nonlinearity* **28** (2015), 1371–1399.

[197] Moës, N.; Dolbow, J. & Belytschko, T.: A finite element method for crack growth without remeshing. *International Journal for Numerical Methods in Engineering* **46** (1999), 131–150.

[198] Mualem, Y.: A new model for predicting the hydraulic conductivity of unsaturated porous media. *Water Resources Research* **12** (1976), 513–522.

[199] Mumford, D. B. & Shah, J.: Optimal approximations by piecewise smooth functions and associated variational problems. *Communications on Pure and Applied Mathematics* **42** (1989), 577–685.

[200] Muskat, M.; Wyckoff, R.; Botset, H. & Meres, M.: Flow of gas-liquid mixtures through sands. *Transactions of the AIME* **123** (1937), 69–96.

[201] Myers, T.: Potential contaminant pathways from hydraulically fractured shale to aquifers. *Groundwater* **50** (2012), 872–882.

[202] Nguyen, T.; Yvonnet, J.; Zhu, Q.-Z.; Bornert, M. & Chateau, C.: A phase field method to simulate crack nucleation and propagation in strongly heterogeneous materials from direct imaging of their microstructure. *Engineering Fracture Mechanics* **139** (2015), 18–39.

[203] Nguyen, V. P.; Stroeven, M. & Sluys, L. J.: Multiscale continuous and discontinuous modeling of heterogeneous materials: A review on recent developments. *Journal of Multiscale Modelling* **3** (2011), 229–270.

[204] Olasolo, P.; Juárez, M.; Morales, M.; D'Amico, S. & Liarte, I.: Enhanced geothermal systems (EGS): A review. *Renewable and Sustainable Energy Reviews* **56** (2016), 133–144.

[205] Øren, P.-E.; Bakke, S. & Arntzen, O. J.: Extending predictive capabilities to network models. *SPE Journal* **3** (1998), 324–336.

[206] Ortiz, M. & Pandolfi, A.: Finite-deformation irreversible cohesive elements for three-dimensional crack-propagation analysis. *International Journal for Numerical Methods in Engineering* **44** (1999), 1267–1282.

[207] Pan, Z.; Ma, R.; Wang, D. & Chen, A.: A review of lattice type model in fracture mechanics: theory, applications, and perspectives. *Engineering Fracture Mechanics* **190** (2018), 382–409.

[208] Pillai, U.; Heider, Y. & Markert, B.: A diffusive brittle fracture model for heterogeneous solids and porous materials with implementation using a user-element subroutine. *Computational Materials Science* **153** (2018), 36–47.

[209] Pise, M.; Bluhm, J. & Schröder, J.: Elasto-plastic phase-field model of hydraulic fracture in saturated binary porous media. *International Journal for Multiscale Computational Engineering* **17** (2019), 201–221.

[210] Rempler, H.-U.: *Damage in Multi-Phasic Materials Computed with the Extended Finite-Element Method*. Disseration thesis, Report No. II-23 of the Institute of Applied Mechanics (CE), University of Stuttgart 2012.

[211] Richards, L. A.: Capillary conduction of liquids through porous mediums. *Physics* **1** (1931), 318–333.

[212] Rountree, C. L.; Kalia, R. K.; Lidorikis, E.; Nakano, A.; Van Brutzel, L. & Vashishta, P.: Atomistic aspects of crack propagation in brittle materials: Multimillion atom molecular dynamics simulations. *Annual Review of Materials Research* **32** (2002), 377–400.

[213] Saad, Y. & Schultz, M. H.: GMRES: A generalized minimal residual algorithm for solving nonsymmetric linear systems. *SIAM Journal on Scientific and Statistical Computing* **7** (1986), 856–869.

[214] Santillán, D.; Juanes, R. & Cueto-Felgueroso, L.: Phase field model of fluid-driven fracture in elastic media: Immersed-fracture formulation and validation with analytical solutions. *Journal of Geophysical Research: Solid Earth* **122** (2017), 2565–2589.

[215] Santillán, D.; Juanes, R. & Cueto-Felgueroso, L.: Phase field model of hydraulic fracturing in poroelastic media: Fracture propagation, arrest, and branching under fluid injection and extraction. *Journal of Geophysical Research: Solid Earth* **123** (2018), 2127–2155.

[216] Sargado, J. M.; Keilegavlen, E.; Berre, I. & Nordbotten, J. M.: High-accuracy phase-field models for brittle fracture based on a new family of degradation functions. *Journal of the Mechanics and Physics of Solids* **111** (2018), 458–489.

[217] Schenke, M.: *Parallel Simulation of Volume-Coupled Multi-Field Problems with Special Application to Soil Dynamics*. Dissertation thesis, Report Nr. II-32 of the Institute of Applied Mechanics (CE), University of Stuttgart 2017.

[218] Schlangen, E. & Van Mier, J.: Simple lattice model for numerical simulation of fracture of concrete materials and structures. *Materials and Structures* **25** (1992), 534–542.

[219] Scholz, B.: *Application of a Micropolar Model to the Localization Phenomena in Granular Materials: General Model, Sensitivity Analysis and Parameter Optimization*. Dissertation thesis, Report No. II-15 of the Institute of Applied Mechanics (CE), University of Stuttgart 2007.

[220] Schrefler, B. A. & Scotta, R.: A fully coupled dynamic model for two-phase fluid flow in deformable porous media. *Computer Methods in Applied Mechanics and Engineering* **190** (2001), 3223–3246.

[221] Schrefler, B. A.; Secchi, S. & Simoni, L.: On adaptive refinement techniques in multi-field problems including cohesive fracture. *Computer Methods in Applied Mechanics and Engineering* **195** (2006), 444–461.

[222] Secchi, S. & Schrefler, B. A.: Hydraulic fracturing and its peculiarities. *Asia Pacific Journal on Computational Engineering* **1** (2014), 1–21.

[223] Sheta, H.: *Simulation von Mehrphasenvorgängen in porösen Medien unter Einbeziehung von Hysterese Effekten*. Dissertation thesis, University of Stuttgart, Institute for Modelling Hydraulic and Environmental Systems (1999).

[224] Smith, M. B. & Montgomery, C.: *Hydraulic fracturing*. CRC Press, Boca Raton (FL) 2015.

[225] Sneddon, I. N.: The distribution of stress in the neighbourhood of a crack in an elastic solid. *Proceedings of the Royal Society of London. Series A. Mathematical and Physical Sciences* **187** (1946), 229–260.

[226] Sonntag, A.; Wagner, A. & Ehlers, W.: Dynamic hydraulic fracturing in partially saturated porous media. *Computer Methods in Applied Mechanics and Engineering* **414** (2023), 116121, 34 pages.

[227] Späth, M.; Herrmann, C.; Prajapati, N.; Schneider, D.; Schwab, F.; Selzer, M. & Nestler, B.: Multiphase-field modelling of crack propagation in geological materials and porous media with Drucker-Prager plasticity. *Computational Geosciences* **25** (2021), 325–343.

[228] Spatschek, R.; Brener, E. & Karma, A.: Phase field modeling of crack propagation. *Philosophical Magazine* **91** (2011), 75–95.

[229] Specht, S.; Bluhm, J. & Schröder, J.: Continuum mechanical description of an extrinsic and autonomous self-healing material based on the theory of porous media. In Hager, M. D.; van der Zwaag, S. & Schubert, U. S. (eds.): *Self-healing Materials*. Springer International Publishing, Cham 2016, pp. 143–184.

[230] Stauffer, F.: *Einfluss der kapillaren Zone auf instationäre Drainagevorgänge*. Dissertation thesis, Eidgenössische Technische Hochschule Zürich (1977).

[231] Steeb, H. & Renner, J.: Mechanics of poro-elastic media: A review with emphasis on foundational state variables. *Transport in Porous Media* **130** (2019), 437–461.

[232] Steinke, C. & Kaliske, M.: A phase-field crack model based on directional stress decomposition. *Computational Mechanics* **63** (2019), 1019–1046.

[233] Stenberg, R.: On some three-dimensional finite elements for incompressible media. *Computer Methods in Applied Mechanics and Engineering* **63** (1987), 261–269.

[234] Taylor, C. & Hood, P.: A numerical solution of the Navier-Stokes equations using the finite element technique. *Computers & Fluids* **1** (1973), 73–100.

[235] von Terzaghi, K.: Die Berechnung der Durchlässigkeitsziffer des Tones aus dem Verlauf der hydrodynamischen Spannungserscheinungen. *Sitzungsberichte der Akademie der Wissenschaften in Wien, Mathematisch-Naturwissenschaftliche Klasse, Abteilung II a* **132** (1923), 125–138.

[236] von Terzaghi, K.: The shearing resistance of saturated soils and the angle between the planes of shear. In Casagrande, A.; Rudledge, P. C. & Watson, J. D. (eds.): *Proceedings of the International Conference on Soil Mechanics and Foundation Engineering*. Harvard University 1936, Vol. 1, pp. 54–56.

[237] Truesdell, C.: Sulle basi della termomeccanica. *Rendiconti Lincei* **22** (1957), 158–166.

[238] Truesdell, C.: The origins of rational thermodynamics. In Truesdell, C. (ed.): *Rational Thermodynamics*. 2nd edition, Springer-Verlag, New York 1984, pp. 1–57.

[239] Truesdell, C.: Thermodynamics of diffusion. In Truesdell, C. (ed.): *Rational Thermodynamics*. 2nd edition, Springer-Verlag, New York 1984, pp. 219–236.

[240] Truesdell, C. & Noll, W.: *The Non-linear Field Theories of Mechanics, Vol. III/3*. Springer-Verlag, Berlin 1965.

[241] Truesdell, C. & Toupin, R.: The classical field theories. In Flügge, S. (ed.): *Handbuch der Physik, Vol. III/1*. Springer-Verlag, Berlin 1960, pp. 226–902.

[242] Vidic, R. D.; Brantley, S. L.; Vandenbossche, J. M.; Yoxtheimer, D. & Abad, J. D.: Impact of shale gas development on regional water quality. *Science* **340** (2013), 1235009, 10 pages.

[243] Wagner, A.: *Extended Modelling of the Multiphasic Human Brain Tissue with Application to Drug-Infusion Processes*. Disseration thesis, Report No. II-27 of the Institute of Applied Mechanics (CE), University of Stuttgart 2014.

[244] Wagner, A.: *Continuum Mechanics of Multicomponent Materials – Modelling, Numerics and Applications for Biological Materials in the Framework of the Theory of Porous Media.* Habilitation thesis, Report No. II-39 of the Institute of Applied Mechanics (CE), University of Stuttgart 2021.

[245] Wagner, A.; Eggenweiler, E.; Weinhardt, F.; Trivedi, Z.; Krach, D.; Lohrmann, C.; Jain, K.; Karadimitriou, N.; Bringedal, C.; Voland, P.; Holm, C.; Class, H.; Steeb, H. & Rybak, I.: Permeability estimation of regular porous structures: A benchmark for comparison of methods. *Transport in Porous Media* **138** (2021), 1–23.

[246] Wagner, A.; Sonntag, A.; Reuschen, S.; Nowak, W. & Ehlers, W.: Hydraulically induced fracturing in heterogeneous porous media using a TPM-phase-field model and geostatistics. *Proceedings in Applied Mathematics and Mechanics* **23** (2023), e202200118, 6 pages.

[247] Wang, J.; Sonntag, A.; Lee, D.; Xotta, G.; Salomoni, V. A.; Steeb, H.; Ehlers, W. & Wagner, A.: Modelling and simulation of natural hydraulic fracturing applied to experiments on natural sandstone cores (2023), submitted.

[248] Wick, T.: Modified Newton methods for solving fully monolithic phase-field quasi-static brittle fracture propagation. *Computer Methods in Applied Mechanics and Engineering* **325** (2017), 577–611.

[249] Wilson, Z. A. & Landis, C. M.: Phase-field modeling of hydraulic fracture. *Journal of the Mechanics and Physics of Solids* **96** (2016), 264–290.

[250] Witherspoon, P. A.; Wang, J. S. Y.; Iwai, K. & Gale, J. E.: Validity of cubic law for fluid flow in a deformable rock fracture. *Water Resources Research* **16** (1980), 1016–1024.

[251] Woltman, R.: *Beyträge zur Hydraulischen Architektur. Dritter Band.* Johann Christian Dietrich, Göttingen 1794.

[252] Wright, R. & Muma, R. D.: High-volume hydraulic fracturing and human health outcomes: A scoping review. *Journal of Occupational and Environmental Medicine* **60** (2018), 424–429.

[253] Wu, J. Y.; Nguyen, V. P.; Nguyen, C. T.; Sutula, D.; Sinaie, S. & Bordas, S.: Phase-field modeling of fracture. In Bordas, S. & Balint, D. (eds.): *Advances in Applied Mechanics*. Elsevier, Amsterdam 2020, Vol. 53, pp. 1–183.

[254] Wu, T. & De Lorenzis, L.: A phase-field approach to fracture coupled with diffusion. *Computer Methods in Applied Mechanics and Engineering* **312** (2016), 196–223.

[255] Wu, Y.-S. & Forsyth, P. A.: On the selection of primary variables in numerical formulation for modeling multiphase flow in porous media. *Journal of Contaminant Hydrology* **48** (2001), 277–304.

[256] Xu, X. P. & Needleman, A.: Numerical simulations of fast crack-growth in brittle solids. *Journal of the Mechanics and Physics of Solids* **42** (1994), 1397–1434.

[257] Yarema, S. Y.: On the contribution of G. R. Irwin to fracture mechanics. *Materials Science* **31** (1996), 617–623.

[258] Yoshioka, K.; Naumov, D. & Kolditz, O.: On crack opening computation in variational phase-field models for fracture. *Computer Methods in Applied Mechanics and Engineering* **369** (2020), 113210, 24 pages.

[259] Zienkiewicz, O.; Qu, S.; Taylor, R. & Nakazawa, S.: The patch test for mixed formulations. *International Journal for Numerical Methods in Engineering* **23** (1986), 1873–1883.

[260] Zienkiewicz, O. C. & Taylor, R. L.: *The Finite Element Method: Solid and Fluid Mechanics. Dynamics and Non-Linearity*, Vol. 2. 4th edition, McGraw-Hill, London 1991.

Presently published contributions in this report series

II-1 Gernot Eipper: *Theorie und Numerik finiter elastischer Deformationen in fluidgesättigten porösen Festkörpern*, 1998.

II-2 Wolfram Volk: *Untersuchung des Lokalisierungsverhaltens mikropolarer poröser Medien mit Hilfe der Cosserat-Theorie*, 1999.

II-3 Peter Ellsiepen: *Zeit- und ortsadaptive Verfahren angewandt auf Mehrphasenprobleme poröser Medien*, 1999.

II-4 Stefan Diebels: *Mikropolare Zweiphasenmodelle: Formulierung auf der Basis der Theorie Poröser Medien*, 2000.

II-5 Dirk Mahnkopf: *Lokalisierung fluidgesättigter poröser Festkörper bei finiten elastoplastischen Deformationen*, 2000.

II-6 Heiner Müllerschön: *Spannungs-Verformungsverhalten granularer Materialien am Beispiel von Berliner Sand*, 2000.

II-7 Stefan Diebels (Ed.): *Zur Beschreibung komplexen Materialverhaltens: Beiträge anläßlich des 50. Geburtstages von Herrn Prof. Dr.-Ing. Wolfgang Ehlers*, 2001.

II-8 Jack Widjajakusuma: *Quantitative Prediction of Effective Material Parameters of Heterogeneous Materials*, 2002.

II-9 Alexander Droste: *Beschreibung und Anwendung eines elastisch-plastischen Materialmodells mit Schädigung für hochporöse Metallschäume*, 2002.

II-10 Peter Blome: *Ein Mehrphasen-Stoffmodell für Böden mit Übergang auf Interface-Gesetze*, 2003.

II-11 Martin Ammann: *Parallel Finite Element Simulations of Localization Phenomena in Porous Media*, 2005.

II-12 Bernd Markert: *Porous Media Viscoelasticity with Application to Polymeric Foams*, 2005.

II-13 Saeed Reza Ghadiani: *A Multiphasic Continuum Mechanical Model for Design Investigations of an Effusion-Cooled Rocket Thrust Chamber*, 2005.

II-14 Wolfgang Ehlers & Bernd Markert (Eds.): *Proceedings of the 1st GAMM Seminar on Continuum Biomechanics*, 2005.

II-15 Bernd Scholz: *Application of a Micropolar Model to the Localization Phenomena in Granular Materials: General Model, Sensitivity Analysis and Parameter Optimization*, 2007.

II-16 Wolfgang Ehlers & Nils Karajan (Eds.): *Proceedings of the 2nd GAMM Seminar on Continuum Biomechanics*, 2007.

II-17 Tobias Graf: *Multiphasic Flow Processes in Deformable Porous Media under Consideration of Fluid Phase Transitions*, 2008.

II-18 Ayhan Acartürk: *Simulation of Charged Hydrated Porous Materials*, 2009.

II-19 Nils Karajan: *An Extended Biphasic Description of the Inhomogeneous and Anisotropic Intervertebral Disc*, 2009.

II-20 Bernd Markert: *Weak or Strong – On Coupled Problems In Continuum Mechanics*, 2010.

II-21 Wolfgang Ehlers & Bernd Markert (Eds.): *Proceedings of the 3rd GAMM Seminar on Continuum Biomechanics*, 2012.

II-22 Wolfgang Ehlers: *Poröse Medien – ein kontinuumsmechanisches Modell auf der Basis der Mischungstheorie*, 2012. Nachdruck der Habilitationsschrift aus dem Jahr 1989 (Forschungsberichte aus dem Fachbereich Bauwesen der Universität-GH-Essen **47**, Essen 1989).

II-23 Hans-Uwe Rempler: *Damage in multi-phasic Materials Computed with the Extended Finite-Element Method*, 2012.

II-24 Irina Komarova: *Carbon-Dioxide Storage in the Subsurface: A Fully Coupled Analysis of Transport Phenomena and Solid Deformation*, 2012.

II-25 Yousef Heider: *Saturated Porous Media Dynamics with Application to Earthquake Engineering*, 2012.

II-26 Okan Avci: *Coupled Deformation and Flow Processes of Partial Saturated Soil: Experiments, Model Validation and Numerical Investigations*, 2013.

II-27 Arndt Wagner: *Extended Modelling of the Multiphasic Human Brain Tissue with Application to Drug-Infusion Processes*, 2014.

II-28 Joffrey Mabuma: *Multi-Field Modelling and Simulation of the Human Hip Joint*, 2014.

II-29 Robert Krause: *Growth, Modelling and Remodelling of Biological Tissue*, 2014.

II-30 Seyedmohammad Zinatbakhsh: *Coupled Problems in the Mechanics of Multi-Physics and Multi-Phase Materials*, 2015.

II-31 David Koch: *Thermomechanical Modelling of Non-isothermal Porous Materials with Application to Enhanced Geothermal Systems*, 2016.

II-32 Maik Schenke: *Parallel Simulation of Volume-coupled Multi-field Problems with Special Application to Soil Dynamics*, 2017.

II-33 Steffen Mauthe: *Variational Multiphysics Modeling of Diffusion in Elastic Solids and Hydraulic Fracturing in Porous Media*, 2017.

II-34 Kai Häberle: *Fluid-Phase Transitions in a Multiphasic Model of CO2 Sequestration into Deep Aquifers: A fully coupled analysis of transport phenomena and solid deformation*, 2017.

II-35 Chenyi Luo: *A Phase-field Model Embedded in the Theory of Porous Media with Application to Hydraulic Fracturing*, 2018.

II-36 Sami Bidier: *From Particle Mechanics to Micromorphic Continua*, 2019.

II-37 Davina Fink: *Model Reduction applied to Finite-Element Techniques for the Solution of Porous-Media Problems*, 2019.

II-38 Jan Lukas Eurich: *A quasi-double-porosity thermo-hydro-mechanical model with application to plant tissues*, 2021.

II-39 Arndt Wagner: *Continuum Mechanics of Multicomponent Materials – Modelling, Numerics and Applications for Biological Materials in the Framework of the Theory of Porous Media*, 2021.

II-40 Alixa Sonntag: *Partially Saturated Porous Solids under Dynamic Hydraulic Fracturing*, 2023.

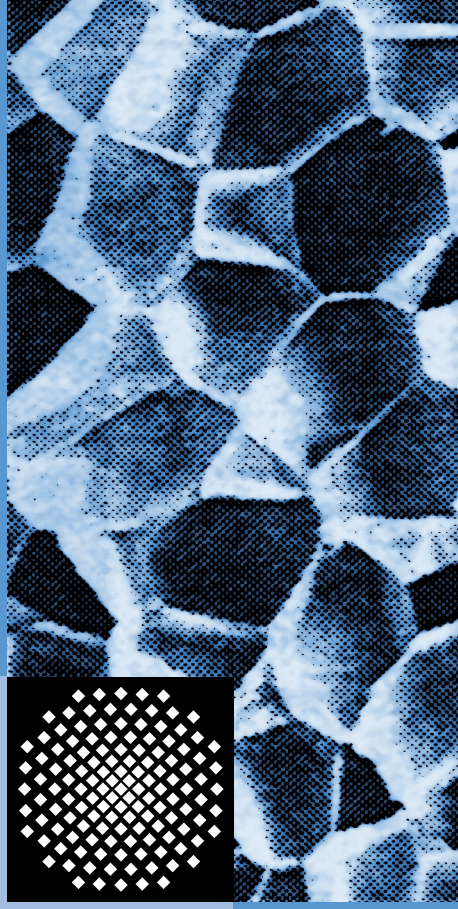

ISBN 978-3-937399-40-9
(D 93 – Dissertation, Universität Stuttgart)